THE ADSORPTION OF CO, N_2 AND Li ON Ru(109) AND Ru(001)

By

Gregg Alvin Morgan, Jr.

B.A Chemistry, Thiel College, 2000

Submitted to the Graduate Faculty of

Arts and Sciences in partial fulfillment

of the requirements for the degree of

Doctor of Philosophy

University of Pittsburgh

2007

UNIVERSITY OF PITTSBURGH

FACULTY OF ARTS AND SCIENCES

This dissertation was presented

By:

Gregg Alvin Morgan, Jr.

It was defended on

August 9, 2007

and approved by

Dr. David Pratt

Dr. David Waldeck

Dr. J. Karl Johnson

Dr. John T. Yates, Jr.
Dissertation Director

The Adsorption of CO, N_2 and Li on Ru(109) and Ru(001)

Gregg Alvin Morgan, Jr., PhD

University of Pittsburgh, 2007

The chemistry of carbon monoxide and dinitrogen on an atomically stepped Ru(109) and an atomically smooth Ru(001) single crystal surface have been thoroughly investigated using ultra high vacuum and surface science techniques. The investigations focused on the effect of the metal surface morphology on the simplest of the surface reactions; adsorption, desorption, and dissociation.

Building on the previous conclusion that CO dissociates on the step sites of Ru(109) producing mobile atomic C and O species, chemisorbed CO was bombarded with atomic hydrogen in an attempt to produce and spectroscopically observe a formyl, HCO, species by IRAS and TPD. The interaction of the two species did not produce any evidence of an HCO species, but resulted in the observation of surface crowding of the CO(a) by H(a) species.

The step sites of Ru(109) have been found to exhibit special N_2 adsorption characteristics compared to the terraces of the Ru(109) surface. Nitrogen desorbs from Ru(109) in three distinct desorption processes. A high temperature desorption feature has been assigned to the molecular desorption from the atomic step sites. The electron stimulated dissociation of chemisorbed nitrogen results in a high temperature recombinative desorption feature between 400 and 800 K.

A direct comparison of the vibrational behavior of nitrogen on Ru(109) and Ru(001) confirms the postulate that the step sites of single crystals exhibit special characteristics. Two vibrational bands, attributed to molecular nitrogen adsorbed on the terrace and step sites, respectively, are observed after thermal ordering of the adlayer. Nitrogen adsorbed on the

terraces of the Ru(109) surface is adsorbed more strongly than on the atomically smooth Ru(001) as indicated by the lower singleton frequency on the Ru(109) surface and the lower maximum desorption temperature on the Ru(001) surface.

The interaction of adsorbed species with Li promoter atoms was investigated to determine the effect promoter atoms would have on catalytic reactions. The coadsorption of Li with CO and N_2 on the two Ru surfaces results in both short and long range interactions. These interactions result in a weakened molecular bond characterized by a red-shifted vibrational frequency in addition to complex formation on the surface.

TABLE OF CONTENTS

LIST OF TABLES

LIST OF FIGURES

PREFACE

This incredible milestone in my life would not have been possible without the continued support and guidance of a variety of individuals. I will do my best to acknowledge the people who have made this incredible achievement possible.

I would like to begin by thanking my research advisor and mentor, Dr. John T. Yates, Jr., for the scientific guidance and advice that he has always been willing to give over the past five and a half years. John has an incredible passion for the scientific research and does his best to instill a similar sense of passion in each and every student that passes through the Surface Science Center. I consider myself very fortunate to have been given the opportunity to work under the direction of John and I hope that the experience gained will enable me to have a very productive and rewarding career.

There are many individuals in the Surface Science Center with whom I have directly worked who deserve my sincerest gratitude: To Dr. Tykhon Zubkov, thank you so much for taking the time to introduce me to the fundamentals of ultra high vacuum technology and surface science. You have always been an excellent source of information throughout our time together in the Surface Science Center and you were always more than willing to take the time to explain those concepts which were critical for the understanding of ultra high vacuum science. I would also like to take this time to thank Dr. Yu Kwon Kim for being an excellent colleague who was always an endless source of scientific ideas and fruitful discussions. I also wish to acknowledge Margie Augenstein for her invaluable assistance and being a source for honest and helpful

advice. She has always been a critical asset to the Surface Science Center and I wish her nothing but the best as she enters the next chapter of her life. I would also like to express gratitude to all of my colleagues at the Surface Science Center, who are too numerous to name here. I am very fortunate to have met all of you and have thoroughly enjoyed the experience.

The various staff members in the Department of Chemistry at the University of Pittsburgh have been a valuable resource and are extremely important to the everyday workings of the department. I wish to thank the members of the machine shop (Mr. Dennis Sicher, Mr. Tom Gasmire, Mr. Jeff Sicher, and Mr. Roy Watters) for their willingness to work as efficiently as possible to keep my apparatus in the surface science center up and running. I have been fortunate to develop a sincere friendship with Tom and I am truly grateful. Without the staff in the electronics shop (Mr. Robert Muha, Mr. Chuck Fleishaker, Mr. Jim McNerney, and Mr. Dave Emala) many of the instruments would not have functioned long enough for me to reach this point in graduate school. I also want to thank Mr. Bob Greer from the glass shop for his assistance over the years and the individuals in the main office for their professional encouragement.

I also wish to express my gratitude to my family and friends. To my parents, Gregg and Kathy Morgan, I thank you for instilling me with the values to be successful. Because of you I have the necessary skills to set and achieve goals and I know that persistence is the key to achieving those goals. To my brothers, Philip and Christopher, I hope that I have been a big brother that you are proud of. You two are really great friends and I wish the best of luck to both of you. I also wish to thank my grandparents for their love, prayers, and encouragement.

Finally I would like to thank my best friend and wife, Jessica, for her constant love and support throughout these last five and a half years. I thank you for your patience during this long, but worthwhile journey.

1.0 THE IMPORTANCE OF ATOMIC STEP SITES IN CATALYSIS

This chapter describes how step defect sites are traditionally prepared on the surface of a single crystal and why there has been tremendous interest in studying the surface chemistry of step sites and their role in heterogeneous catalysis. A detailed understanding of the adsorption of CO on the step sites of Ru(109) is critical for understanding the various mechanisms of the Fischer Tropsch Synthesis (the reaction between CO and H_2 to produce hydrocarbons) and a brief account of our work on CO is presented. The detailed insight into the bonding of CO on the Ru surface is essential and ultimately serves as a precursor to our investigation into the adsorption of N_2 on the Ru(109) and Ru(001) single crystal surfaces because of the similarity between the two molecules. The adsorption and dissociation of nitrogen is important for understanding the mechanism of the Haber-Bosch catalytic process (the reaction of N_2 and H_2 to form NH_3). In addition to a brief discussion on the Haber Bosch process, the importance of alkali metals as promoter ions on transition metal surfaces for various catalytic reactions is presented.

1.1 THE USE OF METALS AS MODEL CATALYSTS

The understanding of heterogeneous catalysis, which is the foundation of the chemical industry, is one the great motivations for studying chemical reactions on surfaces. A catalyst is an active chemical spectator, as it takes part in the chemical reaction, but is not consumed. A catalyst

provides an alternative route of reaction where the activation energy is lower than the activation of the original chemical reaction in the absence of the catalyst. The role of the catalyst is not simply to accelerate chemical reactions, but to selectively accelerate certain reactions and not other reactions.

In the late nineteenth century, catalysis was just beginning to be used industrially on a large scale. Even at that time, the typical catalyst was metallic in nature. In the early 1920s, Taylor postulated that the surfaces of various catalysts are not uniformly active. This led to the idea that the properties of the surface atoms were directly related to the coordination number of the atoms [1]. It is expected that the lower the metal-metal coordination number, the larger the difference in the surface properties between the edge/corner atoms compared to the bulk atoms. All surfaces, regardless of how atomically smooth the surface is, are composed of various atoms with fewer neighbors compared to the bulk. This is illustrated by the representation of a catalyst granule in which a completely ordered arrangement of the atoms in the metal has not been attained and is shown in Figure 1. Because the catalytic activity is determined by the coordination of the metal atoms, the most catalytically active sites are therefore the atoms with the most unsaturated chemical bonds according to Taylor.

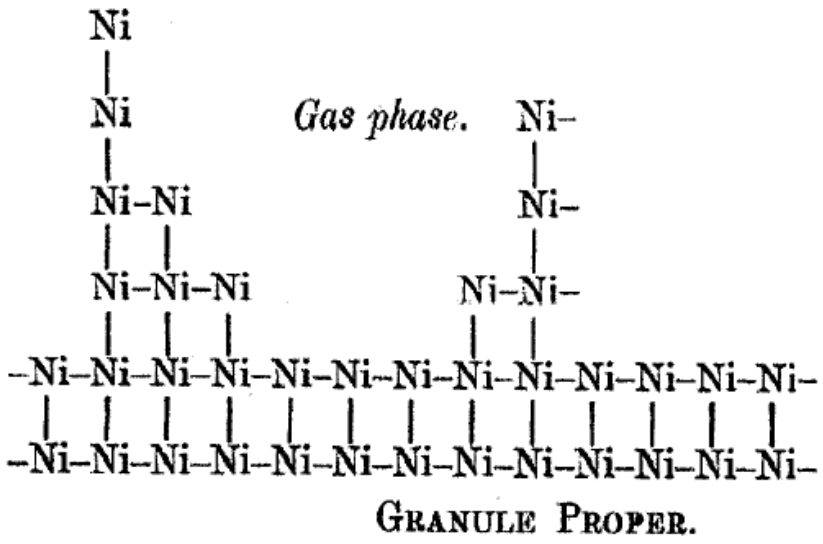

Figure 1: Atomic coordination heterogeneity on the surface of a Ni catalyst. From Ref [1].

The defect sites are sites where significant chemistry occurs and are present in a considerably lower concentration than the rest of the surface atoms. This led to Taylor's postulate that the defect sites are the active sites of the catalyst. A step defect is a microscopic surface irregularity on a single crystal surface where the top atomic layer ends abruptly along a compact row of particles comprising the crystal, leaving the second layer uncovered. These defect sites, which include crystalline edges, atomic steps, kinks, vacancies, dislocations, and islands, have a lower coordination than the atoms composing the atomically smooth portion of the surface. The presence of the defect sites on a surface has a dramatic effect on the thermodynamics and kinetics of a variety of surface chemical processes compared to atoms and sites that are found on the "perfect" or atomically smooth surface.

A few examples in which the catalytic properties of a metal are significantly influenced by the presence of atomic defect sites are presented below. Recent experiments have suggested that the various defect sites on CeO_2 promoter species are the active sites for the hydrogenation of unsaturated aldehydes on Ru-based catalysts due to their influence on the C=O bond

activation [2]. We have recently reported the activation of a molecular oxygen species on the step defect sites on a Ru surface to produce CO_2 in the presence of CO [3]. The higher adsorption energy of molecules adsorbed at the edges and corner sites of a metal crystallite compared to the flat facets is also verified theoretically [4].

1.1.1 Supported Metal Catalysts

Many catalytic reactions are structure sensitive, and therefore the overall rate of the reaction depends on the detailed geometrical structure of the surface atoms of the catalyst [5]. The rate per surface atom depends on the average size of the catalyst particles. The relative number of available step and kink sites increases dramatically with decreasing diameter for particles with a diameter, d, < 100 Å. The lower coordinated surface atoms have a substantially different ability to interact with the molecules from the gas phase. The variation in the ability of the surface atoms to participate in surface chemistry is related to the structure of the surface. This dependence on the surface structure is often regarded as being mainly due to an electronic effect.

The earliest investigations of catalytic particles utilized small metal particles which were deposited on well-defined supports, typically oxide single crystals [6]. These high area supported catalysts were structurally similar to real supported metal catalysts, but the systematic investigation of the defect sites was complicated by an inhomogeneity of particle sizes and shapes [7].

1.1.2 Single Crystal Metal Surfaces

In the 1950s, Germer and Farnsworth separately studied low energy electron diffraction patterns from single crystal surfaces and adsorbate layers [8-13], building on the early diffraction studies of Farnsworth in the 1930s [14-18]. The development of ultra-high vacuum technology and electron spectroscopic and diffraction methods enabled the first characterization of single crystal surfaces and the adsorbate layer. The earliest diffraction patterns were obtained from a silicon crystal, a germanium crystal, a tungsten crystal, a nickel crystal, and an adsorbate layer on the surface of the single crystal. For reasons of structural simplicity, many of the early studies utilized close packed surfaces as well as low index metal surfaces.

It is incredibly difficult to investigate the chemistry of adsorbates on natural defect sites because of the low concentration of the available sites. If 0.1% of the surface is comprised of defect sites and saturated with an adsorbate, the absolute coverage of the adspecies to be detected is 10^{12} cm^{-2}, which is below the detection limit of most surface science spectroscopic techniques. A higher coverage of surface defects can be "created" by means of two methods.

Initially point and step defect sites were artificially "created" by the ion bombardment of low Miller index surfaces. Miller indices are a symbolic vector representation for the orientation of an atomic plane in a crystal lattice and are defined as the reciprocals of the fractional intercepts which the plane makes with the crystallographic axes. Directions are defined by a set of three or four rational numbers. Low index planes can be thought of the basic building blocks of the surface structure as they represent some of the simplest and flattest fundamental planes. The resulting surfaces after the bombardment were used for a comparative study between perfect and defective surfaces [19,20]. The energetic Ar^+ ions cause sputtering of some of the surface

atoms, leaving defect sites on the surface. There is very little control over the resulting surface, which contains multiple types of defects with an inhomogeneous distribution.

The second and preferred method of creating atomic defect sites involves cutting single crystals in a high-index direction. When single crystals are cut in this manner, surfaces with a periodic array of defect sites are created, resulting in predictable and reproducible surfaces. When the crystal is miscut at a small angle with respect to the low Miller index plane, a surface with low Miller index planes periodically interrupted by atomic steps, and possibly kinks, is created. The surface structure created by this method is well defined and measurable by a multitude of surface science techniques.

Metal particles with a $d < 100$ Å can usually be modeled by truncated octahedrons made of atoms occupying crystal lattice points and display facets with geometries corresponding to the lowest free energy surface, such as (111) and (100) in the case of an *fcc* crystal. In idealized models of catalyst particles as semi-regular and truncated polyhedra, the edge and corner sites, which correspond to the lowest coordinated atoms, have structures that are very similar to the atomic steps and kinks found on a defective surface (Figure 2).

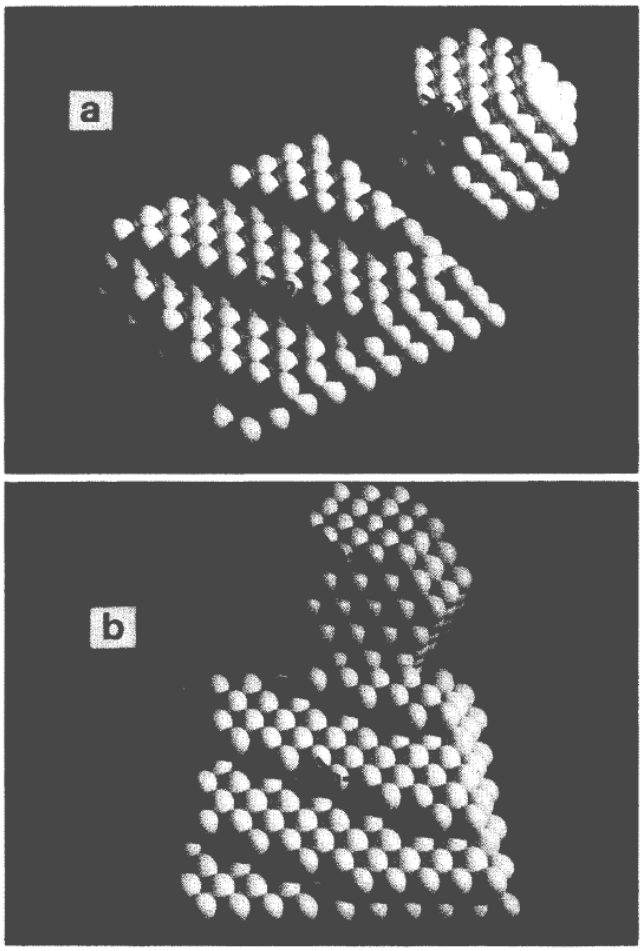

Figure 2: (a) Stepped surface (Pt(533)) with step atoms that mimic edge atoms in the truncated octahedron. (b) Step-kinked surface (Pt(432)) with kink atoms that mimic corner atoms in the truncated octahedron. From Ref. [21]. ***Reprinted with permission from Elsevier, Copyright 1985.***

Due to the structural similarity between the edge and corner atoms and the defect sites, Somorjai proposed that the various atomic step sites of a stepped single crystal surface can accurately model the edge and corner sites of the metal catalyst particles [22]. The atomically smooth surface atoms of the single crystal simulate the particle facets of the catalyst. These principles are illustrated in Figure 3.

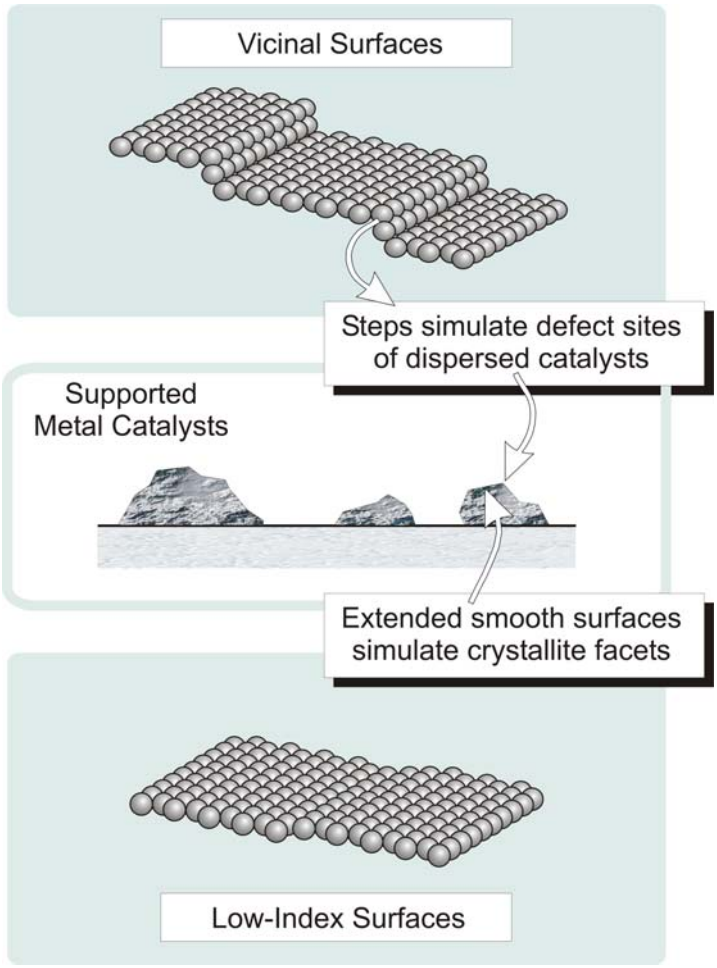

Figure 3: Surface science approach to approximating the surface sites of the dispersed metal particles with atomically-stepped and smooth single crystal surfaces.

The biggest advantage of stepped single crystals is that they contain a large number of structurally similar defect sites when the single crystal is cut in a vicinal direction. Stepped single crystals can be characterized by a multitude of surface science techniques which include electron spectroscopies and diffraction methods, vibrational spectroscopies, as well as imaging at atomic levels of resolution. The structure of the single crystal as well as the properties of the adsorbed species can be determined by these methods under UHV conditions and there are certain methods that can even be used at elevated pressures. Stepped single crystal surfaces have

been a convenient common ground between experimental investigations and theoretical modeling.

1.2 CHARACTERISTICS OF ATOMIC STEP SITES

Since the discovery of atomic step sites, it has typically been common practice to compare atomically smooth surfaces to their vicinal counterparts containing periodic steps [23]. The multitude of studies on stepped single crystal surfaces has led to the deduction of four basic trends in the properties of the step sites:

(1) The three available types of sites are populated sequentially, first the kinks, then the steps, and finally the terrace sites. Molecules and atoms are typically more strongly adsorbed at the step sites and kink sites compared to the terrace sites [24-26], which explains the preferential adsorption at the step sites [26-31]. The preferential adsorption of the step sites to CO and N_2 is discussed in detail in Section 1.5 and Chapter 4, respectively.

(2) Molecules and atoms adsorb at the atomic steps with a higher initial sticking coefficient than on the terraces [24,25].

(3) In addition to the increased binding energy at the step sites, the vibrational frequency of an adsorbed molecule, which is dependent on the coordination number of the surface atom, is typically different for adsorbates at the step sites compared to the terrace sites. Previous reports have indicated that the vibrational frequency of molecules at the step sites is typically 10-20 cm^{-1} less than those adsorbed at the terrace sites [26,30,32,33]. This has previously been observed for CO adsorption on the step and terrace sites of a Pt single crystal [26,30]. We have reported a difference of ~10 cm^{-1} in the vibrational frequency of N_2 adsorbed on the terraces compared to

N_2 adsorbed on the step sites of Ru(109) [33]. This observed effect of N_2 on Ru(109) is presented in detail in Chapter 6 of this thesis.

(4) Dissociative chemistry is often facilitated at the step sites because the activation barrier of intermolecular bond breaking is typically lower at the step sites [31,34-40]. We have observed the dissociation of CO and N_2 exclusively on the steps of Ru(109) [41-44]. There are also cases in which the overall kinetics of a surface reaction are completely dominated by the properties of the atomic step sites, given the enhanced reactivity of the active sites [34,37]. The dissociation of CO on the step sites of Ru(109) has been thoroughly studied and is discussed in Section 1.5 as a precursor to the studies presented in the later chapters of this thesis. The investigation into the dissociation of N_2 on Ru(109) is discussed in extensive detail in Chapters 4 and 5.

1.3 ELECTRONIC FACTORS IN THE ADSORPTION AND REACTIVITY AT METAL STEP SITES

One of the long term goals of surface science is to establish an understanding of the physical properties of a surface that determines its chemical reactivity. This detailed understanding of the electronic effect has become possible with the recent introduction of powerful theoretical methods, such as density functional calculations [45].

The coupling of the electronic states of a metal leads to the formation of bands of states, which differ in the role they play in surface chemistry. Calculations have shown that the surface reactivity of adsorbates on metals is determined by the following electronic factors; (1) the energy of the adsorbate bonding and anti-bonding electronic states relative to the metal d-bands,

(2) the coupling matrix element between the molecular orbitals and the metal d-states, and (3) the degree of filling of the molecule-surface antibonding states given by the position of the Fermi level, E_F [46]. The interaction between the bonding and anti-bonding molecular states and the metal d-states, the rehybridization, and the degree of overlapping of these states contribute to the above electronic factors. A one-electron state in an atom or molecule outside a metal surface will interact with all the valence states of the surface atoms. These states form a band or several bands of states. The degree of the interaction between the atom (or molecule) and the metal surface is related to the energy of the center of the projection of the d density of states onto the adsorption site, relative to the Fermi level. Since there are many d-states with different densities, a weighted average, or "center" is computed. On corrugated metal surfaces, the d-states are strongly directionally patterned according to the surface morphology, while the surface states with s-p character are typically distributed uniformly and isotropically [47].

On transition metals, a weak, non-site-specific adsorption site is provided by the broad s-band and the d-states form much narrower bands [45]. The interaction of an adsorbate state with the d electrons of a surface gives rise to bonding and antibonding states due to the narrowness of the d-band (Figure 4) [45]. When the d-band is low and broad, only a single resonance can be observed at the bottom of the band. The lack of empty antibonding states results in a weak chemisorption of the adsorbate on the surface. However, as the energy of the d-band center shifts up toward the Fermi level, a distinct antibonding state appears above the Fermi level. These antibonding states are empty and the bond strength increases as the number of empty antibonding states increases. This statement generally holds true for a large number of both atomic and molecular adsorbates on transition metal surfaces. Strong chemisorption also occurs as bonding states shift down through the Fermi level and become filled.

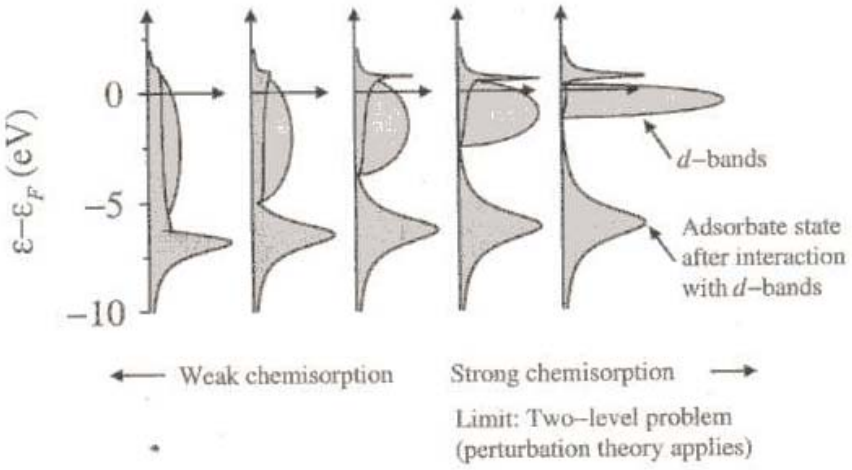

Figure 4: The local density of states projected onto an adsorbate state interacting with the d-bands at a surface. From Ref. [45]. ***Reprinted with permission from Elsevier, Copyright 2000.***

The lower coordinated atoms at the step edge have a smaller d-band width because of the reduced coupling of the neighboring d-states and therefore a higher energy of the d-band center. The energetically higher d-band center ultimately leads to the observed reactivity at the atomic step sites. In the case of most transition metals where the d-band is more than half filled, the filling of the d-band is kept fixed so that as the center of the band shifts up toward the Fermi level, the band width decreases.

In the absence of a surface adsorbate, a good prediction of the chemisorption bond strength can be obtained by the projection of the center of the d-bands onto different adsorption sites as shown in Figure 5. Figure 5 shows that the d-band center is closer to the Fermi level for the kink sites than for either the step sites or the terrace sites [48]. This clearly indicates that the reactivity of the kinks is the highest, whereas the reactivity at the higher coordinated terrace sites is the lowest. DFT calculations predict an increase in binding energy of CO on Pt sites from terrace sites to step sites in good agreement with previously reported experimental data as shown in Figure 6 [48].

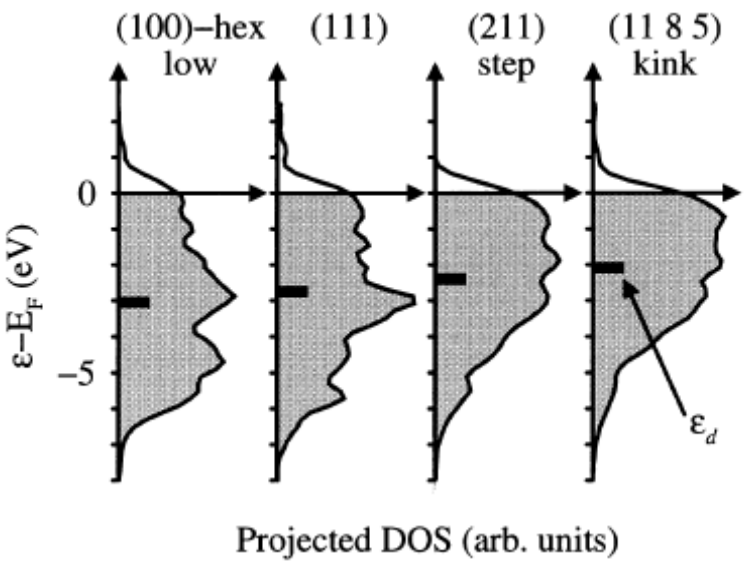

Figure 5: The d-density of states before the chemisorption of the CO at selected adsorption sites. From Ref. [48]. ***Reprinted with permission from Springer Link, Copyright 1997.***

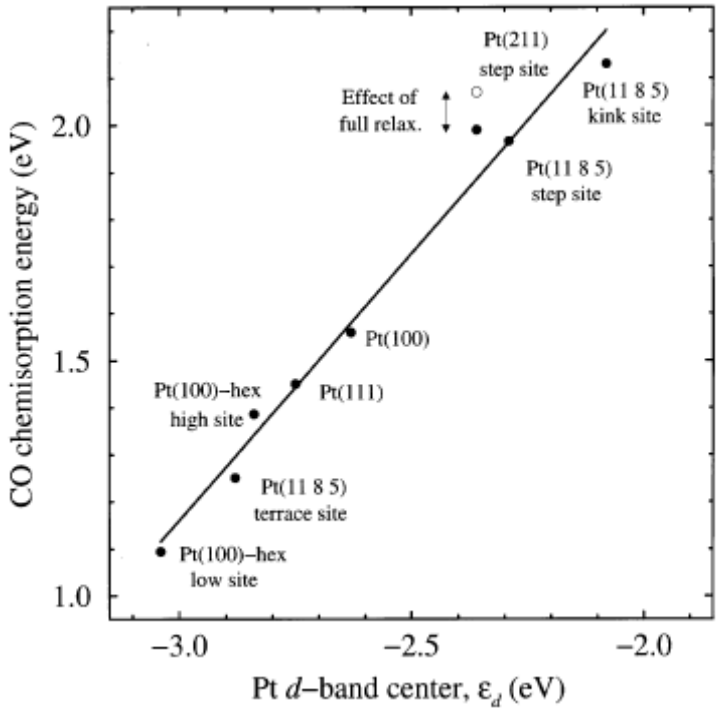

Figure 6: Calculated CO binding energy shown as a function of the d-band center for the adsorption site. The solid circles are for CO in the fixed adsorption geometry over the rigid surfaces. An open circle is the result for CO over Pt(211) calculated with a full structural relaxation. From Ref. [48]. ***Reprinted with permission from Springer Link, Copyright 1997.***

1.4 THE FISCHER-TROPSCH SYNTHESIS

1.4.1 History of the Fischer-Tropsch Synthesis

The Fischer-Tropsch (F-T) synthesis is the reaction of carbon monoxide and hydrogen in the presence of a catalyst which is primarily composed of nickel, cobalt, iron, or ruthenium [49,50].

$$n\mathrm{CO} + (2n+2)\mathrm{H_2} \rightarrow \mathrm{C}_n\mathrm{H}_{2n+2} + n\mathrm{H_2O}$$

The principal products resulting from this hydrogenation process are primarily straight chain paraffin hydrocarbons. Aliphatic alcohols, aldehydes, alcohols, and other branched-chain hydrocarbons constitute many of the secondary products. The synthesis of various hydrocarbons from the CO hydrogenation over transition metal catalysts is perhaps the most promising source of chemicals and fuels from a non-petroleum based supply [51]. The initial reactants in the above reaction can be produced through the partial combustion of a hydrocarbon or by the gasification of coal or biomass. Additional hydrogen can also be supplied by means of the water gas shift reaction in which CO and H_2O are reacted to form CO_2 and H_2. This reaction is not an efficient means of generating hydrogen due to the high temperatures required for the reaction to proceed. This reaction is, however, a very important part of the Fischer-Tropsch synthesis reaction as the water gas shift reaction is used to adjust the hydrogen and carbon monoxide ratio in order to find the optimal gas mixture. The resulting mixture of carbon monoxide and hydrogen is called synthesis gas, or syngas. Currently South Africa operates a combined total production capacity of about 4 million tons per year from the three Sasol plants [52]. Additional F-T synthesis plants in New Zealand (the Mobil MTG plant in 1985) and the 1993 Shell plant in Malaysia are evidence of the long term interest in hydrocarbon synthesis from CO.

At the beginning of the twentieth century, Sabatier and Senderens [53] were the first to demonstrate the successful hydrogenation of CO using a Ni catalyst forming methane at elevated temperatures and pressures. The scientific and industrial importance of the chemical behavior of carbon monoxide and its reactions has increased tremendously since Sabatier's groundbreaking work as indicated by the vast number of reviews and articles published on the Fischer-Tropsch synthesis in recent years [51,54-65]. The Fischer-Tropsch synthesis originated in 1923 in an observation made by Franz Fischer and Hans Tropsch in which hydrogen when reacted with CO in the presence of alkalized iron turnings at elevated temperatures (400 – 450 °C) and pressures (100 - 150 atm) resulted in the formation of "synthol", a mixture of mostly oxygenated compounds. It wasn't until 1925 that Fischer discovered that by using an iron-zinc oxide catalyst and pressures on the order of 1 atm that a mixture of mostly hydrocarbons could be formed [49,50]. This truly was the first Fischer-Tropsch synthesis.

1.4.2 Fischer-Tropsch Catalytic Activity of Metals

Vannice [66] determined the specific activity of various metals as Fischer-Tropsch catalysts so as to facilitate a comparison between the various metals. In his work he found that ruthenium was the most active F-T catalyst. The reactivity of other metals was as follows: Ru > Fe > Ni> Co > Rh > Pd > Pt but the average hydrocarbon molecular weight decreased in the order Ru > Fe > Co > Rh > Ni > Ir > Pt >Pd.

1.4.3 Mechanism of the Fischer-Tropsch Synthesis

Even though the Fischer-Tropsch synthesis has been investigated in detail for nearly 70 years there is still no clear understanding of the mechanism that is sufficient to accurately predict the products under various conditions or to unify the many observations in a detailed way [65]. There are two proposed pathways of the Fischer Tropsch synthesis to be discussed below.

1.4.3.1 CO Insertion Mechanism

The first pathway proceeds via the molecular chemisorption of CO on the surface, which is preceeded by a very brief stage of physisorption. In the chemisorbed phase the CO is adsorbed on the metal surface in a carbonyl-like mode. The bonding of the CO occurs through one or more metal atoms through the carbon by donation of the CO 5σ electrons to the metal and by the back donation of metal d electrons into the CO $2\pi^*$ antibonding orbital [67-71]. The metal-carbon bond will strengthen as the number of metal atoms involved in the bonding increases and the strength of the C-O bond will subsequently weaken. The CO will then be more susceptible to hydrogenation, which is the second step in the reaction mechanism, or other reactions. Molecular adsorbed CO can react with adsorbed hydrogen yielding two possible products. When the CO is reacted with hydridic hydrogen a formyl intermediate is formed as indicated in mechanism I and the structure is indicated in Figure 7.

$$M\text{—}CO + M\text{—}H \leftrightarrow M\text{—}CHO + M \qquad (I)$$

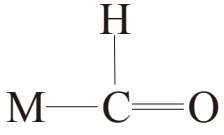

Figure 7: Formyl Intermediate.

The CO can also react with protonic hydrogen forming an alcoholic intermediate as indicated by mechanism II and Figure 8.

$$M—CO + M—H \leftrightarrow M—COH + M \qquad (II)$$

Figure 8: Alcoholic Intermediate.

Mechanisms I and II are the initial steps in the CO insertion mechanism. The formyl (or alcohol) intermediate is then hydrogenated forming CH_3 adsorbed on the surface. The reaction proceeds by a CO-insertion mechanism as indicated in Figure 9. In this mechanism the CO is inserted into the M-H (or M-R) bond and then the oxygen is removed from the species through reaction with hydrogen forming water. As the chain grows in length the M-C bond begins to weaken. When the hydrocarbon intermediate becomes saturated, with methyl groups at each end of the hydrocarbon chain, a stable hydrocarbon molecule can desorb from the surface.

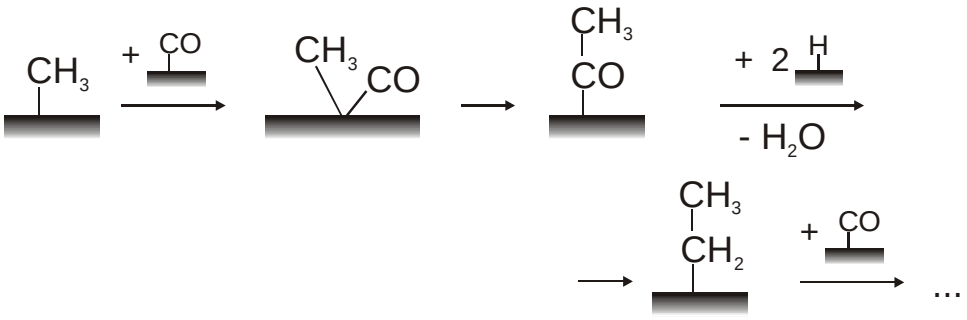

Figure 9: CO Insertion Mechanism for the Fischer-Tropsch Synthesis.

1.4.3.2 Carbide Mechanism

The second pathway proceeds via a possible initial chemisorbed CO state, followed by the dissociation of CO into atomic C and O at the temperatures of the Fischer-Tropsch synthesis.

It has been postulated by Muetterties [72,73] and Masters [74] that a more strongly adsorbed form of CO exists which is bonded side-on to the metal. This species should be more active towards hydrogenation and carbon-carbon bond formation and is most likely an intermediate to dissociation. There is evidence of CO dissociation on the surface of many of the Fischer-Tropsch metal catalyst surfaces [69,75-88]. The carbon atoms on the surface will then react with the adsorbed hydrogen in the following manner:

$$M—C + M—H \leftrightarrow M—CH + M \quad \text{(III)}$$

$$M—CH + M—H \leftrightarrow M—CH_2 + M \quad \text{(IV)}$$

$$M—CH_2 + M—H \leftrightarrow M—CH_3 + M \quad \text{(V)}$$

The overall mechanism of the carbide mechanism is shown in Figure 10:

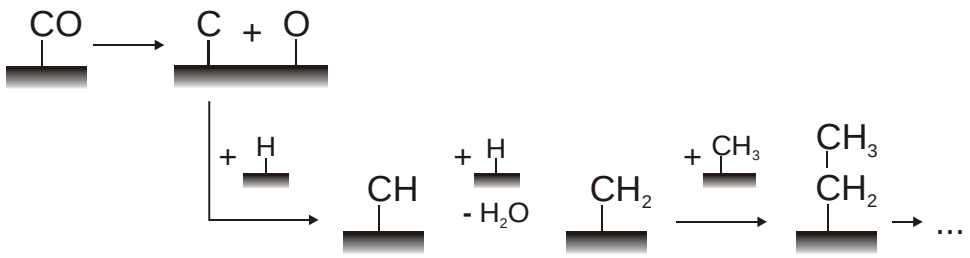

Figure 10: Carbide Mechanism of the Fischer Tropsch Synthesis.

1.4.3.3 Current Mechanisms

It is well accepted that the Fischer-Tropsch synthesis involves a very complex reaction scheme that is composed of a myriad of different reactive intermediates and elementary reaction paths. The overall reaction paths include CO activation, C_xH_y hydrogenation, hydrocarbon coupling, and termination pathways. Even after nearly forty years of extensive research in the

area of Fischer-Tropsch chemistry, there is considerable debate regarding the overall controlling reaction mechanism [89].

In addition to the carbide (or carbene) mechanism and the CO insertion mechanism, there is one additional mechanism of the Fischer-Tropsch synthesis which has been proposed and debated for some time. The hydroxy-carbene mechanism is similar to the carbide mechanism, but with the exception that two neighboring CO intermediates react with hydrogen to form two reactive hydroxyl carbene intermediates. The addition of hydrogen and subsequent elimination of water from the adsorbed RCHOH intermediates leads to the formation of a growing hydrocarbon chain as shown in Figure 11. There is evidence that the overall mechanism may depend on the catalyst chosen for the reaction. A recent report by Davis indicates that on an Fe surface, the CO insertion mechanism takes precedence, whereas the surface carbide mechanism appears to be dominant on the Co surface [56].

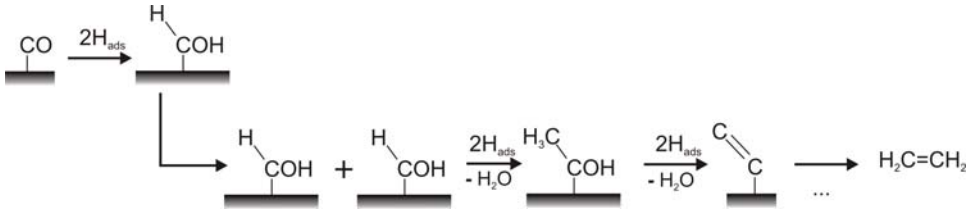

Figure 11: Hydroxy-Carbene Mechanism of the Fischer Tropsch Synthesis.

1.5 SPECTROSCOPIC DETECTION OF CO DISSOCIATION ON DEFECT SITES OF Ru(109): IMPLICATIONS OF FISCHER-TROPSCH CHEMISTRY

1.5.1 Introduction

As indicated in the previous sections, there has been tremendous interest in the role of atomic defect sites on various catalytic metal surfaces. A detailed investigation into the properties of the atomic steps on a Ru surface using CO as a probe molecule has been carried out in our laboratory. The surface chemistry of ruthenium is of great importance because of the catalytic usefulness in Fisher-Tropsch chemistry. It is most likely that the initial breaking of CO bond upon chemisorption is one of the fundamental steps in the Fischer-Tropsch synthesis.

Using infrared reflection absorption spectroscopy, temperature programmed desorption, and isotopic mixing techniques, the behavior of CO on Ru(109) was thoroughly investigated. The Ru(109) single crystal surface contains terraces of the (001) orientation separated by double atom height steps of the (101) orientation. A schematic of the crystal structure is shown in Figure 26. The investigation of CO, while important on its own for understanding the role of the step sites on Ru(109), laid the foundation for future experiments which are presented in chapters 3-10 of this thesis. CO and N_2 are isoelectronic molecules and therefore might be expected to behave similarly when adsorbed on the Ru surfaces; however, we have found that these molecules actually behave differently due to the difference in the bonding to the substrate. These effects will be discussed in the later chapters of this thesis. The Ru(109) sample used in these studies was cleaned and prepared according to the procedure outlined in Chapter 2.

1.5.2 Results

1.5.2.1 Infrared Spectral Development of CO

The development of the infrared reflection absorption spectra was followed as a function of coverage of adsorbed $^{12}C^{16}O$ on the surface of the Ru. After exposure to a particular dose of $^{12}C^{16}O$ the surface was linearly heated to 250 K and cooled immediately in order to equilibrate and order the CO adlayer. No CO desorption occurs up to this temperature. The infrared spectra can be seen in Figure 12.

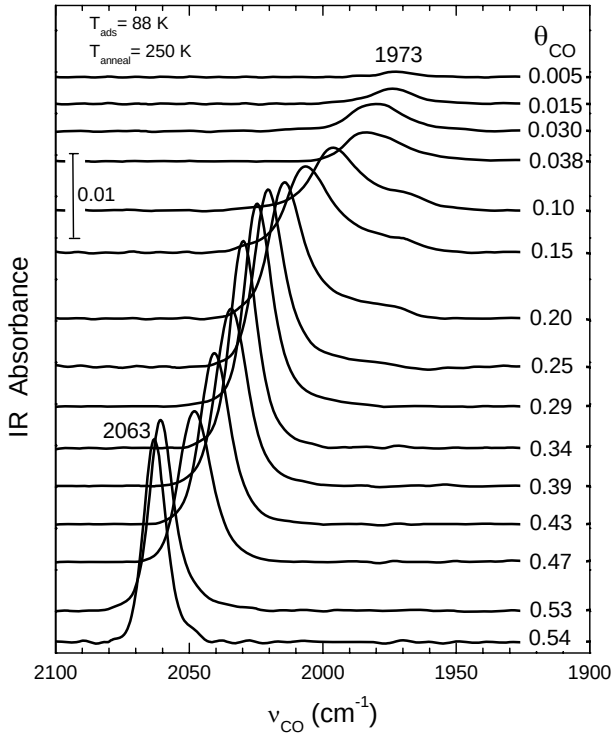

Figure 12: Infrared spectra of $^{12}C^{16}O$ adsorbed on Ru(109) at 88 K at increasing coverages.
Reprinted with permission from Elsevier, Copyright 2003.

For all CO coverages a single infrared band was observed. At the lowest coverage of θ_{CO} = 0.005 (hereafter relative to the available Ru surface atoms) the singleton band is located at 1973 cm^{-1}. As the coverage is increased, the band grows in intensity and constantly shifts

upward in frequency until the point of saturation at 2063 cm^{-1}. The vibrational frequency of an adsorbate molecule in the limit of very low coverage is termed the singleton frequency. This frequency is indicative of the character and strength of the primary chemical bond to the metal surface and is characteristic of the adsorbed molecule in the absence of intermolecular interactions.

The upward shift in the vibrational frequency of CO with increasing coverage can be explained by several basic effects. The symmetrical vibrational coupling between neighbor CO molecules causes an upward shift in the observed mode as a result of the direct interaction between the dynamic dipoles and the interactions with the image dynamic dipoles [90]. In addition, as the coverage increases, the increasing competition for back-donating electrons from the metal to enter the empty $2\pi^*$ orbital, will result in an upward shift in the vibrational frequency and a weakened CO bond. The antisymmetrical coupling between neighboring CO molecules produces an interacting mode with cancelling dynamic dipoles which is invisible using reflection IR.

The behavior as well as the range of the infrared spectra coincides very closely with the results reported for CO adsorbed on atomically smooth Ru(001) throughout the entire coverage range [91-93]. It was previously reported that CO is adsorbed in an atop configuration given the observed vibrational frequency. A bridging CO species would have a significantly lower vibrational frequency (~1800 cm^{-1}). Based on these previous results we conclude that the CO is adsorbed in a singly coordinated on-top configuration on the terraces and possibly the steps of the Ru(109) surface.

1.5.2.2 IR Spectral Changes Accompanying the Thermal Depletion of CO

The thermal depletion of the chemisorbed CO was followed by means of infrared reflection absorption spectroscopy. $^{13}C^{18}O$ was adsorbed on the surface at a coverage of about 5.2×10^{13} cm^{-2} (θ_{CO} = 0.038) on the Ru surface. Since small amounts of $^{12}C^{16}O$ are always present in the UHV chamber, the $^{13}C^{18}O$ isotopomer was used in these studies to eliminate any potential interference from the background $^{12}C^{16}O$. The crystal was heated linearly at a rate of 2.0 K/s and then cooled immediately after reaching the designated annealing temperature. The cooling process typically took 1-2 minutes before the base temperature of 88 K was reached. The $^{13}C^{18}O$ exhibits a single vibrational band at about 1891 cm^{-1} immediately after adsorption and prior to annealing the sample. The same coverage of $^{12}C^{16}O$ exhibits a vibrational mode at about 1980 cm^{-1} (data not shown here). As the temperature is gradually increased, the vibrational mode gradually decreases in frequency and intensity as indicated in the sequential series of spectra in Figure 13.

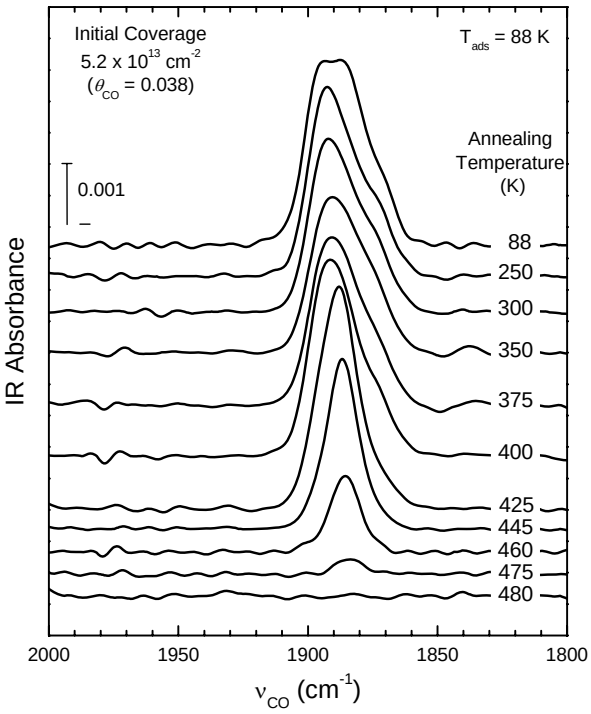

Figure 13: Infrared spectra of $^{13}C^{18}O$ adsorbed on Ru(109) surfaces at 88 K and annealed to various temperatures. All spectra were recorded after the sample was cooled to 88 K.
Reprinted with permission from Elsevier, Copyright 2003.

In the temperature range of 100 - 400 K, there is very little shifting of the infrared band, but there is a narrowing of the band as the annealing temperature is increased. As the annealing temperature was increased to 425 K, the peak shifts from 1891 cm^{-1} to 1888 cm^{-1} and becomes more symmetric. The relative area of the absorbance spectrum remains fairly constant up to 425 K. There is no desorption of CO up to this temperature as indicated by the constant integrated absorbance. This speculation is confirmed in the series of TPD spectra in Figure 14. A continued increase in the annealing temperature of the sample results in a further decrease in the frequency of the vibrational band as well as the integrated absorbance until all of the infrared active species of CO have completely disappeared at a temperature of about 480 K.

1.5.2.3 Temperature Programmed Desorption of CO

$^{12}C^{16}O$ was adsorbed on the surface at increasing coverage up to the point of saturation of the surface. The thermal desorption spectra of the adsorbed CO can be seen in Figure 14.

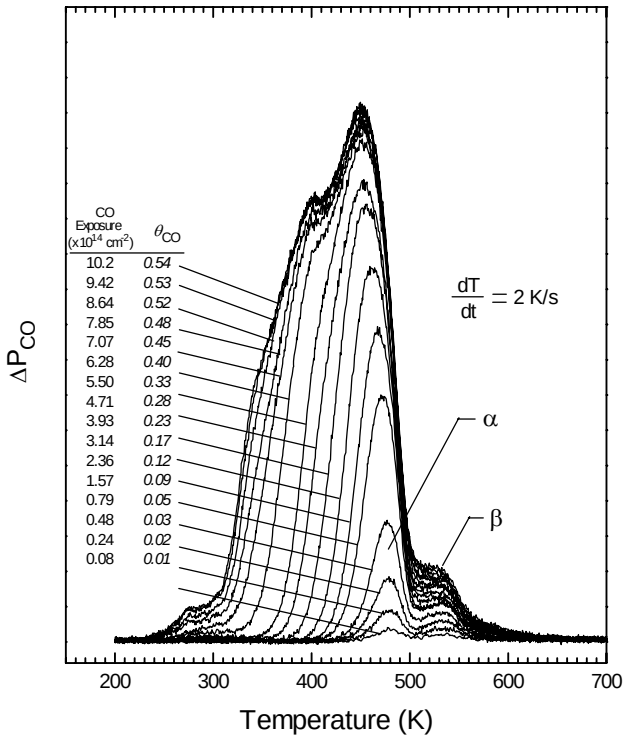

Figure 14: Thermal desorption spectra of CO adsorbed on Ru(109) at 88 K. The indicated CO exposures include the minor contribution from the background exposure.

It can be seen in all of the spectra that there are two main features of the TPD spectra. At the lowest observable coverage of CO, there are two features in the CO desorption spectra, one at 480 K and the other at 535 K. The peak at 480 K, termed the α peak, continues to increase while shifting to lower temperatures until the coverage reaches saturation. The second feature of the spectra, the β peak, grows only gradually and does not shift in temperature as the coverage is increased. From the TPD spectra it is evident that there is CO desorbing from the surface after

480 K even though from the infrared spectra it was found that all molecular CO was completely removed from the surface after 480 K.

1.5.2.4 Isotopic Mixing of $^{12}C^{16}O$ and $^{13}C^{18}O$ on Ru(109)

The two stable isotopomers of CO, $^{12}C^{16}O$ and $^{13}C^{18}O$, when adsorbed simultaneously on the surface, provide an excellent opportunity to detect the dissociation of CO on the Ru surface through the formation of the various mixed isotopomers. Each of the two isotopomers were adsorbed on the Ru surface in equimolar amounts at a coverage of 3.0×10^{13} cm^{-2} ($\theta_{CO} = 0.022$). The two isotopomers were initially mixed in the gas handling line prior to exposure of the crystal. The incoming gas was monitored with the QMS, which showed that the two species were sufficiently mixed. During the TPD scan, the signals from 28 amu, 29 amu, 30 amu, and 31 amu ($^{12}C^{16}O$, $^{13}C^{16}O$, $^{12}C^{18}O$, and $^{13}C^{18}O$ respectively) were monitored by QMS multiplexing. In Figure 15a it can be seen that only the two initial isotopomers desorb in the region below 480 K. However, above 480 K, all four isotopomeric combinations desorb in comparable amounts forming the β peak in each of the TPD traces. The fraction of isotopic mixing between the species was determined from the TPD traces and the results are plotted in Figure 15b. Isotopic mixing occurs primarily in the high temperature region of the TPD spectra. This clearly indicates that the β peak is attributed to the recombination of some mobile C and O species that is formed by the dissociation of the CO by some type of active site on the Ru surface. The high temperature CO desorption feature was not seen on the atomically smooth Ru surface nor was any isotopic mixing observed in the TPD spectra of CO/Ru(001) [94,95]. In agreement with the previous experimental evidence we also have not observed the high temperature β desorption feature during the desorption of CO from the atomically smooth Ru(001) surface as indicated in

Figure 16. Therefore it is very likely that the step sites which are present on the Ru(109) surface are solely responsible for the dissociation and subsequent recombination of CO on the surface.

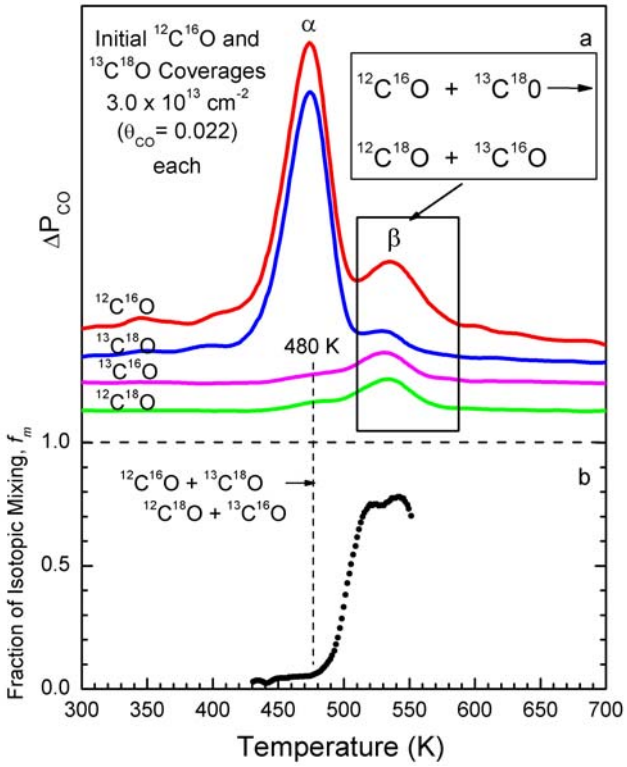

Figure 15: CO isotopic mixing during TPD on Ru(109). (a) TPD of CO from Ru(109). The initial coverage was 3.0 x 10^{13} CO / cm^2 for each isotopomer. (b) Fraction of isotopic mixing, f_m, between the CO isotopomers, as determined by multiplex mass spectrometry during TPD: $f_m = \dfrac{X_{^{13}C^{16}O}}{(X_{^{13}C^{16}O} + X_{^{13}C^{18}O})(X_{^{13}C^{16}O} + X_{^{12}C^{16}O})}$, **where X_i is the mole fraction of the *ith* isotopomer in the desorbing CO.**

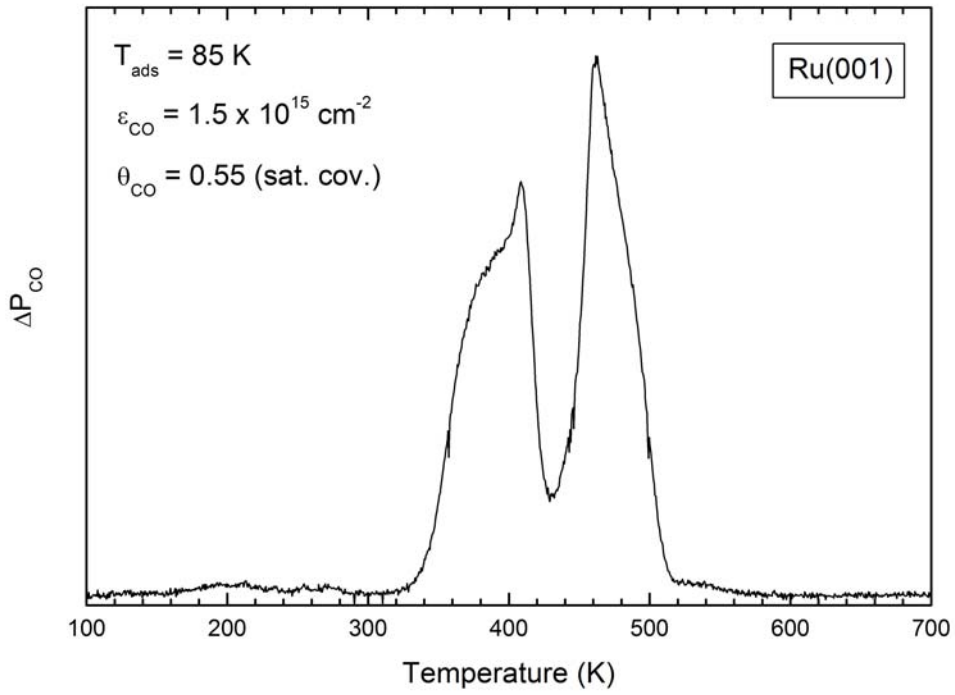

Figure 16: Temperature desorption spectrum of a saturated CO coverage from Ru(001).

1.5.2.5 Site Blocking of CO Dissociation by Carbon

It is known that the thermal decomposition of ethylene on Ru produces carbon deposits on the surface between the temperature range of 350-650 K [96]. The effects of the controlled deposition of carbon on the CO desorption from the Ru(109) surface were studied. Ethylene was initially adsorbed at 88 K on the stepped Ru(109) surface at coverage up to 10 % of the available Ru surface atoms. After deposition of the ethylene, the sample was linearly heated to 800 K in order to decompose the adsorbed ethylene leaving carbon atoms on the Ru surface in an amount up to ~20% of the surface sites. CO was then adsorbed on the surface at 88 K in order to produce a coverage of $\theta_{CO} = 0.095$. The CO adlayer was then subjected to thermal desorption and the subsequent spectra at varying initial coverages of C_2H_4 are plotted in Figure 17.

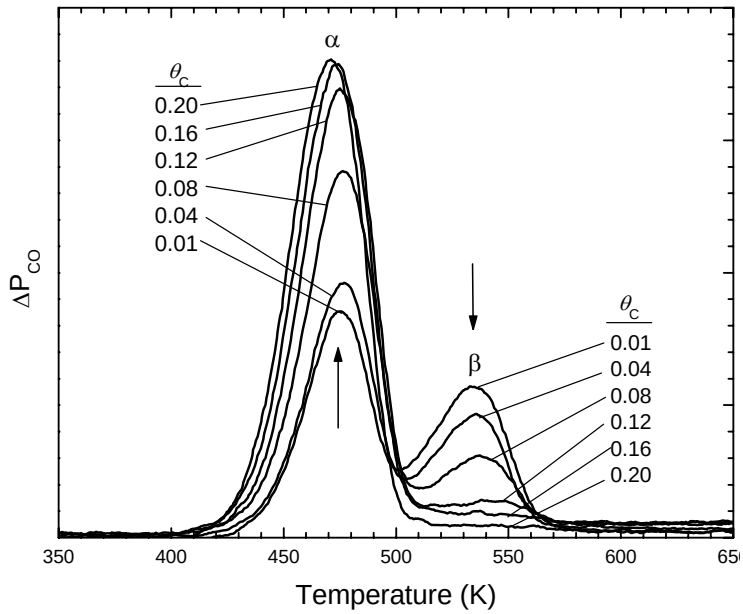

Figure 17: Thermal desorption spectra of CO adsorbed on Ru(109) at 88 K at different coverages of preadsorbed carbon. ***Reprinted with permission from Elsevier, Copyright 2003.***

The preadsorption of carbon affected the overall features of the TPD trace but not the total area under the curves indicating that the amount of adsorbed CO on the surface remains the same in each trace. As the initial coverage of C_2H_4 is increased, the β feature decreases in intensity while at the same time the α peak gains intensity. After an initial carbon coverage of $\theta_C = 0.20$, the β peak is completely suppressed indicating that the CO dissociation and hence recombination is no longer occurring on the surface. This low carbon coverage of only 20 % is enough to completely block the dissociation and recombination of CO on the surface, and therefore the surface sites responsible for this phenomenon must constitute a fraction of the surface that is less than 20 %.

1.5.3 Discussion

The above results indicate that the CO dissociation process primarily occurs at the steps as there was no evidence of CO dissociation and recombination on the Ru(001) surface [94]. Previous work by Menzel et al. [97] has shown that electron bombardment of a CO adlayer on Ru(001) results in a high temperature feature in the TPD spectra around 560 K. This high temperature feature was attributed to CO that had recombined from C(a) and O(a) prior to desorption. When CO was chemisorbed on the Ru(110) surface, it was reported that this more open surface is capable of dissociating up to 20% of a CO monolayer producing a high temperature TPD state at 500 K and 540 K which was attributed to recombinative desorption as investigated by TPD and High Resolution Electron Energy Loss Spectroscopy (HREELS) [98]. Upon prolonged exposure to CO at 501 K, the stepped Ru(1 1 10) yielded a TPD peak at 580 K. Tamaru et al. conclusively demonstrated by means of an isotopic mixing experiment that this peak was indeed due to dissociatively adsorbed CO [95]. Westre et al. had previously observed a small high temperature state in the TPD spectra of CO on a stepped Ru surface [99]. This peak which was near 520 K was not attributed to dissociated CO that had recombined, but rather to a spurious source that originated from somewhere other than the front side of the crystal. The conclusions were based on various coverage measurements as well as the lack of specific Auger features characteristic of dissociated CO.

In Figure 14 it is found that the β feature of the TPD comprises nearly one third of the total area of the TPD trace at the lowest coverages. The information obtained from the ethylene deposition experiments (Figure 17) supports the fact that the high temperature peak in the CO TPD reported here (Figure 14) is indeed a real occurrence. The deposition of small (< 20%) amounts of carbon from ethylene causes the β peak to decrease in intensity while simultaneously

causing the α feature to increase by a comparable amount. This information alone strongly supports the conclusion that both of the desorption peaks arise from the same front surface of the crystal.

These results therefore demonstrate conclusively that the atomic step or defect sites on the Ru(109) surface are responsible for the CO dissociation observed near 480 K, resulting in a high temperature β peak at 535 K. The results of the experiments in the previous section are summarized below as the principal reasons for this conclusion. (1) The 1891 cm^{-1} feature in the infrared spectra of $^{13}C^{18}O$ on Ru(109) is assigned to undissociated CO molecules. In the temperature range of 445 K – 480 K this feature disappears as can be seen in Figure 13, which corresponds to the α-desorption process. After the vibrational band attributed to the on-top CO species disappears from the IR spectra, the β-desorption process begins to occur near 500 K and continuing to 535 K. The β-desorption process therefore corresponds to the recombinative desorption of dissociated CO on the Ru surface. (2) During the isotopic mixing experiment the mixing of the $^{12}C^{16}O$ and $^{13}C^{18}O$ occurs exclusively during the β-desorption process (Figure 15) even though the β peak accounts for a minor fraction of the overall area of the TPD trace. From this information we determine that the α peak corresponds to the desorption of molecularly adsorbed CO, whereas the β feature is attributed to the recombination of the dissociated CO. The CO dissociates on the Ru surface at temperatures below 530 K, but the exact onset temperature of dissociation is not known. (3) The CO dissociation/recombination process on the Ru(109) surface is completely suppressed by the preadsorption of carbon from ethylene at a coverage of θ_{CO} = 0.20 (Figure 17). The close packed terraces constitute a majority of the overall surface and therefore can not be blocked by the deposition of such a small amount of carbon on the surface. Therefore, the dissociation of CO must occur primarily at the steps.

The explanation as to why the dissociation of the CO molecule occurs at the steps relates directly to the special steric environment of the Ru step sites. The step atoms are coordinated to neighboring Ru atoms less completely that the Ru atoms in the close packed atomically smooth planes.

The phenomenon observed here is strikingly similar to previous behavior of CO on the early transition metals such as Cr(110) [100-102], Fe(110) [103-105], Mo(100) [106], and Mo(110) [107,108]. Hoffman et al. had also observed the CO dissociation on K-promoted Ru(001) [109]. In much of the previous work on the early transition metals the recombination of C(a) and O(a) occurred at temperatures that were much higher than the temperature at which the CO dissociation occurred. For Ru the difference in the dissociation temperature of the CO and the temperature at which the recombined molecule desorbs is small. This may possibly indicate that either the C(a) or O(a) are more mobile on the Ru surface than on other transition metal surfaces. Since the recombination of the adsorbed species must involve some degree of surface mobility, it is quite possible that the special Fischer-Tropsch activity of Ru may be due to the relatively low dissociation temperature and the C(a) and O(a) surface mobility at 500 K. This temperature range of the mobile carbon existence coincides with the temperatures of the industrial Fischer-Tropsch synthesis. These findings therefore support the hypothesis in which the mobile C(a) species, which is provided by CO dissociation at temperatures below 480 K, may act as an intermediate surface species in the F-T catalysis on Ru.

1.5.4 Summary

The atomic step defect sites of the Ru(109) surface exhibit enhanced CO dissociation activity as compared to the atomically smooth Ru(001) surface which contains only an “infinite” terrace.

The high dissociation activity of the Ru step sites is most likely due to the lower coordination number of the steps compared to the terraces or to the special steric environment at the vicinity of the Ru step sites. This enhanced dissociative behavior leads to C and/or O mobility on the surface which ultimately leads to recombination of the adsorbed C and O species and hence desorption at a higher temperature than observed for the molecularly adsorbed CO. It is very likely that the enhanced mobility of the adsorbed species and the interaction of those species with adsorbed hydrogen are involved in Fischer-Tropsch chemistry forming long linear alkane products and water.

1.6 NITROGEN CHEMISTRY ON RUTHENIUM

1.6.1 The Haber Bosch Process

The Haber-Bosch process, which is the catalyzed conversion of N_2 and H_2 into NH_3, has often been called the most important technological advance of this century. The synthesis of ammonia is important because of the industrial application in which synthetic fertilizers have contributed enormously to the survival of mankind through the significant increase of agricultural yields. Even before the discovery of the Haber-Bosch process, many attempts had been made to study the synthesis and decomposition of ammonia with minimal success. As far back as 1823, ammonia was first synthesized from the combustion of hydrogen with a deficiency of air in the presence of a platinum catalyst, according to a report by Dobereiner [110]. Fritz Haber began work on the thermodynamic equilibria in the reaction of N_2 and H_2 using iron as a catalyst in 1904. Initially, Haber worked at 1300 K and atmospheric pressure even though he speculated

higher pressures would yield higher concentrations of ammonia. Even though the total amount of ammonia obtained at equilibrium was extremely small, Haber estimated that the reaction temperature necessary for the commercial synthesis at atmospheric pressure would have to be lower than 300°C. It wasn't until 1908 that Haber was able to synthesize considerable amounts of ammonia from nitrogen and hydrogen using a closed circulating system at elevated temperatures (600°C) and pressures (roughly 200 bar). The first large scale synthesis of ammonia from its elements took place in 1912, after Carl Bosch had developed the high pressure technology for the chemical industry. This process became known as the Haber-Bosch process, which was the first industrial process to make use of extremely high pressures (200-400 atmospheres) and high temperatures (400-650 °C).

The synthesis of ammonia is of critical importance because it is the primary ingredient in artificial fertilizers, without which, modern day agricultural yields would be impossible. In order to be used as a fertilizer the ammonia must first be converted to nitric acid, which is then converted to ammonium nitrates for use by the plants. Plants are also capable of using the liquid ammonia directly although the available nitrogen is not as readily available for use as in the ammonium nitrate. When ammonia is used as a source of nitrogen, the ammonium nitrogen is converted to the useable nitrate form by nitrifying bacteria in the soil. During the first decade of the 20^{th} century, the world's supply of fixed nitrogen was declining rapidly relative to the demand, spurring interest in the artificial synthesis of nitrates.

Today, nearly one century after the development of the Haber Bosch process, it is still applied all over the world to produce nearly 500 million tons of artificial fertilizer per year. Roughly 1% of the world's energy supply is used for the production of ammonia [111] and the process sustains nearly 40 % of the population [112].

1.6.2 Mechanism of the Haber Bosch Process

There has been considerable interest in Ru as a Haber Bosch catalyst to replace the traditional Fe catalyst for the conversion of N_2 and H_2 into NH_3. The promoted Ru catalyst is more efficient than the iron catalyst and is less susceptible to blocking of the active sites by excess nitrogen and poisoning by traces of oxygen [113]. For the Fe-based catalyst, the underlying reaction mechanism consists of the dissociative adsorption of N_2 followed by the hydrogenation of N on the catalyst surface. The same reaction scheme holds true for the Ru-based catalyst and consists of six single steps as schematically indicated in Figure 18.

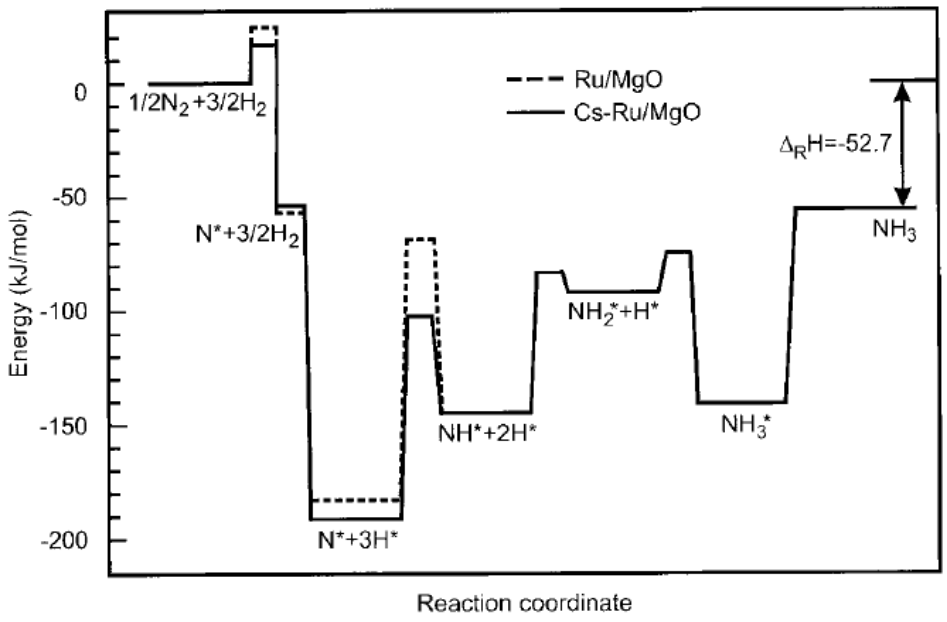

Figure 18: Potential energy diagram for the ammonia synthesis on the Ru/MgO catalyst (dashed line) and the Cs-Ru/MgO catalyst (solid line) as derived from microkinetic modeling of results from a flow reactor. The adsorbed species are marked by an asterisk. From Ref. [114] and references therein. ***Reprinted with permission from Wiley-VCH Verlag, Copyright 2000.***

The production of NH_3 from N_2 and H_2 on metallic catalysts proceeds initially through the dissociation of N_2 and H_2 which is then followed by a reaction of the atomic species on the surface [115]. Various defect sites on the Ru(001) have been identified experimentally as well as

theoretically [34] as the sites responsible for N_2 adsorption and activation which leads to dissociation. Chorkendorff et al. [34] showed that the N_2 dissociation occurs at the step sites with a dissociation barrier of about 0.4 eV and the terrace sites with a dissociation barrier of 1.3 eV. These values were determined by thermal sticking coefficient measurements and desorption experiments of nitrogen on a clean Ru(001) surface and on a gold passivated surface, in which the gold atoms poison the step sites. Chapter 5 of this thesis discusses in detail our experimental determination of the activation barrier of dissociation for N_2 on the atomically stepped Ru(109) surface, which was measured to be 0.26 eV.

The measured rate of the dissociative adsorption at the step sites is at least 9 orders of magnitude higher at the step sites than at the terrace sites at a temperature of 500 K [34]. The calculated difference in the activation barrier between the steps and terraces is slightly higher with an approximate value of 1.5 eV [34] as shown in Figure 19. This huge difference between the reactivity at the steps and terraces leads to two consequences. The first is that even a fraction of a percent of steps on the Ru surface can completely dominate the rate of N_2 dissociation. Second, it means that the ammonia synthesis reaction should therefore be extremely sensitive to the step sites on the Ru(109) surface. In the ammonia synthesis the rate limiting step is the dissociation of the N_2 molecule and therefore all catalytic activity is expected to be directly related to the steps on the surface. Recent density functional theory calculations by Nørskov et al. have confirmed this to be true on the surface of a Ru(001) catalyst [116]. Their results indicated that the intermediates of the NH_3 synthesis reaction are bound considerably stronger to the active sites (located at the step sites) than the atomically flat terrace sites.

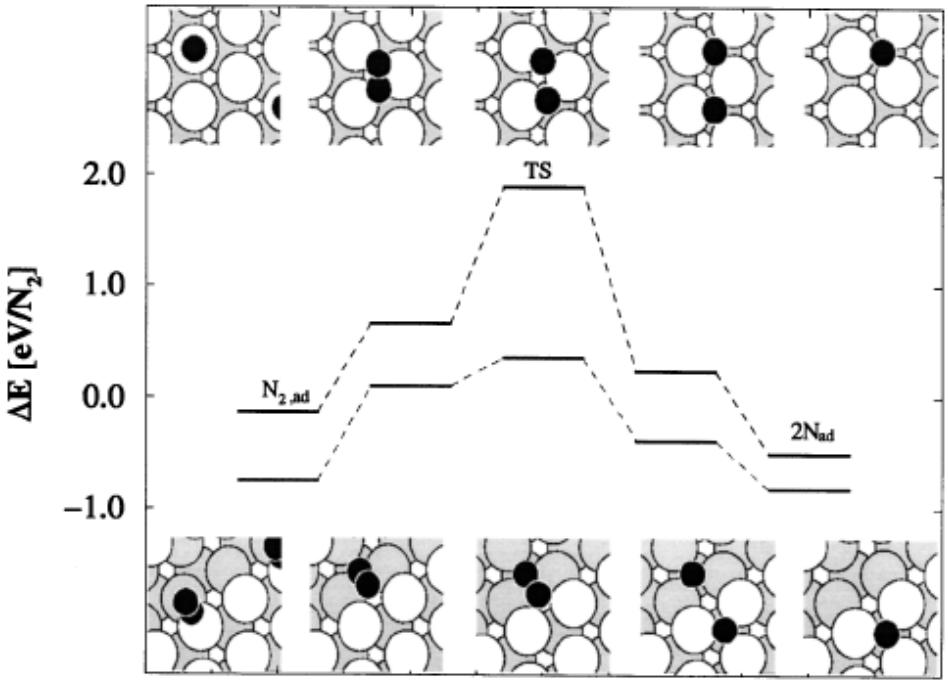

Figure 19: Results from density functional calculations comparing N_2 dissociation on a terrace and at a step on Ru(001). The upper curve shows the adsorption and transition state (TS) energies for the dissociation on the terrace, whereas the lower curve shows the same energies at the step. From Ref. [34]. ***Reprinted with permission from American Physical Society, Copyright 1999.***

1.6.3 Bonding of N_2 to Ru

Even though N_2 and CO are isoelectronic molecules, the bonding to transition metal surfaces is considerably different from each other. CO has been found to bind to the surface via the 5σ and $2\pi^*$ molecular orbitals. The HOMO of CO is the 5σ orbital and is roughly nonbonding with respect to the C-O bond, whereas the $2\pi^*$ orbital, the LUMO, is antibonding with respect to the C-O bond.

The 5σ orbital is localized on the carbon end of the molecule and is completely occupied as it lies below the Fermi level. The electron density of the 5σ orbital is effectively donated to

the metal as there is a strong interaction with the metallic electronic states [117]. In addition, electrons are donated into the $2\pi^*$ orbital from the metal in a process known as backdonation. CO adsorbs in a carbon down configuration due to the overlap of the 5σ orbital with the metal state. Because the 5σ orbital is a nonbonding orbital with respect to the M-CO bond, modification of this orbital does not have a large effect on the C-O bond. The C-O bond is weakened due to the backdonation into the $2\pi^*$ orbital as this orbital is antibonding with respect to the C-O bond. The weaker the C-O bond the higher the reactivity of the CO.

Nitrogen, on the other hand, has been found to bind to the surface only through σ-donation through various coadsorption experiments of nitrogen with alkali metals and oxygen [118,119]. When nitrogen is adsorbed in the presence of a "charge donor" such as an alkali metal, the M-N_2 bond is weakened due to the increase in the local density of states near the Fermi level [118]. In the presence of a charge acceptor, such as oxygen, there is a decrease in the density of states near the Fermi level and σ-donation from the N_2 is facilitated resulting in a stronger M-N_2 bond. The adsorption of nitrogen is dominated by the electron donation from the $3\sigma_g$ orbital to the metal surface.

Due to the antibonding character of the $2\pi^*$ orbital, an increase in the occupation of this orbital subsequently weakens the intramolecular bond and can be detected by a downward shift of the vibrational frequency. There is only a minimal shift of the vibrational frequency of nitrogen as the coverage increases on a clean Ru(001) surface or on a potassium or oxygen predosed surface [118,119]. This indicates then that π-backdonation is involved to only a minor extent in the bonding of N_2 to transition metals.

1.7 ALKALI METAL ADSORPTION

In many chemical reactions a catalyst is used to enhance the rate of formation of a desired product. There are certain instances, however, when a clean metal catalyst surface is not as reactive as desired in order to be an effective catalyst.

In the industrial synthesis of ammonia from N_2 and H_2, iron particles containing potassium on the surface are used to increase the overall efficiency of the reaction [117]. The catalytic activity of the iron is significantly increased by the potassium, making it a promoter species. The barrier of a chemical reaction, which utilizes a promoted metal catalyst, will be lower than if an unpromoted metal catalyst was used. Alkali metals are used extensively as promoters in heterogeneous catalysis and surface science studies have helped to understand the electronic origin of the alkali promoter atoms [120,121]. The understanding of alkali metal interactions with metal surfaces has been acquired over decades [122,123]. The general picture of alkali metal adsorption is based on the Langmuir-Gurney model [123], in which there is a partial charge transfer from the alkali metal atoms to the metal substrate. In this model, as the alkali metal coverage increases, depolarization effects set in causing a reduction in the dipole moment of the alkali atom.

Promoters such as alkali metals are known to produce positive outward electric fields in their vicinity. In the case of adsorbed CO and N_2, the electric field weakens the C-O or N-N bond causing a decrease in the vibrational frequency, enhanced dissociation, and surface complex formation [109,124-127]. In addition to the promotion of an iron based catalyst for use in the ammonia synthesis, alkali-promoted catalysts are also necessary when using a Ru-based catalyst [128,129]. Figure 20 shows the calculated reaction path of molecular nitrogen as a function of the dissociation reaction coordinate on a clean Ru(001) surface as well as an alkali

promoted Ru(001) surface. It can clearly be observed that the presence of the alkali metal lowers the energy of the transition state, thereby lowering the overall activation energy of the reaction.

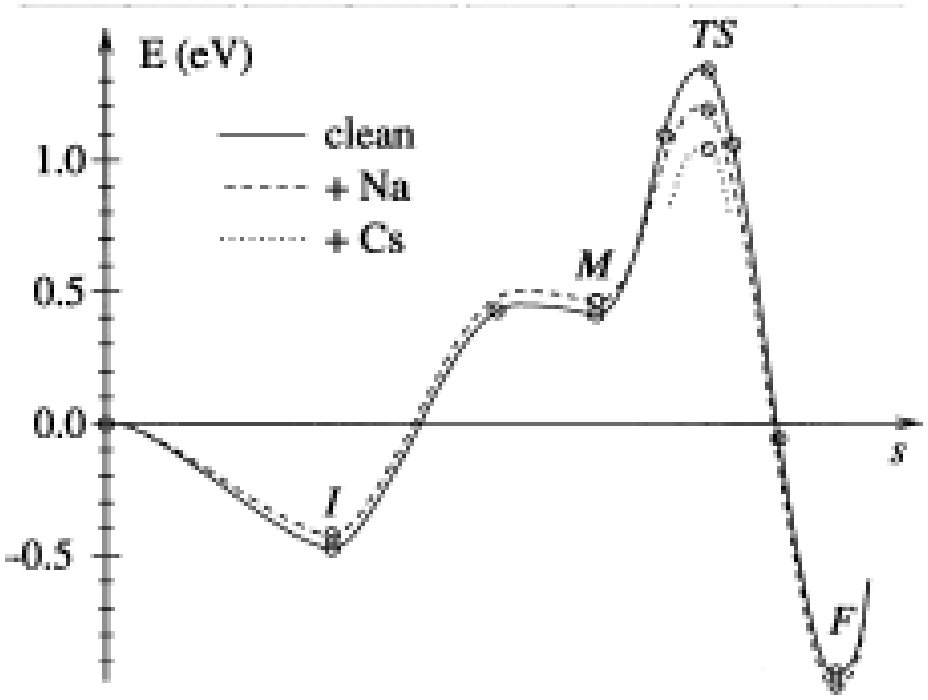

Figure 20: The energy path for the dissociation of N_2 on Ru(001). From Ref. [120]. ***Reprinted with permission from American Physical Society, Copyright 1998.***

From the vast number of reports on the alkali promotion of adsorbates, there are two general schools of thought that have emerged regarding the interaction with an adsorbate. The first focuses on the alkali-induced changes in the density of the metal states at the Fermi level [130]. As indicated previously, the filling of the antibonding states leads to an increase in the binding of a molecular species to the surface [45]. The strengthening of the metal-adsorbate bond results in the weakening of the intramolecular bond, thus facilitating dissociation on the surface. If the promoter is able to facilitate charge transfer from the substrate into the antibonding electronic states of the adsorbate, dissociation of the adsorbate is therefore more likely, and the overall activation barrier of the reaction will be lowered. The molecular states

which are near the Fermi energy, E_F, are the most sensitive to changes in the electronic structure of the substrate. Slight shifts in the position of these states relative to E_F can change their separation and the extent of mixing with the substrate levels. In the presence of an alkali metal, which is an electropositive adsorbate that donates electrons to the substrate, the surface density of states near E_F is significantly perturbed. Due to the greater availability of electrons near E_F, the substrate has an increased ability to donate electrons into the adsorbate, thereby lowering the dissociation barrier [130].

The second interpretation regarding the interaction of the alkali metal with the adsorbate focuses on the electrostatic interaction between the adsorbed alkali metal atoms and the chemisorbed molecules [131]. If it is believed that if the transition state is stabilized relative to the initial state of the reactants by promoter atoms, then the activation energy of the reaction will be lower. Transition states typically exhibit a distorted electronic structure as well as extended bonds. This results in larger dipole moments of the transition states compared to the ground state molecules [131]. The increased dipole moment makes the transition state more susceptible to the influence of the electrostatic fields arising from the presence of alkali metal ions on the surface. The interaction of the field with the transition state reduces the energy of the state and therefore the barrier of the reaction through this transition state.

It is not clear which promotion mechanism predominates during the adsorption of alkali metals and it is quite possible that the actual mechanism of promotion is system specific. Calculations by Nørskov et al. have suggested that the alkali metal promoted dissociation of N_2 on Ru surfaces is due to the electrostatic stabilization of the transition state [120]. However, on a K-promoted Fe surface, the promotional effect arises from the stabilization of the chemisorbed

N_2(a) [132]. Chapters 7, 8, and 9 of this thesis will examine the interaction of CO with Li promoter atoms on two Ru surfaces, while Chapter 10 deals with the coadsorption of N_2 and Li.

2.0 EXPERIMENTAL

2.1 ESSENTIAL EXPERIMENTAL FACTORS

A number of experimental variables must be under control before a successful surface science experiment can be performed. In the case of the work in this thesis, single crystals of metals are used to investigate chemical processes which occur on the crystal surface. The ultimate goal is to use the simplification afforded by a single crystal surface of known structure to understand surface processes which occur on more complex surfaces, such as catalyst surfaces, which are not controlled in structure, but which contain surface features similar to those which can be built up on a single crystal. The examples provided in this thesis deal with the role of atomic step defect sites on the vibrational and desorption kinetic properties of CO, N_2 and Li adsorbates. The work is done by comparing a stepped, high index crystal to a non-stepped, planar low index crystal surface. The work involves the use of single crystals of known orientation, investigated in ultrahigh vacuum, under conditions of atomic cleanliness (< 1% surface impurities). The crystals are studied by infrared reflection absorption spectroscopy (IRAS), and temperature programmed desorption (TPD). The adsorbate molecules are quantitatively transferred to the crystal surface using a molecular beam doser delivering a known flux of adsorbate molecules. Prior to adsorption, the crystals are cleaned by sputtering and by chemical means, and the surface purity is evaluated by Auger Electron Spectroscopy (AES). Adsorbate molecules may be

bombarded by electrons to cause dissociation at low temperatures. In other experiments, to test the effect of alkali promoter atoms on both stepped and planar crystals, Li atoms are quantitatively dosed from a heated source known to deliver pure metal, and the effect of the Li is investigated using work function studies, IRAS, and TPD. The subsequent sections of this chapter deal with the details of the experimental methods employed.

The various properties of the surface can be affected considerably by even trace quantities of impurities. Metal single crystal surfaces are typically cleaned by extensive Ar^+ ion sputtering, oxygen cleaning, and annealing procedures. Once an atomically clean surface is obtained, it is absolutely critical to maintain a clean surface, which requires a very low background pressure as most transition metals are very reactive. The major components of residual gases in a UHV chamber are H_2, CH_4, H_2O, CO, Ar, and CO_2, with only CO, H_2O, and CO_2 being reactive. In a well baked UHV chamber, the concentration of the residual active gases is typically less than 40 % of the total residual gases. The use of a turbo molecular pump, an ion pump, and a Ti sublimation pump has been found to be an excellent combination to achieve the desired vacuum.

2.2 ULTRA HIGH VACUUM CHAMBER

All of the experiments reported here were performed in an ultra high vacuum (UHV) chamber that has been described in detail previously [133]. The custom designed, cylindrical, stainless steel UHV chamber was built by Leybold-Heraeus GambH and the schematic is shown in Figure 21.

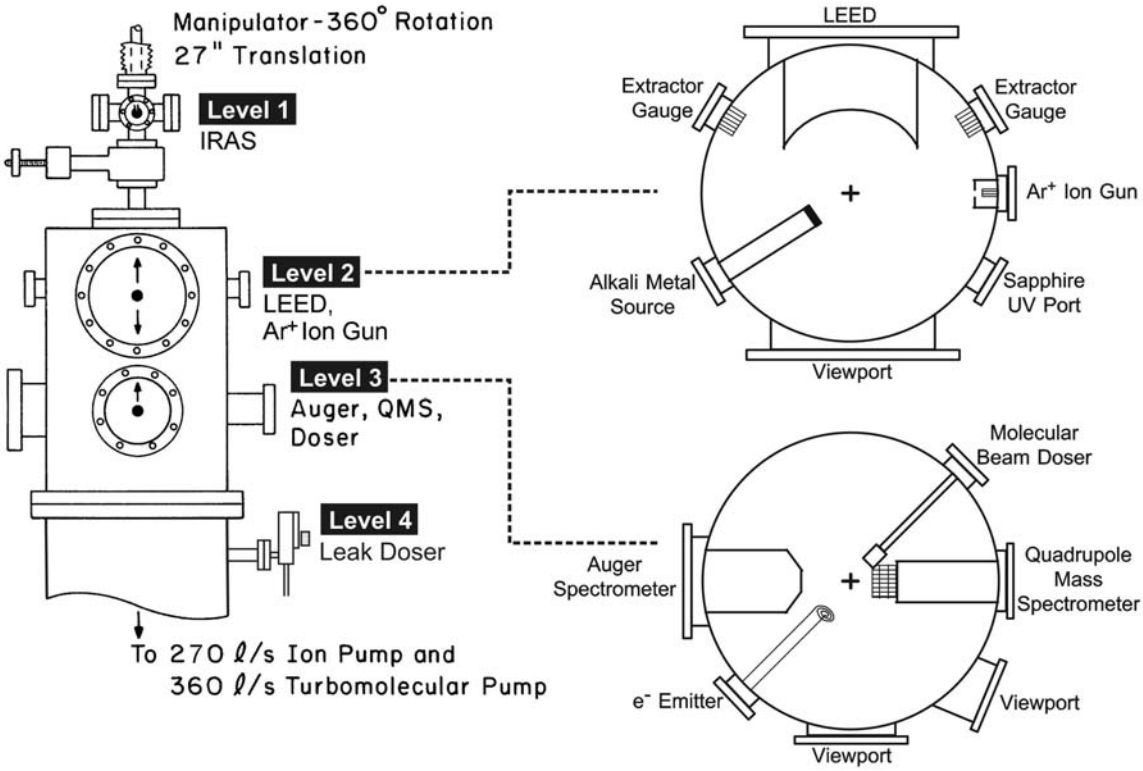

Figure 21: Schematic diagram of the UHV apparatus.

The chamber is divided into four distinct levels as shown by the left side of Figure 21. All of the major and minor analytical tools are contained in the top three levels of the chamber, with the bottom level containing the tools necessary to achieve the ultra high vacuum conditions.

The top most level of the chamber, Level 1, contains the optical path and the instrumentation for infrared reflection absorption spectroscopy (IRAS), which was the primary technique used in the investigations reported in this thesis. The external optical bench is constructed around the ultra high vacuum chamber. The infrared cells are constructed of stainless steel and contain four KBr windows as shown in Section 2.6.2, Figure 33. The KBr windows enclose two interconnected infrared cells which are either evacuated or contain the same gas at the same pressure. The differentially pumped windows are sealed with viton O-rings and are pumped by a 2 L/s diode ion pump (Varian, VA2-mini-vac-B). One of the infrared cells

is used as a reference path for the infrared beam and the sample is positioned in the other infrared cell to perform IRAS. With this design, vibrational measurements can be performed under ultra high vacuum conditions as well at elevated pressures. The infrared compartment is separated from the rest of the UHV chamber by a 2 ¾" viton seal gate valve enabling spectroscopic measurements at pressures up to 1 atm.

Level 2, the preparation level, consists of equipment that is important for the initial preparation of the single crystal surface. A four-grid low energy electron diffraction (LEED) apparatus with a hemispherical phosphor screen for characterization of the single crystal surface and adsorbate layer and a 8" viewport directly across from it for viewing the LEED images are the major components at the second level. Also contained in the second level are two nude extractor gauges (Leybold, IE511), an ion gun (Leybold, IQE 10/35) for sputtering, and a Li getter source (SAES getters) mounted in a homemade evaporation source. The ion gun contains a direct feed of gas (in this case Ar) into the ionizer region for a higher efficiency of sputtering compared to simply backfilling the chamber with argon. The second level also contains a commercial Kelvin Probe system (Besocke Delta Phi GmbH) for work function measurements.

A shielded quadrupole mass spectrometer (UTI 100C) with a 5 mm aperture and a Auger spectrometer with a single-pass cylindrical mirror analyzer (Physical Electronics, 10-155, base system 3017) are mounted directly across from each other at the third level of the chamber. This level also contains a capillary array molecular beam doser mounted on a linear transfer mechanism for accurate positioning relative to the crystal, a tungsten coil for hydrogen dissociation, and two glass viewports (6" and 4 ½"). The capillary array molecular beam doser is used for the quantitative exposure of the surfaces to molecular adsorbates. The flux of the gas is limited by a pinhole aperture (~5 μm), randomized by a baffle inside the doser housing, and

subsequently collimated by a capillary array of parallel capillaries with a 10 μm diameter and a length of 500-1000 μm fused together into a hexagonal arrangement. Additional details concerning the molecular beam doser as well as its construction can be found in Appendix A.

The lowest level of the chamber contains an additional nude extractor gauge (Leybold, IR 511), an all metal high-precision leak valve (Leybold, 873-05) for controlled admission of gas into the chamber, and a three-filament Ti sublimation pump (Leybold). The Ti sublimation pump is capable of producing a getter layer of titanium on the walls of the lower part of the chamber. A metal shield above the filaments prevents the deposition of a Ti film onto the rest of the chamber.

Under normal experimental conditions, a 270 L/s diode sputter ion pump (Leybold, IZ 270) exclusively pumps the 100 L chamber in order to maintain the vacuum to the desired base level. The chamber can also be pumped by a 360 L/s turbomolecular pump (Leybold, Turbovac 360) in cases of high gas loads. The turbo pump is backed by a 400 L/min dual-stage rotary vane roughing pump (Leybold, D16A). The chamber is isolated from the turbo pump via a viton seal gate valve under normal experimental conditions such that only the ion pump is responsible for maintaining vacuum. After an extensive bakeout of the chamber at 150°C the base pressure in the chamber is consistently less than $\sim 1 \times 10^{-10}$ mbar.

The various instruments and equipment are positioned radially relative to the center axis of the chamber and therefore it is necessary to be able to position the sample in front of any of the various ports. The sample is mounted on a removable holder (see section 2.3), which is attached to a stainless steel tube via a copper finger that is silver soldered at the end of the tube. The entire sample assembly is mounted to a manipulator (UHV instruments, 2150) and can be accurately and reproducibly positioned inside the UHV chamber using four degrees of freedom.

The manipulator assembly (Figure 22) can be rotated 360° on top of the IR cell assembly by means of a two stage differentially pumped rotary seal with Teflon gaskets [133,134]. The first stage of pumping consists of rotary roughing pump (Welch Duo-Seal 1400) and the second stage is pumped by a 2 L/s diode ion pump (Varian, VA2-mini-vac-B). The manipulator enables translation of the sample by up to 1" in each of the x- and y- directions (horizontally) with a precision of 0.001-0.002" using the micrometric screws. The stainless steel tube is contained in a long welded stainless steel flexible bellows which enables up to 20" of translation in the z-direction (vertically).

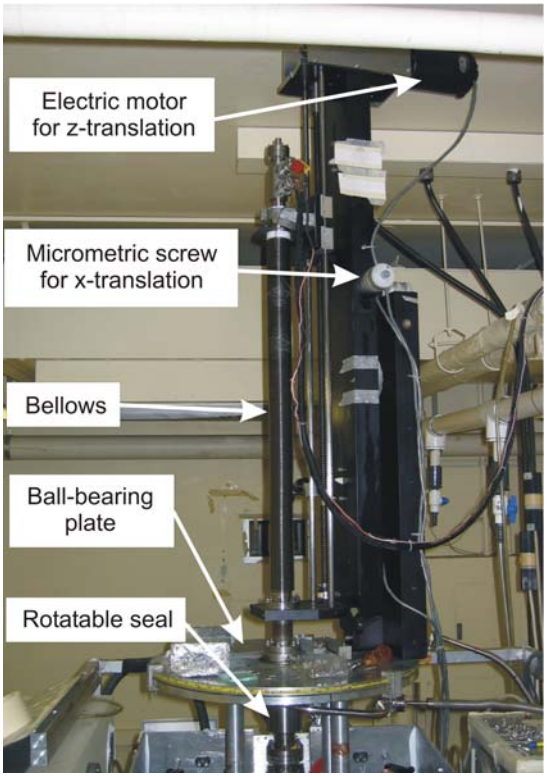

Figure 22: Manipulator for x-, y-, and z-translation and 360° rotation of a sample in the UHV chamber.

2.3 SAMPLE MOUNTING

The critical component of the sample assembly is a removable sample holder which is mounted at the end of the long stainless steel tube. The sample holder mounts to the copper "cold" finger, which is silver soldered to the bottom end of the stainless steel tube (Figure 23). The hollow cavity in the copper cold finger as well as the tube is filled with liquid nitrogen for very efficient cooling of the sample.

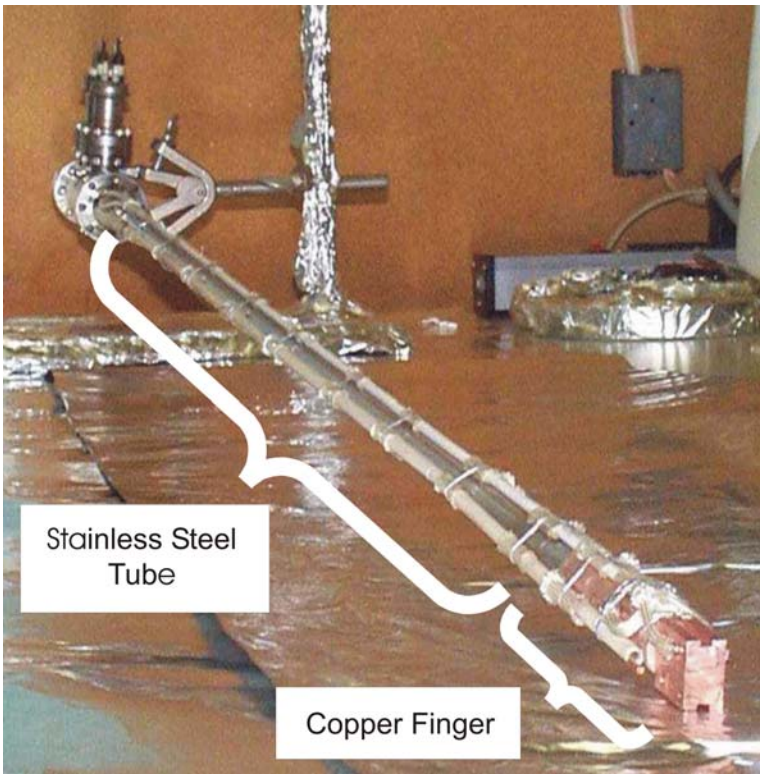

Figure 23: Tubular liquid nitrogen reservoir with copper cold finger welded to the open end.

The sample is heated by resistive heating and the pair of power heating leads is enclosed in insulating ceramic tubes along the entire length of the tubular shaft as shown in Figure 23. In addition there are two pair of thermocouple wires that are also insulated in ceramic tubes for

measuring the temperature of the sample. The upper end of the stainless steel tube is connected to a manifold with three UHV ceramic feedthroughs; one pair for the power heating leads, the second pair for a Type K (chromel-alumel) thermocouple feedthrough, and the third pair for a Type C (W-Re(5 %) –W-Re(26%)) thermocouple feedthrough. The wires (power and thermocouple) are connected to the feedthrough wires with small nuts and bolts. This manifold assembly and the insulated connections are designed to be kept intact for a permanent installation and are only disassembled in the event of a problem with one of the wires or feedthroughs.

The removable sample holder (Figure 24) installed at the lower end of the copper cold finger enables the single crystal sample to be changed with relative ease through a 8”- flange on the side of the UHV chamber. The sample holder is constructed of OFHC copper and facilitates the efficient cooling of the sample through heat transfer with the cold finger.

Two 1.0 mm tungsten wires are spot welded to the edges of the single crystal in order heat and cool the sample. The power heating leads (from the upper manifold) are connected to the external copper plates of the sample holder via a copper connector and an additional copper wire, which is held in place by the upper two screws in the copper plates. The two lower screws in the copper plates hold the W-wires in place and ultimately support the weight of the crystal. The two copper plates are electrically isolated from the main center part of the sample holder by 1 mm thick sapphire wafers which are cut and polished perpendicular to the crystallographic c-axis, as the thermal conductivity of sapphire is highest along the c-axis. This type of construction has routinely enabled resistive heating to 1700 K and cooling to 85 K with liquid nitrogen or to 75 K by bubbling He through the liquid N_2 coolant [135,136].

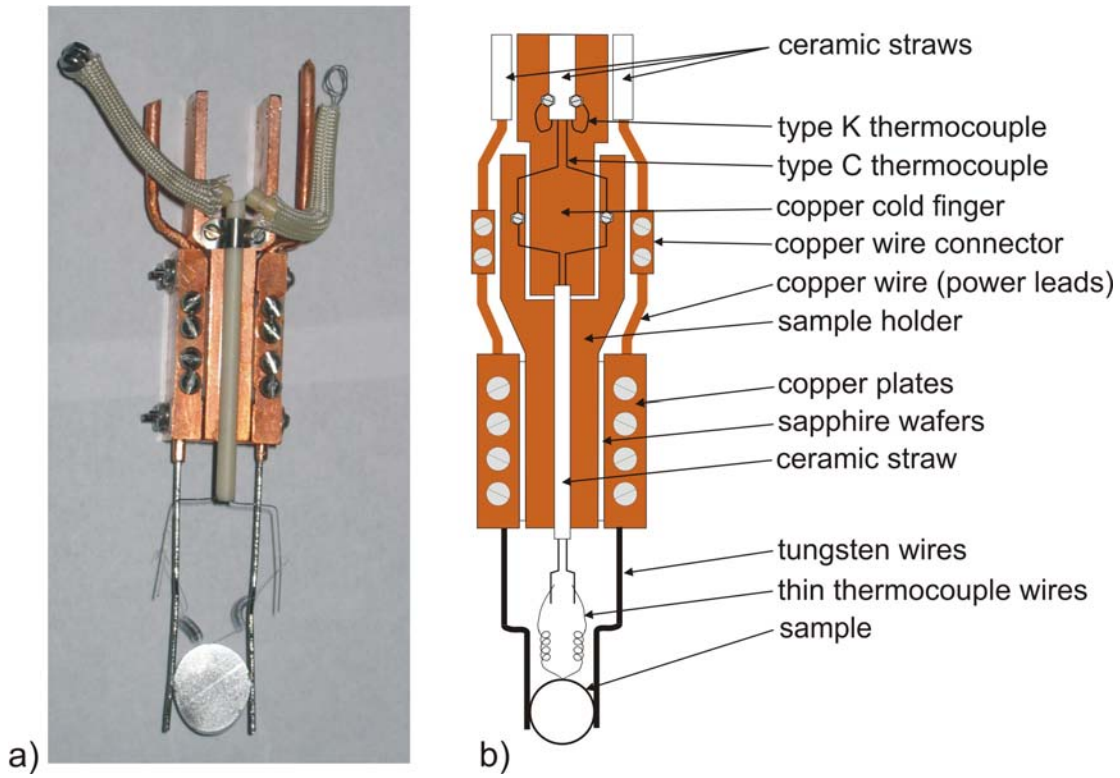

Figure 24: (a) Removable sample holder. (B) Schematic of sample mounting. Upper thermocouple connections are electrically insulated with glass-fiber sleeves as shown in (a).

At 0 K all molecular motion apart from that associated with the zero point energy ceases, which means that if the temperature is low enough all chemical substances will condense. Therefore, it is highly desirable in surface science studies to work at sample temperatures as low as possible in order to promote chemisorption as well as physisorption. The two most commonly used cryogens are liquid nitrogen and liquid helium, but in the experiments presented here, only liquid nitrogen was used for cooling purposes.

An electronic ice point was used to convert the thermocouple voltages into 0°C referenced signals for exportation into a Labview Data Acquisition program. Unfortunately, a factory calibration for the type C thermocouple is not available below 255 K. It was therefore necessary for the type C thermocouple to be calibrated against the type K thermocouple, which has a calibration table. The initial calibration of the type C thermocouple was accomplished

through the use of a "dummy" sample to which both sets of thermocouples were attached. The sample was cooled using liquid N_2 and an algorithm was determined from the data to relate the type K voltage to the uncalibrated type C voltage. The type C thermocouple was able to be calibrated to ~85 K and any readings below this temperature are subject to question. It was imperative during the calibration process that liquid nitrogen was added more or less continuously to the dewar atop the tubular shaft such that it was always filled to ensure a constant temperature of the manifold. This minimized any potential errors associated with a temperature fluctuation of the thermocouple feedthroughs. The thermocouple (type C) feedthroughs are extremely temperature sensitive due to the fact that they are composed of an alloy different from the standard tungsten-rhenium combination due to the brittleness of the tungsten. An additional method to minimize the errors associated with the type C feedthrough was to construct a styrofoam shield around the thermocouple feedthrough to prevent the cold vapors from the liquid N_2 from altering the temperature of the feedthrough.

The choice of thermocouple depends on the sample being studied. Due to the high temperatures required for removal of oxygen from the Ru surface, a type C thermocouple will be used in these studies. The type C thermocouple wires are connected to the corresponding pair of wires running along the stainless steel shaft with tiny nuts and bolts. As indicated previously, there are two pairs of thermocouple wires encased in the ceramic tubing running alone the stainless steel tube. In order to monitor the temperature of the sample (and hence the internal temperature of the chamber) during the bakeout process, the type K thermocouple wires are used. The type C thermocouple can not be used to record the temperature during the bakeout process as the calibration is only valid when the tube is filled with liquid nitrogen and the manifold is cold. The type K thermocouple wires located at the base of the shaft are carefully immobilized

by tying them to the base of the shaft with tantalum wire. It is critical to make sure that both type K thermocouple wires are actually touching the shaft/coldfinger (as they are not connected together) or it will be impossible to read the internal temperature during the bakeout process. The bolt and nut thermocouple connections are electrically insulated from the grounded steel shaft, copper cold finger, and grounded parts of the sample holder using fiber glass sleeves. At the bottom of the sample holder the larger (0.010") thermocouple wires are connected to 0.003" thermocouple wires which are ultimately spot-welded to the rim of the single crystal. The small coil in the middle of the 0.003" thermocouple wire gives the tiny thermocouple wires increased flexibility and significantly reduces the chance of breaking the weld between the thermocouples and the rim of the crystal from mechanical stress during the mounting process. The coil also serves to reduce the heat transfer through the thermocouple wires thus making the temperature measurements more accurate.

It is imperative that a specific welding sequence be followed in order to successfully mount the single crystal to the sample holder. Initially the small, coiled thermocouple wires are welded together and the resulting weld is carefully inspected. The welded thermocouple assembly is then spot-welded to the crystal. The goal is to weld the actual junction of the two thermocouple wires to the crystal to reduce the risk of inaccuracies in the temperature measurements. A successful weld will be able to support the weight of the suspended single crystal prior to welding the crystal to the rigid tungsten heating wires. The two W-wires are then simultaneously welded to the edges of the single crystal. This is the most critical step in the assembly process as the quality of the welds of the heating wires to the crystal determines the overall efficiency of the heating and cooling processes. The final step in the assembly process is to weld the 0.003" thermocouple wires to the 0.010" thermocouple wires on the sample holder.

The completed sample holder is then carefully installed in the chamber and after making all of the necessary electrical connections it is absolutely critical to ensure that there is no contact of the sample/thermocouple wires/power leads to any grounded part of the chamber. If there is any connection to ground then it would impossible to apply an electrical bias to the crystal during the TPD process or for electron bombardment of the sample.

2.4 GAS HANDLING AND DOSING

2.4.1 Gas Handling Line

The external gas handling line was used to dose various gases into the UHV chamber and was described in detail previously [134,137] and is shown in its modified form in Figure 25.

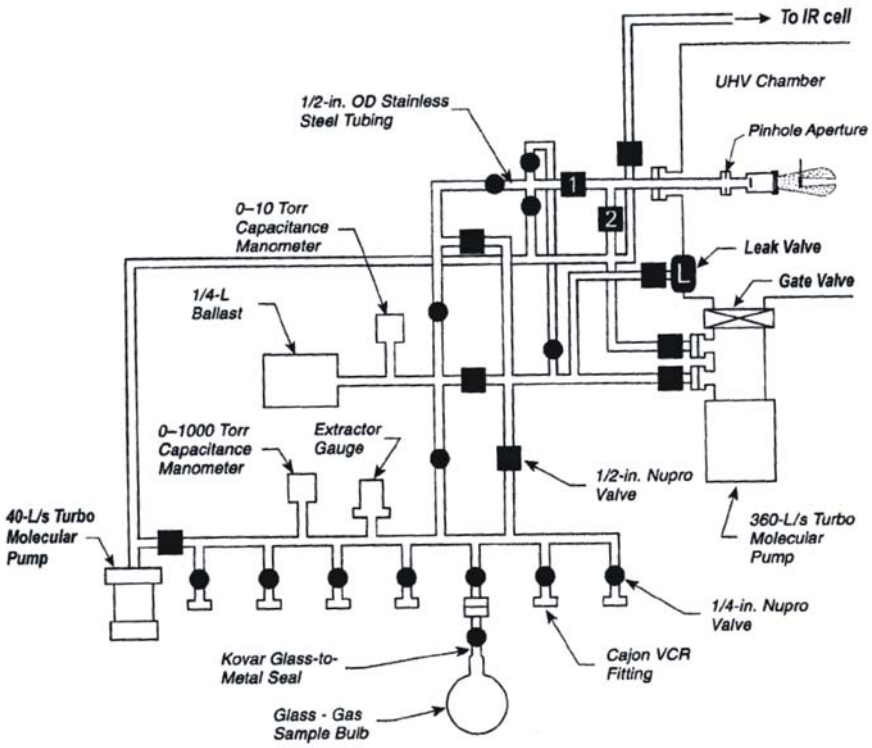

Figure 25: Gas handling line. Modified from Ref. [134].

The line is constructed of stainless steel tubing separated into sections by all metal bellows sealed Nupro valves. The gas line can be pumped by a either a dedicated 40 L/s turbomolecular pump (Pfeiffer-Balzers, TPU-040A) or by the 360 L/s turbomolecular pump typically used to pump the main UHV chamber. The line can be baked to 150-200°C with heating tapes while being pumped with either of the turbo pumps. Baking of the gas line for roughly 24 hours eliminates much of the contamination from the various reactive gases that had adsorbed on the internal walls of the stainless steel tubing resulting in a base pressure in the gas line of at least 1×10^{-7} mbar and measured with the ion gauge.

Up to six glass storage bulbs can be conveniently connected to the gas line through the ports using ¼" Cajon face-seal fittings and a small copper gasket. The gases are stored at pressures ≤ 760 torr in order to prevent an accidental over-pressurization of the gas line. Using

one of three Baratrons (10 torr, 100 torr, and 1000 torr), the line can be controllably and reproducibly pressurized to 0.01 – 1000 torr.

The total volume of the gas line as well as the volume of each of the individual sections was determined by a series of gas expansions of an inert gas (either N_2 or Ar). The pressure was recorded following each expansion and the volume was determined using the relationship of $P_1V_1 = P_2V_2$ for an ideal gas. A calibrated glass bulb with a known volume of 108.46 ± 0.11 cm^3 was used as a reference for determining the volumes with a precision of about 1.5 % in the volume measurements.

The gas line is connected by two separate routes to the UHV chamber by means of an all metal variable flow leak dosing valve (for back filling) or a capillary array molecular beam doser. The actual method of gas exposure used depends on the pressure needed to achieve the desired exposure as well as on the vapor pressure of the solid or liquid source.

2.4.2 Variable Leak Doser

Backfilling the chamber to a certain pressure for a desired amount of time is the most uniform method of exposing an adsorbate gas to the sample surface. The exposure, ε, (per cm^2) can then be calculated as

$$\varepsilon = \frac{P}{\sqrt{2\pi mkT}} * t \qquad (2.1)$$

where P is the gas pressure, m is the absolute molecular mass, k is Boltzmann's constant, T is the absolute temperature, and t is the exposure time.

An all-metal precision leak valve which connects the gas line to the chamber was used to backfill the chamber. During backfilling, the chamber was pumped exclusively with the turbo pump to avoid excessive regurgitation of spurious gases from the ion pump.

If the gas of interest originates from a solid or liquid source with a very low vapor pressure at room temperature or when high exposures requiring high pressures (10^{-7} to 10^{-5} mbar) are needed, then backfilling the chamber is the preferred method of gas exposure in order to reduce the exposure time. Backfilling results in the adsorption of gas on the entire surface of the sample, including the rim and back side, making quantitative desorption measurements inaccurate. During backfilling various impurities are displaced from the chamber walls and can subsequently adsorb on the crystal surface, thus affecting the quality of the measurements. Exposing the UHV chamber to high pressures can often result in difficulty in recovering the ultra high vacuum conditions following the exposure of the adsorbate.

2.4.3 Molecular Beam Doser

Because of the numerous disadvantages associated with backfilling the chamber, a microcapillary array molecular beam doser can be used for the delivery of the gas adsorbates instead [134]. The molecular beam doser, which is either comparable to or slightly larger than the sample target, is designed to create a semi-collimated gas beam. The molecular beam doser must be absolutely calibrated for the accurate and reproducible delivery of adsorbates to the surface. Additional information regarding the molecular beam doser including the actual construction as well as the method of calibration is discussed in detail in Appendix A.

2.4.4 Delivery of Adsorbates

An absolutely calibrated capillary array molecular beam doser was used to deliver the adsorbates to the Ru single crystal in all of the experiments reported in this thesis unless otherwise mentioned. All of the following gases were used without further purification unless otherwise mentioned: $^{12}C^{16}O$(g) (AGA Specialty, 99.999% purity); $^{13}C^{18}O$(g) (CIL, 99% ^{13}C, 95% ^{18}O purity); $^{1}H_2$ (Valley National Gases, 99.9995% purity); $^{16}O_2$(g) (BOC gases, 99.999% purity); $^{14}N_2$(g) (BOC Edwards, 99.9999% purity); and $^{15}N_2$(g) (CIL, 98 % isotopic purity). The coverages (θ_{xx}) of all adsorbates are reported relative to the available Ru surface atoms (1.57×10^{15} cm^{-2} for Ru(001) and 1.37×10^{15} cm^{-2} for Ru(109)).

2.5 SINGLE CRYSTAL PREPARATION AND CHARACTERIZATION

Ru has a close packed crystal structure of the hexagonal (hcp) type, in which the hexagonally close packed layers of atoms are stacked in an ABAB order. In the experiments reported here two different Ru single crystals were used: an atomically stepped Ru(109) single crystal surface and an atomically smooth Ru(001) single crystal surface.

2.5.1 Ru(109)

The first sample was a Ru(109) single crystal (diameter ~ 10 mm) prepared by *ESCETE Single Crystal Technology B.V.* The crystal was oriented, cut and, polished 11.46° from the <001> direction toward the <100> direction. The Ru(109) surface is composed of periodic close-

packed (001) terraces of 9 atomic row width (22 Å) separated by double height atom steps of (101) orientation as seen in Figure 26.

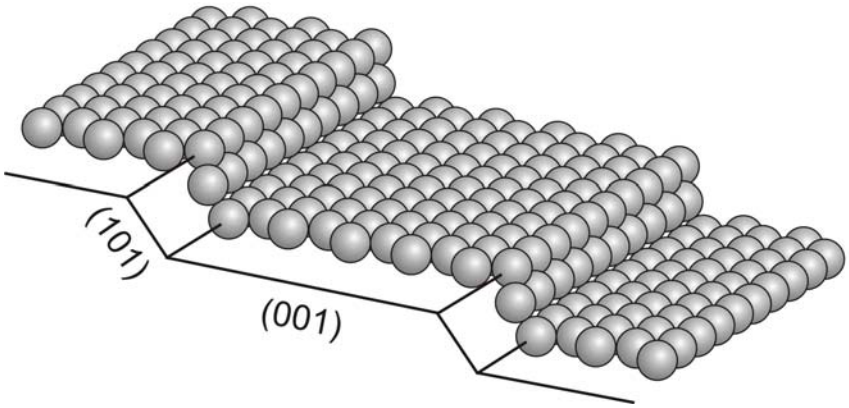

Figure 26: Atomic arrangement of the Ru(109) stepped surface.

A detailed characterization of the single crystal was achieved by means of low energy electron diffraction (LEED) and the results are reported in detail by Zubkov et al. [42]. It was initially thought that when the crystal was cut it would consist of five atom wide terraces interrupted by single height steps of alternating three-fold and four-fold symmetry as indicated in Figure 27. It was found that after a LEED analysis of the surface of the crystal that the surface had reconstructed upon annealing to form a surface with 9 atom wide terraces separated by double height steps. An energy dependent LEED investigation using an electron beam energy in the range of 50 - 300 eV was performed in order to determine the structure of the surface [42]. The resulting patterns were stacked in 1 eV increments in the beam energy. The experimental LEED results were compared to kinematic LEED simulations and it was subsequently determined that the crystal structure was as shown in Figure 26 [42].

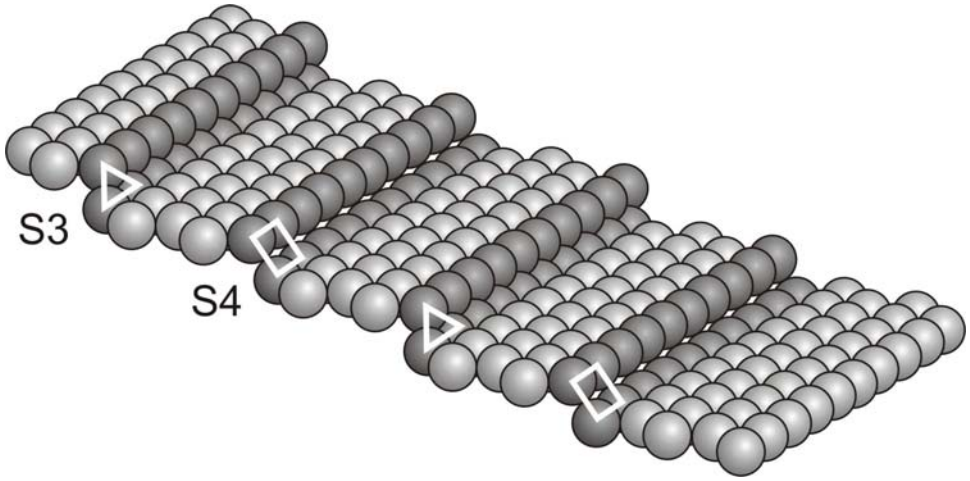

Figure 27: Structure of the unreconstructed Ru(109) surface.

2.5.2 Ru(001)

The second sample was a Ru(001) atomically smooth single crystal surface. The Ru(001) single crystal (diameter ≈ 13 mm), also obtained from the same supplier, was oriented and mechanically polished within 0.5° as measured by Laue X-ray diffraction, yielding an overall random step density of < 0.5% of the available surface sites based on the miscut angle. The structure of the Ru(001) surface is shown in Figure 28.

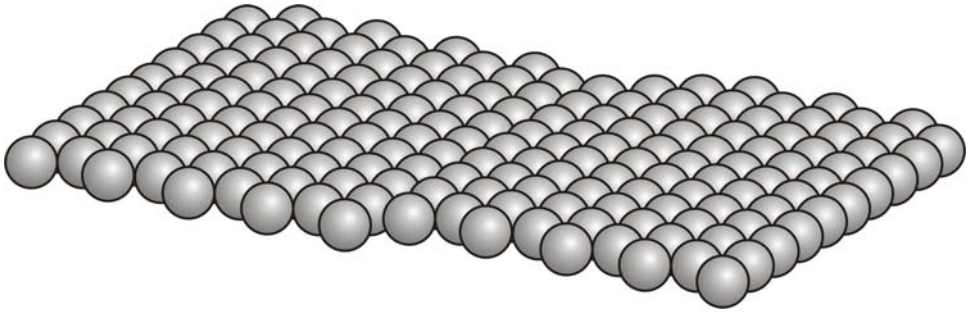

Figure 28: Atomic arrangement of the atomically smooth Ru(001) surface.

2.5.3 Crystal Preparation

Auger Electron Spectroscopy initially indicated that the Ru surfaces were heavily contaminated with Ca, Si, S, O, and very large amounts of C such that the Ru signal was not even observed in the AES spectrum. The non-volatile impurities (Ca, Si, and some C) can be removed initially by extensive Ar^+ ion sputtering. Additionally, it has been reported that the Ru surface can be heated between 500 and 1500 K in an O_2 atmosphere (10^{-7}-10^{-4} mbar) in order to oxidize and remove sulfur [138] as well as carbon from the surface [95,139,140]. The final procedure involves the removal of oxygen by heating in an H_2 atmosphere [95], or more frequently annealing the sample repeatedly to 1500-1550 K in UHV [95,139-143]. In previous reports, a chromel-alumel thermocouple was used to monitor the temperature of the crystal. The type K thermocouple is prone to degradation and melting above 1500 K and therefore when using the type K thermocouple, multiple annealing cycles were necessary to remove the adsorbed oxygen from the Ru surface. It is preferred that the oxygen be removed from the surface in a single annealing cycle by briefly heating to 1700 K, which can be achieved by using the type C (W-5%Re and W-26%Re) thermocouple [141].

Throughout the entire cleaning procedure, the Ru samples were monitored by Auger spectroscopy. The two samples were initially cleaned by extensive Ar^+ ion sputtering ($I_{Ar+} \sim 1$ μA, ~24 hours, 1000-1500 eV, room temperature) followed by a series of alternating cycles of sputtering (~ 5-6 hours, 600 eV, room temperature) and annealing in an O_2 beam (~5-6 × 10^{13} molecules/cm^2 s) at 1200 K. During annealing of the samples, impurities present in the bulk will migrate to the surface, facilitating the need for a series of sputtering/cleaning cycles. Ca and Si, as well as the majority of C contamination were removed after the initial sputtering and annealing cycles. Additional oxygen treatments were necessary to remove the remaining carbon

from the surface. The Ru samples were annealed at 1200 K in an oxygen flux (~5-6 × 10^{13} molecules/cm^2 s) for 30 minutes. The adsorbed oxygen was easily removed by a brief annealing (~60 seconds) to ~ 1700 K, achieved by resistive heating. During the final annealing, the pressure in the UHV chamber did not typically exceed 6 × 10^{-10} mbar, thereby insuring that minimal contamination will occur on the surface. In order to maintain the contamination at a level below 1 % of the available Ru surface atoms, the pressure in the chamber must remain at this level for less than ~ 70 seconds for impurity molecules with a sticking coefficient of unity. At 1700 K the sticking coefficient is significantly lower than unity and therefore the contamination level will be much less than 1 % resulting in an atomically clean single crystal surface. It took roughly 10-15 oxygen cleaning/annealing cycles before the Ru crystals exhibited a clean Auger spectrum (see Figure 29).

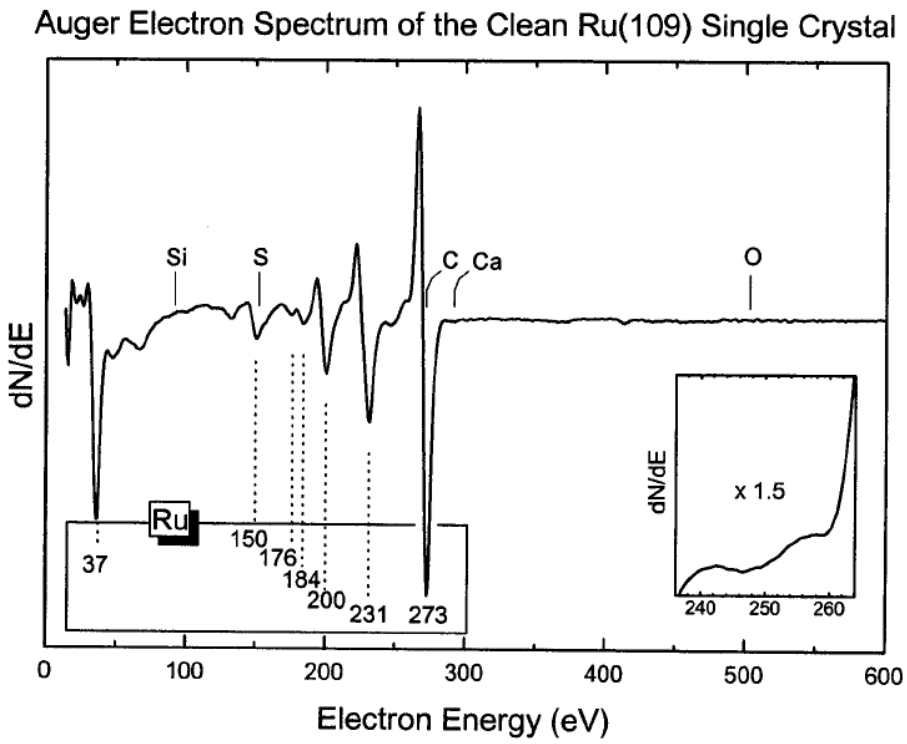

Figure 29: Auger electron spectrum of the clean Ru(109) crystal. The electron excitation energy = 2000 eV. Common impurities, if present, would exhibit their Auger transitions at the energies indicated. The region between 240 and 260 eV is magnified by a factor of 1.5 in the inset to show the absence of the carbidic carbon transition at 251 eV [144].

The AES spectrum clearly indicates the absence of the most common impurities, sulfur, silicon, and oxygen. One of the problems associated with the use of Ru, other than the difficulty in obtaining an atomically clean surface due to the high desorption temperature of O_2 from the Ru surface, is the fact that the Auger signals of C and Ru overlap significantly at 272-273 eV. This overlap makes it difficult to immediately verify the presence or absence of carbon on the Ru surface and additional analysis is needed. Carbidic carbon exhibits an Auger peak at 251 eV on the ruthenium surface [144] and the insert in Figure 29 shows this region enlarged to show the absence of such a carbon signal. Graphitic carbon does not exhibit Auger features at 251 eV and therefore can be easily overlooked. Because of the overlap of the C and Ru features it is necessary to carefully examine the symmetry and ratios of the Ru 273 eV and Ru 231 eV Auger

peaks. As the amount of carbon decreases (due to cleaning) on the Ru surface, the peak to peak intensity ratio of the 273 eV peak to the 231 eV peak will decrease due to the fact that the 273 eV peak will have contributions from the carbon and the 231 eV peak is solely from the Ru. Typically the ratio of the 273 eV peak to the 231 eV peak has been reported in the range of 1.57-2.6 for different clean Ru crystals [145-147]. This is a rather large range of values and therefore this ratio alone can not be used to accurately monitor the cleanliness of the samples.

An additional criterion for the cleanliness of the Ru surface is the ratio of the negative to positive parts of the 273 eV peak. This ratio changes dramatically in the presence of carbon as the C Auger feature is dominated by the negative part, with an intensity ratio of the negative to the positive part of > 4 [148]. The Ru signal is characterized by a more symmetrical ratio (273-/273+) in the range of 1.3-1.39 [145-147]. As the surface carbon is removed, this ratio decreases.

During the various stages of cleaning of the Ru surfaces, the two ratios of interest change accordingly. A plot of how the ratios change for the Ru(109) surface is shown in Figure 30. The most significant change in the Auger ratios occurs after the extensive initial sputtering and 10 cycles of oxygen cleaning. The surface is then very near to its final condition and repeated cycles of O_2 cleaning do not result in considerable changes in the Auger spectrum; however additional annealing cycles are necessary to achieve reproducible experimental behavior of the Ru(109) and Ru(001) surfaces following the sputtering. The spectrum of the clean Ru(109) surface contains a fairly symmetric (273-/273+) intensity ratio of 1.33, which is in perfect agreement with other Ru surfaces reported. Similarly, we have found that the clean Ru(001) single crystal surface exhibits a 273-/273+ ratio of 1.23, slightly lower than previously reported. The less stringent ratio of Ru(273)/Ru(231) is determined to be 2.67 on the clean Ru(109) and

2.73 on the clean Ru(001) surface, both of which are slightly higher than the values reported in the literature. This parameter should not be used to determine the surface cleanliness given the wide scatter of the previously reported values.

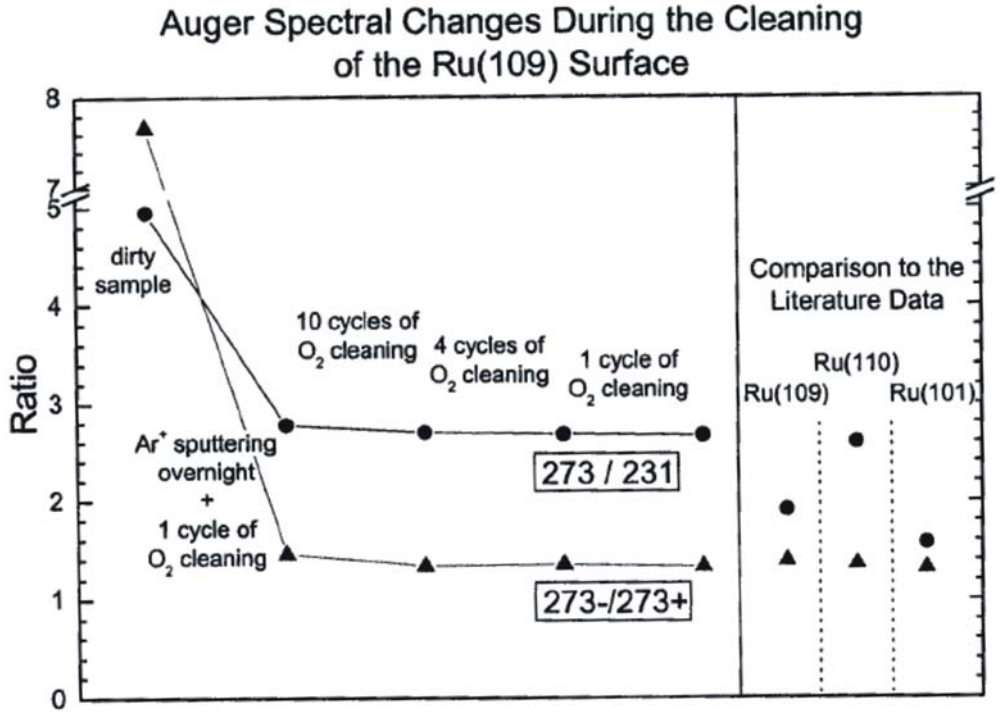

Figure 30: The changes in the (273/231) and (273-/273+) peak intensity ratios in the Auger spectrum of the Ru(109) surface at the different stages of cleaning. The right panel shows the corresponding values reported in the literature for clean Ru(109) [146], Ru(110) [145], and Ru(101) [147].

2.6 INFRARED REFLECTANCE ABSORBANCE SPECTROSCOPY

2.6.1 Theory of IRAS

Infrared reflection absorption spectroscopy (IRAS), or reflection absorption infrared

spectroscopy (RAIRS) as it is sometimes termed, is used to perform vibrational spectroscopy of adsorbed molecules in submonolayer quantities on well-defined single crystal metal surfaces. Pickering and Eckstrom [149] were the first to report results using reflection IR to record spectra from an adsorbed layer of CO on thin metal films. These primitive measurements contained a substantial amount of noise and do not even come close to comparing to the quality of the measurements presented in this thesis.

The interaction of the infrared radiation with the adsorbed layer on the surface depends significantly on the optical properties of the substrate, as metal substrates behave substantially different than semiconductor substrates. The polarization of the incoming radiation determines how the light will interact with the metal surface. When electromagnetic radiation strikes a metal surface, the electric field can be separated into two components, one in the plane of incidence (p-component) and another perpendicular to the plane of incidence (s-component). This is illustrated in Figure 31.

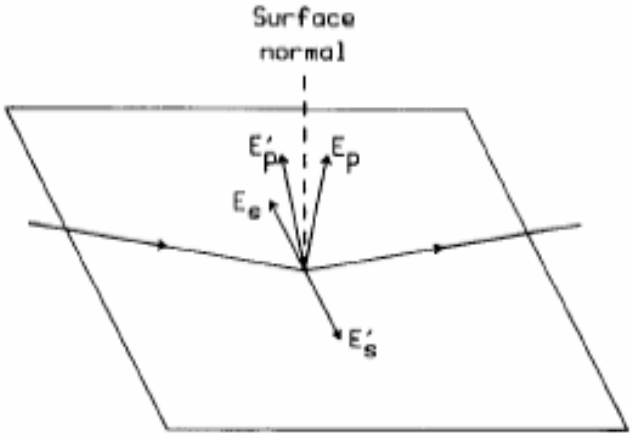

Figure 31: Electric vectors of the s- and p- polarized components of radiation incident on a metal surface. From ref. [150]. ***Reprinted with permission from Elsevier, Copyright 1994.***

The s-polarized infrared radiation will be phase shifted about 180° after reflection and the amplitude of the reflected radiation is almost the same as the incident radiation. There is almost

complete cancellation of the two fields occurring in the vicinity of the surface and therefore the s-component is very small and is not absorbed by the adlayer. There is also a change in the phase of the p-component upon reflection but the change depends strongly on the angle of incidence. The p-component can also be separated into two components. There is a component that is parallel to the surface and there is a component perpendicular to the surface. The parallel components of the incident and reflected beam are in opposite directions and therefore the main effective component of the IRAS measurement is the $E_{P\perp}$. As can be seen from Figure 32a, the perpendicular component is largest when the angle of incidence is close to grazing incidence between 85-90°. The intensity of the absorption is determined by the surface intensity function, E_P^2 sec ø, is also largest when the angle of incidence approaches grazing incidence as can be seen in Figure 32b.

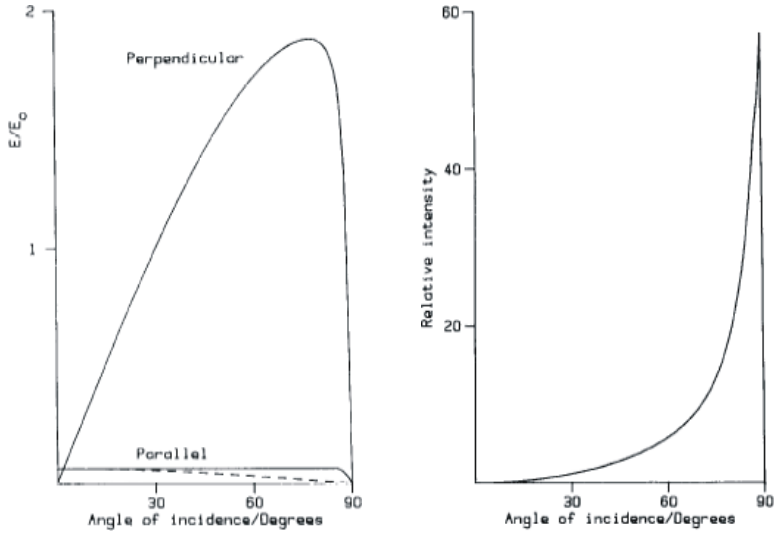

Figure 32: (a) (Left) Surface electric field components as a function of the angle of incidence and (b) (Right) Surface relative absorption intensity function, E_P^2 sec ø, for the perpendicular component of E_P as a function of the angle of incidence. From ref. [150]. ***Reprinted with permission from Elsevier, Copyright 1994.***

For an IRAS experiment the following conditions are of critical importance [151]:

(1) The incident light should have a component that is p-polarized (i.e., parallel to the plane of incidence) as the adlayer will only absorb p-polarized radiation. Therefore only vibrations with a dynamic dipole component that is perpendicular to the surface will be excited. This is termed the so called metal selection rule.

(2) In order to maximize the absorption the incident light should be p-polarized as the s-component is not absorbed by the adlayer.

(3) The incident light should reflect from the surface at near grazing incidence (~85°)

In addition to the above conditions, spectral information is collected by means of a single reflection from the surface of the crystal on most transition metal surfaces.

2.6.2 Infrared Reflection Absorption Spectrometer

The infrared reflection-absorption spectra were obtained by means of a Mattson-Cygnus 100 FTIR spectrometer upgraded to model 4236 with Galaxy 7020 Firmware. It has a water-cooled globar source, a KBr Michelson beam splitter, a He-Ne laser for calibration of the moving mirror system, a system of flat and parabolic mirrors, as well as an IR plane polarizer in the focus of the IR beam. The double beam optical bench is shown in Figure 33 and is described in detail elsewhere [152]. The infrared beam is directed into the external optical bench and then splits into two parts: one beam travels through the reference cell while the second beam passes through the sample cell which contains the Ru sample. Each beam can be operated independently through the use of electrically controlled shutters. A liquid nitrogen cooled narrow band HgCdTe (MCT) detector allows collecting the data in the spectral region of 700-4000 cm^{-1}. The spectrometer and the external optical bench are continuously purged with dry nitrogen to avoid significant atmospheric IR absorption (due to CO_2 and H_2O). The infrared radiation was p-

polarized with respect to the surface of the crystal and spectra were collected using either 4 cm^{-1} or 2 cm^{-1} resolution averaged over 1500-2000 scans.

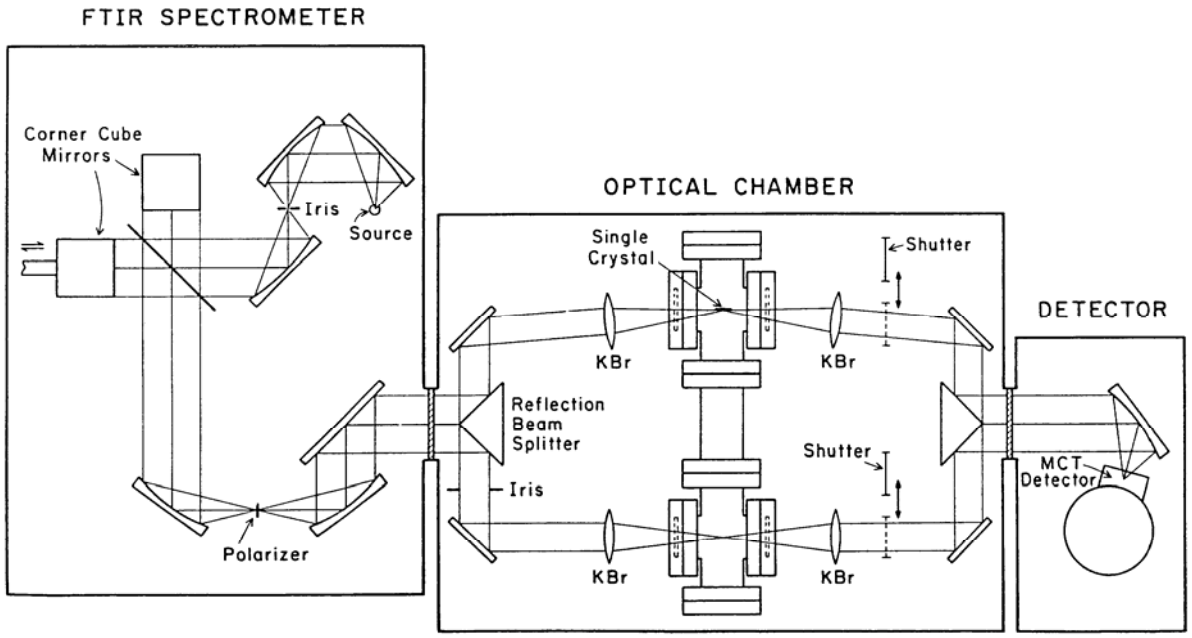

Figure 33: Optical arrangement of the double beam FTIR reflection absorption spectrometer

The double beam feature helps to compensate for fluctuations in source intensity, detector responsivity, and composition of the purging gas. It also allows for the acquisition of IR spectra at higher ambient pressures of gases in the chamber as the spectral contribution due to the gas phase absorption can be cancelled almost completely. The path length through the two cells is not exactly the same, such that complete cancellation does not occur. In the traditional single beam measurements, the background spectrum signal is S_1 and the adsorbate spectrum signal is S_2, and the absorbance spectrum for the adsorbate is defined as $\log(S_2/S_1)$. In the double beam configuration, the background absorbance spectrum can be recorded as $\log(S_1/R_1)$, where S_1 and R_1 are the background spectral intensity measured from the sample beam and reference beam, respectively. The adsorbate spectrum is recorded as $\log(S_2/R_2)$. The difference absorbance

spectrum is obtained by subtracting the background absorption spectrum from the adsorbate absorption spectrum:

$$A_s - A_r = \log \frac{S_2 R_1}{S_1 R_2} = \log \frac{S_2}{R_2} - \log \frac{S_1}{R_1} \qquad (2.2)$$

In Eq. 2.2, the term R_1/R_2 produces a cancellation of all changes in the environment during the period of taking the two spectra.

2.7 ALKALI METAL ADSORPTION METHODS

The Li was deposited by means of a commercial Li getter source (SAES Getters Inc.) installed in a homemade shielded evaporator. A schematic of the evaporation source is shown in Figure 34. The alkali metal dispenser is a compact source of alkali metals which utilizes a powdered mixture of an alkali metal chromate, Li_2CrO_4, with a reducing agent. The reducing agent is the well known St(101) getter material (Zr 84% -Al 16%), which is able to irreversibly sorb almost all chemically active gases produced during the reduction reaction. The sorption of gases prevents the contamination of the alkali metal vapor.

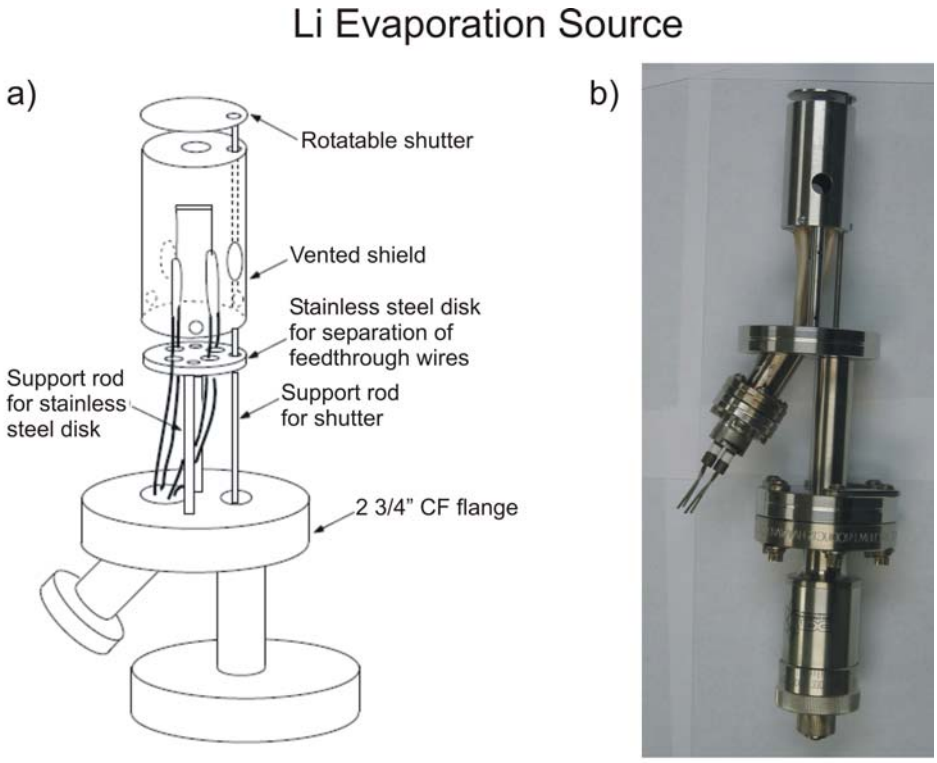

Figure 34: (a) Schematic of Li evaporation source and (b) Li evaporation source.

In order to release the alkali metal, the dispenser must be heated to a suitable temperature under vacuum. The Li evaporates from the source between 550 and 850°C and the higher the operating temperature, the higher the evaporation rate. A rough correlation between the temperature and the current is shown in Figure 35. The overall oxidation reduction equations are shown in Figure 36.

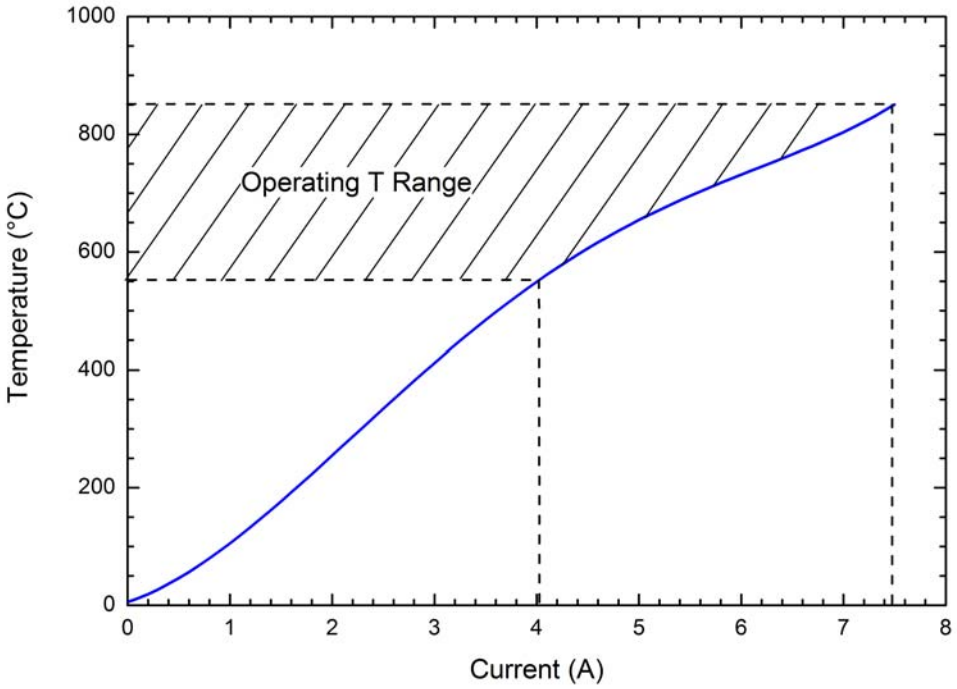

Figure 35: Temperature/current curves for alkali metal dispensers.

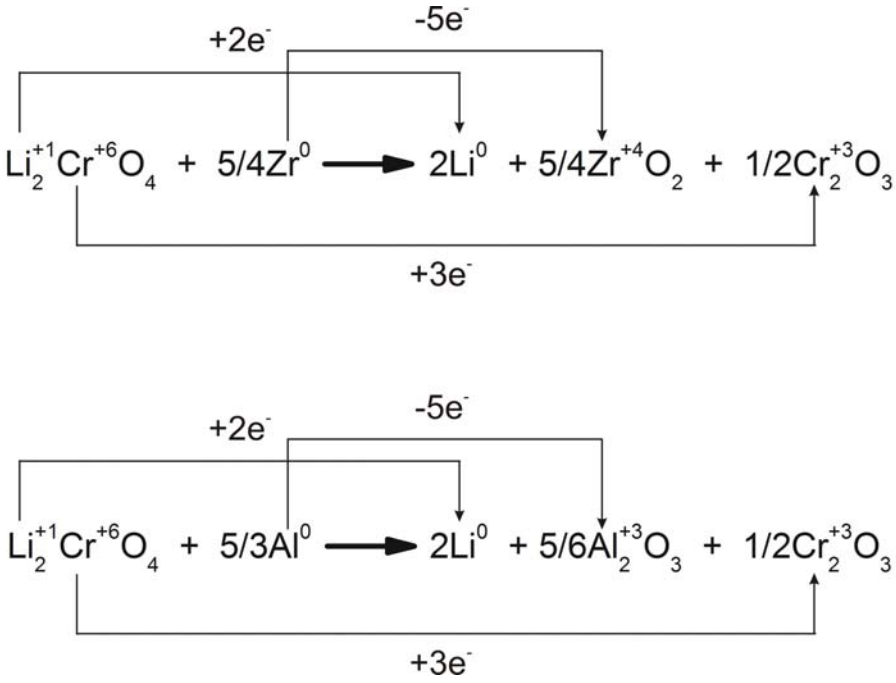

Figure 36: Redox reaction - using Zr or Al. From Ref. [153].

The source is equipped with a shutter for the accurate and reproducible delivery of Li to the substrate. The Li getter source was spot-welded to two 0.015" tungsten loops that can be thoroughly outgassed separately from the source [154]. The Li source was outgassed until the background level of CO reached a minimum level. The W-loops were connected to a feedthrough flange via Ni extension rods welded to the feedthrough wires. A constant evaporation rate of about 0.05 ML/min to 0.10 ML/min was employed. During evaporation, the impurity CO partial pressure was monitored by the QMS and was maintained at the base CO partial pressure level. The Li coverage was calculated from the Li desorption area from the Li-TPD trace in the region between 500 K and 1100 K such that 1 ML corresponds to the Li coverage that completes the first layer (See Section 7.4). Multilayer desorption is characterized by a desorption feature developing around 550 K [155,156]. All Li coverages (θ_{Li}) are presented relative to the available surface Ru atoms (1.37×10^{15} cm^{-2} for Ru(109) and 1.57×10^{15} cm^{-2} for Ru(001)). It has previously been determined that on Ru(001), the saturation of the monolayer Li thermal desorption feature corresponds to 0.76 Li/Ru [155]. By comparison of the Li TPD spectra on Ru(001) to Li on Ru(109), the saturation monolayer coverage of Li corresponds to 0.86 Li atoms/Ru.

2.8 KELVIN PROBE AND WORK FUNCTION MEASUREMENTS

The Kelvin probe is a non-contact, non-destructive, and extremely sensitive measurement device used to investigate properties of materials [157]. It measures changes in the contact potential difference between a reference material and a sample. The essence of the contact potential difference is the difference in the Fermi levels, and hence the work functions, of the two

materials. The Kelvin probe is a non-invasive technique that is extremely sensitive to changes in the top most atomic layers, such as those caused by adsorption, deposition, and atomic displacement [158].

It is well known that when the surfaces of two dissimilar conductors are placed in electrical contact, a potential is generated between the surfaces of the materials. This was first discovered in the early 1900s by Sir William Thomson, also known as Lord Kelvin [159]. The work function is the amount of energy needed to remove electrons from a material's surface to infinity, which is described as the area outside of the electric field created by the image charge. The use of the contact potential difference in order to determine the change in the work function is the most commonly used, as well as the most accurate, method to determine the work function change [160]. In other words, the work function, ϕ, is defined as

$$\phi = E_{vac} - E_F \tag{2.3}$$

where E_F is known as the Fermi energy, which is the energy of the highest occupied electronic state at 0 K, and E_{vac} is defined as the vacuum energy, which is the energy of a material and an electron at infinite separation [117]. As early as 1916, the term "work function" was first used by Lester, even though the concept of work function had been around for several years in the writings of Langmuir and Richardson [161].

For metals, the value of the work function ranges from 2-5 eV and is attributed to the sum of two contributing factors. The first factor arises from the difference between the chemical potential of an electron located in the bulk of the metal and one which is located above the surface of the metal in the absence of other electrons. The electronic chemical potential is a measure of the escaping tendency of electrons from a material in its ground state. Secondly, electrostatic effects at the surface, which vary with the crystalline structure of the surface, have a

significant effect on the value of the work function [162]. This electrostatic effect arises from the fact that the interior electron cloud of the metal does not immediately cease at the surface of the metal. The gradual decay of the electron cloud results in a spill-over effect in which there is a deficiency of electrons at the surface of the metal. This results in a dipole layer at the surface of the metal whose field acts on the electrons that are emitted. The potential associated with this spill-over effect is included in the value of the work function and decays as $1/r^2$. The electrostatic contributions to the work function therefore decrease with increasing distance from the surface. On an atomically rough surface, there is an additional spill-over effect of the electrons. The electrons flow into the low-lying regions of the surface, subsequently smoothing out the sharp edges of the step sites along the surface [163]. The spill-over of electrons at the step sites results in the formation of an electrostatic dipole which is oriented opposite to the dipole associated with the spill-over of the electron cloud. The presence of the step sites on the surface therefore causes a reduction in the net dipole compared to the atomically smooth surface.

Not only is the value of the work function dependent on the surface structure, but it also influenced by the adsorption of atoms and molecules on the surface. The adsorption of atomic or molecular species results in changes to the electronic charges on the surface [164]. The adsorption of molecules on the surface results in the formation of additional dipoles on the surface due to the shifting of charge from the substrate to the adsorbed atom or molecule. The redistribution of charge results in changes in the work function as follows:

$$\Delta\phi = 2\pi P_i N_s \theta , \tag{2.4}$$

where P_i is the dipole moment that is associated with each adsorbed particle, N_s is the maximum number of adsorption sites per unit area, and θ is the fraction of filled adsorption sites [165].

Electrons will flow from the material with the lower work function to the material with the higher work function when two materials with different Fermi levels, and hence work functions, are placed in electrical contact with each other [159]. Several electron energy diagrams for two conducting species are illustrated in Figure 37. The Fermi levels, ε_1 and ε_2, and work functions, ϕ_1 and ϕ_2, of the two materials when not in contact with each other are illustrated in Figure 37a. When the two conductive materials are brought into electrical contact with each other, their respective Fermi levels equalize and a potential gradient, termed the contact potential, is produced from the flow of charge between the electrodes. This subsequently causes the two surfaces to become equally and oppositely charged as indicated in Figure 37b. The material with the smaller work function will charge positively, while the material with the larger work function will become negatively charged. The transfer of electrons stops once the electric field between the two conductors compensates for the difference in the work function. The potential associated with this electric field is exactly equal to the difference in the work functions of the materials. It is possible to bias one electrode with respect to the other electrode through the use of a variable backing potential as indicated in Figure 37c.

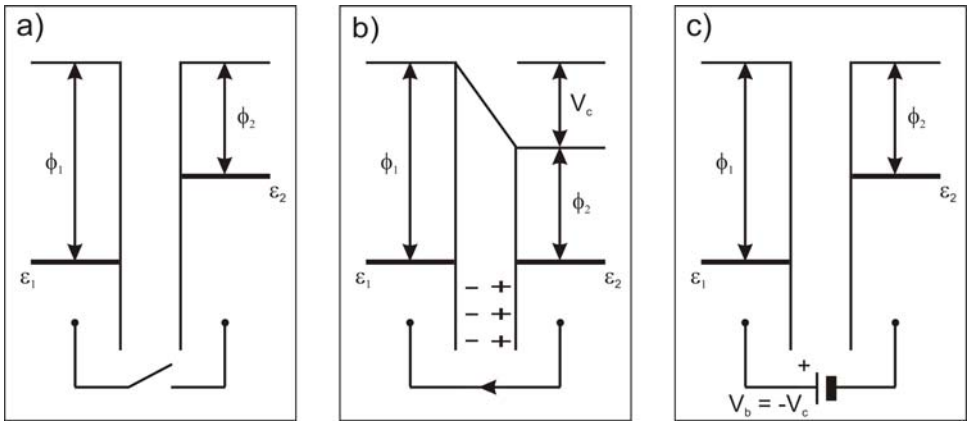

Figure 37: Electron energy diagrams of two different metals a) without contact, b) with external electrical contact, and c) with inclusion of the backing potential, V_b. ϕ_1 and ϕ_2 are the work functions of the materials and ε_1 and ε_2 are the respective Fermi levels. Modified from Ref. [166].

The above method can be used to measure the work function difference of the two materials simply by measuring the resulting flow of charge when the two conductors are placed in electrical contact (Figure 37b). This method, although convenient, only produces a single measurement and therefore the surface charges must be dissipated prior to making an additional measurement. This problem can be overcome through the use of a vibrating reference electrode, which forms a parallel plate capacitor. The varying capacitance produced by the vibrating probe allows for the renewal of charge as given by the following equation:

$$C = \frac{Q}{V} = \frac{\varepsilon_0 A}{d} \tag{2.5}$$

where C is the capacitance, Q is the charge, V is the potential, ε_0 is the permittivity of the dielectric, A is the surface area of the capacitor, and d is the separation distance between the plates. As the separation distance, d, increases between the probe and the sample surface, the capacitance decreases and as the charge remains constant, the voltage must increase accordingly [159].

The varying capacitance with time is given by:

$$i = \frac{dQ}{dt} = \frac{VdC}{dt} \tag{2.6}$$

and thus the derivative of the charge becomes a measurable AC current, defined as i [167]. In the Kelvin method of measuring the work function, the AC voltage produced by the vibrating electrode can be adjusted to zero by a variable DC voltage. When the AC voltage is zero, the surface potential is equal and opposite of the applied DC voltage. A lock-in amplifier is used to monitor the current generated by the oscillation of the reference electrode [158]. The current changes as the distance between the surfaces changes to maintain the electric field between the surfaces.

The Kelvin probe is a technique for measuring work function differences, rather than an absolute technique, and is capable of approximately 1 mV resolution. In order to determine the absolute work function of a sample, the work function of the electrode must therefore be known [159]. The Kelvin probe used in these studies is mounted on a linear transfer mechanism for positioning of the gold reference electrode very close to the crystal surface and is shown in Figure 38. The vibration of the gold electrode is piezoelectrically driven. Certain materials possess the ability to change shape when an electric field is applied to the material. The oscillation of this applied voltage causes the material, a reed which is connected to the gold electrode, to vibrate. The small screw above the gold electrode is used to accurately and reproducibly position the gold electrode relative to the surface of the single crystal surface. This is absolutely critical in order to obtain reproducible work function measurements [158]. This method of using a vibrating capacitor to measure the contact potential difference is advantageous in that the surfaces do not need to touch each other. Only very weak electrical fields are needed and therefore are not likely to influence the electrical or chemical structure of the single crystal or the adsorbates.

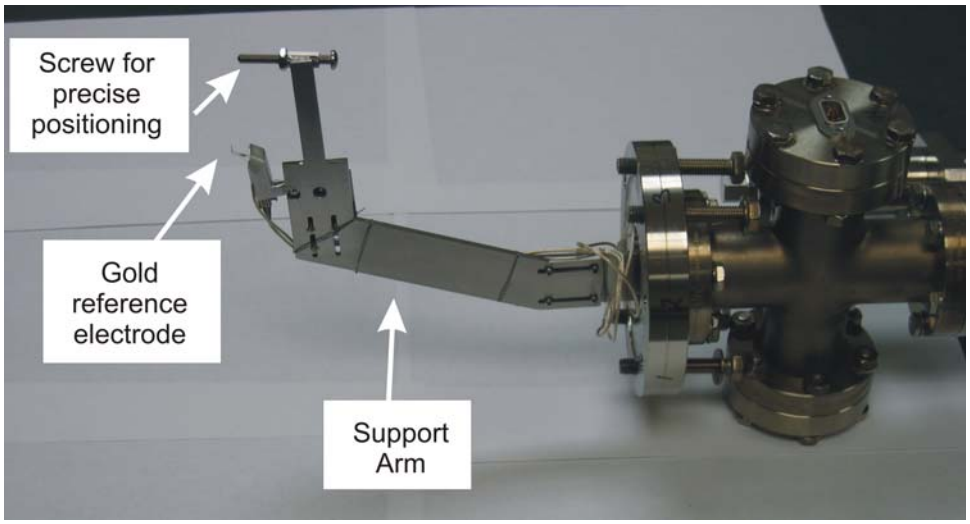

Figure 38: Kelvin probe assembly mounted on a linear transfer mechanism.

2.9 TEMPERATURE PROGRAMMED DESORPTION (TPD) MEASUREMENTS

Thermal Desorption Spectroscopy (TDS), or temperature programmed desorption (TPD) as it is often referred, is one of the earliest and most often used methods of surface science to investigate adsorbates on surfaces.

In a typical TPD measurement, the sample that contains a particular adsorbate is heated at a programmable rate (which is usually linear and constant) while the chamber is being pumped efficiently. Redhead [168] was the first investigator to use a slow linear heating rate to show how a thermal desorption spectrum could be used for the determination of the surface desorption kinetics. A linear heating rate is used so that the plot of the temperature versus time is linear, making it possible to determine the activation energy of desorption. The information that can be obtained from the desorption spectra include (1) the number of the various desorbing phases and the corresponding population of each phase; (2) the activation energies of desorption of the various phases; and (3) the order of the desorption reaction. The desorption of the adsorbed species can be detected in a general sense by the change in the pressure in the chamber as measured by an ion gauge. This method will not provide information as to the composition of the desorbing species and does not discriminate against background gases in the chamber. A better method of detection is to use a quadrupole mass spectrometer (QMS) which is capable of mass selectively measuring the pressure rise.

The Polanyi-Wigner equation describes the rate of a particular chemical process. In this case we are interested in the overall rate of desorption, r_{des}. The most general form (Arrhenius) of the equation shows that the overall rate of desorption r_{des} is directly related to the surface coverage of a particular adsorbate, N, and the temperature of the substrate, T

$$r_{des} = -\left(\frac{dN}{dt}\right) = k_m N^m e^{-Edes/RT} \tag{2.7}$$

where k_m is the preexponential factor of the chemical process of order m and E_{des} is the activation energy of the desorption process. For a first order reaction, where no interactions occur between surface species, the particles desorb independently of each other. In a second order desorption process the particles must combine prior to desorption from the surface.

It is possible to use the overall pressure change, ΔP, during desorption as a means of determining the surface kinetics when the rate at which species desorb from the walls as well as the overall pumping speed of the chamber, S, is constant, as indicated by the following equation:

$$\frac{d\Delta P}{dt} = \frac{kTA_S}{V}\left(-\frac{dN}{dt}\right) - \frac{S\Delta P}{V} \tag{2.8}$$

where V is the volume of the chamber and A_S is the sample surface area [117]. The rate of desorption can then be determined as follows by combining equations 2.7 and 2.8.

$$r_{des} = \left(\frac{V}{kTA_S}\right)\frac{d\Delta P}{dt} + \frac{S\Delta P}{kTA_S} \tag{2.9}$$

In the limit of high pumping speeds as is the case in most UHV experimental situations the first term on the right side of equation 2.9 becomes negligible and therefore

$$r_{des} = \frac{S\Delta P}{kTA_S} \tag{2.10}$$

Equation 2.10 shows that the rate of desorption is directly proportional to the change in pressure when the desorption rate is much lower than the pumping speed of the chamber [117]. The position and shape of the desorption peak contains information about the various kinetic parameters that affect the rate, such as the preexponential factor as well as the desorption energy.

A shielded quadrupole mass spectrometer (QMS) (UTI 100C) with an electron multiplier to amplify the current by a factor of ~ 10^5 was used for acquiring the thermal desorption spectra of adsorbates from the Ru surface unless otherwise mentioned. The conical shaped shield has an aperture of ~ 5 mm, whereas the diameter of the crystal is ~ 10 mm and ~13 mm for the Ru(109) and Ru(001) single crystals, respectively, thus insuring that desorption from the front surface of the crystal is mainly being sampled and not desorption from the W-leads or the back side of the sample. The crystal was positioned approximately 4 mm from the aperture of the shield during TPD with the face of the crystal perpendicular to the axis of the QMS. All TPD spectra were recorded using a heating rate of 2.0 ± 0.1 K/s. During the measurements the crystal was biased at -100 V so as to prevent thermionically generated electrons from the emitter of the QMS from reaching the crystal and possibly causing an electron stimulated process [44]. In all TPD spectra of CO, only the signal from 28 amu (or 31 amu in the case of isotopic $^{13}C^{18}O$) was recorded, but it was possible to monitor up to 5 masses simultaneously by means of multiplexing. In all TPD spectra of $^{14}N_2$, the signals from 14 amu and 28 amu masses were recorded by means of QMS multiplexing. A small background pressure of $^{12}C^{16}O$ was present in the chamber which overlapped with the 28 amu signal from nitrogen and therefore the signal from 14 amu is used in all of the TPD traces. The different cracking patterns for $^{12}C^{16}O$ and $^{14}N_2$ (CO: mass 28/mass 14 = 100/0.8; N_2: Mass 28/Mass 14 = 100/14) enable one to quantitatively distinguish between CO and N_2 desorption [169]. CO contamination during N_2 adsorption was maintained to < 1% of a ML.

2.10 TUNGSTEN COIL FOR HYDROGEN CRACKING

A tungsten coil mounted in the UHV chamber was used to dissociate molecular hydrogen to create the energetic atomic hydrogen species. The ¾" outer diameter coil (0.010" wire, CM Furnaces) was spot-welded by its legs to two 0.015" tungsten loops as indicated in Figure 39. Small pieces of Ta-foil were sandwiched between the W-wires for a stronger tungsten-to-tungsten weld, since it very difficult to weld tungsten to itself. The overall mechanical stability of the weld is also enhanced by welding additional pieces on the outside of the W-W weld. The W-loops were connected to a feedthrough flange via copper connectors and Ni extension rods. The entire assembly was mounted on a linear transfer mechanism consisting of a welded bellows allowing roughly 2" of linear motion for accurate positioning of the coil close to the front face of the Ru sample. The tungsten loops can be outgassed separately thus minimizing outgassing during the coil operation [154] and thereby reducing the overall contamination on the surface.

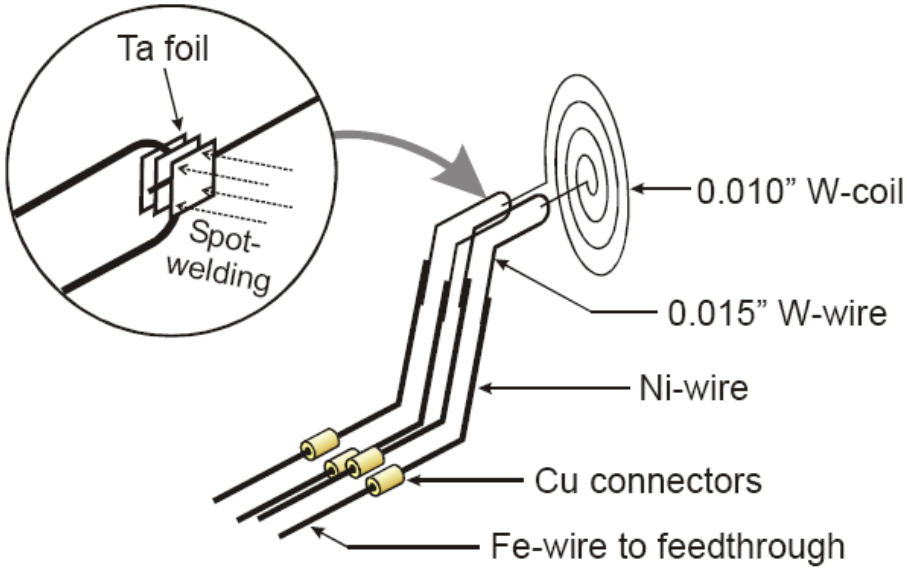

Figure 39: Mounting of the W-coil for creation of atomic hydrogen.

3.0 THE FORMATION AND STABILITY OF ADSORBED FORMYL AS A POSSIBLE INTERMEDIATE IN FISCHER TROPSCH CHEMISTRY ON RUTHENIUM

The information contained in this chapter is based on the following research publication:

Gregg A. Morgan, Jr., Dan C. Sorescu, Tykhon S. Zubkov, and John T. Yates, Jr., *"The Formation and Stability of Adsorbed Formyl as a Possible Intermediate in Fischer-Tropsch Chemistry on Ruthenium"* J. Phys. Chem. B. **108** (2004) 3614-3624.

3.1 ABSTRACT

Density functional theory has been used to study the formation and stabilization of the chemisorbed formyl species, HCO, on the Ru(001) surface. It has been found that the η^1-HCO species, attached to a Ru atom by a single Ru-C bond is unstable, and that it will convert to more strongly bound η^2- and η^3-HCO surface species. These more highly-coordinated species decompose readily to produce H(a) and CO(a) via low activation energy reactions, indicating that the observation of HCO(a) species in any bonding mode at temperatures above 90 K is unlikely. Additionally, we found that abstraction of H from HCO(a) upon atomic H bombardment is another low-barrier reaction mechanism leading to the formation of adsorbed CO and desorption of an H_2 molecule. Using a stepped Ru(109) surface, containing atomic steps

periodically located every 22 Å along the Ru(001) surface, we have bombarded chemisorbed CO with atomic H at T< 170 K in an attempt to produce and spectroscopically observe adsorbed HCO species by infrared reflection absorption spectroscopy. These experiments have been unsuccessful, and instead we have observed the surface crowding of CO(a) by H(a) species, and the displacement of CO(a) at high H(a) coverages. Both the experimental and theoretical results support the conclusion that the formyl species can be easily dissociated on the Ru surface. These studies throw into question previous measurements indicating that the interaction of atomic hydrogen with CO is effective in producing stable adsorbed formyl species on Ru.

3.2 INTRODUCTION

The hydrogenation of CO adsorbed on metal surfaces has been widely investigated due to its importance to the Fischer-Tropsch synthesis. Previous studies on the hydrogenation of CO utilized molecular hydrogen and were performed at pressures up to one atmosphere on both a clean Ru(001) substrate [170,171] as well as on a potassium promoted Ru(001) surface [127,172,173]. Reaction products, as identified by vibrational spectroscopy, on the unpromoted surface include CH_x and C-C species, whereas the K-promoted surface exhibited vibrational modes attributed to formyl as well as formate species.

Much work has been done on the coadsorption of CO and hydrogen in ultrahigh vacuum conditions on metal surfaces such as Pt [174-176], Pd [177], Ni [175,178,179], Ru [93,180-184], and Rh [185]. In all of these studies, it has been found that chemisorbed hydrogen, filling in the surface after CO adsorption, pushes the CO into immiscible islands in which the local coverage is elevated as a result of compression by the chemisorbed hydrogen. The first work, done on

Rh(111) [185], showed that a p(2 x 2) CO structure was reversibly compressed into a √3 x √3 R 30º structure due to repulsive H…CO forces. Similar immiscibility between H(a) and CO(a) occurs on the Ru(001) surface [182-184]. No reaction is observed between H(a) and CO(a) under these conditions [186].

Mitchell and Weinberg [187-189] reported that atomic H could drive chemisorbed CO to produce HCO(a) species at low temperatures on Ru(001). Their observations were made using high resolution electron energy loss spectroscopy (HREELS). Both formyl and formaldehyde surface species were reported to be formed. This reactivity observed was attributed to the high chemical potential of atomic H compared to 1/2 H_2(g).

We performed density functional calculations to examine the stability of the HCO(a) species in different bonding configurations, finding that decomposition to H(a) and CO(a) is likely to occur rapidly at the temperature of the experiments. Additionally, we found that abstraction of H from HCO(a) upon interaction with gas phase atomic H, resulting in the formation of CO(a) and the desorption of H_2(g), is another possible HCO(a) decomposition mechanism. We have also restudied the interaction of atomic H with CO(a) on the Ru(109) surface (which combines 22 Å wide Ru(001) terraces with stepped sites), finding that atomic H does not produce observable C-O or C-H infrared modes characteristic of chemisorbed HCO or H_2CO.

3.3 THEORETICAL METHODS

The calculations performed in this study were done using the ab initio total-energy VASP code [190-192]. This program evaluates the total energy of periodically repeating geometries based

on density-functional theory and the pseudo potential approximation. In this case only the valence electrons are represented explicitly in the calculations; the electron-ion interaction is described by fully non-local optimized ultrasoft pseudo potentials similar to those introduced by Vanderbilt [193] and provided by Kresse and Hafner [194]. Periodic boundary conditions are used with the occupied electronic orbitals expanded in a plane-wave basis. The expansion includes all plane waves whose kinetic energy $\hbar^2 k^2 / 2m < E_{cut}$ where k is the wave vector, m the electronic mass, and E_{cut} is the chosen cutoff energy. A cutoff energy of 396 eV has been employed in these studies. Electron smearing is employed via the Methfessel-Paxton technique [195] with a smearing width σ=0.2 eV in order to minimize the errors in the Hellmann-Feynman forces due to the entropic contribution to the electronic free energy. All energies are extrapolated to σ=0.

Calculations were performed using spin-polarized generalized gradient approximation (GGA) density functional theory using the PW91 exchange-correlation functional [196]. The minimization of the electronic free energy was performed using an efficient iterative matrix-diagonalization routine based on a sequential band-by-band residuum minimization method (RMM) [190,191] or alternatively, based on preconditioned band-by-band conjugate-gradient (CG) minimization [197]. The optimization of different atomic configurations was performed based on a conjugate-gradient minimization of the total energy.

The surface model used in this study consists of a supercell with 3x3 surface units containing a four-layer slab. A vacuum width of about 10 Å has been chosen to separate neighbor slabs. The total number of Ru atoms in this model is 36. In calculations of molecular adsorption on the surface we have relaxed all atomic positions of the molecule as well as the Ru atoms positioned in the first layer of the slab. The k-points sampling was generated based on

the Monkhorst-Pack scheme [198] with a 3x3x1 mesh. Minimum energy paths between different minima were optimized by use of the nudged elastic band (NEB) method of Jónsson and co-workers [199,200]. In this approach, the reaction path is "discretized", with the discrete configurations, or images, between minima being connected by elastic springs to prevent the images from sliding to the minima in the optimization. Further checks of the convergence of the NEB calculations have been done by additional calculations in which the images corresponding to the transition state have been optimized using a quasi-Newton algorithm.

3.4 THEORETICAL RESULTS

3.4.1 Methods Testing for Bulk Ru and Isolated HCO Molecule

Preliminary calculations to benchmark the accuracy of our DFT calculations have indicated that very good agreement is obtained for the prediction of bulk equilibrium crystallographic parameters. For example, from minimizations of the total energy of Ru(001) with respect to the volume of the unit cell within the experimental determined $P6_3/mmc$ hexagonal space group symmetry, we have obtained the equilibrium lattice constants of a=2.729 Å and c=4.318 Å (c/a=1.5822). These values are within 0.8% from the corresponding experimental numbers of a_{exp}= 2.7058 Å and c_{exp}=4.2816 Å (c_{exp}/a_{exp}=1.5824) [201].

An equally good representation has been observed for the geometric parameters of the isolated formyl radical. Based on optimizations of the isolated formyl radical in a cubic box of 12x12x12 $Å^3$ we have determined the following equilibrium bond lengths, r(C-O)=1.189 Å, r(C-H)=1.128 Å and the bond angle θ(H-C-O)=124.5°. These values are in close agreement (within

1.1%) with the experimental values r_{exp}(C-O)=1.175 Å, r_{exp} (C-H)=1.119 Å, and θ_{exp} (H-C-O)=124.4° reported by Hirota [202]. Consequently, the good agreement of our results for both bulk Ru and for isolated formyl molecular species made us confident to proceed to the next step; *i.e*. the investigation of molecular adsorption of HCO on the Ru(001) surface.

3.4.2 HCO adsorption on Ru(001)

The adsorption of the formyl radical on the Ru(001) surface has been examined for several different bonding configurations of this radical relative to the surface. For each configuration studied, the adsorption energy was determined according to the expression

$$E_{ads}=E_{molec} + E_{slab} - E_{(molec+slab)}, \quad (3.1)$$

where E_{molec} is the energy of the adsorbate species, E_{slab} is the total energy of the slab in the absence of the adsorbate, $E_{(molec+slab)}$ is the total energy of the adsorbate/slab system. A positive E_{ads} corresponds to a stable adsorbate/slab system. The energy of the isolated adsorbate has been determined from calculations in a large simulation box of dimensions 12.0×12.0×12.0 $Å^3$ and includes spin polarization corrections. The same Brillouin-zone sampling has been used to calculate the energies of the bare slab and of the adsorbate-slab systems.

Mitchell et al. [187-189] have suggested that exposing gas-phase atomic hydrogen to a saturated CO overlayer at 100 K on the Ru(001) surface will lead to formation of η^1 and η^2-formyl species similar to those depicted in Figure 40a and Figure 40b.

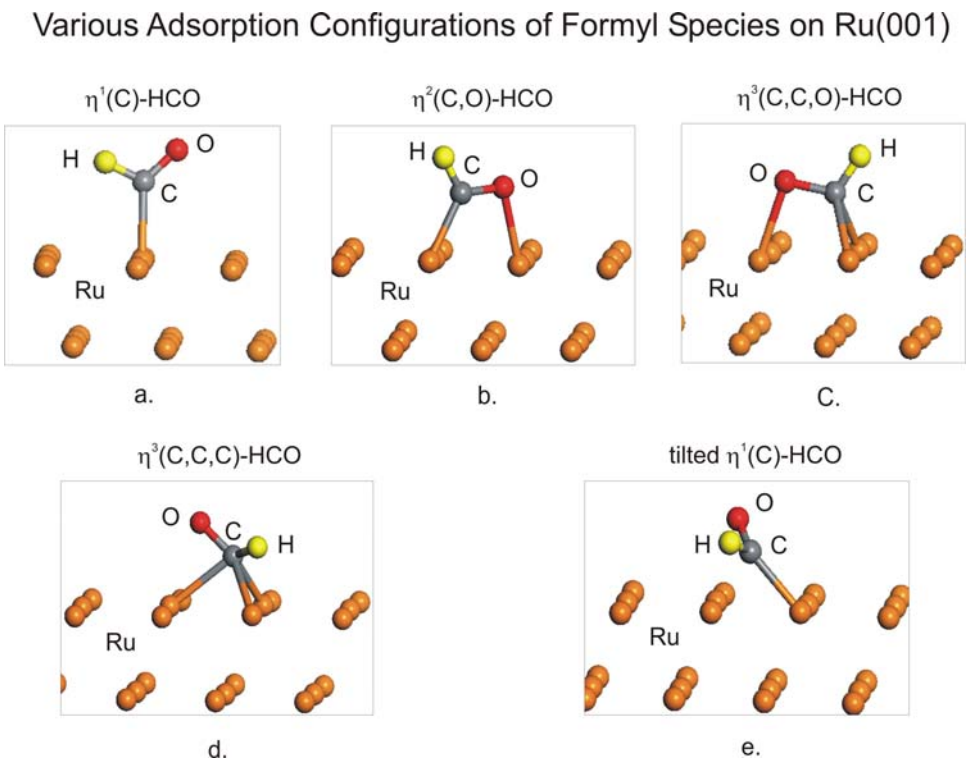

Figure 40: Pictorial view of the different adsorption configurations of the formyl radical on the Ru(001) surface considered in this study: (a) η^1(C)-HCO; (b) η^2(C,O)-HCO; (c) η^3(C,C,O)-HCO; d) tilted η^3(C,C,C)-HCO; e) tilted η^1(C)-HCO. Only the η^2(C)-HCO and η^3(C,O)-HCO have been identified as having a stable local minima. The other configurations correspond to saddle points on the potential surface.

Upon annealing to 180 K, part of the η^1-formyl was reported to decompose to adsorbed CO and hydrogen, while the rest of η^1-formyl is converted to η^2-formyl. Following the previous experimental findings [187-189], we considered first in our investigations the chemisorption properties of the formyl species in the vertical η^1 configuration (see Figure 40a). In this case the calculations have been done for the case of a single formyl molecule in the 3x3 surface supercell, corresponding to a coverage θ=1/9. Based on full optimizations of the formyl radical we have found that the η^1 adsorption configuration is not stable. Actually, during the optimization this configuration evolves toward the η^2 adsorption configuration depicted in Figure 40b. Despite starting the optimization procedure from several initial η^1-type configurations of formyl with

different orientations and at different distances from the surface, we found that upon optimization all these lead to the η^2- or η^3- type (see below) adsorption configurations.

For the η^2 stable adsorption configuration the C-O bond of formyl is almost parallel to the surface. Representative geometric and energetic parameters of this adsorption configuration denoted η^2(C,O)-HCO are given in Table 1. The "C,O" symbol used in the notation η^2(C,O)-HCO denotes the approximate bonding of the C and O atoms to the surface. We find that in this case the molecule binds to the surface through both C and O atoms at about 1.99-2.14 Å from the Ru atoms. In this configuration the C-O bond is stretched by 0.086 Å relative to the gas phase equilibrium distance in HCO. An overall binding energy of 59.6 kcal/mol has been determined for this adsorption configuration.

Table 1: The calculated geometric parameters, adsorption energies, and vibrational frequencies for formyl species adsorbed on the Ru(001) surface[a]

Configuration	r(Ru-O)	r(Ru-C)	r(C-O)	r(C-H)	φ^{b}	E_{ads}
HCO (gas phase, exp.)[c]			1.175	1.119	124.4	
HCO (gas phase, theo.)			1.188	1.129	124.5	
η^2(C,O)-HCO (theo.)	2.146	1.987	1.274	1.108	115.6	59.6
η^3(C,C,O)-HCO (theo.)	2.061	2.125	1.320	1.105	114.4	60.5
tilted η^3(C,C,C)-HCO (theo.)	…	2.055 2.186 2.142	1.264	1.317	112.5	
tilted η^1(C)-HCO (theo.)		2.045	1.262	1.254	112.3	

Configuration	ν_1 (C-H str)	ν_2 (C-O str)	ν_3(HCO-bend)
HCO (matrix isolated, exp)[d]	2488	1860	1090
HCO (gas phase, exp.)[e]	2434	1868	1081
HCO (gas phase, theo.)	2625[f]	1861	1077
η^2(C,O)-HCO (theo.)	2911	1352	1210
η^3(C,C,O)-HCO (theo.)	2929	1142	1169
η^2(C,O)-HCO (exp)[g]	2900	1180	1400
η^2(C,O)-HCO (exp)[h]	2970	1190	1190

a. **All distances are in Å, adsorption energies are in kcal/mol, and frequencies are in cm^{-1}**
b. **Angle between H-C-O, in degrees**
c. **Data from Ref. [202]**
d. **Data from Ref. [203]**
e. **Data from Ref. [204] and references therein**
f. **The calculated normal mode frequency using VASP code in the harmonic approximation gives a value of 2625 cm^{-1}. However previous experimental [202,205] and theoretical [206] studies have indicated the existence of strong anharmonic effects and intermode coupling for the C-H stretching mode. When such effects are considered [206], the calculated vibrational frequency decreases from 2815 cm^{-1} to 2448 cm^{-1} in agreement with the experimental value of 2434-2488 cm^{-1} [203,204]**
g. **Data from Ref. [207], referring to HCO(a) on Ru(001)**
h. **Data from Ref. [188], referring to HCO(a) on Ru(001)**

Another stable adsorption configuration of formyl we have determined is the η^3(C,C,O)-HCO horizontal configuration depicted in Figure 40c. In this case the C atom binds in a bridge-type configuration to two-neighboring Ru atoms while the O atom is bonded to a single Ru atom. The binding energy of this configuration is slightly larger than that of the η^2(C,O)-HCO with a value of 60.5 kcal/mol. In this configuration the CO bond is even more stretched by 0.132 Å relative to the isolated gas phase equilibrium distance of HCO.

Finally, we present in panels d) and e) of Figure 40 two other configurations, the tilted η^3(C,C,C)-HCO and the tilted η^1(C)-HCO that were obtained by simple energy optimizations. Geometric parameters of these configurations are detailed in Table 1. However, further analyses of the potential energy surface (see the next paragraphs) have indicated that these configurations do not correspond to real equilibrium states but to saddle points.

Concluding this section, we note that in the limit of low coverages where these calculations have been done we have identified two major adsorption configurations of the formyl radical denoted as η^2(C,O)-HCO and η^3(C,C,O)-HCO. The binding energies of these configurations are similar, in the range 59.6-60.5 kcal/mol.

3.4.3 HCO Formation on Ru(001)

Besides individual adsorption configurations of HCO on Ru(001) surface, a first problem we investigated was the minimum reaction path for the formation of adsorbed HCO upon interaction of gas phase atomic H with an adsorbed CO molecule. These calculations have been done using the nudged elastic band method with 8 images distributed along the reaction path and are presented in Figure 41. The initial configuration corresponds to H atom positioned at about 4.2

Å from the C atom of the CO molecule, while the final state represents HCO in a η^2(C,O) adsorption configuration. From these calculations it follows that the activation energy of this process is about 9 kcal/mol, indicating that HCO(a) can be readily be formed as a result of H bombardment of a CO molecule. However, we note that we have not attempted to map the angular distribution of the activation energy upon various incidence directions of the incoming atomic H. It is expected that higher activation energies might be required for more unfavorable attack directions of atomic H.

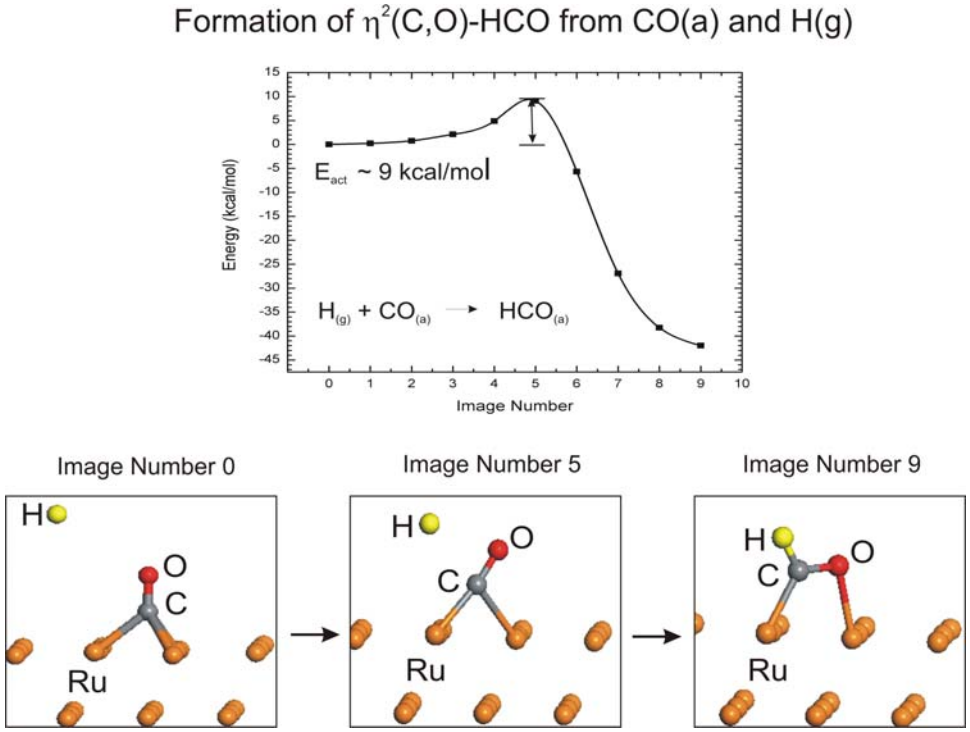

Figure 41: Potential energy surface for interaction of atomic H with adsorbed CO leading to formation of η^2(C,O)-HCO on Ru(001) surface.

3.4.4 HCO dissociation on Ru(001)

A second problem we have analyzed theoretically is related to the energetic requirements for dissociation of the formyl species on the Ru(001) surface. We have analyzed the dissociation process for both η^2(C,O)-HCO and η^3(C,C,O)-HCO adsorption configurations. These calculations have been done using the nudged elastic band method with 8 images distributed along the reaction path. The corresponding minimum energy reaction pathways for dissociation of η^2 and η^3 formyl species are presented in Figure 42 and Figure 43, respectively. We note that in both cases the activation energy for dissociation is relatively small with values of 7.4 kcal/mol for dissociation of η^2(C,O)-HCO and 4.1 kcal/mol for dissociation of η^3(C,C,O)-HCO. These results indicate that even if formyl species can be formed on the Ru(001) surface, these species will dissociate readily to CO and H. As a result, unless done at very low temperatures, measurements of vibrational bands should probe the stretching mode of CO adsorbed on the surface and not the CO stretching mode in formyl radical.

Overall, the theoretical results presented in this section indicate that dissociation of formyl on the Ru(001) surface leading to adsorbed CO and H takes place with relative small activation energies between 4.1-7.4 kcal/mol depending on the starting adsorption configuration.

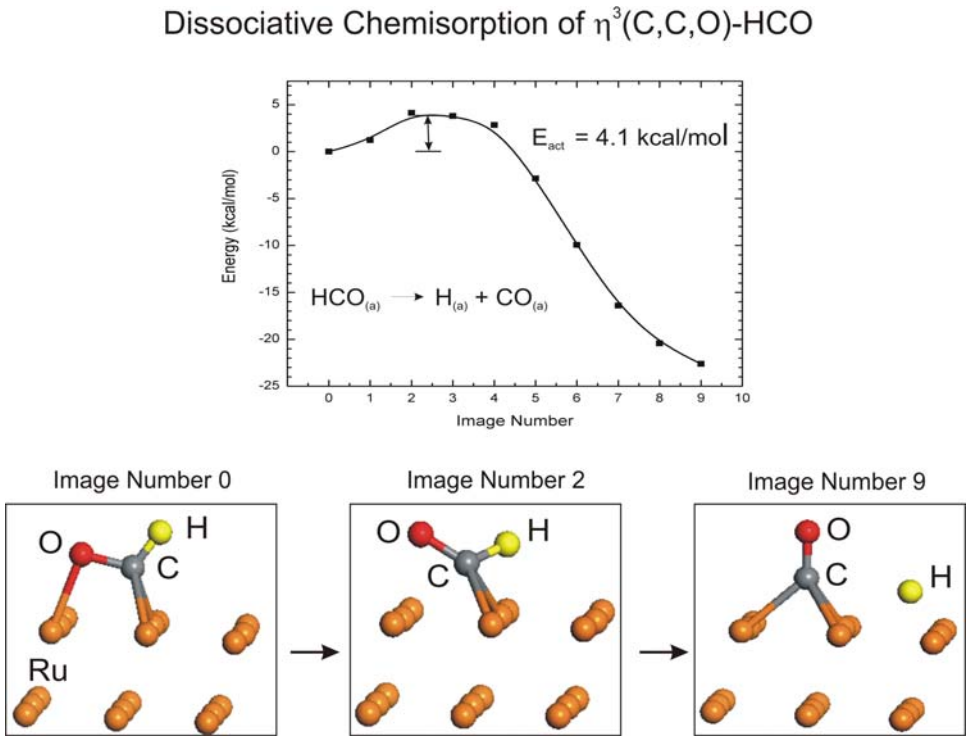

Figure 42: Potential energy surface for dissociation of formyl to CO and H starting from the η^2(C,O)-HCO adsorption configuration.

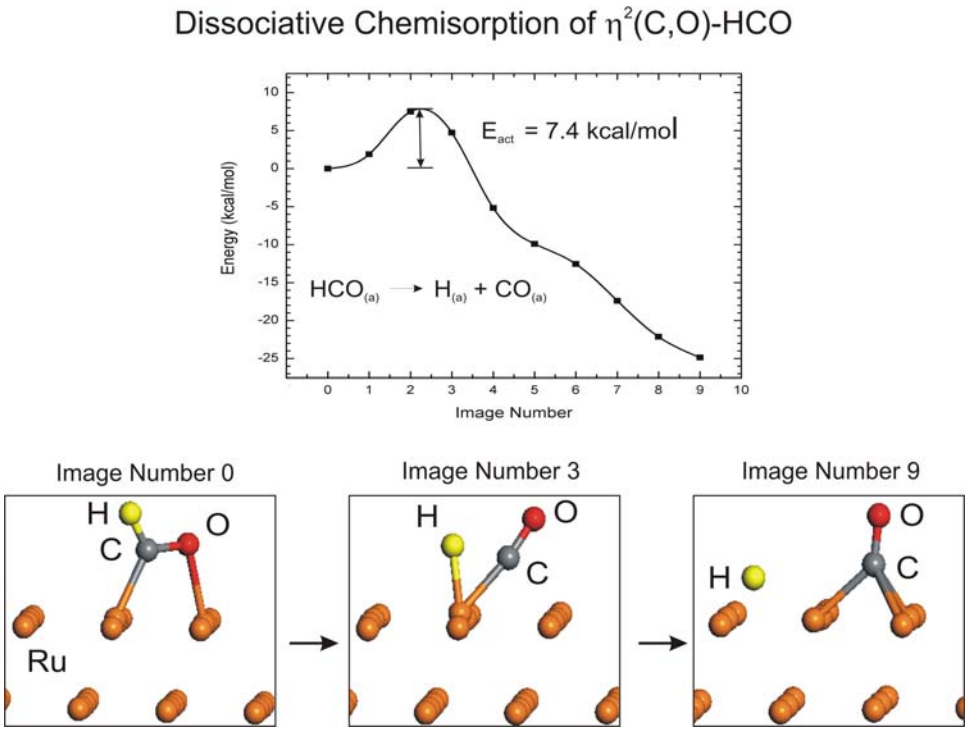

Figure 43: Potential energy surface for dissociation of formyl to CO and H starting from the η^3(C,C,O)-HCO adsorption configuration.

3.4.5 Stability Investigations of the Tilted HCO Adsorption Configurations

We have further analyzed theoretically the potential energy surface for dissociation of formyl starting from the other configurations; i.e. tilted η^3(C,C,C)-HCO and tilted η^1(C)-HCO, identified in the optimization procedure and depicted in Figure 40d and Figure 40e. Our calculations show that in both of these cases formyl dissociates to CO and H without an activation barrier. We present in Figure 44 only the corresponding potential energy path for dissociation of the tilted η^3(C,C,C)-HCO. As can be seen from this figure, the tilted η^3(C,C,C)-HCO configuration corresponds to a saddle point on the potential energy surface and does not represent a stable minimum.

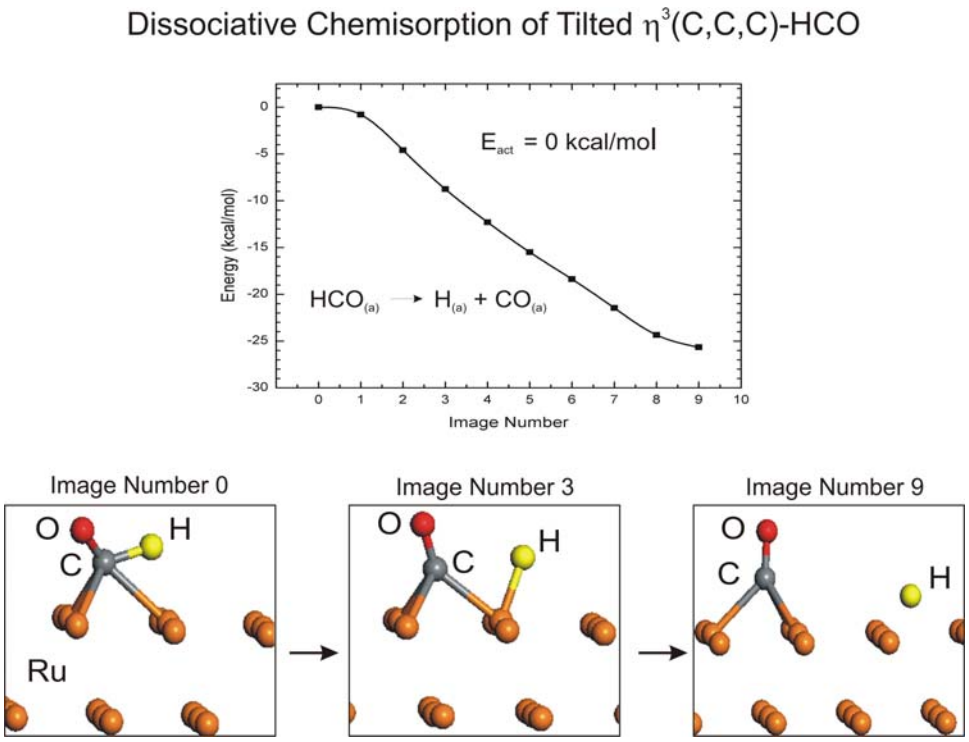

Figure 44: Potential energy surface for dissociation of formyl to CO and H starting from the tilted η^3(C,C,C)-HCO configuration.

3.4.6 Hydrogen abstraction from adsorbed HCO

A final process we have analyzed theoretically corresponds to the interaction of gas phase atomic H with HCO adsorbed in a η^2(C,O) configuration. Such a process is depicted in Figure 45. Initially, atomic H approaches the HCO molecule in a direction perpendicular to the surface, above the H atom of the HCO molecule. As a result of the interaction, the H atom of the HCO is abstracted leading to formation of H_2(g) and the adsorbed CO molecule. As illustrated in Figure 45 the activation energy for the abstraction process is quite small indicating that such a reaction mechanism is likely even at low temperatures. This result further suggests that in practical experiments performed at ordinary temperatures upon bombardment with atomic H, the

concentration of HCO species on the surface will be low due to high reactivity with atomic H forming CO(a) and H_2(g). As in the case of the H(g) reaction with CO(a) we have not attempted to determine the angular dependence of the potential energy surface for different incident directions of atomic H upon adsorbed HCO. It is expected that the corresponding activation energies, even if they would have slightly larger values than those determined in the present case, will still indicate that abstraction of H from HCO is a readily possible mechanism.

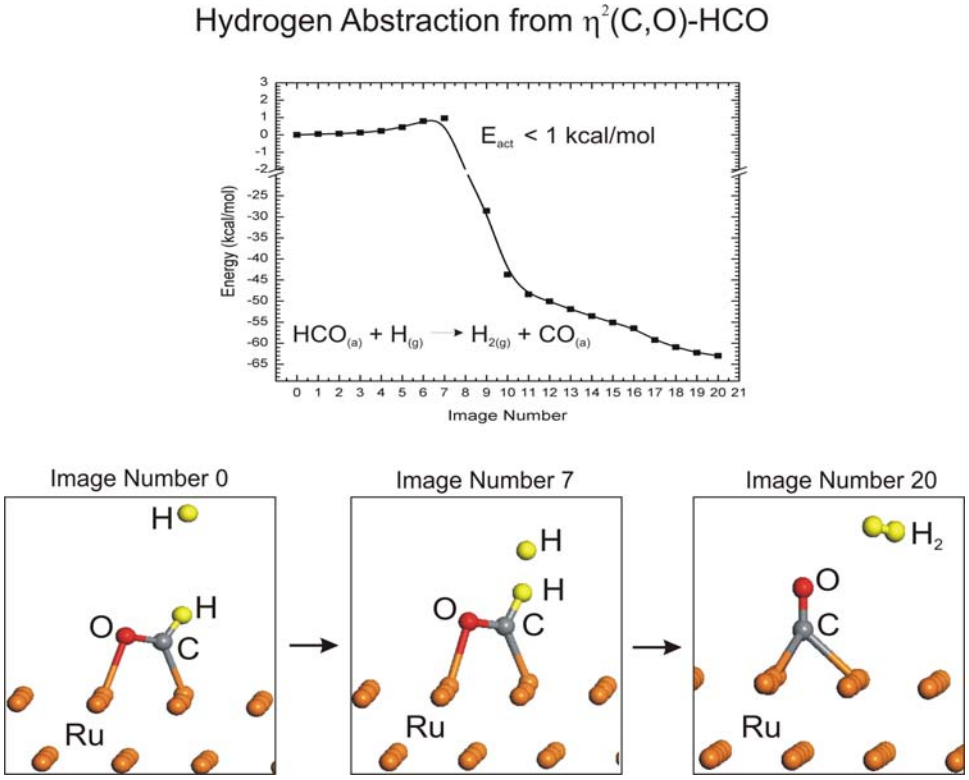

Figure 45: Potential energy surface for H abstraction from η^2(C,O)-HCO with the formation of adsorbed CO and desorption of an H_2 molecule.

3.4.7 Estimates of the lifetime of adsorbed HCO versus temperature

If we assume a range of reasonable preexponential factors for adsorbed HCO decomposition, and use the activation energies calculated here, an estimate of the lifetime of the surface species can be made. We employ 170 K as the temperature, which is the highest temperature reached in our

experiments to be described later. Thus, for the most stable η^2(C,O)-HCO species, with an activation energy of dissociation of 7.4 kcal/mol, the half life at 170 K ranges from 0.2 s to 2 x 10^{-5} s for preexponential factors from 10^{10} to 10^{14} s^{-1}. The next most stable η^3(C,C,O)HCO species, with an activation energy of dissociation of 4.1 kcal/mol, has a half life at 170 K of only 10^{-5} to 10^{-9} s for the same range of preexponential factors. The η^1- HCO species is unstable, converting to η^2-HCO without appreciable activation energy. These estimates suggest that adsorbed HCO species in any bonding configuration would not be spectroscopically detectable at 170 K.

3.4.8 Calculated Vibrational Frequencies for Adsorbed HCO

The vibrational frequencies for the C-H stretching mode and for the C-O stretching mode of adsorbed HCO have been calculated. For the equilibrium adsorption configurations, η^2(C,O)-HCO and η^3(C,C,O)-HCO, we have determined the corresponding vibrational frequencies (within the harmonic approximation) using a direct finite difference algorithm. The corresponding results are given in Table 1. As can be seen from this data upon adsorption on the surface the CH stretch significantly increases from the gas phase value (2434 cm^{-1}) to about 2911 cm^{-1} for η^2(C,O)-HCO and 2929 cm^{-1} for η^3(C,C,O)-HCO. In contradistinction, the CO stretch decreases from the gas phase value (1868 cm^{-1}) to 1352 cm^{-1} for η^2(C,O)-HCO and to 1142 cm^{-1} for η^3(C,C,O)-HCO, suggesting a significant weakening of the C-O bond. These values are significantly smaller than the frequency of individual CO molecules adsorbed on the Ru(001) surface. For completeness we have also calculated the vibrational frequencies of CO when adsorbed at different surface sites, namely the on-top and hcp sites. Our results indicate that

upon adsorption, CO vibrational frequency shifts from the calculated gas phase value of 2096 cm^{-1} to 1950 cm^{-1} when adsorption takes place on-top or to 1700 cm^{-1} for an hcp adsorption site. As these values are well separated from those of CO in formyl they should provide a practical procedure to separate C-O modes from HCO(a) and from chemisorbed CO.

3.5 EXPERIMENTAL METHODS

The experimental conditions as well as the surface science techniques used in these experiments were reported in detail in Chapter 2. The infrared radiation was p-polarized with respect to the surface of the crystal and spectra were collected using 4 cm^{-1} resolution averaged over 2000 scans.

Following any exposure to CO, the crystal was heated to 250 K and cooled immediately to 88 K. This procedure was designed to equilibrate and order the CO adlayer without depletion as no CO desorbs from the surface at this temperature [41]. Atomic hydrogen was generated by dissociating $^1H_2$ (Valley National Gases, 99.9995% purity) with a hot tungsten coil (approximately 1800 K as measured by an optical pyrometer). The measured brightness temperature of the tungsten coil was corrected for the emissivity of tungsten as well as for absorption by the window. The hydrogen was admitted into the chamber by means of the variable flow leak valve in order to back fill the chamber. An ion gauge was used to measure the pressure in the chamber and the readings were corrected for gauge sensitivity, using a relative sensitivity factor of 0.6 for hydrogen. The crystal was positioned about one centimeter in front of the W-coil with the (109) face directed towards the W-coil. During the atomization of the hydrogen, the temperature of the crystal rose from 88 K to approximately 150 K, for a 50 second

exposure. For a 100 second exposure the temperature rose to approximately 170 K. Following each exposure to atomic hydrogen, the sample was linearly heated to 150 K to desorb any water, which may have been generated by H atoms striking the chamber walls [189]. All hydrogen exposures are reported in Langmuirs (1 L = 1×10^{-6} Torr·s), and represent the molecular hydrogen exposure. The efficiency of the atomization of the molecular hydrogen, and therefore the actual atomic hydrogen exposure, is not known. The crystal was biased at –100 V during the hydrogen exposure so as to avoid thermionically-generated electrons from the W-coil from reaching the crystal.

3.6 EXPERIMENTAL RESULTS

$^{12}C^{16}O$ was initially adsorbed on the surface up to a saturation coverage which corresponds to 7.47 x 10^{14} cm^{-2}, (θ_{CO} = 0.54 relative to the available ruthenium surface atoms). An infrared spectrum of the saturated adlayer was recorded and is plotted in Figure 46a. A single infrared band at 2064 cm^{-1} is the only observable feature. This frequency corresponds to the C-O stretching frequency of an on-top CO species and is consistent with our previous results [41]. The saturated surface was then exposed to 1250 L of H/H_2. The resulting infrared spectrum is plotted in Figure 46b. A single infrared band at 2052 cm^{-1} was the only observable feature. The peak intensity of this feature was approximately ¼ of the peak intensity of the infrared band of the saturated surface. The integrated band absorbance corresponding to the pure CO layer is approximately 5 times larger than the band corresponding to the CO layer treated with atomic H. In addition to a decrease in the intensity and hence the area of the absorbance peak there is also a significant broadening of the infrared band. The infrared band of the pure CO on the surface has

an initial full width at half maximum (FWHM) of approximately 9 cm^{-1}, whereas the infrared band after the H/H_2 exposure has a FWHM of about 22 cm^{-1}. This increase in the CO linewidth may be attributed to the increased inhomogeneity of the CO adlayer as the CO adlayer is initially ordered in Figure 46a. The broad scan spectrum in Figure 46b shows that no other infrared features in the range of 3500 cm^{-1} to 800 cm^{-1}, expected for a chemical reaction between atomic H and chemisorbed CO, are observed after extensive atomic H exposure. The sensitivity of the measurements is < 0.0006 A units.

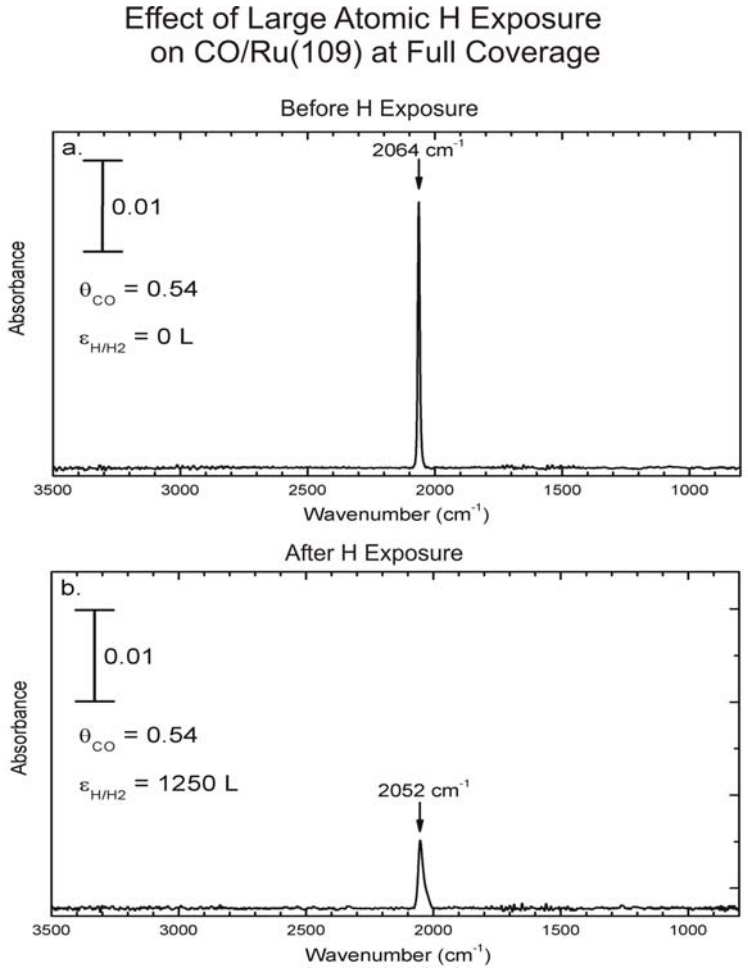

Figure 46: Infrared spectra of chemisorbed CO on Ru(109), $\theta_{CO} = 0.54$. (a) Prior to atomic hydrogen exposure; and (b) after 1250 L of atomic hydrogen exposure.

In a separate experiment $^{12}C^{16}O$ was adsorbed on the surface to a coverage of 5.51 x 10^{14} cm^{-2} (θ_{CO} = 0.40 relative to the available ruthenium surface atoms), approximately 74% of the saturation coverage. The behavior of the CO adlayer following various H/H_2 exposures was followed by infrared spectroscopy. The initial infrared spectrum of the pure CO adlayer produced a single band at 2038 cm^{-1}. The CO adlayer was then exposed to increasing exposures of atomic hydrogen from 6 L to 1250 L H/H_2, with a spectrum being recorded after each exposure. After an initial exposure of 6 L of H/H_2 the infrared frequency shifted rapidly upward to 2055 cm^{-1}. The CO band continues to increase in frequency as the cumulative hydrogen exposure increases, reaching a maximum frequency of 2061.5 cm^{-1} after an exposure of 19 L of H/H_2. As the cumulative H/H_2 exposure continues to increase, the infrared band then shifts downward in frequency and gradually loses intensity. After an exposure of 1250 L of H/H_2 the frequency of the band is 2045 cm^{-1} as can be seen in Figure 47. Again no other development of absorbances over the frequency range 3500 cm^{-1} to 800 cm^{-1} is observed. A control experiment was performed in order to verify that the atomic hydrogen (and not spurious effects from the walls of the chamber) was in fact responsible for the observed effect on the CO adlayer. In this control experiment $^{12}C^{16}O$ was adsorbed on the surface at the same coverage as in the previous experiment (θ_{CO} = 0.40 relative to the available ruthenium surface atoms), but the back side of the crystal (instead of the front side (109 face) as previously) was directed towards the W-coil during the generation of atomic hydrogen. In this experiment the single infrared band shifted from an initial frequency of 2038 cm^{-1} upwards to 2054 cm^{-1} (data not shown) while gradually losing intensity and becoming broader as the exposure of H/H_2 increases to its maximum value of 1250 L.

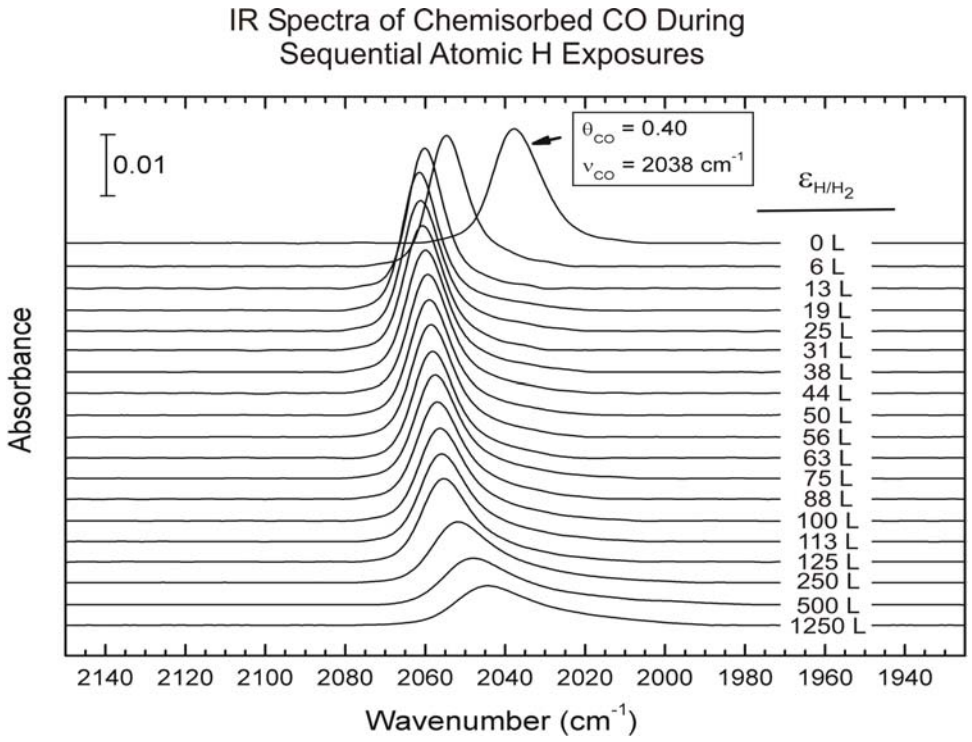

Figure 47: Infrared spectra of chemisorbed CO on Ru(109) at an initial coverage of θ_{CO} = 0.40, after sequential atomic hydrogen exposures. The hydrogen gas was admitted to the chamber through a variable flow leak valve and was atomized by means of a tungsten coil at approximately 1800 K. The temperature of the crystal rose to about 150 K during the exposures. The crystal was biased -100 V during the exposures.

The changes in the CO-frequency are plotted against the hydrogen exposure in Figure 48. In a control experiment, the same coverage of CO was adsorbed onto the surface of the Ru(109) crystal, but instead of being exposed to atomic hydrogen, the adlayer was only exposed to molecular hydrogen and the results are plotted in Figure 48. There is a very gradual increase in the CO frequency, from 2035 cm^{-1}, as the exposure of molecular hydrogen is increased. The slight difference in the initial frequencies can be attributed to a slight difference in the initial coverage of CO adsorbed on the surface. After an H_2 exposure of 1250 L, the CO frequency shifted upwards, by 11 cm^{-1}, to 2046 cm^{-1}. This comparison between H/H_2 and H_2 exposures shows that most of the effect with the H/H_2 mixture is due to the presence of atomic H in the

incident gas mixture. It is likely that supplying hydrogen atoms at high chemical potential (compared to H_2) causes rapid H coadsorption with CO.

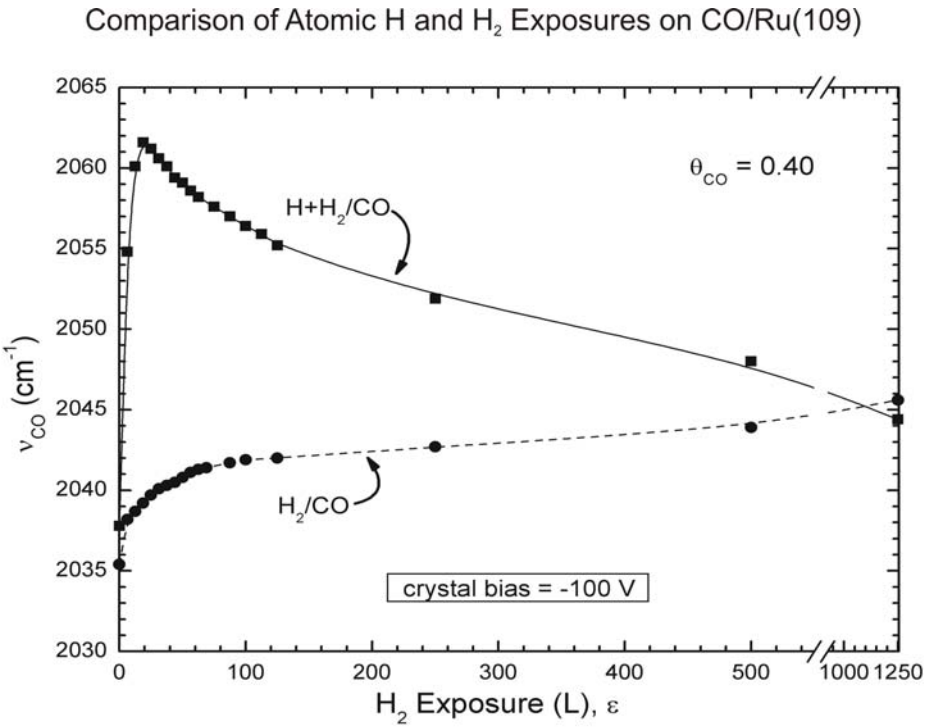

Figure 48: Comparison of infrared spectra of chemisorbed CO on Ru(109) at an initial coverage of θ_{CO} = 0.40, after sequential exposures of atomic and molecular hydrogen. The crystal was biased -100 V during the exposures.

3.7 DISCUSSION

3.7.1 The production of HCO(a) from atomic H and CO on Ru

The theoretical investigations of the adsorbed HCO species on Ru(001) indicate that at 150 K, the temperature employed in this work, if these species were produced they would not be observable by vibrational spectroscopy. Work by Anton et al. [207] and by Mitchell et al.[187-

189] has reported the presence of stable η^1-HCO at 100 K and the conversion of this species to η^2- HCO at 180 K, as well as its decomposition. The production of adsorbed H_2CO is also reported [187-189]. These results are in disagreement with our theoretical estimates of the stability of η^2-HCO, and also with our reflection infrared measurements, where neither C-H modes nor C-O modes of HCO(a) were observed.

It is possible that the explanation of our experimental results is connected with the stringent normal-dipole selection rule for infrared reflection spectroscopy [151], a limiting rule less strongly applicable to HREELS [117,208]. As shown in Figure 40a, the η^1-HCO species presents a C-O and a C-H bond which each possess a large normal component, and η^1-HCO should therefore be observable by IR reflection spectroscopy, if it is thermally stable. However, the η^2-HCO species does not have a large normal component for the C-O stretching mode, although the C-H stretching mode should be visible by reflection IR.

Previous studies involving transmission IR spectroscopy on Al_2O_3-supported Rh catalysts have been carried out in a search for the production of adsorbed HCO by reaction of chemisorbed CO with atomic H at 170 K [209]. These experiments, which are not limited by the dipole selection rule, were also completely negative. The use of a high surface area metallic catalyst adds extra sensitivity to the infrared measurements.

3.7.2 Shifts in the C-O stretching mode following exposure of chemisorbed CO to atomic H: CO compression and displacement effects

It is well known that when the coverage of CO is increased on Ru(001), the CO frequency shifts upward [91]. This effect has also been seen on Ru(109) [42]. The upward shift is due to interaction between the dynamic dipoles of the CO oscillators, in which the in-phase coupling,

leading to a higher mode frequency, is preferentially intensified compared to out-of-phase coupling [151] as the coverage is increased.

When hydrogen coadsorbs with chemisorbed CO, immiscible islands of H(a) and CO(a) are formed, causing the local coverage in the CO islands to increase. The upward frequency shift initially observed in the C-O mode (Figure 48) when either atomic H or H_2 interacts with the surface containing CO is therefore likely to be due to this CO compression effect. The same effect is seen with D atoms interacting with chemisorbed CO on Ru(001) [180]. The higher chemical potential of atomic H causes this coadsorption process to be kinetically accelerated compared to experiments employing H_2. An alternate explanation [93,180] involving an electronic interaction between H(a) and CO(a) is unlikely to be strongly involved.

After an exposure to H/H_2 of only about 20 L, the increase in C-O frequency is reversed, and ν_{CO} begins to decrease. This is likely due to the displacement of chemisorbed CO by atomic H. The reduction in C-O frequency at higher atomic H exposures is accompanied by a large loss in C-O band intensity, also suggesting that CO displacement by atomic H has occurred. The extra potential energy of atomic H compared to H_2 [1/2 D_0 (H_2) = 52.1 kcal/mol] may kinetically drive CO displacement. At θ_{CO} = 0.40, we have measured that the binding energy of CO is only about 15 kcal/mol [42]. The exothermicity of atomic H adsorption is 58-65 kcal/mol [210], based on the desorption activation energy of H_2 (11-26 kcal/mol of H_2) [211].

3.7.3 HCO as an intermediate in Fischer-Tropsch Chemistry

These experiments do not address the possibility that chemisorbed HCO intermediates may be involved in the Fischer-Tropsch catalytic reaction. If HCO is an intermediate in the reaction, its steady state surface concentration will be very low at ordinary synthesis temperatures. For high

pressure H_2, where pressure is employed to elevate the chemical potential, it is likely that CO displacement processes will occur under catalytic conditions. Many other studies suggest that the alternative kinetic route to Fischer-Tropsch alkane products involving C-O bond scission is active [49-51,65].

3.8 SUMMARY

Theoretical investigations suggest that at temperatures of 170 K, formyl species adsorbed on Ru(001) will be unstable, and will rapidly decompose to H(a) and CO(a). HCO species multiply bound in different ways on Ru via C and O moieties exhibit low dissociation activation energies of only 7.4 - 4.1 kcal/mol and are unstable at T > 170 K. Additionally, our theoretical results suggest that H atom-induced H abstraction from formyl species with formation of CO(a) and desorption of H_2(g) is another possible reaction mechanism at low temperatures.

Using reflection IR spectroscopy, a search for HCO species produced by atomic H bombardment of chemisorbed CO has not revealed the production of these species, consistent with theoretical expectations on Ru.

Atomic H is observed to cause CO overlayer compression effects, based upon observations of an initial increase in C-O vibrational frequency as immiscible H(a) and CO(a) islands are produced. Continued exposure to atomic H causes desorption of CO at 150-170 K as deduced by a downward shift in the C-O frequency as well as a large decrease in integrated CO IR absorbance.

4.0 ELECTRON-STIMULATED DISSOCIATION OF MOLECULAR N_2 ADSORBED ON Ru(109): A TPD AND IRAS INVESTIGATION

The information contained in this chapter is based on the following research publication:

Gregg A. Morgan, Jr., Yu Kwon Kim, and John T. Yates, Jr. *"Electron-Stimulated Dissociation of Molecular N_2 Adsorbed on Ru(109): A TPD and IRAS investigation"* Surf. Sci. **598** (2005) 1-13.

4.1 ABSTRACT

Temperature programmed desorption (TPD) and infrared-reflection absorbance spectroscopy (IRAS) studies have been performed on the molecular adsorption state of N_2 and its subsequent electron-induced dissociation on an atomically-stepped Ru(109) single crystal surface. IRAS results revealed that N_2 adsorbates exhibit only a single infrared absorption band at ~2198-2196 cm^{-1} up to saturation, indicating an on-top configuration. TPD results show three distinct features (termed α_1, α_2, and α_3), where at the lowest coverage, only α_1 grows up to saturation with desorption at 184 K, followed by the α_2 feature which desorbs at 136 K, and then, the surface saturates with the development of the α_3 feature desorbing at 112 K. The IRAS results confirm that the three N_2 desorption states comprise the molecular adsorption states on Ru(109)

by the complete depletion of the IR band after annealing up to 200 K. The α_1-N_2 state is shown to be due to adsorption on the step sites of Ru(109). Electron-stimulated dissociation of the molecular N_2 adsorbates produces two distinct recombinative, N(a) + N(a), desorption states (β_1 and β_2) between 400-800 K. The appearance of the β_2 state is shown to be due to the coverage of atomic N produced by electron bombardment.

4.2 INTRODUCTION

The Haber-Bosch process is an industrially important catalytic reaction for the synthesis of ammonia from atmospheric nitrogen and hydrogen. In addition to the traditional iron catalyst, ruthenium has recently emerged as a viable contender to become an ammonia synthesis catalyst [129,212]. Major steps in the catalytic reaction involve the dissociation of N_2 and H_2, which is then followed by a reaction between the chemisorbed atomic N and H species [115]. Thus, there have been extensive experimental studies on the adsorption of N_2 on the Ru(001) surface by temperature programmed desorption (TPD) [34,35,115,169,213-219], high resolution electron energy loss spectroscopy (HREELS) [115,216,217,220,221], low energy electron diffraction (LEED) [115,213,216,222], Fourier transform-infrared reflection absorption spectroscopy (FT-IRAS) [119], scanning tunneling microscopy (STM) [223,224], and ion scattering spectroscopy (ISS) [225,226] as well as theoretical studies [34,121,218,219,227] in an attempt to understand adsorption, desorption, and dissociation kinetics.

The rate limiting step in the ammonia synthesis is very likely the N_2 dissociation on the Ru surface. One of the most important findings is that the N_2 dissociation is not mediated by the whole surface, but entirely by some specific active sites that are attributed to the various random

atomic steps present on the Ru(001) surface [34]. Chorkendorff *et al*. [34] showed that the N_2 dissociation occurs at random step sites on Ru(001) with a dissociation barrier of about 0.4 eV and on the terrace sites with a dissociation barrier of 1.3 eV from their study of the thermal dissociation of N_2 on clean and Au-passivated Ru(001). The measured rate of dissociative N_2 adsorption at 500 K is at least 9 orders of magnitude higher at the step sites than at the terrace sites [34]. The calculated difference in the activation barrier between the steps and terraces is slightly higher than experimentally reported, with an approximate difference of 1.5 eV. Two consequences can be drawn from the reactivity of the steps and the terraces: (1) N_2 dissociation is extremely structure sensitive such that even a small percentage (< 1%) of step defects on the Ru surface could dominate the overall N_2 dissociation rate; (2) The high dissociation probability on the step sites indicates that the ammonia synthesis reaction should be extremely rapid on a dispersed Ru catalytic surface in which a much higher percentage of defects are present.

This paper reports the behavior of N_2 on the Ru(109) surface containing double height steps separated by Ru(001) terraces of ~9 atom width. N_2 dissociation is carried out by electron impact at low temperatures. A second paper deals with the thermal dissociation of N_2 on Ru(109) [43].

4.3 EXPERIMENTAL

All of the experiments reported here were performed in a stainless steel ultrahigh vacuum (UHV) chamber which was discussed in detail in Chapter 2. The general experimental conditions are also discussed in detail in Chapter 2, but a few specific conditions are mentioned here.

A shielded Quadrupole Mass Spectrometer (QMS) (UTI 100C) was used for acquiring the thermal desorption spectra of N_2 adsorbed on the surface. The conical shaped shield has an aperture of ~ 9 mm, whereas the diameter of the crystal is ~ 10 mm thus insuring that desorption from the front surface of the crystal is mainly being sampled. The crystal was positioned approximately 4 mm from the aperture of the shield during TPD with the face of the crystal perpendicular to the axis of the QMS. For electron-induced dissociation of N_2/Ru(109), the electrons were extracted from the QMS onto the crystal (biased +100 V) giving a nearly uniform current density of 1.6×10^{-6} A cm^{-2} at 170 eV electron kinetic energy at the crystal.

The infrared reflection-absorption spectra were collected using 2 cm^{-1} resolution averaged over 1500 scans.

4.4 EXPERIMENTAL RESULTS AND DISCUSSIONS

4.4.1 IRAS Measurements

4.4.1.1 IR Spectral Development

The development of the infrared reflection absorption spectra for $^{14}N_2$ adsorption on Ru(109) at 75 K with increasing N_2 coverages is shown in Figure 49. It is noted that a single infrared band is observed for almost all coverages of N_2 except for the lowest detectable coverage of 4.1×10^{13} cm^{-2} ($\theta = 0.03$, hereafter relative to the available Ru surface atoms, 1.37×10^{15} cm^{-2}). There are two bands present at this coverage with vibrational frequencies of 2208 and 2198 cm^{-1}, respectively. As the coverage is increased, only a single band grows in intensity. The vibrational frequency of this band remains nearly constant as the coverage is increased,

shifting from 2198 cm^{-1} at small coverages to 2196 cm^{-1} at saturation coverage. At a coverage around 1.37 x 10^{14} cm^{-2} (θ = 0.10), the vibrational frequency shifts gradually from 2198 cm^{-1} to 2196 cm^{-1} and then back to 2198 cm^{-1} as the coverage approaches 3.84 x 10^{14} cm^{-2} (θ = 0.28). At coverages larger than 3.84 x 10^{14} cm^{-2} (θ = 0.28), the vibrational band again shifts down in frequency to 2196 cm^{-1} until saturation at 5.07 x 10^{14} cm^{-2} (θ = 0.37).

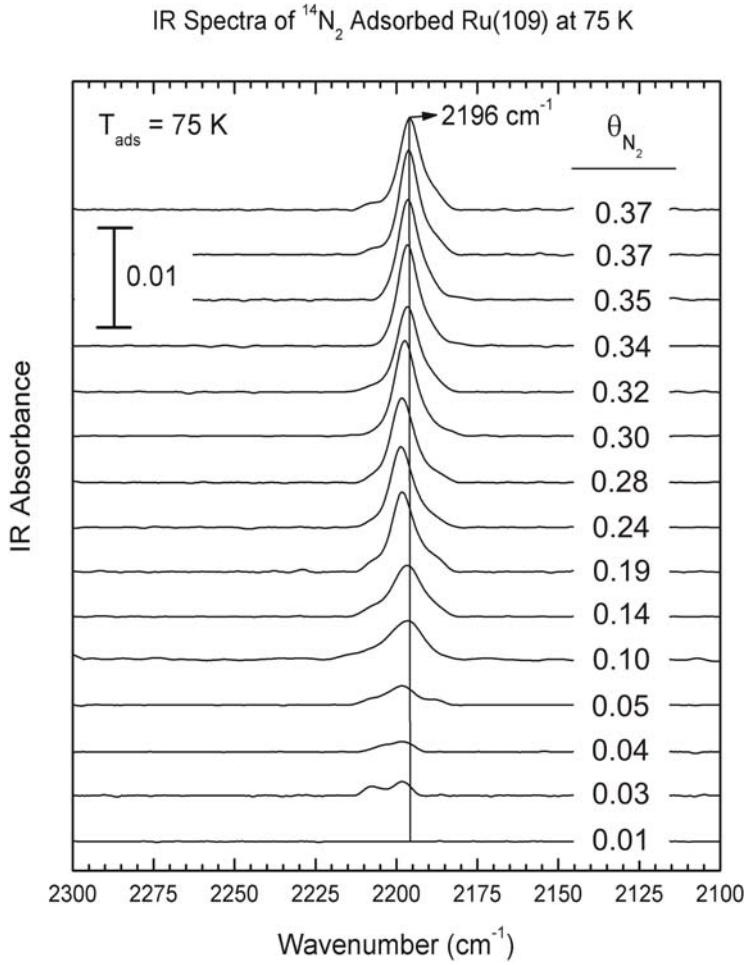

Figure 49: Infrared spectra of $^{14}N_2$ after adsorption on Ru(109) at 75 K. The resolution is 2 cm^{-1} with each spectrum being averaged over 1500 scans. θ_{N_2} values are given relative to the available Ru surface atoms, 1.37 × 10^{15} cm^{-2}.

In addition to a shifting in the frequency of the band, the peak also changes shape as the coverage is increased. Up to a coverage of 1.92 × 10^{14} cm^{-2} (θ = 0.14) the band is broad (FWHM

= 10-12 cm^{-1}), but at a coverage of 3.84×10^{14} cm^{-2} ($\theta = 0.28$) the band narrows down to ~8 cm^{-1} and continues to narrow to < 8 cm^{-1} at the saturation coverage. The integrated absorbance of the IR band increases until $\theta = 0.37$, corresponding to the saturation coverage as can be seen in Figure 50.

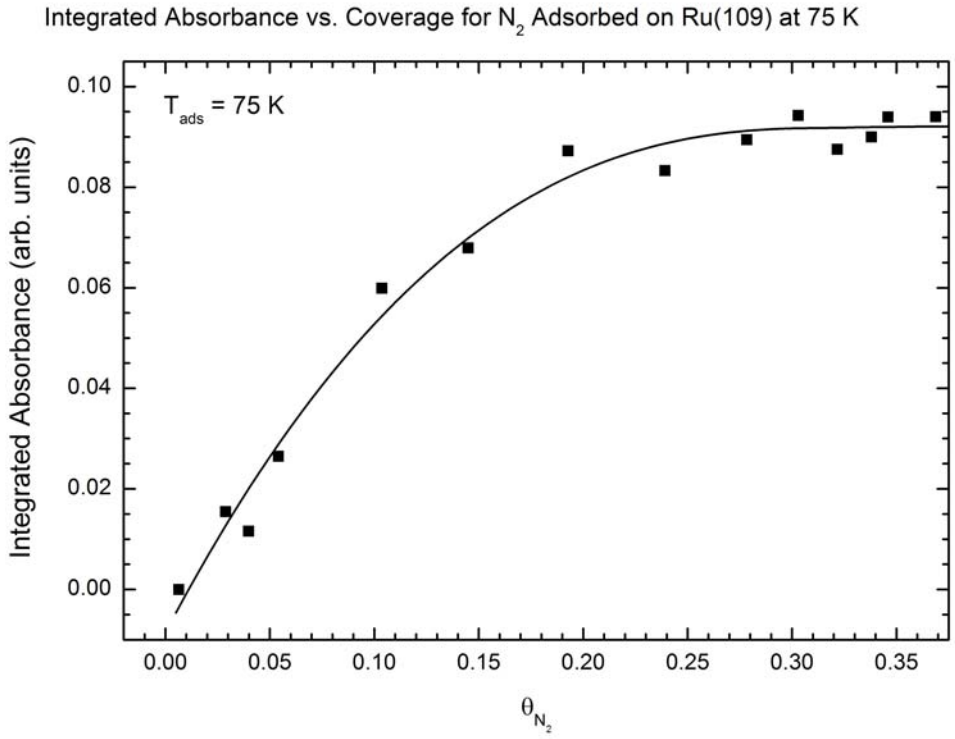

Figure 50: Integrated absorbance of the infrared spectra versus N_2 coverage (relative to the available Ru surface atoms, 1.37×10^{15} cm^{-2}) for N_2 adsorbed on Ru(109) at 75 K. The curve is drawn to guide the eye.

4.4.1.2 N_2 Binding to Stepped Ru(109)

The infrared peak is caused by N_2 molecules adsorbed on top of a single ruthenium atom. [115]. The observed nitrogen-nitrogen stretching frequency of ~ 2200 cm^{-1} may be correlated with previously observed vibrational frequencies of linear Ru-N_2 species within metal complexes [115]. The N_2 species bonds primarily to the substrate through a completely decoupled $4\sigma/2\pi$ bonding interaction [119]. The infrared activity of the N-N bond in the chemisorbed phase

indicates that the adsorption process breaks the symmetry of the nitrogen molecule, thus producing inequivalent N atoms within the molecule.

The observed variation in peak position with coverage is in reasonable agreement with previous HREELS data from Anton *et al.* for N_2 on Ru(001), which has reported that as the N_2 coverage increases the nitrogen-nitrogen vibrational band shifts from 2252 cm^{-1} at the lowest coverages to 2212 cm^{-1} at saturation coverage when nitrogen is adsorbed at 95 K [228]. However, when N_2 was adsorbed at 75 K on Ru(001), the vibrational band shifted from 2247 cm^{-1} to 2198 cm^{-1} [228]. De Paola *et al.* reported that the N-N vibrational band shifts from 2209 cm^{-1} to 2189 cm^{-1} for the Ru(001) surface as found by IRAS, which provides more accurate frequency measurements than HREELS [119]. However on the more open Ru(100) surface, it was found by HREELS that the vibrational frequency of the N-N band does not decrease with increasing coverage as has been previously reported, but remains constant at 2194 cm^{-1} [229].

Coverage dependent changes in the N-N frequency could cause the downward shift in the vibrational frequency as has been previously observed for N_2 adsorption on Ru(001). A possible explanation for the constant frequency of the vibrational band for N_2/Ru(109) arises from two opposing and compensating interactional effects. An upward shift in vibrational frequency is due to dipolar coupling in the adlayer. As the coverage increases, the dipolar coupling increases which therefore causes the vibrational frequency to increase and has been previously observed for CO adsorption on Ru(001) [91] and Ru(109) [42]. The decrease in frequency with increasing coverage may be attributable to the formation of a $1\pi_g$ band as $1\pi_g$ orbitals of adjacent molecules overlap with increasing coverage, which ultimately broadens the IR band due to dispersion [115]. If the $1\pi_g$ level broadens significantly in energy to cross the Fermi level, the N-N bond

would weaken causing ν(N-N) to decrease. It is possible that these two effects compensate each other, resulting in the relatively constant vibrational frequency.

In the course of the infrared studies, individual resolved IR features attributable to N_2 adsorbed on the steps and on the terraces could not be observed. There are two explanations which can be offered to explain the lack of IR spectral evidence for N_2 adsorption on the step sites of Ru(109). Possible intensity sharing effects between step-N_2 and terrace-N_2 could occur causing spectral discrimination to be impossible [30]. Alternatively, the difference in the bonding and the electronic character of N_2 on step and terrace sites may be too small to be observed by infrared spectroscopy as a large shift in frequency. However, our studies do indicate that at low coverages, when step sites are preferentially occupied, there is a split in the IR band near $\theta_{N_2} = 0.03$.

The observed linewidths (FWHM) are roughly similar to those observed by de Paola [119] for N_2 adsorption on Ru(001). These linewidths are much narrower than those observed for the C-O stretching vibration on Ru(109) [42].

4.4.2 Temperature Programmed Desorption of $^{14}N_2$/Ru(109)

4.4.2.1 TPD of $^{14}N_2$ from clean Ru(109)

The thermal desorption spectra for N_2 molecules adsorbed on Ru(109) at 75 K and 150 K are shown in Figure 51 and Figure 52, respectively. In Figure 51, a single desorption feature (termed α_1) appears around 195 K from the lowest coverage to its saturation at 4.8×10^{13} cm^{-2} ($\theta = 0.11$) with the peak shifting to lower temperature (184 K). At even higher coverages, a second desorption feature (α_2) develops until it saturates at a coverage of 3.84×10^{14} cm^{-2} ($\theta = 0.28$)

with a maximum desorption temperature of 135 K, which is followed by a third desorption feature (α_3) at 112 K. The TPD traces in Figure 51a are those of mass 14 and the TPD traces in Figure 51b are those of mass 28. The high temperature feature near 550 K in Figure 51b is due to the desorption of contaminant CO from the surface, which comprises less than 1% of the saturation coverage.

The inset in Figure 51a indicates that all of the molecular nitrogen adsorbates desorb completely from the surface by 200 K, without yielding any other higher temperature desorption states related to the nitrogen species. The IRAS results indicate that the three N_2 desorption states comprise all the molecular adsorption states on Ru(109) by the complete depletion of the IR band after annealing up to 200 K (data not shown).

Note that the development of α_2 and α_3 with increasing N_2 coverage quite closely resembles the two desorption features observed in previous TPD studies of N_2/Ru(001) [228,230]. Therefore, these two features are attributed to the desorption of molecular nitrogen from the terraces of Ru(109). On the Ru(001) surface all chemisorbed N_2 is removed from the surface by 140 K [228,230], and no desorption features similar to α_1 have been observed on Ru(001). Thus, the α_1 feature can be assigned to the desorption of molecular nitrogen from the steps, whereas the α_2 and α_3 peaks are assigned to molecular nitrogen desorbing from the terrace sites. Nitrogen adsorbed on the Ru steps has a higher binding energy than nitrogen adsorbed on the terraces as indicated from the higher desorption temperature of the α_1 state. The α_1 desorption feature corresponds to a coverage of roughly 1/3 ($\theta = 0.12$) of the saturation coverage. The step atoms in the double height Ru(109) step constitute 12% of the surface Ru atoms.

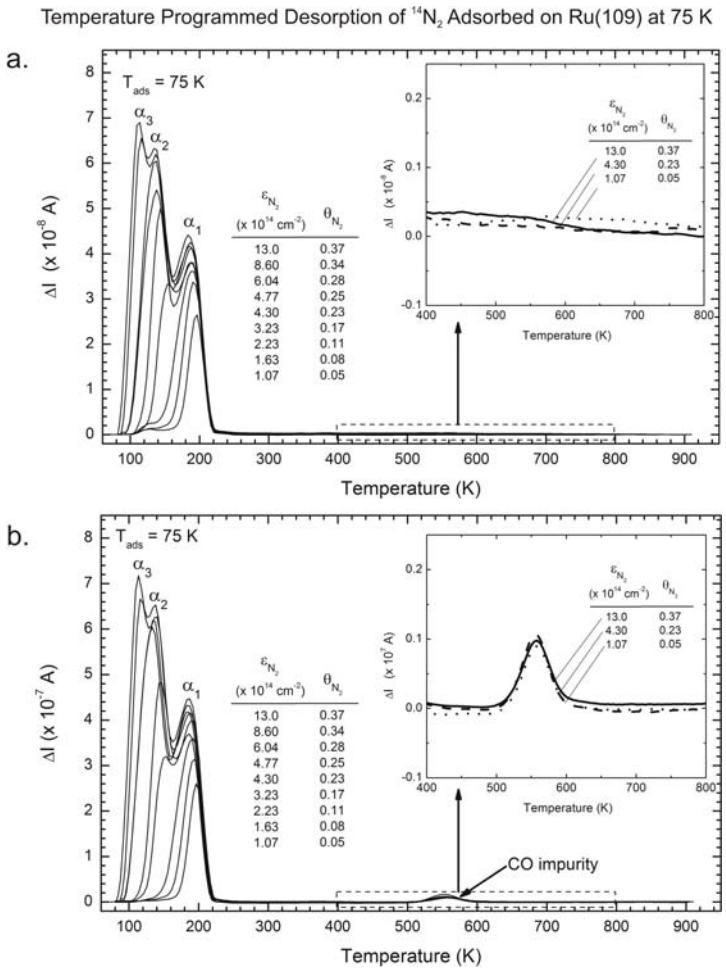

Figure 51: Temperature programmed desorption spectra of N_2 adsorbed on Ru(109) at 75 K. The heating rate is 2.0 K/s. a) The TPD trace of 14 amu was followed so as to avoid overlap in the 28 amu signals. b) The TPD trace of mass 28 was plotted to show that the amount of CO co-adsorption from the background is very small and negligible. The insets in both a) and b) show a magnified view of the temperature region between 400 K and 800 K.

Figure 52 shows the sequential TPD spectra for $^{14}N_2$/Ru(109) when N_2 is adsorbed at 150 K. After the exposure, the substrate is cooled down to 85 K prior to the TPD measurement. The α_1 feature is the only desorption feature, which saturates at a coverage of 1.64×10^{14} cm^{-2} (θ = 0.12) without any desorption of the α_2 and α_3 features. The inset in Figure 52 again shows that no high temperature desorption states are present.

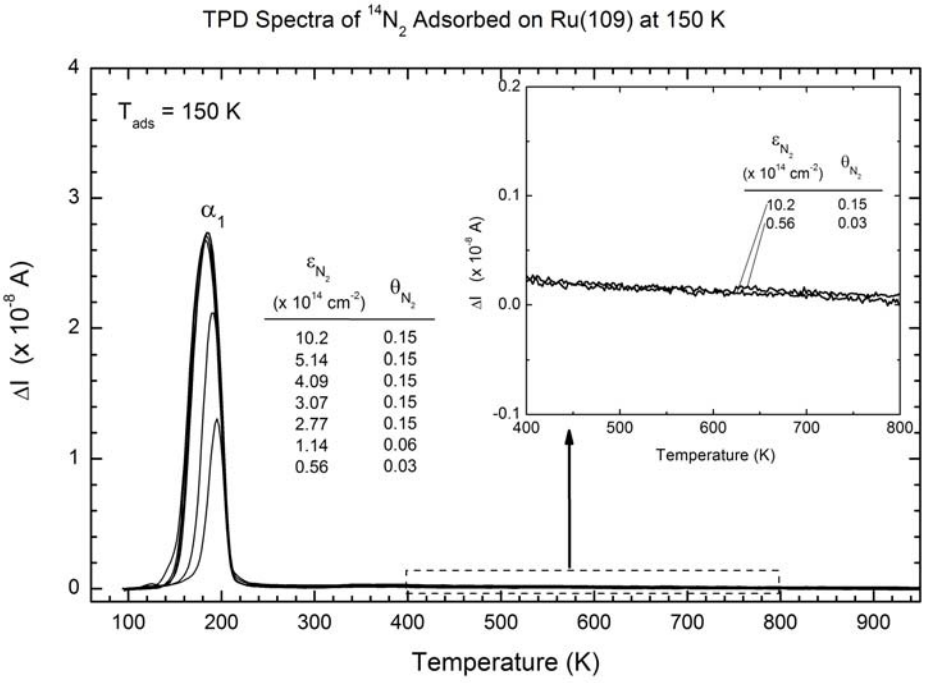

Figure 52: Temperature programmed desorption of N_2 adsorbed on Ru(109) at 150 K. The heating rate is 2.0 K/s. The TPD trace at 14 amu was followed so as to avoid overlap in the 28 amu signals. The inset shows a magnified view of the temperature region between 400 K and 800 K.

4.4.2.2 TPD of $^{14}N_2$ from Carbon-Covered Ru(109)

In an attempt to verify the conclusion that the α_1 desorption feature is attributed to N_2 desorption from the step sites, the steps were intentionally poisoned with carbon. Thermal decomposition of ethylene on Ru produces carbon deposits on the surface between the temperatures 350-650 K [42,96]. The effect of carbon deposition from ethylene on the N_2 desorption kinetics was studied and the effects can be seen in Figure 53. Ethylene was adsorbed on the Ru(109) surface at 88 K at coverages up to ~ 20% of the available Ru surface atoms. Therefore, heating up to 800 K decomposes the adsorbed C_2H_4 into surface carbon in the stoichiometric amount up to a maximum of ~40% of the available Ru surface atoms. When C_2H_4 was adsorbed at a coverage corresponding to 10% of the available Ru surface atoms and thermally decomposed, a carbon coverage of $\theta_C = 0.20$ was sufficient to block CO dissociation

which occurred at the step sites [42]. Details of our observations of C_2H_4 decomposition on Ru(109) are given in the footnote[1]. N_2 was then adsorbed on Ru(109) with various coverages of carbon from $\theta_C = 0$ to $\theta_C = 0.40$ with the crystal at 150 K using a N_2 exposure of 5.0×10^{14} N_2 cm^{-2} (the exposure used to produce a maximum α_1-N_2 coverage of 1.64×10^{14} cm^{-2} ($\theta = 0.12$) on a clean surface) and subsequently followed by TPD. As the coverage of the carbon increased, the α_1 peak decreased in intensity and integrated area. At $\theta_c = 0.28$ the amount of α_1-nitrogen able to adsorb on the surface reaches a minimum. Preadsorbed carbon on the Ru(109) surface does not completely block N_2 adsorption at the step sites as was previously seen for CO/Ru(109) [42]. The ~86% blockage of α_1-N_2 by carbon strongly suggests that α_1-N_2 is associated with the atomic steps on the Ru(109) surface.

[1] At C_2H_4 coverages less than 1.0×10^{14} cm^{-2} ($\theta = 0.07$) the only desorption product present during the thermal decomposition of C_2H_4 is H_2 (2 amu). There is no evidence of 28 amu, 26 amu, or 25 amu desorbing from the surface as the C_2H_4 is decomposed (data not shown). At C_2H_4 coverages above 2.0×10^{14} cm^{-2} ($\theta = 0.15$) there is evidence of minimal desorption for 25 amu and 26 amu. This indicates that there is not a complete decomposition (into surface C and gaseous H_2 species) of the C_2H_4 adsorbed on the Ru(109) surface. At large surface coverages (> 4.0×10^{14} cm^{-2} ($\theta = 0.29$)) there is evidence of 28 amu desorption in addition to desorption of 25 and 26 amu.

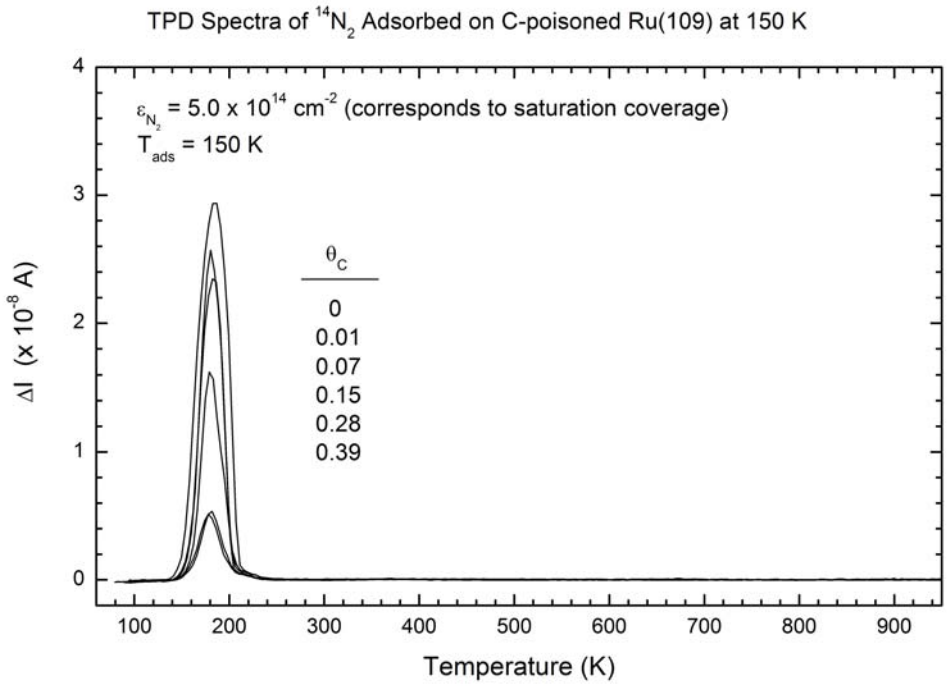

Figure 53: Temperature programmed desorption spectra of N_2 adsorbed on Ru(109) at 150 K at varying coverages of pre-deposited carbon from ethylene. The initial N_2 exposure = 5.0 × 10^{14} cm^{-2} corresponds to a saturation coverage (on a clean surface) at 150 K. The heating rate is 2 K/s.

4.4.2.3 Electron Stimulated Dissociation of $^{14}N_2$/Ru(109)

The electron stimulated dissociation of chemisorbed N_2 molecules on Ru(109) was explored. $^{14}N_2$ was adsorbed on Ru(109) up to a saturation coverage of 5.07 × 10^{14} N_2 cm^{-2} (θ = 0.37) at 75 K. The saturated N_2/Ru(109) surface was then subjected to varying fluences of electrons, which was followed by a TPD measurement as can be seen in Figure 54. Note that all molecular desorption states (α_1 – α_3) decrease with increasing electron exposure, which is accompanied by the development of a high temperature desorption feature around 600-700 K (labeled as β_1). As the β_1 feature increased in intensity, the β_1 desorption peak shifted to lower temperature (620 K), indicative of a second-order desorption process. After an exposure of 1.2 x 10^{17} electrons cm^{-2}, another state (β_2) develops at 500 K. The β_2 feature continued to increase in

intensity with very little shift in temperature as the exposure was increased sequentially up to 3.6 $\times 10^{17}$ electrons cm^{-2}.

From the TPD spectra in Figure 54, the cross-section for electron stimulated desorption (Q_{Des}) and dissociation (Q_{diss}) were calculated from the plot in the inset. The cross section for desorption (Q_{Des}) is determined from the loss of the total integrated area for all of the N_2 desorption processes ($\alpha + \beta$) due to electron stimulated desorption and was determined to be 1.1 $\pm$ 0.1 $\times 10^{-18}$ cm^{-2}. The cross-section of electron stimulated dissociation (Q_{diss}) is determined from the increase in the integrated area of β_1 and β_2 and was determined to be 1.6 $\pm$ 0.6 $\times 10^{-18}$ cm^{-2}. $Q_{Des} + Q_{diss}$ are determined from the depletion of the integrated area of α_1, α_2, and α_3. This decrease is a result of dissociation as well as desorption, occurring with a measured cross-section of 3.2 $\pm$ 0.4 $\times 10^{-18}$ cm^{-2}. The sum of Q_{diss} and Q_{Des} is equal to the overall calculated cross section of depletion ($Q_{Des} + Q_{diss}$), within the error limits of the measurement.

Figure 55 shows results of the electron stimulated process for depletion of only α_1-N_2/Ru(109). A coverage of 1.64 $\times 10^{14}$ cm^{-2} ($\theta = 0.12$), the saturation α_1 coverage, was adsorbed on the Ru(109) surface at 150 K. The saturated adlayer was then bombarded with increasing exposures of electrons. As the electron exposure increased, note that the decrease in α_1 is accompanied by the production of only β_1 until its saturation after an exposure of 6.0 $\times 10^{17}$ electrons cm^{-2}. There was no development of the β_2 state, even after the saturation of β_1, as there was when N_2 was adsorbed to higher coverages at 75 K.

Using the integrated area of the TPD spectra in Figure 55, the cross-section for electron stimulated desorption (Q_{Des}) and dissociation (Q_{diss}) of the α_1-N_2 species were calculated from the plot in the inset. The cross section for desorption (Q_{Des}) is determined from the loss of the total integrated area (relative to the initial TPD spectrum) due to electron stimulated desorption

and was determined to be $1.5 \pm 0.1 \times 10^{-18}$ cm^{-2}. The cross-section of electron stimulated dissociation (Q_{diss}) is determined from the increase in the integrated area of β_1 and was determined to be $1.8 \pm 1.0 \times 10^{-18}$ cm^{-2}. $Q_{Des} + Q_{diss}$ are determined from the depletion of the integrated area of the α_1 state. This decrease is a result of dissociation as well as desorption, resulting in a cross-section of $4.4 \pm 0.9 \times 10^{-18}$ cm^{-2}.

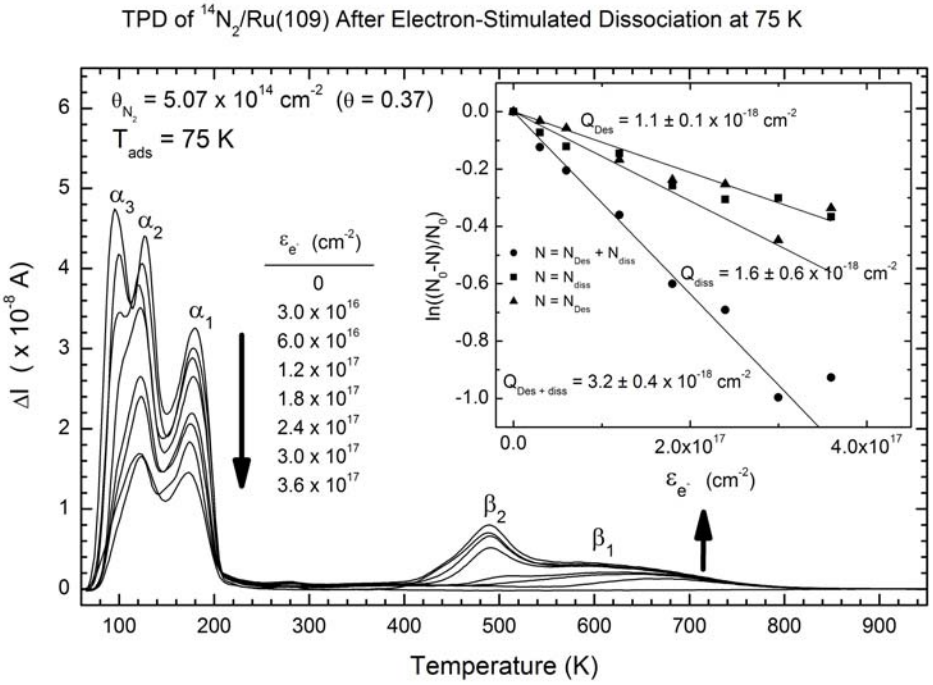

Figure 54: Temperature programmed desorption spectra of N_2 adsorbed on Ru(109) at 75 K after exposure to varying fluences of 170 eV electrons. The heating rate is 2 K/s. The initial N_2 coverage = 5.07×10^{14} cm^{-2} (θ = 0.37). The TPD trace at 14 amu was followed so as to avoid overlap in the 28 amu signals. The inset shows the calculated cross sections of desorption (Q_{Des}), dissociation (Q_{diss}), and depletion ($Q_{Des} + Q_{diss}$) from the areas of the corresponding TPD spectra.

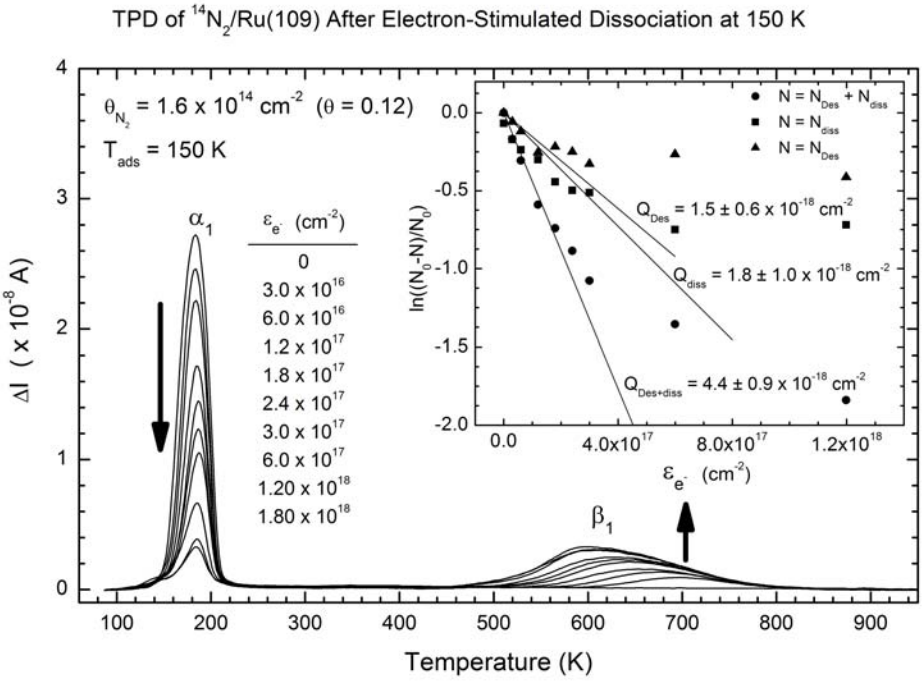

Figure 55: Temperature programmed desorption spectra of N_2 adsorbed on Ru(109) at 150 K after exposure to varying fluxes of 170 eV electrons. The heating rate is 2.0 K/s. The initial N_2 coverage = 1.64 × 10^{14} cm^{-2} (θ = 0.12). The TPD trace at 14 amu was followed so as to avoid overlap in the 28 amu signals. The inset shows the calculated cross sections of desorption (Q_{Des}), dissociation (Q_{diss}), and depletion (Q_{Des} + Q_{diss}) from the areas of the corresponding TPD spectra.

4.4.2.4 Isotopic Mixing of $^{14}N_2$ and $^{15}N_2$/Ru(109)

To verify the hypothesis that the β_1 and β_2 phases are due to recombinative desorption of dissociated nitrogen it was necessary to utilize an additional N_2 isotopomer. Two stable isotopomers – $^{14}N_2$ and $^{15}N_2$ – were employed to detect electron impact dissociation of N_2 on the surface by detecting the formation of the mixed isotopomer –$^{14}N^{15}N$. $^{14}N_2$ and $^{15}N_2$ were adsorbed simultaneously on the Ru(109) surface (using a 50/50 mixture of the two isotopomers) in the amount of θ = 0.10 (1.37 × 10^{14} cm^{-2}) each, which was then followed by electron bombardment with 6.0 × 10^{17} electrons cm^{-2}. During the subsequent TPD scan, the signals from 14, 28, 29, and 30 amu masses were recorded by QMS multiplexing. The 28 amu trace was generated from the 14 amu trace as there was evidence of a small amount (roughly 1% of a

saturated layer) of $^{12}C^{16}O$ desorbing . This was possible by using the fact that in a 50/50 mixture of isotopomers 2/3 of the 14 amu signal (when rescaled to match the 28 amu signal) originates from the $^{14}N_2$. In Figure 56, the α_1 and α_2 peaks remaining after electron bombardment are composed of the initial isotopomers in nearly equal amounts. As the temperature is increased, resulting in the desorption of the β_1 and β_2 states, 28 amu and 30 amu desorb in nearly equal amounts whereas the amount of 29 amu desorbing from the surface is nearly twice the amount of 28 amu and 30 amu.

There is a slight amount of 29 amu desorbing around 180 K with the initial isotopomers, but this is due to the presence of 29 amu in the $^{15}N_2$ as a 2% impurity.

The result from Figure 56 indicates that 100% isotopic mixing (and hence dissociation) occurs after exposure of the α-N_2 species to the electron beam and that the β features are attributable to the recombination of mobile atomic N species formed by N_2 dissociation by the impinging electron beam. This can be understood from the recombination of two kinds of N adsorbates (^{14}N and ^{15}N) which are randomly distributed on the steps as well as on the terraces. Thus, the two desorption features are naturally attributed to the recombinative desorption of atomic N adsorbates irrespective of the adsorption sites.

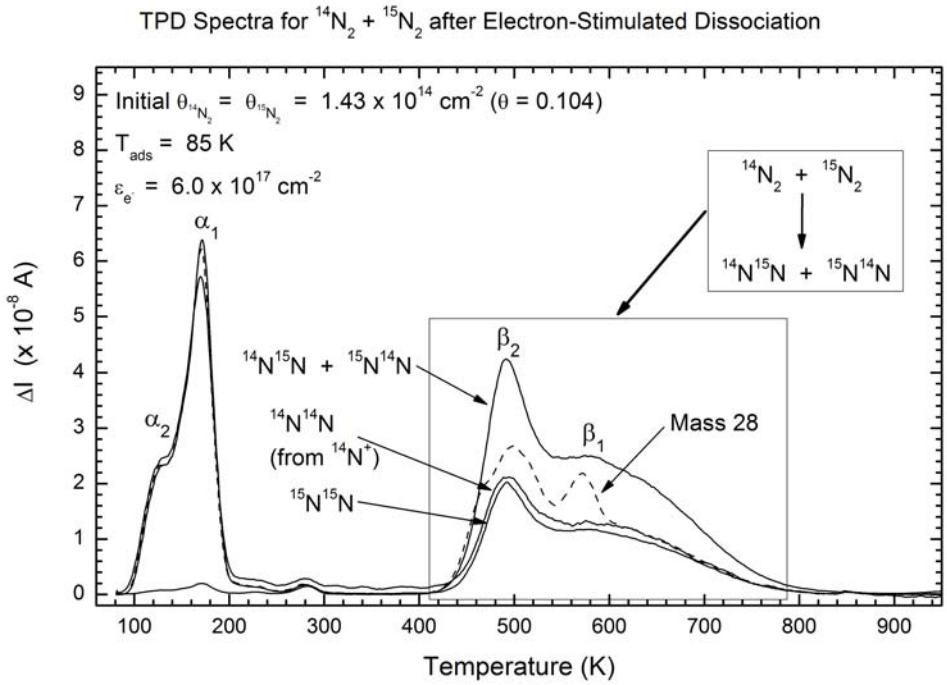

Figure 56: Isotopic mixing of $^{14}N_2$ and $^{15}N_2$ during temperature programmed desorption of N_2 adsorbed on Ru(109) at 85 K after exposure to 6.0 × 10^{17} electrons/cm^2 (170 eV). The heating rate is 2 K/s. The initial θ_{N_2} = 0.10 for each isotopomer. The dashed curve is the actual mass 28 signal from $^{14}N^{14}N$ and $^{12}C^{16}O$. The difference between the calculated mass 28 signal and the actual mass 28 signal is due to CO co-adsorption from the background.

4.4.3 Assignment of β_1 and β_2 Desorption Features to Steps and Terraces

From the calculated results of the dissociation and desorption cross-sections as can be found from Figure 54, the electron impact process induces both dissociation and desorption with roughly equal probability. Thus, upon electron impact roughly the same number of N_2 molecules desorb from the surface as dissociate on the surface, regardless of whether adsorption exists on the steps or terraces. A similar ratio of desorption and dissociation cross sections is observed when only α_1-N_2 is present (Figure 55) indicating that the electron impact processes are fairly site-insensitive. In addition, the number of molecules desorbing from the β_1 state (9.5 × 10^{13} cm^{-2}) is roughly the same as the number desorbing from the β_2 state (9.9 × 10^{13} cm^{-2}).

Two separate desorption states (β_1 and β_2) clearly reflect two different kinetic processes originating from two distinct N recombination/desorption reaction channels. Assuming second-order desorption kinetics since the β features are attributable to recombinative desorption, the desorption energy, E_{des}, for the β_2 feature was estimated to be 108.7 kJ/mol using the method developed by Chan and Weinberg [231]. This method was also used to estimate the preexponential factor, $\nu_0 = 9.3 \times 10^{-4}$ cm^2 s^{-1}. In the calculation, the full width at ¾ height (of the desorption peak) was used instead of the full width at ½ height because at lower heights the curve deviates from an ideal shape. Dietrich *et al.* [217] has calculated an activation energy of 130 kJ/mol for strikingly similar thermal desorption spectra following the adsorption of NH_3 on Ru(001) assuming first-order kinetics. Previous desorption data of N_2 from Ru(001) in which N atoms were adsorbed by means of an atomic N beam yielded a desorption energy of 154 kJ/mol [215] assuming second-order desorption. In both cases of the higher desorption energy, the initial N coverage is roughly double the N coverage achieved in the present work on the Ru(109) surface. The desorption parameters were not calculated for the β_1 desorption state because of experimental uncertainties in the deconvolution of the two desorption processes.

A feature very similar to the β_1 desorption feature has been observed in several other thermal desorption studies on Ru(001) [34,144,169,217,219,221,232,233]. This desorption feature in the range of 700 – 1000 K has previously been attributed to N adsorbates dissociated by the steps regardless of the initial adsorption sites [34]. The difference reported here in the desorption temperature range compared to the early results on Ru(001) containing random step defect sites may be attributed to the different substrate structure as well as to the possible contamination by C or O adsorbates in the early work which are reported to induce the β_2 desorption peaks to shift to higher or lower temperature, respectively [214]. As has been pointed

out by previous studies on the Ru(001) surface, the desorption feature similar to the β_1 feature is related to dissociative N_2 processes mediated by defect sites, steps, on the Ru(001) surface (~1% of the overall surface sites) [34,35,207].

Finally, it is noted in Figure 55 that α_1-N_2 may be converted to β_1-N by electron bombardment. It was also observed in a separate experiment (data not shown) that β_2-N can be produced from the α_1-N_2 by replenishment of that state. Thus the appearance of the β_2 state is related to the coverage of atomic N and not to the molecular N_2 state from which it is produced by electron bombardment.

4.5 CONCLUSIONS

The following conclusions have been revealed in this work: (1) The IRAS result indicates that the bonding of N_2 on the atomically stepped Ru(109) surface is very similar to that observed on the atomically smooth Ru(001), exhibiting a single infrared band for all coverages at ~ 2196 cm^{-1}; (2) From thermal desorption measurements, we observed three distinct molecular desorption states (α_1, α_2, and α_3) from the Ru(109) surface; The α_1 feature above 150 K is attributed to the desorption of N_2 adsorbed on the steps of the Ru(109) surface; (3) Electron stimulated dissociation of the α_1-, α_2-, and α_3-N_2/Ru(109) species has been found to generate chemisorbed N atoms which desorb as two desorption states, β_1 and β_2; (4) The appearance of two atomic N recombinative states (β_1 and β_2) is shown to be dependent on the coverage of atomic N produced from molecular α-N_2.

5.0 SITE-SPECIFIC DISSOCIATION OF N_2 ON THE STEPPED Ru(109) SURFACE

The information contained in this chapter is based on the following research publication:

Yu Kwon Kim, **Gregg A. Morgan, Jr.,** and John T. Yates, Jr., *"Site-Specific Dissociation of N_2 on the Stepped Ru(109) Surface."* Surf. Sci. **598** (2005) 14-21.

5.1 ABSTRACT

The dissociative adsorption of molecular nitrogen on Ru(109) is investigated by temperature-programmed desorption (TPD) and low-energy electron diffraction (LEED). This surface presents double-height steps separated by ~9-atom wide Ru(001) terraces. Thermal dissociation of N_2 is shown to be site-specific to the steps leaving atomic N on the steps (step-N), while electron-stimulated dissociation of N_2 adsorbed on Ru(109) can also provide atomic N on the terraces (terrace-N) as well as on the steps. The corresponding activation energy for the thermally-activated N_2-dissociation on the steps is measured to be 0.26 ± 0.05 eV. We postulate that the steps on Ru(109) catalyze not only a unique reaction channel for the N_2-dissociation but also provide active sites during subsequent catalytic reactions by providing more stable adsorption sites for dissociated N atoms.

5.2 INTRODUCTION

Low-coordinated surface atoms, such as those at atomic steps on metal surfaces, have attracted a great attention because they are generally believed to act as low-barrier reaction sites for catalytic reactions [26,36,218,234]. For the Ru(001) surface, which has been studied as a model catalyst for ammonia synthesis, random steps have been found to dissociate the strong N-N bonds in N_2 molecules [34,235].

Ru(001) presents a low density of reactive steps of the order of few % [34] with structures which are not clearly characterized and may vary for various types of steps depending on their orientation [31]. In addition, even more defective structures such as kinks, or point defects may exist as random defects on Ru(001). The low density of random steps on Ru(001) tend to be susceptible to contamination. These facts may explain some of the contradicting results on the dissociation energy barrier of N_2 on Ru(001), which varies significantly from 0.3 to 1.2 eV, depending on the experimental methods used [34,219,236]. In addition, large variations in the theoretical predictions of the energy barrier (0.3-1.5 eV) exists for N_2 dissociation, depending on the structure models as well as on the calculational methods employed [120,237,238].

The dissociation probability for N_2 on a Ru(001) surface containing a low density of atomic steps is reported to be of the order of 10^{-12} at 300 K [169]. Thus, other methods are sometimes employed to produce atomic N surface species, using dissociative adsorption of NO [31,224], or NH_3 [217], or using a hot filament [224], or an electron beam to dissociate chemisorbed N_2 molecules [44].

Interestingly, despite these variations in dissociation methods, similar ordered phases have been found for N/Ru(001) ranging from the well-ordered p-2×2 surface phase at 1/4ML-N

[223], to some metastable phases of $\sqrt{3} \times \sqrt{3}$R-30° structure and the 1×1-structure as the N coverage approaches 1 monolayer (ML) [214]. Strong repulsive interactions between N adsorbates on Ru(001) are postulated to produce the ordered N phases [113].

Some interesting results have been reported for N_2 dissociation of the random atomic steps present on a Ru(001) surface. A preferential accumulation of N atoms on the step sites occurs at low N coverages and these step-bound N atoms exhibit activated diffusion to the smooth terrace sites with an activation energy of 0.94 eV [224]. In this study, we employed the Ru(109) surface with regularly-spaced rows of double-atom height steps separated by ~9-atom-wide terraces to study N_2-dissociation [42]. This surface involves about 12 % of the surface atoms at the atomic steps facilitating a quantitative understanding of these sites for N_2 dissociation. In order to compare thermally-produced surface N atoms with those produced by an artificial method, electron-stimulated dissociation of chemisorbed N_2 molecules has also been studied.

5.3 EXPERIMENTAL

All of the experiments reported here were performed in a stainless steel ultrahigh vacuum (UHV) chamber which was discussed in detail in Chapter 2. The general experimental conditions are discussed in detail in Chapter 2 as well, but a few specific conditions are mentioned here.

For the thermal dissociation of N_2 on Ru(109), N_2 (99.9999% pure) gas is further purified by passing through several cold-traps installed in the gas line before introduction into the small chamber designed for the high-pressure gas exposure and the resulting contamination is maintained below 1-2% of a monolayer up to 10^8 L [1L = 1×10^{-6} Torr·s] of N_2 exposure, as

confirmed from TPD as well as AES measurements. For the electron-stimulated dissociation experiments, nitrogen molecules are dosed on to the stepped surface through the capillary array doser. Then, stray electrons from the QMS are extracted to the Ru surface by biasing the crystal to +100V, to give a uniform electron flux of 1.6×10^{-4} A cm^{-2} at 170 eV energy. The resulting N profile generated on Ru(109) was found to be quite uniform across the crystal surface, as confirmed from the intensity of the N KLL peak at 380 eV.

5.4 RESULTS AND DISCUSSION

5.4.1 TPD of N/Ru(109) Prepared by Two Different Dissociation Methods

The TPD spectra taken for N/Ru(109), produced by the two different dissociation methods, are shown in Figure 57. For thermally dissociated N (denoted as thermal-N hereafter) on Ru(109), the desorption spectra show only a single broad component with its peak maximum shifting from 730 K at the very low N coverage limit to about 600 K with increasing N coverages (labeled as β_1). A very similar N_2 desorption state can be also observed from N/Ru(109) prepared by electron-stimulated dissociation of N_2 molecules adsorbed on Ru(109) at 150 K. In addition to β_1-desorption, another N-desorption state at 490 K (labeled β_2) grows simultaneously when N_2 molecules are adsorbed on Ru(109) at 75-100 K and are subjected to electron-stimulated dissociation at that temperature. The β_2 state is distinguished from β_1 by almost no peak shift with increasing N coverages, as well as its narrow peak width. The TPD spectra for molecular N_2 adsorption on Ru(109) are shown in the inset of Figure 57. At 75 K, three molecular N_2 states (α_1-α_3 -N_2) are formed.

From the isotope exchange measurement reported previously [44], both desorption states (β_1 and β_2) are confirmed to be due to recombinative N_2 desorption from atomic N adsorbates on Ru(109), while the α_1-α_3 desorption processes are related to the desorption of molecular N_2. Here we define β_1-N and β_2-N as those N atoms which desorb as the β_1 and β_2 states, respectively. Information in ref. [44] shows that the appearance of β_2-N is a consequence of the coverage of atomic N.

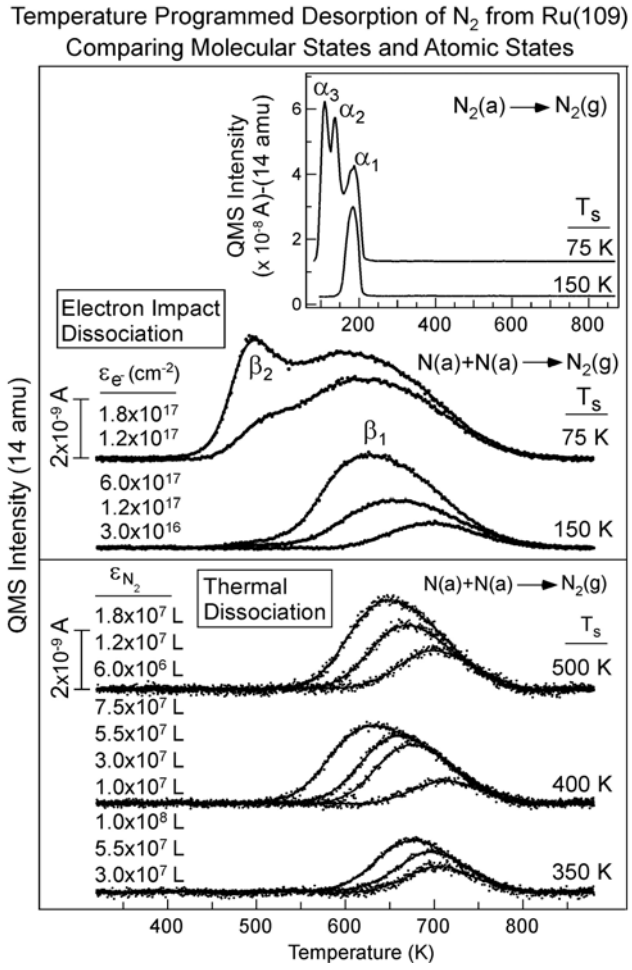

Figure 57: The TPD spectra for N/Ru(109) prepared by thermal dissociation of N_2 at 350, 400, and 500 K as well as by electron-stimulated dissociation at 75 and 150 K. The inset shows the TPD spectra for saturated N_2/Ru(109) at 75 and 150 K. 1 L(Langmuir) corresponds to the N_2 exposure (ε_{N_2}) of 3.8×10^{14} cm^{-2}.

We postulate that the β_1 process results from thermally or electron-induced N_2 dissociation producing atomic N on the step sites of Ru(109) and that the β_2 process occurs only for higher coverages of N atoms which may be artificially achieved by electron-stimulated dissociation of molecularly-bound N_2.

In separate experiments (not shown here), the selective poisoning of atomic steps on Ru(109) by carbon derived from ethylene (heated to 800K) completely suppresses thermally-activated N_2 dissociation, or β_1-N formation even at 500 K for N_2 exposures up to 10^9 L. This step-poisoning method has also been shown to block the dissociative adsorption of CO on the same Ru(109) surface [42].

5.4.2 Activation Energy Barrier for N_2 Dissociation on Ru(109)

Since the thermal dissociation of N_2 on Ru(109) generates only β_1-N, the activation energy for N_2 dissociation on the Ru steps can be obtained from the analysis of temperature-dependent dissociation rates. Figure 58 shows the Arrhenius plot of the initial dissociative sticking coefficient (S_0) of N_2 molecules on Ru(109) vs. 1/T. As shown in the inset of Figure 58, the S_0 is obtained from the initial dissociation rate of N_2, where the amount of dissociated N atoms are calculated from the measured β_1 peak area of the TPD spectra. The activation energy for the dissociation of N_2 on the Ru steps is determined to be 0.26 ± 0.05 eV. This value is slightly lower than the reported value of about 0.4 ± 0.1 eV for N_2 dissociation on random step sites present on Ru(001) (see the dotted line in Figure 58) [34].

Note in Figure 58 that the dissociation probability for Ru(109) is higher than that for Ru(001) by a factor of ~10. The number of Ru step sites estimated from the structure model is 1.72×10^{14} cm^{-2}. Assuming that the number of Ru surface atoms is 1.39×10^{15} cm^{-2}, the surface

step density is about 12 %. Since the defective step density on Ru(001) is postulated to be around 1 %, the increased dissociation probability for Ru(109) can, then, be readily related to the increased number of 'reactive sites' provided by the steps.

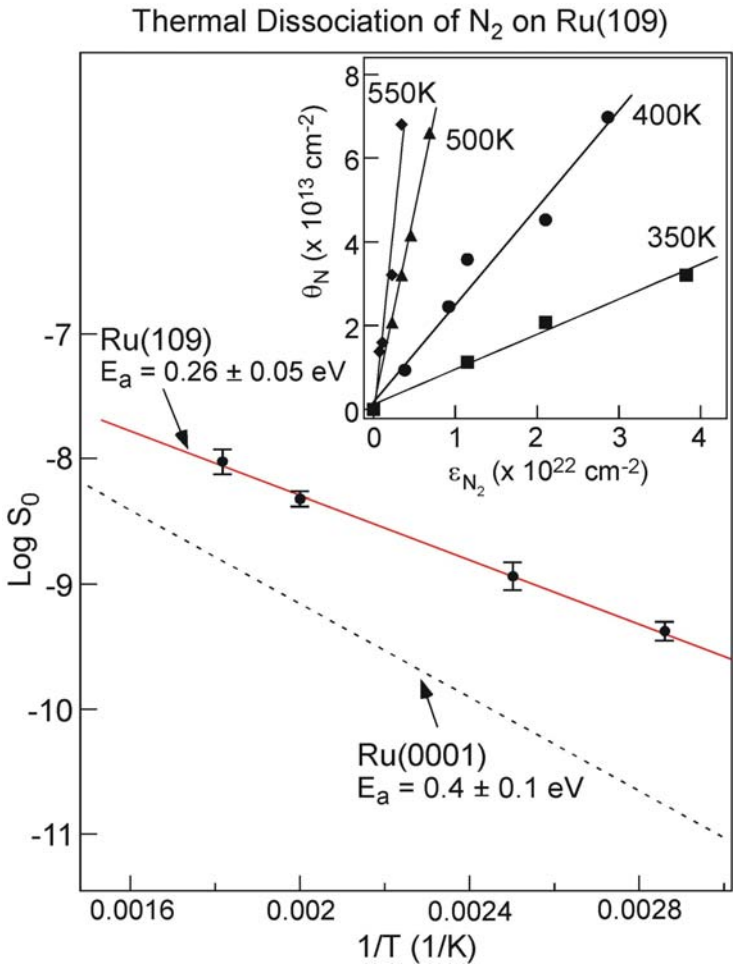

Figure 58: Arrhenius plot of the initial sticking coefficient for the thermal dissociation of N_2 on Ru(109) as a function of 1/T. The result is compared with that of Chorkendorff [34] for the Ru(001) surface, which is shown as the dotted line. The inset shows the plot of N coverage (θ_N) vs. N_2 exposure (ε_{N_2}).

The slightly lower, but apparent difference in the activation energy barrier for the Ru steps on Ru(109) may be due to the double-atom height step nature of Ru(109) compared to single-atom height steps. These may provide a more favorable dissociation channel through the formation of a more stable N_2 transient state on the Ru steps. The early report that one type of

steps are more reactive toward NO dissociation than another on Ru(001) [31] stresses the importance of step structure in a specific reaction.

5.4.3 Comparison of LEED Patterns for (β_1 (+β_2))-N/Ru(109)

Figure 59 shows a series of LEED patterns for N/Ru(109) compared to β_1- and β_2-N thermal desorption, achieved by annealing the surface at two different nitrogen coverages; that is, the one which has only the β_1 desorption state at low N coverages and the one with both β_1 and β_2 desorption states at high N coverages. The LEED measurement is performed after sequential annealing up to 200-400 K. TPD spectra taken after the LEED measurement indicate that there is no noticeable change in the spectral shape of β_1 and β_2 before and after the LEED measurement, indicating that annealing at 200-400 K does not desorb N as N_2. In the case of higher-coverage N, a half-order LEED streak is observed after annealing above 300 K (called ×2), whereas for low-coverage N, no half-order streak is apparent after 400 K annealing.

The appearance of the ×2 feature in the LEED pattern is due to the ordered 2×2-N superstructure on the terraces. This is analogous to the 2×2-LEED pattern for N/Ru(001) that has been attributed to the 2×2 ordering of N adsorbates with 1/4 ML-N coverage at room temperature [217,223]. Streaks instead of discrete spots are often observed for stepped surfaces with narrow terrace width mainly due to the poor correlation along the direction perpendicular to the rows of steps. The triplet-split integer spots running along the horizontal axis of the LEED pattern in Figure 60b are characteristic features of the stepped Ru(109) surface with ~9-atom-wide terraces separated by double-atom height steps along that direction [42].

The fact that the β_2-N is related to the ordered 2×2 superstructure from the terraces while the β_1-N is not, can be explained by a model in which β_1-N is associated with step sites and β_2-N

is associated with terrace sites forming a 2×2 ordered phase with a local saturation coverage of 1/4 ML on the terraces.

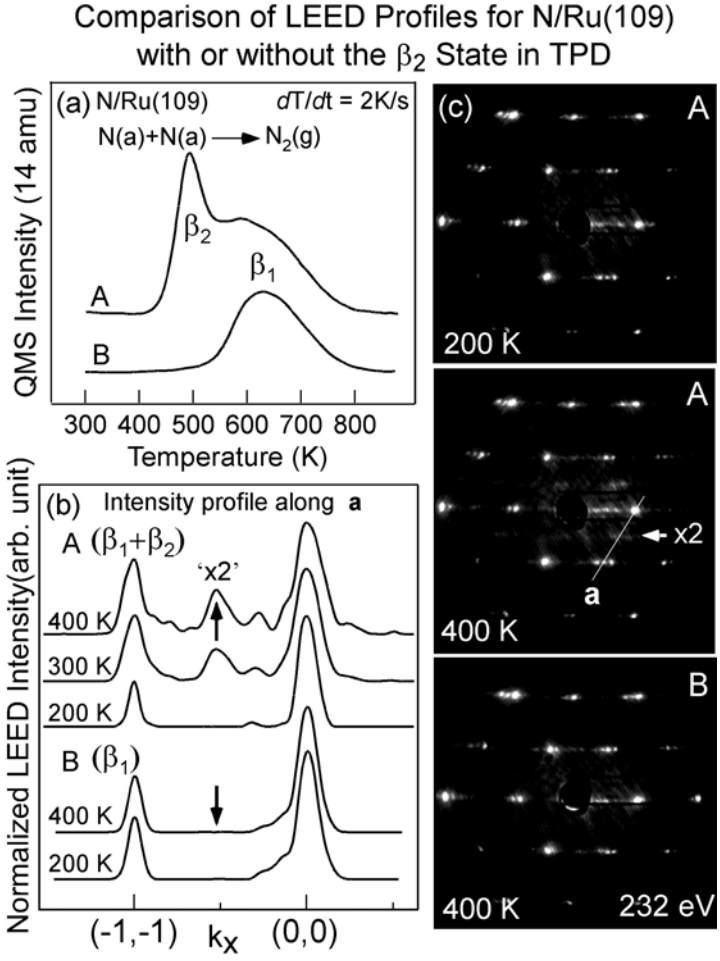

Figure 59: (a) Comparison of TPD and LEED profiles for N/Ru(109) with both states (β_1 and β_2) (A) and with only β_1 state (B). A and B are obtained by exposing e^- flux of 1×10^{15} $cm^{-2}s^{-1}$ to Ru(109) either under constant N_2 flux of 2×10^{13} $cm^{-2}s^{-1}$ for 4 min (A) or with pre-adsorbed N_2 with θ_{N2} of 1.5×10^{14} cm^{-2} for 10 min (B) at 150 K. LEED measurements in (b)-(c) are performed after subsequent annealing up to 200, 300, and 400 K, respectively.

This correlation is further confirmed in Figure 60, where the integrated intensity (Figure 60a and Figure 60d) of the β_2-N desorption feature is shown to vary monotonously with the normalized intensity of the "×2" LEED feature, and to be absent when only β_1-N species are present. These data show that the ×2 intensity is directly proportional to the population of β_2-N. All the LEED measurements in Figure 60b-c are made after post-annealing up to 400 K to let

terrace-N produce the ×2 feature in LEED. TPD spectra taken after the LEED measurements (see Figure 60a) indicate that the β_2 state increases gradually from **C** to **H**. The normalized LEED intensity profiles for **A-H** are compared in Figure 60c. In Figure 60d, the normalized ×2 peak intensities are plotted as a function of the β_2-N coverages, which are shown as hatched areas in Figure 60a.

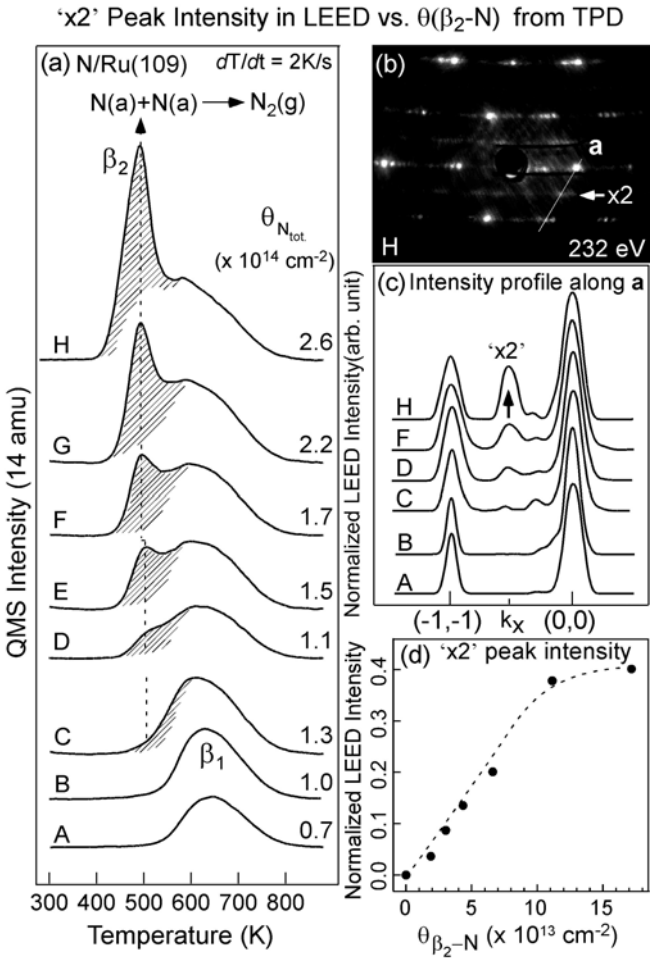

Figure 60: The TPD spectra in (a) as well as corresponding LEED profiles in (c) for N/Ru(109) with both states (β_1 and β_2). All LEED measurements are made after post-annealing at 400 K, which is followed by TPD measurement. A **and** B **are obtained by exposing** e^- **flux of** 1×10^{15} $cm^{-2}s^{-1}$ **to Ru(109) with pre-adsorbed** N_2 **with** θ_{N_2} **of** 1.5×10^{14} cm^{-2} **for 3 (**A**) and 10 (**B**) min, respectively, at 150 K or under** N_2 **flux of** 2×10^{13} $cm^{-2}s^{-1}$ **for 2, 3, 4, 6, and 10 min, respectively, for** D-H**.** C **is obtained from** B **after producing more N under the** N_2**- and** e^-**-flux for 30 s. The dotted line in (d) is to guide the eyes.**

Note also from the comparison of Figure 60a and Figure 60c that the ×2 feature in LEED is related to the β_2-N instead of the total amount of atomic N adsorbates ($\beta_1 + \beta_2$). This fact further corroborates the idea that the β_2-N is the only N adsorbate responsible for the ×2 feature in LEED. The β_1-N is not associated with the ×2 feature.

Interestingly, the β_1-N/ β_2-N ratio does not change much by thermal treatment, despite the facile diffusion of atomic N along the Ru terrace as is evident by the appearance of ×2 feature above 300 K. This may be due to a possible high kinetic barriers for the diffusion of N adsorbates between terrace and step.

5.4.4 Further Discussion on the Interaction of Dissociated N Atoms with the Step Sites

Judging from the above results, the step sites provide a more stable adsorption sites for dissociated N atoms with higher recombinative desorption barrier than the terrace sites. That is, the N atoms dissociated on the step sites are confined within the steps, instead of being diffused away to the terrace sites; LEED patterns for N/Ru(109) with only β_1-N indicate no apparent ×2 feature up to the saturation N coverage of the β_1 state. The observed strong preference of atomic N to the steps is also consistent with the early STM observation of NO dissociation on Ru(001), which showed that the dissociative adsorption of NO leaves more N on the steps while O diffuses away from the steps [31,224].

The above picture for the role of steps on Ru(109), however, is somewhat different from that of Chorkendorff *et al*. [34] for Ru(001). The defective steps on Ru(001) were suggested to be 'a low-energy barrier recombinative desorption channel of atomic N' in addition to 'a low-energy barrier N_2-dissociation channel for populating the terraces with atomic N' from the TPD

study of N/Ru(001) with Au-passivated steps [34]. Our study indicates that the steps of Ru(109) are more stable adsorption sites of N atoms as well as being specific dissociation channels for N_2 molecules. The above difference might come from a different nature of the step structure; Ru(109) has double-atom height steps, while Ru(001) does not. Combined with the fact that the N_2 dissociation takes place exclusively on the steps, however, our results suggest that the steps on Ru(109) are the 'active sites' for the whole sequence of catalytic reactions that involve the dissociation of N_2 molecules. By providing stable molecular N_2 (α_1-N_2) adsorption sites as well as the low activation barrier channel for N_2 dissociation, the step sites may be directly involved in the subsequent reaction of the dissociated N atoms causing N-H bond formation and NH_3 formation in the ammonia synthesis.

5.5 CONCLUSION

In conclusion, we have shown: (1) The N_2 dissociation on highly stepped Ru(109) is exclusively specific to the Ru steps with the activation energy barrier of 0.26 ± 0.05 eV and; (2) The dissociated N atoms are confined within the Ru steps, where the step-N atoms desorb recombinatively as the β_1 state in TPD. By employing electron-stimulated dissociation of N_2 adsorbed on Ru(109), it has been shown that the Ru terraces can also be populated with atomic nitrogen at higher N coverages, which is identified by the clearly-resolved separate desorption state (β_2) in TPD as well as the clear ×2 features in LEED, which features have not been observed for the thermal dissociation of N_2. The above experimental results shows the specific role of the Ru steps as the low-barrier N_2 dissociation channel to populate N atoms in the Ru steps, rather than the terraces.

6.0 COMPARISON OF THE ADSORPTION OF N_2 ON Ru(109) AND Ru(001) – A DETAILED LOOK AT THE ROLE OF ATOMIC STEP AND TERRACE SITES

The information contained in this chapter is based on the following research publication:

Gregg A. Morgan, Jr., Dan C. Sorescu, Yu Kwon Kim, and John T. Yates, Jr., *"Comparison of the Adsorption of N_2 on Ru(109) and Ru(001) – A Detailed Look at the Role of Atomic Step and Terrace Sites"* Surf. Sci. (2007), In Press.

6.1 ABSTRACT

We present a direct side-by-side comparison of the adsorption and desorption of nitrogen on the atomically-stepped Ru(109) surface and the atomically-flat Ru(001) surface. Both infrared reflection absorption spectroscopy (IRAS) and temperature programmed desorption (TPD) are employed in this study, along with density functional theory (DFT). We find that the chemisorptive terminal binding of N_2 is stronger on the atomic step sites than on the terrace sites of Ru(109) as indicated by TPD and by a reduction of the singleton vibrational frequency, $\nu(N_2)$, by ~ 9 cm^{-1}, comparing steps to terraces. In addition, we find that metal-metal compression effects on the terrace sites of Ru(109) cause stronger binding of N_2 than found on the Ru(001) surface, as indicated by a reduction of the terrace-N_2 singleton vibrational frequency by ~ 11

cm^{-1} when compared to the singleton N_2 mode on Ru(001). These spectroscopic results, comparing compressed terrace sites to Ru(001) sites and confirmed by TPD and DFT, indicate that N_2 bonds primarily as a σ-donor to Ru. Using equimolar $^{15}N_2$ and $^{14}N_2$, it is found that dynamic dipole coupling effects present at higher N_2 coverages may be partially eliminated by isotopically detuning neighbor oscillators. These experiments, considered together, indicate that the order of the bonding strength for terminal-N_2 on Ru is: atomic steps > atomic terraces > Ru(001). DFT calculations also show that 4-fold coordinated N_2 may be stabilized in several structures on the double-atom wide steps of Ru(109) and that this form of bonding produces substantial decreases in the N_2 vibrational frequency and increases in the binding energy, compared to terminally-bound N_2. These highly coordinated N_2 species are not observed by IRAS.

6.2 INTRODUCTION

Infrared reflection absorption spectroscopy (IRAS) is an extremely versatile tool for studying adsorbates on surfaces. The sensitivity to very small coverages of some adsorbates (< 0.01 ML) as well as a potential resolution and frequency accuracy of < 0.5 cm^{-1} makes IRAS a very useful surface probe to explore the effects of site character on the properties of adsorbed molecules. There have been extensive studies of the vibrational behavior of nitrogen adsorbed on single crystal surfaces by means of IRAS [29,119,239-242] and high resolution electron energy loss spectroscopy (HREELS) [115,228,229,243]. Regardless of the substrate, which previously has included Ni [239-242], Pt [29], Ru [115,119,228,229], and Pd [243], adsorbed N_2 typically exhibits a single vibrational band near 2200 cm^{-1} due to the N-N stretching mode.

Traditionally Fe has been used as an effective catalyst for the conversion of H_2 and N_2 to NH_3 by means of the Haber-Bosch process. There is, however, considerable interest in Ru as a viable replacement for the traditional Fe catalyst since the promoted Ru catalyst is more efficient than the Fe catalyst [113]. The Fe surface is more susceptible to blocking of the active sites by an excess of nitrogen and poisoning by traces of oxygen [113]. Significant work has already been reported on the adsorption of N_2 on Ru single crystal surfaces [34,43,44,115,116,119,218,228,229,244,245]. The atomic steps present on the Ru(109) surface have been shown to dissociate N_2 molecules with an activation energy of 25 kJ/mol [43]. This process is very likely the rate-controlling elementary step in the activation of N_2 for catalyzed reactions such as the ammonia synthesis.

This paper, which builds on our previous results on the adsorption and desorption of N_2 on the Ru(109) single crystal surface [43,44], presents a direct side-by-side comparative study of N_2 adsorption on a stepped Ru(109) single crystal surface and an atomically flat Ru(001) single crystal surface in which the experiments were performed in the same apparatus under identical experimental conditions. The Ru(109) surface presents double atom height step sites separated by 9 atom wide terraces [42] and is an ideal surface for probing the role of atomic steps on chemisorption. Significant differences are observed in both the thermal desorption as well as the vibrational spectra of the N_2 adlayer on the Ru(109) surface compared to the Ru(001) surface. The rather significant differences in the desorption and vibrational characteristics of chemisorbed N_2 on the two single crystals are attributed to the presence of the step sites on the Ru(109) surface.

The bonding of N_2 to the terrace sites on Ru(109) is stronger than the bonding on Ru(001) as indicated by the singleton frequency, which has been found to be ~11 cm^{-1} lower on

the Ru(109) surface as compared to the Ru(001) surface. This is significant because it confirms the long standing notion that N_2 is σ-bonded to the Ru surfaces, since d back-donation would be expected to show the opposite trend for the N_2 singleton frequency.

6.3 EXPERIMENTAL METHODS

All of the experiments reported here were performed in a stainless steel ultrahigh vacuum (UHV) chamber which was discussed in detail in Chapter 2. The experimental conditions are also discussed in detail in various sections of Chapter 2. The infrared reflection-absorption spectra were collected using 2 cm^{-1} resolution averaged over 2000 scans.

6.4 THEORETICAL METHODS

The adsorption properties of N_2 on the Ru(109) surface have been also investigated with first principles calculations using the Vienna *ab initio* simulation package (VASP) [190-192]. This program evaluates the total energy of periodically repeating geometries based on density-functional theory and the pseudopotential approximation. In this case the electron-ion interaction was described using the projector augmented wave (PAW) method of Blöchl [246] in the implementation of Kresse and Joubert [247]. All calculations were done using the generalized gradient approximation with the Perdew, Burke and Ernzerhof (PBE) exchange-correlation functional [248].

The Ru(109) surface and the adsorption of N_2 molecules on this surface have been simulated using a symmetric slab model as indicated in Figure 61. The simulation supercell contains two surface units along the <010> direction in order to minimize the lateral interactions between adsorbates in the neighboring unit cells. In this model there are 84 atoms distributed over six layers parallel to the (001) terrace. A vacuum width of at least 13 Å (see Figure 61) separates the neighbor slabs along the <109> direction. Our slab model also considers periodic double Ru atom height step sites separated by 9 atom wide smooth Ru(001) terraces. This model is consistent with previous experimental results [42] which indicate the existence of double atom height steps due to reconstruction of the Ru(109) surface.

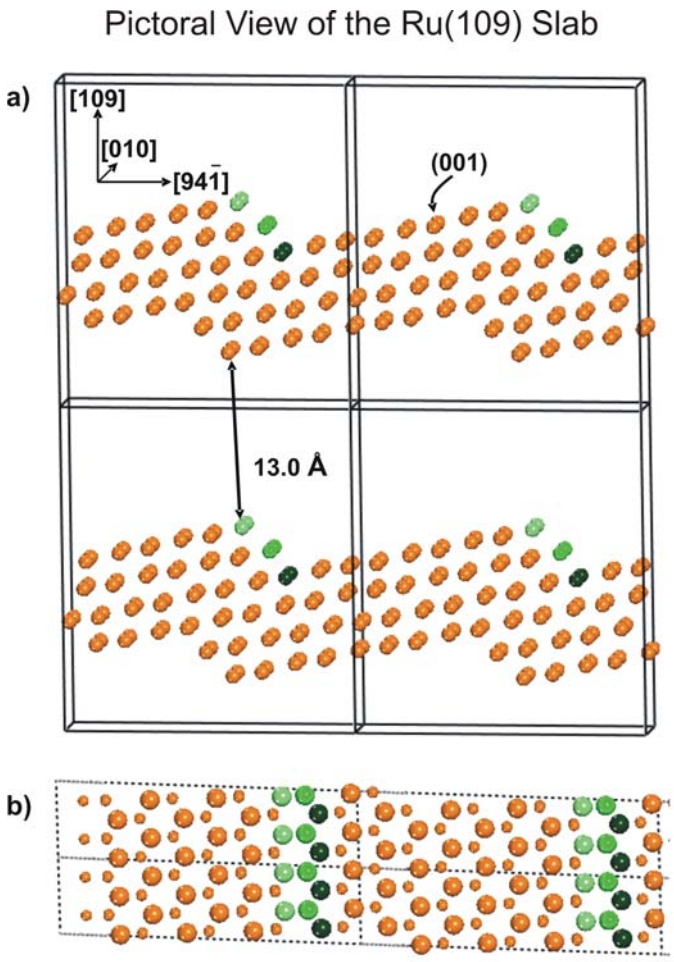

Figure 61: (a) Side and (b) top views of the Ru(109) slab model used in calculations. The model contains double Ru atom height step defect sites separated by 9 atom wide smooth Ru(001) terraces. The atoms at the step sites have been colored in different tones of green with the darker atom representing the bottom of the step. The top view indicated in b) is represented in a direction perpendicular to the (001) terrace. In this case the size of the atoms in the top layer is increased relative to atoms at deeper layers for additional clarity.

The optimizations were performed by relaxing the coordinates of the adsorbate species and of the Ru atoms in the first three layers of the slab (measured perpendicular to the (001) terrace). The remaining atoms of the slab were frozen at the bulk optimized positions. Periodic boundary conditions were used, with the one electron pseudo-orbitals expanded over a plane wave basis set with a cutoff energy of 400 eV and a 1 × 5 × 1 Monkhorst-Pack grid of k-points

[198]. Electron smearing was employed via the Methfessel-Paxton technique [195], with a smearing width consistent with $\sigma = 0.1$ eV. All energies were extrapolated to T = 0 K.

For the optimized adsorbed configurations we evaluated the corresponding N_2(a) vibrational frequencies. This has been done under the frozen phonon mode approximation in which the metal atoms were fixed at the relaxed geometries. The Hessian matrix has been determined based on a finite difference approach with a step size of 0.02 Å for the displacements of the individual atoms of the adsorbate along each Cartesian coordinate. By diagonalization of the mass-weighted Hessian matrix the corresponding frequencies and normal modes have been determined. No scaling of the calculated vibrational frequencies has been used either for the gas phase or for the adsorbed molecular species.

The computational method described above has been first tested by predicting the equilibrium properties of bulk Ru and of the isolated N_2 molecule. Based on a gamma centered k-point mesh of 15 × 15 × 6 we have determined the optimized equilibrium constants for bulk Ru of a_0=2.7258 Å, c_0=4.2987 Å (c_0/a_0 = 1.577). These values compare well with experimental values of a_{0exp}=2.7058 Å, c_{0exp}=4.2816 Å (c_0/a_{0exp}=1.582), respectively [201]. Similarly, based on optimizations of the isolated N_2 molecule in a cubic box of 12 Å side we have determined an equilibrium bond length of 1.117 Å and a vibrational frequency of 2428 cm^{-1} using the harmonic approximation. These values are also very close to those of 1.11 Å and 2413 cm^{-1}, reported previously by Mortensen et al. [244] based on PW91 DFT calculations. The calculated N-N equilibrium bond length agrees very well with the experimentally determined bond length of 1.098 Å, but the experimentally determined vibrational frequency of 2359 cm^{-1} is much lower than the calculated vibrational frequency [201].

As a final test we have analyzed the adsorption energy and vibrational frequency of the N_2 molecule on the Ru(001) surface at low coverages. This set of calculations has been performed by using a (4x4) and a (3x3) surface supercell model with six Ru layers and a vacuum width of 14 Å. The N_2 molecule has been placed on one side of the slab and optimizations included both the adsorbate and the Ru atoms in the top two layers of the slab. Our calculations indicated only small variations in this regime of low coverages. Specifically the binding energy decreases slightly from 53.72 kJ/mol at θ_{N_2} = 0.063 to 52.97 kJ/mol at θ_{N_2} = 0.11. Correspondingly, the N-N vibrational frequency shifts from 2211 cm^{-1} (θ_{N_2} = 0.063) to 2209 cm^{-1} (θ_{N_2} = 0.11). These binding energies are close to the value of 45.28 kJ/mol at θ=1/4 ML reported by Mortensen et al. [244]. Also, our calculated vibrational frequency at θ_{N_2} = 0.063 resembles very well the experimental measurements as will be detailed later in this manuscript.

The good agreement obtained between our results related to bulk properties of the Ru crystal, the isolated N_2 molecule, or N_2 adsorbed on the Ru(001) surface with either experimental values or other high-level first principles calculations gives us confidence in pursuing the next step of our study, namely the theoretical investigation of the interactions of the N_2 molecule with the Ru (109) surface.

6.5 EXPERIMENTAL RESULTS

6.5.1 Temperature Programmed Desorption Measurements

The desorption of the $^{14}N_2$ from the Ru surfaces was studied by means of TPD and the results are shown in Figure 62. The desorption characteristics of $^{14}N_2$/Ru(109) have been previously discussed in detail and the results are reported elsewhere [44].

The N_2 desorbs in three distinct processes (α_1-, α_2-, and α_3-N_2) from the Ru(109) surface. The α_1- feature develops initially with a maximum desorption temperature near 195 K and gradually shifts downward to 184 K as the coverage increases up to $\theta_{N_2} = 0.11$. As the coverage continues to increase, a second desorption feature, α_2, develops near 154 K and shifts to 136 K as the coverage approaches $\theta_{N_2} = 0.28$. As the coverage nears saturation, $\theta_{N_2} = 0.37$, a third desorption feature, α_3, develops at 115 K. The high temperature α_1-feature is due to molecular desorption from the step sites, whereas the α_2-N_2 and α_3-N_2 features are due to the molecular desorption from the terrace sites [44].

The TPD spectra for $^{14}N_2$/Ru(001) are significantly different from the TPD spectra for $^{14}N_2$/Ru(109), even though there are still three desorption features, which will be termed α_1-, α_2, and α_3- in accordance with the nomenclature used for the Ru(109) surface. The α_1-N_2 desorption feature from Ru(001) is relatively small compared to that on the Ru(109) surface and is probably due to adsorption on random defect sites. In addition to this most obvious difference in the α_1-N_2 coverage, there are also subtle differences between the N_2 desorption spectra from the Ru(109) and Ru(001) surfaces. At the lowest coverage, the α_1-N_2 species desorbs from Ru(001) with a maximum desorption temperature of 176 K. The α_2-N_2 feature also develops

from the lowest coverage on Ru(001) and the maximum desorption temperature shifts from 138 K to 125 K at θ_{N_2} = 0.31 when the α_2-feature saturates. The α_3- desorption feature again only develops as the N_2 coverage nears saturation (θ_{N_2} = 0.39) and desorbs with a maximum desorption temperature of 92 K. The area of the α_1- and α_2-features relative to the total area of the desorption trace is plotted in the insets of Figure 62. The inset in Figure 62a clearly shows that on Ru(109) the α_1-state develops initially and after saturation of the α_1-state, the α_2-feature then begins to develop. However on the Ru(001) surface the α_1- and α_2-desorption processes occur simultaneously as shown in the inset in Figure 62b.

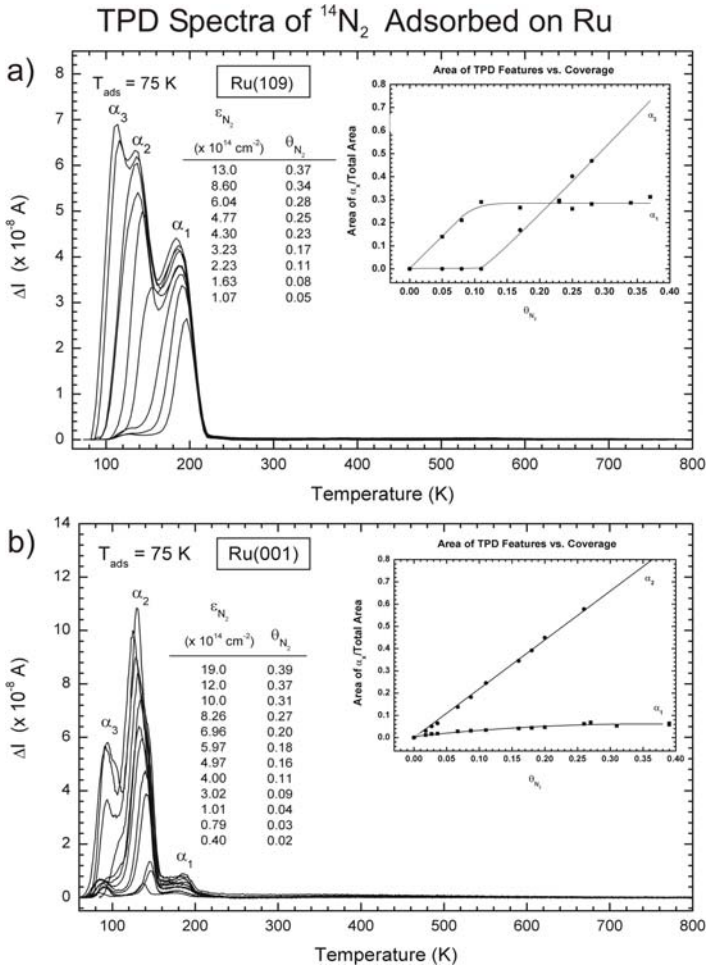

Figure 62: Temperature programmed desorption spectra of $^{14}N_2$ adsorbed on (a) Ru(109) and (b) Ru(001) at 75 K. The area of the α_1 and α_2 features relative to the total desorption area is plotted as a function of coverage in the insets of both sets of desorption traces. The heating rate was 2.0 ± 0.1 K/s.

6.5.2 IR Spectral Development

6.5.2.1 N_2-Ru(109)

The development of the infrared reflection absorption spectra for $^{14}N_2$ adsorption on Ru(109) and Ru(001) at 75 K with increasing N_2 coverages is shown in Figure 63a and Figure 63b, respectively. The data in Figure 63a have been reported previously [44] and are shown here for convenience in making comparisons between Ru(109) and Ru(001). It is noted that a single infrared band is observed for all coverages of N_2 during adsorption at 75 K on both the stepped Ru(109) surface (Figure 63a) and the atomically smooth Ru(001) surface (Figure 63b). The vibrational frequency of this N-N band shifts downward from 2203 cm^{-1} (singleton frequency) at low coverages to 2197 cm^{-1} at saturation coverage on the Ru(109) surface. In the coverage range $\theta_{N_2} = 0.102 \rightarrow \theta_{N_2} = 0.372$, the absorption band sharpens and moves upward in frequency from 2197 cm^{-1} to 2198 cm^{-1} at $\theta_{N_2} = 0.253$ before moving downward to 2197 cm^{-1} at $\theta_{N_2} = 0.372$.

In addition to the small shift in the frequency of the band, the spectral shape of the band for N_2/Ru(109) also changes as the coverage is increased. Up to a coverage of $\theta_{N_2} = 0.102$ the band is broad (FWHM, full width at half maximum = 10-14 cm^{-1}), but at coverages higher than $\theta_{N_2} = 0.16$ the band narrows down to ~7-8 cm^{-1}. The broad peak at low N_2 coverages may reflect occupancy of multiple adsorption sites; i.e. the step and the terrace sites.

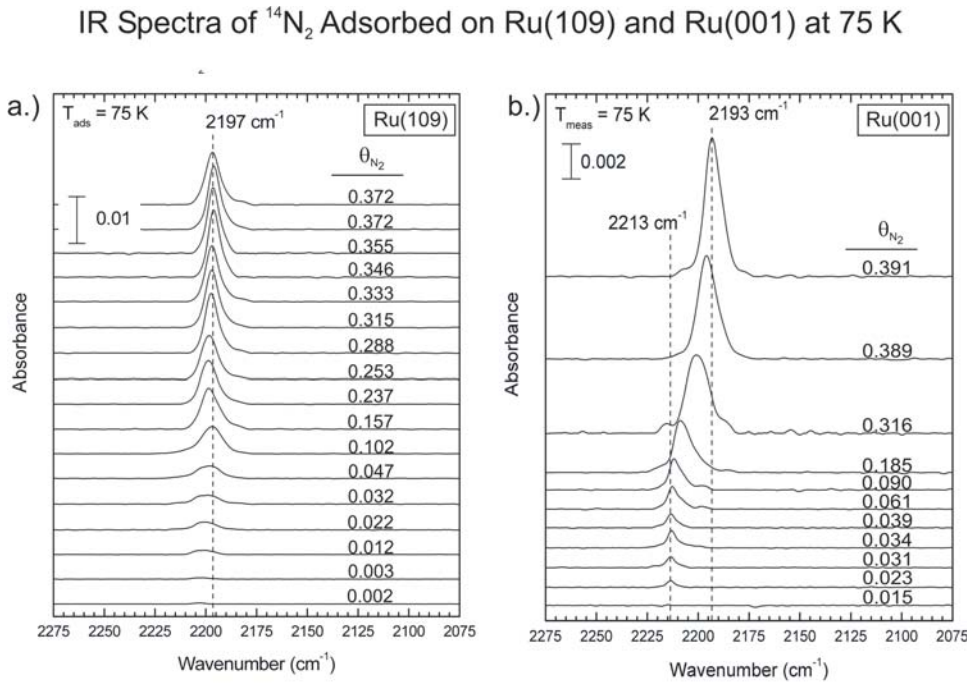

Figure 63: Infrared spectra of $^{14}N_2$ after adsorption on (a) Ru(109) and (b) Ru(001) at 75 K. The resolution is 2 cm^{-1} with each spectrum being averaged over 2000 scans. θ_{N_2} values are given relative to the available Ru surface atoms, 1.37 × 10^{15} cm^{-2} for Ru(109) and 1.57 × 10^{15} cm^{-2} for Ru(001).

6.5.2.2 N_2-Ru(001)

On the Ru(001) surface the lowest detectable coverage of nitrogen has a vibrational frequency of 2213 cm^{-1} (singleton frequency), which decreases to 2193 cm^{-1} as the coverage reaches saturation. The coverage induced shift of the N-N vibrational band on Ru(001) is roughly -20 cm^{-1}, whereas on Ru(109) the overall shift was only -5 cm^{-1} or so.

Up to a coverage of θ_{N_2} = 0.039 on Ru(001), the N_2 vibrational band is much narrower (FWHM < 5.5 cm^{-1}) than the N_2 vibrational band at low coverage on Ru(109). As the coverage on the Ru(001) surface increases, the FWHM gradually increases up to a FWHM of about 10 cm^{-1} at saturation coverage.

6.5.3 IR Spectral Changes Accompanying Thermal Depletion of Chemisorbed N_2

6.5.3.1 N_2-Ru(109)

Starting with near saturation coverage of nitrogen (θ_{N_2}= 0.330 for Ru(109) and θ_{N_2}= 0.340 for Ru(001)) each layer was heated at 2.0 K/s to a designated temperature. Following the programmed heating, the crystal was immediately cooled to 90 K over a period of 1-2 minutes and the infrared spectrum was measured. The resulting N_2 coverage after the partial desorption was determined by the area of the TPD spectra taken after the infrared measurements. Figure 64a and Figure 64b shows the results of the sequential IRAS measurements. At high N_2 coverage, a single N-N vibrational band appears at ~2198 cm^{-1} (following adsorption at 90 K) for adsorption on Ru(109). As the N_2 is partially depleted by heating to 105 K the band begins to broaden from an initial FWHM of 7.5 cm^{-1} to 8.7 cm^{-1}.

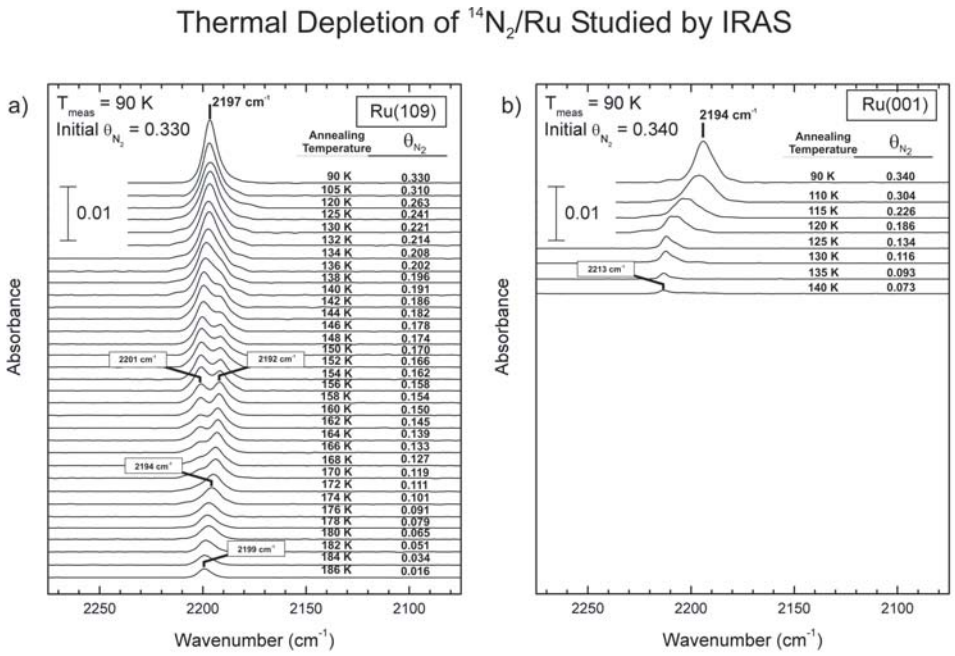

Figure 64: Thermal depletion of (a) $^{14}N_2$/Ru(109) and (b) $^{14}N_2$/Ru(001) studied by IRAS. The resolution is 2 cm^{-1} with each spectrum being averaged over 2000 scans. The nitrogen adlayer was readsorbed prior to each thermal depletion experiment and each spectrum is recorded at 85 K. The coverage of nitrogen was determined from TPD measurements following temperature programming to the indicated temperature.

Above 120 K, the FWHM increases to ~11 cm^{-1} and remains relatively constant until the formation of a doublet feature is first clearly observed around 138 K (θ_{N_2} = 0.196). The low frequency component (~2192 cm^{-1}) of the doublet initially develops as a shoulder on the high frequency peak (~2199 cm^{-1}) at θ_{N_2} = 0.202. This shoulder continues to develop into a well-resolved feature as the annealing temperature is increased stepwise, causing a continued depletion of the N_2 adlayer. At a coverage of θ_{N_2} = 0.154 (achieved by heating to 158 K) the two vibrational bands (2201 cm^{-1} and 2192 cm^{-1}) of the doublet are nearly equal in intensity. The high frequency mode begins to decrease in intensity as the coverage is further depleted by additional heating, while the low frequency mode shifts to higher frequency. By 168 K (θ_{N_2} = 0.127) the high frequency mode is no longer detectable in the IR spectrum. The low frequency

mode continues to shift higher in frequency and to lower integrated absorbance as the coverage is decreased. Even after heating up to 186 K (θ_{N_2} = 0.016), there is evidence of a small amount of molecular nitrogen remaining on the surface with a vibrational frequency near 2199 cm^{-1}. The observation of the spectroscopic behavior of chemisorbed N_2 agrees with our TPD measurements (Figure 62a), which indicate that on Ru(109) N_2 continues desorbing until ~200 K.

6.5.3.2 N_2-Ru(001)

For Ru(001), the spectral developments during N_2 depletion differ significantly from those observed for Ru(109). At near saturation coverage, θ_{N_2} = 0.34, the N-N vibrational band has a frequency of 2194 cm^{-1}. This band gradually shifts upward in frequency to about 2213 cm^{-1} at θ_{N_2} = 0.073. Initially the band has a FWHM of about 10 cm^{-1} and the band broadens to about 15 cm^{-1} at θ_{N_2} = 0.226. As the coverage continues to decrease as the adlayer is heated to higher temperatures the vibrational band narrows down to 5 cm^{-1}. In the low coverage limit, the singleton frequency is 2213 cm^{-1}. Significantly, the formation of two IR bands is not observed for Ru(001) during depletion of the N_2 adlayer.

6.5.4 Vibrational Frequency Comparison of Ru(109) and Ru(001)

The change in the vibrational frequency of the two IR modes as the coverage decreases is plotted in Figure 65a for Ru(109) and in Figure 65b for Ru(001). For Ru(109), the frequency prior to the observation of the doublet remains relatively constant (near 2197 cm^{-1}) until the coverage decreases to θ_{N_2} ~ 0.20. At this point, the two IR components begin to be resolved, and as coverage decreases both modes shift upward in frequency. In Figure 65b, on Ru(001), a gradual

upward shift occurs in the frequency of the single mode as the coverage of N_2 is thermally depleted. It is immediately evident that the shift in the $\nu(N_2)$ as the coverage decreases to zero is $\sim +5$ cm^{-1} for terrace-bound N_2 on Ru(109) compared to $\sim +20$ cm^{-1} for N_2 on Ru(001)

Measurements of CO production, by means of TPD and residual oxygen impurity by AES indicate that neither C nor O impurities (< 1% ML level) could interfere significantly with the infrared results for chemisorbed N_2. The IR spectra do not reveal the small coverage of CO contaminant detected by TPD.

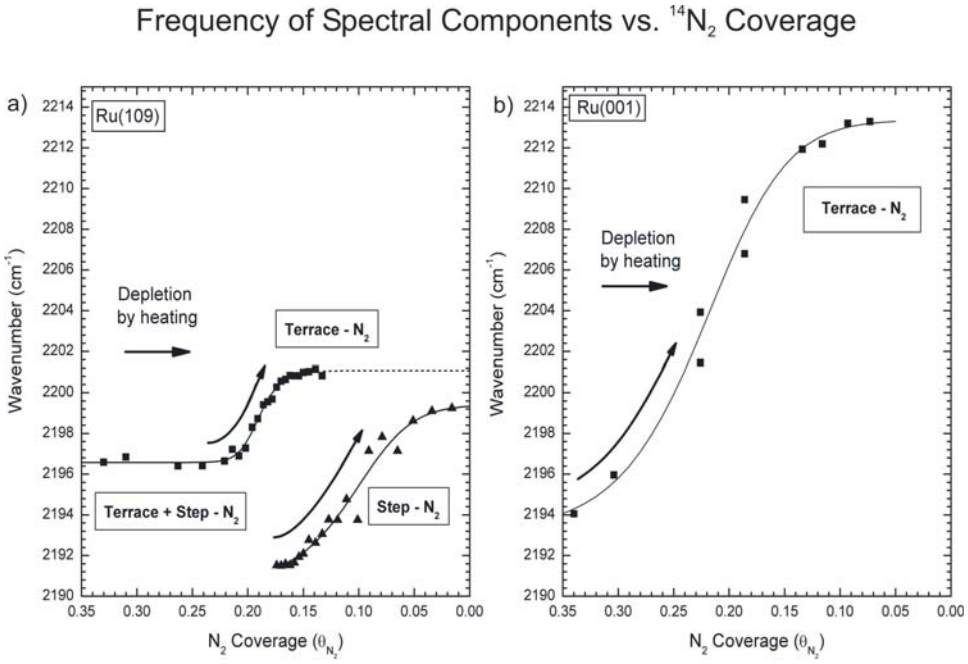

Figure 65: The change in the frequency of the vibrational bands as the sample is heated to increasing temperatures is plotted against the coverage of nitrogen remaining on the surface for (a) Ru(109) and (b) Ru(001).

6.5.5 Temperature Programmed Desorption Measurements After Heating

Some of the TPD spectra taken after the IR measurements in Figure 64 are shown in Figure 66a and Figure 66b for Ru(109) and Ru(001), respectively. The desorption of N_2 from both surfaces

following the partial desorption from the adlayer is nearly identical to the TPD spectra for equivalent N_2 coverages obtained following the adsorption of N_2 at 75 K.

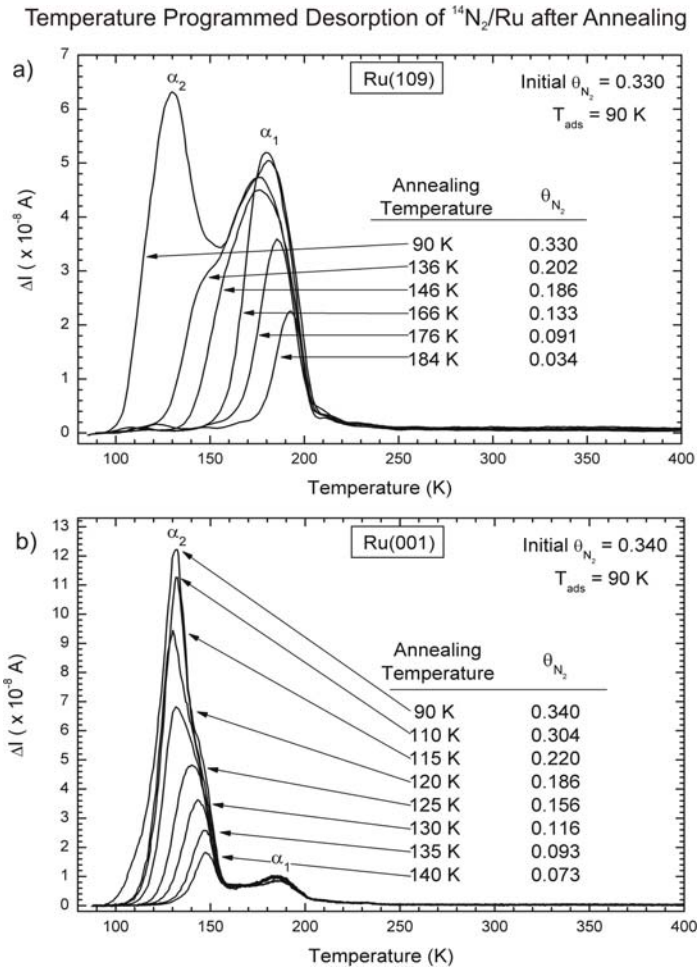

Figure 66: Temperature programmed desorption spectra of N_2 adsorbed on (a) Ru(109) and (b) Ru(001) at 90 K and annealed to various temperatures. The heating rate is 2.0 ± 0.1 K/s. The TPD trace of mass 14 was measured so as to avoid interference for the 28 amu signals due to low levels of CO adsorption (< 1% of a ML).

6.5.6 Comparison of Isotopic N_2 Vibrational Spectra in Pure and Isotopically Mixed Layers on Ru(109)

The vibrational frequencies of the isotopic species on Ru(109) for pure $^{14}N_2$ or $^{15}N_2$ layers have been compared with the frequencies for each isotopomer in a 50% - 50% mixture of isotopes.

Small differences will indicate weak coupling effects which are expected to differ for $^{14}N_2$-$^{14}N_2$, $^{15}N_2$-$^{15}N_2$, and $^{14}N_2$-$^{15}N_2$ interactions due to frequency mismatching in the 50% - 50% isotopomer mixture. Since molecules of the same isotopic identity (i.e. vibrational frequency) will couple strongly with each other, partial vibrational decoupling can be attained by using isotopic mixtures [151].

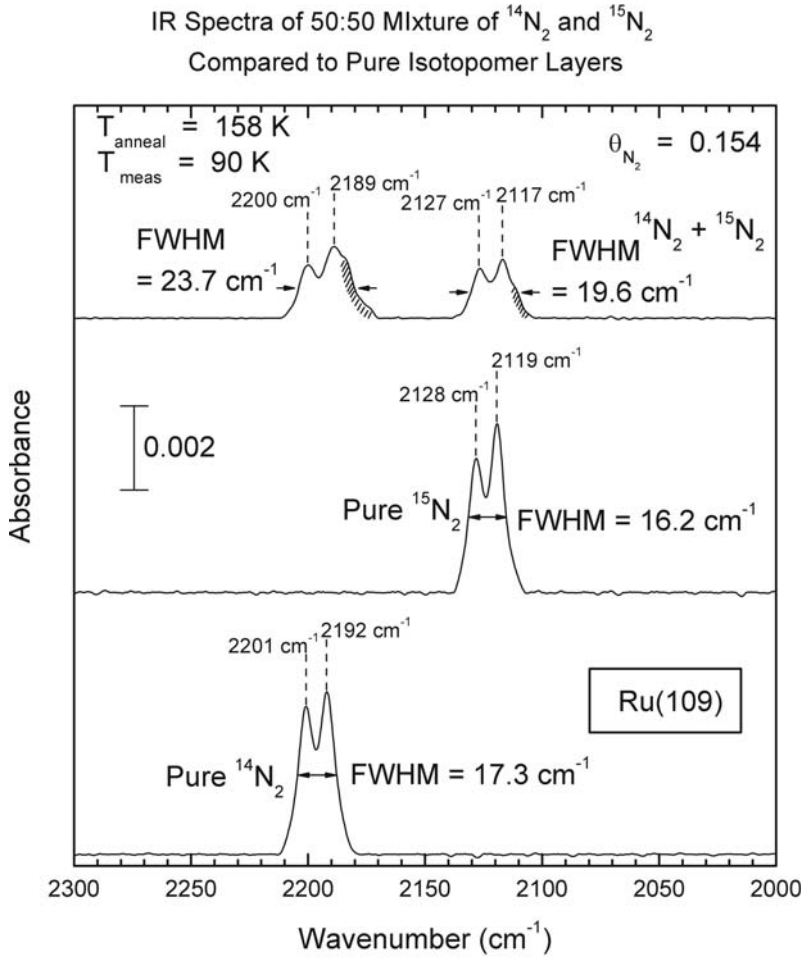

Figure 67: Infrared spectra of $^{14}N_2$, $^{15}N_2$, and a 50:50 mixture adsorbed on Ru(109) and heated to 158 K. In order to calculate the FWHM of the doublet features the maximum of the doublet was determined by averaging the absorbance height of the two peaks, and the widths are determined at one-half of the average absorbance. The resolution is 2 cm^{-1} with each spectrum being averaged over 2000 scans.

Figure 67 shows a comparison of the pure isotopic layer to the mixed isotopomer layer at identical surface coverages on Ru(109). The surface condition shown in Figure 67 has been

achieved by heating the fully-covered surface to 158 K where the full development of the doublet infrared spectrum is observed as shown in Figure 64a. Because of overlap of the various spectral features in the $^{14}N_2$ + $^{15}N_2$ mixture, the frequencies of the sharp absorption peaks observed in the experimental spectra are employed in our analysis. We observe three key spectroscopic characteristics of the $^{14}N_2$ + $^{15}N_2$ mixture compared to the pure isotopomer mixture: (1) Modes centered midway between the pair of doublets are not present, indicating that no $^{14}N^{15}N$ species due to dissociation and recombination are present on the surface. The lack of such spectroscopic features also indicates the absence of strongly asymmetric and symmetric coupled modes involving pairs of N_2 molecules on a single Ru atom ($^{14}N_2$-Ru-$^{15}N_2$) on the surface; (2) The four prominent vibrational modes for the $^{14}N_2$ + $^{15}N_2$ mixture are 1-3 cm^{-1} lower in frequency than the comparable frequencies in the pure isotopomer layer; (3) The $^{14}N_2$ + $^{15}N_2$ layer exhibits low frequency shoulders on the $^{14}N_2$ and $^{15}N_2$ spectral components as shown by the cross hatching, as well as by the increased FWHM of the composite spectral features.

6.5.7 Displacement of Adsorbed N_2 by CO on Ru(109)

A saturated layer of N_2 molecules was adsorbed on the Ru(109) surface and then annealed to 158 K to produce the characteristic doublet feature in the infrared spectra. The preferential displacement of N_2 by the sequential addition of CO to this N_2 adlayer was observed spectroscopically and the results are shown in Figure 68. CO is more strongly bound to Ru(109) than is N_2 and will therefore displace the adsorbed N_2 species [228]. From the series of IR spectra taken after successive additions of CO it is seen that the peak absorbance of both spectral features diminish simultaneously. Note the higher rate of reduction of the high frequency

spectral feature as shown in the insert of Figure 68. The concomitant development of the ν(CO) mode is observed in the 2000 cm^{-1} region.

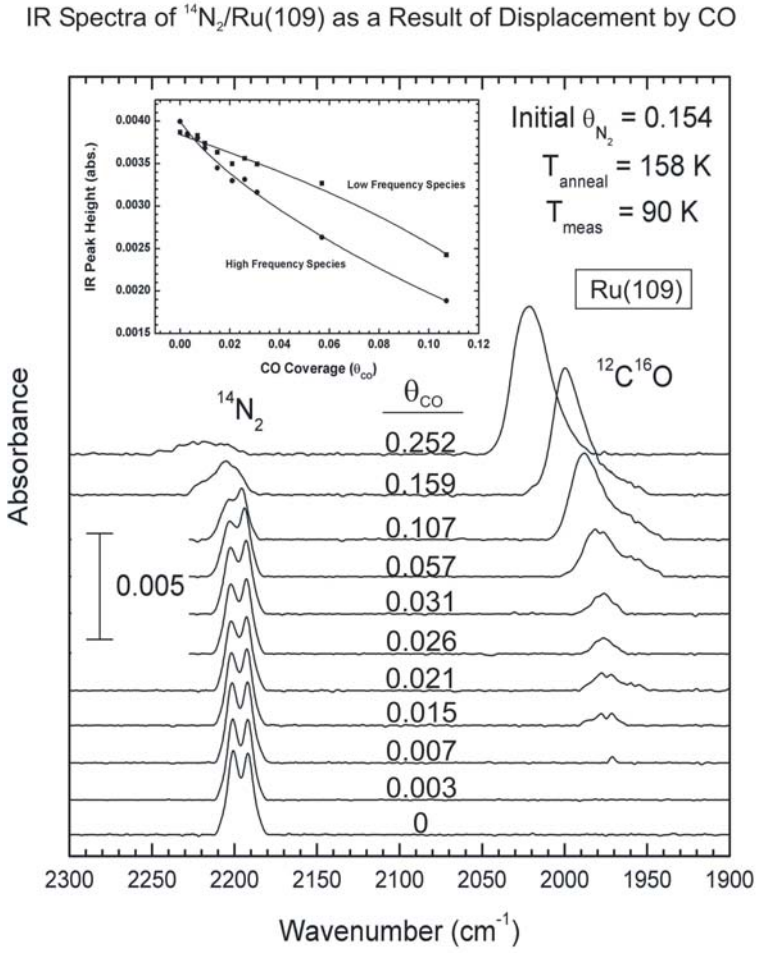

Figure 68: Infrared spectra of $^{14}N_2$ adsorbed on Ru(109) and heated to 158 K. Following heating, the surface was exposed to small, increasing amounts of CO. The resolution is 2 cm^{-1} with each spectrum being averaged over 2000 scans. The inset shows the change in the peak absorbance of each of the peaks of the doublet as the coverage of CO increases.

6.6 THEORETICAL RESULTS

Characterization of the chemisorption properties of N_2 molecules on Ru(109) surface has been performed theoretically using the $Ru\left[[94\bar{1}]x2[010]\right]$ slab model described in Section 6.4 (see Figure 61). For all the results reported in this work the adsorption energies were calculated based on the expression

$$E_{ads} = E_{molec} + E_{slab} - E_{(molec+slab)} \tag{6.1}$$

6.6.1 Adsorption and Vibrational Properties of N_2 on Ru(109) Terraces

The calculated binding energies and the vibrational frequencies for an N_2 molecule adsorbed at each site of the Ru(109) terrace are summarized in Figure 69. We have determined that in the case of sites 2-8 of the (001) terrace (see Figure 69c) the N_2 molecule adsorbs perpendicular to the surface at distances ranging from 1.971-1.989 Å. In these cases the equilibrium N-N bond distances have similar values in the range 1.134-1.135 Å. One such representative configuration corresponding to adsorption at site # 4 is indicated in Figure 69c. Additional configurations exist in which N_2 is singly and multiply bound in various ways to the step sites of the Ru(109) crystal (designated S1, S2 , S3, and S4).

The variation of the binding energies for the individual adsorption sites along the terrace sites is detailed in Figure 69a. From the data it appears that some variation in the binding energies exists along the terrace, particularly for the edge sites of the terrace. Specifically, we found that the edge sites of the terrace, i.e. sites # 1, # 2, and # 8, have smaller binding energies than the middle sites 3-7 where a fairly narrow energy distribution in the range 57.3-59.0 kJ/mol is observed. We note that these values compare very well to the theoretically calculated binding

energy of 58.83 kJ/mol reported previously by Mortensen et al. [244] in the case of N_2 adsorption at θ_{N_2} =1/3 coverage on the Ru(001) surface. Based on these results it can be concluded that the molecule will possibly preferentially occupy the middle sites; i.e. 3-7, which have the highest binding energies of the terrace sites.

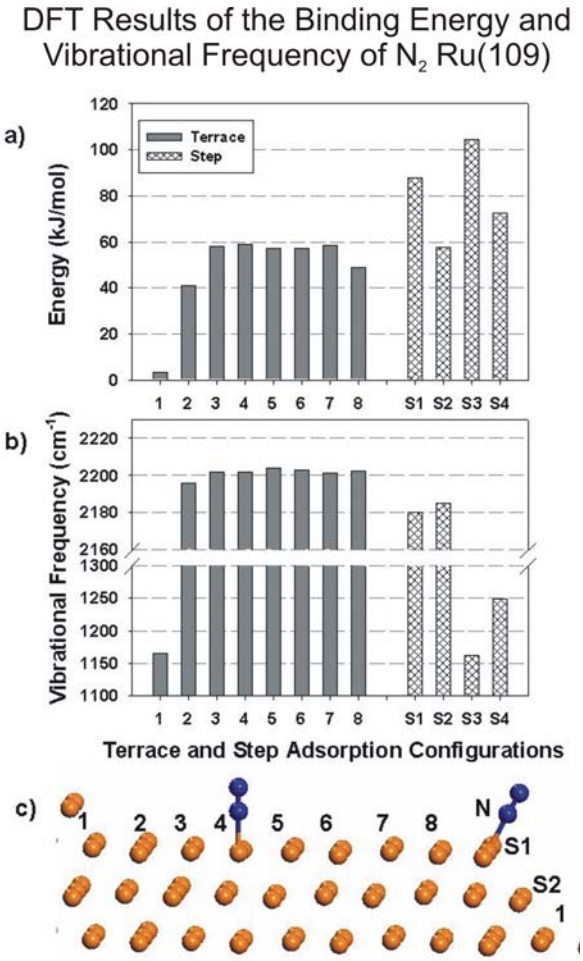

Figure 69: Variation of the (a) binding energies and (b) vibrational frequencies of N_2 molecule adsorbed at different surface sites on Ru(109) surface. Labels 1-8, and S1, S2 correspond to individual sites along (001) terrace and along the double step, respectively. Labels S3 and S4 denote the 4-folded binding configurations of the N_2 molecule adsorbed along the step with orientations perpendicular, and parallel, respectively, to the <010> direction as shown in Figure 70. Figure 69c illustrates two representative adsorption configurations, i.e. on the terrace at site #4 and at the step site (S1) as obtained from independent calculations.

Consistent with the small variation of the N-N bond distances, we found there is little change in the ν(N-N) stretching frequencies, particularly for the case of the most stable adsorption sites on the terrace. In such instances the vibrational frequencies were found to vary slightly from 2201.5 - 2203.0 cm^{-1} (as indicated in Figure 69b).

6.6.2 Adsorption and Vibrational Properties of N_2 on Ru(109) Step Sites

The second set of adsorption configurations investigated in this study corresponds to adsorption of an N_2 molecule at step sites on the Ru(109) surface. In this case we have identified two main categories of states, among which the most stable are depicted in Figure 69c (configuration S1) and Figure 70 (configurations S2, S3 and S4).

In the first group, corresponding to states S1 and S2, the molecule adopts a tilted configuration relative to the (001) plane and binds by one end to the surface. The difference between these two states is the location of the Ru atom involved in molecular bonding, positioned at the top or the middle of the step, respectively. In the second group, represented by states S3 and S4, the molecule binds parallel to the step surface with the molecular axis perpendicular and parallel, respectively, to the <010> crystallographic direction. In these cases both ends of the molecule are involved in bonding leading to the formation of four Ru-N bonds.

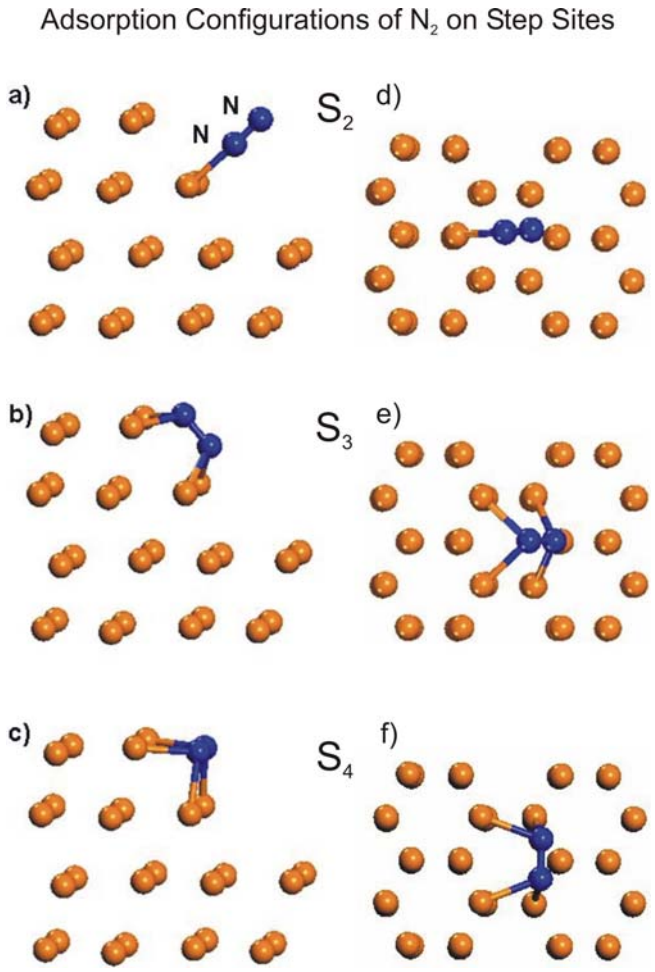

Figure 70: Lateral and top view (perpendicular to the 001 terrace) of the adsorption configurations of N_2 at the double step corresponding to (a) and (d) site S2 and (b) and (e) S3 configuration which is parallel to the step plane and perpendicular to the <010> direction and (c) and (f) S4 configuration which is parallel to the step plane and parallel to the <010> direction. In the S3 and S4 configurations the molecule is bonded to four neighbor surface atoms.

The binding energies for states S1-S4 are also represented in Figure 69a. The largest energies are obtained for the case of state S1 with a binding energy of 87.45 kJ/mol and for the state S3 with a binding energy of 104.60 kJ/mol. By comparing these values to the results obtained for adsorption on the terraces it can be seen that binding at step sites is more favorable than binding at the terrace sites.

Adsorption at the step sites also leads to more pronounced modifications of the N-N bond distances than those observed for the terrace sites. For example, we found that N-N equilibrium

bond distance increases to 1.138 Å for the case of the S1 state while bond lengths as large as 1.286 Å and 1.265 Å are obtained for S3 and S4 states, respectively. Concurrently with these geometric changes the N-N vibrational frequencies are red shifted relative to the vibrations at terrace sites. Specifically, for the S2 state the vibrational frequency is 2180 cm^{-1} while significantly lower frequencies of 1162 cm^{-1} and 1249 cm^{-1} are obtained for states S3 and S4, respectively. Both these geometric and spectral changes indicate a weakening of the N-N bond upon adsorption at the step sites relative to the terrace sites. This is particularly the case for the most stable configuration we have identified at the step sites, i.e. state S3, which is a good candidate for molecular dissociation with the formation of adsorbed N species. A final point we have analyzed is the variation of the binding energy in the case when both S1 and S3 states are populated. In this case, due to the close proximity of the two N_2 molecules which share a common Ru atom the average binding energy of the N_2 molecule decreases to 77.40 kJ/mol indicating the existence of repulsive interactions. This important decrease of the binding energy, particularly relative to the energy of the S3 state, indicates that simultaneous population of both S1 and S3 states is very unlikely.

Based on the results obtained in this and the previous sections it can be concluded that in the regime of low temperatures, adsorption on both the terrace and step sites is possible. By the increase in temperature the steps should become the most populated due to the increased N_2 stability on steps relative to terrace sites. Consistent with this temperature evolution, the N-N vibration signature will be modified from values in the range 2201-2203 cm^{-1} as seen for adsorbed species on the terrace, to 2180 cm^{-1} or even lower to 1162 cm^{-1}, corresponding to the adsorbed species at the step sites. The multiply-bound species corresponding to the S3 and S4

configurations in Figure 70 would not have been observed experimentally because of the surface dipole selection rule in reflection IR [151].

6.7 DISCUSSION

6.7.1 Desorption Energies of N_2 on Ru(109) and Ru(001)

Three separate desorption processes, α_3-; α_2-; and α_1-, for weakly-bound N_2 molecules on Ru(109) have been observed here and in previous work [44]. The α-N_2 species have all been shown to be molecular since they do not undergo isotopic mixing ($^{14}N_2 + {}^{15}N_2 \rightarrow 2\ {}^{14}N^{15}N$) on Ru(109) [44]. Among them, the α_1-N_2 state is attributed to the desorption of nitrogen from the Ru step sites since the α_1 –N_2 species is only observed on the stepped Ru surface and not on the atomically flat Ru(001) surface in this work and in studies from other laboratories [228,230], whereas the α_2 and α_3 species are attributed to desorption from the terrace sites. The small α_1 – N_2 desorption feature on the Ru(001) surface can be attributed to the small percentage of random atomic step sites present on the Ru(001) surface due to crystal misorientation. The coverage of N_2 desorbing as α_1 corresponds to 5.39×10^{13} cm^{-2} ($\theta_{N_2} = 0.034$).

The α_1 and α_2 desorption peak temperatures at low coverages have been used to estimate the activation energies for desorption using the Redhead method [168] with an assumed preexponential factor of 10^{12} s^{-1}. This method yields activation energies of 46.86 kJ/mol for the α_1-process, 36.40 kJ/mol for the α_2 process, and 27.20 kJ/mol for the α_3 process on the Ru(109) surface. These desorption energies are slightly higher than those measured for the Ru(001)

surface where the desorption energies have been calculated from the peak desorption temperature in a similar fashion. The desorption energy of the α_1-process on Ru(001) involving N_2 species on random defect sites was determined to be 43.10 kJ/mol, whereas the desorption energy for the α_2 and α_3 features has been calculated from the peak desorption temperatures to be 33.47 kJ/mol and 21.34 kJ/mol, respectively. The comparison of the theoretical desorption energies from the DFT calculations and the Redhead analysis (assuming a preexponential factor of 10^{12} s^{-1}) of the data show that poor agreement is found. For the α_1 desorption process from the step sites of Ru(109), differences ranging from 25 % to 220 % are found depending upon which of the S1 to S4 states is used in the comparison. However the experimental trend of higher desorption energies for the N_2 states bound to Ru(109) compared to comparable states bound to Ru(001) is confirmed by the theoretical analysis.

6.7.2 The Singleton Vibrational Frequency of Chemisorbed N_2 on Ru

The vibrational frequency of an adsorbate molecule in the limit of very low coverage is termed the singleton frequency. This frequency is characteristic of the adsorbed molecule in the absence of intermolecular interactions and is indicative of the character and strength of the primary chemical bond to the surface.

There are a variety of factors which determine the singleton vibrational frequency of a diatomic molecule chemisorbed on a metal substrate. These factors shift the frequency from that of the gas phase molecule to either higher or lower frequency. An upward shift from the gas phase frequency is expected from the mechanical renormalization effect [151]. Here the infinite effective mass of the substrate will cause the oscillator frequency to shift upward purely from the effect of the added mass to the oscillator. In the case of chemisorbed CO this effect is calculated

to be about +2.5% [151]. The mechanical renormalization effect is typically compensated by a larger downward frequency shift attributable to several factors. In the case of adsorbed CO the charge transfer as a result of the formation of a chemical bond with the surface will cause a downward frequency shift [249,250]. The back donation of charge from the metal to the adsorbed CO molecule, into the unoccupied $2\pi^*$ orbital, stabilizes the metal-C bond and destabilizes the C-O bond [251]. In addition, a downward singleton frequency shift will occur as a result of the interaction of the dynamic dipole, $\partial\mu/\partial q$, with its image in the metal substrate [252,253].

These basic effects change as the CO coverage increases. Thus, vibrational coupling between neighbor CO molecules causes an upward shift in the observed mode (symmetrical coupling) as a result of direct interaction between the dynamic dipoles as well as interactions with the image dynamic dipoles [90]. In addition, for increasing coverage, the increasing competition for back-donating electrons from the metal, to enter the empty $2\pi^*$ orbital, will result in an upward shift in frequency [251,254].

It might be expected that the same general trends will occur for the adsorption of N_2 on Ru surfaces since N_2 and CO are isoelectronic. A report by de Paola et al. suggests however that back donation into the $2\pi^*$ orbital is of minor consequence and that σ-electron donation to the Ru surface is the major factor in N_2 chemisorptive bonding [119]. The frequency of $^{14}N_2(g)$ is 2359 cm^{-1} [201]. Thus, the adsorption of N_2 on the two Ru surfaces produces rather large decreases (~-8%) in the singleton oscillator frequency from the mechanically renormalized frequency (which will be above the frequency of gas phase N_2 at 2359 cm^{-1}). A different chemical effect on the N_2 vibrational frequency (added to the image effect) is the cause of the difference between the singleton mode frequency of 2202 cm^{-1} (Ru(109)) and 2213 cm^{-1} (Ru(001)) and the

mechanically renormalized N_2 frequency above 2359 cm^{-1}. The singleton frequency of 2202 cm^{-1} on Ru(109), which is 11 cm^{-1} below the singleton frequency on Ru(001), indicates that the Ru-N_2 bond is stronger for isolated N_2 molecules on the Ru(109) terrace sites compared to isolated N_2 molecules on Ru(001). This observation is in agreement with the comparison from thermal desorption results described above; both the thermal desorption measurements and singleton vibrational frequencies indicate that N_2, bound to terrace sites of Ru(109), is more strongly bound than N_2 bound to the smooth Ru(001) surface.

It is interesting to compare the N_2 singleton frequency experimentally observed in this work on Ru(109) terraces and Ru(001) with the frequency calculated by DFT and displayed in Figure 69 ($\theta_{N_2} = 0.11$). This comparison is summarized in Table 2. For terrace sites on Ru(109) labeled 2-8, an N_2 stretching frequency in the range 2197 – 2203 cm^{-1} is calculated (no N_2-N_2 interactions) which compares very favorably with the measured singleton frequency of 2202 cm^{-1}. On the Ru(001) surface the singleton frequency (at $\theta_{N_2} = 0.063$) was calculated to be 2211 cm^{-1}. This value also agrees exceptionally well with the experimentally determined singleton frequency of 2213 cm^{-1}. This high level of agreement between the calculated vibrational frequencies and the experimental values might be a fortuitous result as the current set of vibrational frequencies have been done only in the harmonic approximation and consequently no anharmonic effects have been included. Nevertheless, the trends of vibrational frequencies calculated on Ru(109) versus Ru(001) are very similar to those observed experimentally. This observation suggests that adsorption of N_2 at 85 K initially populates the terrace sites of Ru(109) and that the infrared band splitting observed upon heating the fully-covered surface to produce a partially-covered surface (Figure 64a and Figure 65a) is due to a redistribution of a fraction of the N_2 molecules to the step sites. In addition, the lower singleton frequency for N_2 adsorption

on Ru(109) terrace sites compared to N_2 on Ru(001) indicates that N_2 bonding to Ru primarily involves σ-electron donation to the metal rather than back donation into $2\pi^*$ orbitals of N_2.

Table 2: Comparison of N_2 Singleton Frequencies on Terrace Sites of Ru(109) and on Ru(001)

	Ru(109)			Ru(001)	
	Singleton Frequency - Terraces			Singleton Frequency	
	Upon Adsorption	Upon Desorption		Upon Adsorption	Upon Desorption
Experimental	2203 cm^{-1}	2201 cm^{-1}		2213 cm^{-1}	2213 cm^{-1}
Theoretical	2200 ± 3 cm^{-1}			2211 cm^{-1}	

6.7.3 Coverage-Dependent Shifts in the Vibrational Frequency of N_2 on Ru

For increasing coverages of N_2, both the Ru(109) and the Ru(001) surfaces exhibit a decrease in $\nu(N_2)$. This has been noted before for Ru(001), where shifts of -40 cm^{-1} (HREELS [115]) or of -20 cm^{-1}(IRAS [119]) are reported over the full range of coverage. Our measurements (Figure 63b) indicate that a shift of -20 cm^{-1} takes place on Ru(001) as coverage increases in agreement with Ref [119]. Based upon theoretical arguments, the contribution of dynamic dipole-dynamic dipole interactions between N_2 molecules to the frequency shift at saturation coverage will be +12 cm^{-1} [228]. Thus, the total shift $\Delta\nu$(chemical) = -32 cm^{-1} may be estimated for Ru(001). A similar analysis (based on the depletion experiments of Figure 65a) of the coverage-dependent shift of $\nu(N_2)$ on Ru(109) for N_2 molecules adsorbed on the terrace sites yields $\Delta\nu$(chemical) = -16 cm^{-1} for the completion of the monolayer, assuming the same +12 cm^{-1} contribution of the dynamic dipole interaction effect. If, because of limited long range interactions, the dynamic dipole interaction effect is smaller on the narrow terraces of Ru(109) compared to the infinitely-wide Ru(001) surface plane, then the absolute magnitude of $\Delta\nu$(chemical) will be even less than

16 cm^{-1} on Ru(109). The smaller $\Delta\nu$(chemical) observed on the stepped Ru(109) surface compared to Ru(001) suggests that the competition between N_2 molecules to donate σ-electrons to the metal is less dependent on coverage on the stepped surface. The reason for this difference is currently unknown. A similar frequency shift (-8 cm^{-1}) from a singleton frequency of 2201 cm^{-1} is observed for N_2 adsorption on Ni(110) as the N_2 coverage increases to its saturation limit [241].

6.7.4 Multiple N_2 Vibrational Bands on Ru(109)

Figure 64a clearly shows that upon heating the Ru(109) surface, previously saturated with N_2, to temperatures in the range 136 K -174 K, a spectroscopic doublet is observed to form as partial desorption of N_2 occurs. The two bands are due to the presence of N_2 molecules adsorbed together on terrace sites and on step sites. As the N_2 coverage decreases from saturation, intensity sharing effects diminish and the low frequency band near 2192 cm^{-1} becomes resolved from the high frequency band at about 2201 cm^{-1}. It is likely that migration of N_2 molecules from the terrace sites to the step sites occurs during heating and that annealing of the layer produces ordering of the surface species. The ~10 cm^{-1} difference in $\nu(N_2)$ for the step and terrace sites is in close accordance with the ~ 20 cm^{-1} difference calculated by DFT for the two types of sites, as summarized in Figure 69.

As the N_2 coverage is further decreased by heating to above 174 K, the high frequency component of the doublet preferentially decreases, as may be seen in Figure 64. This indicates that N_2 desorption from terrace sites occurs preferentially, leaving N_2-occupied step sites in accordance with the thermal desorption measurements which show that α_1-N_2 is the last desorption process to occur during TPD from Ru(109) (Figure 62).

The assignment of the low frequency mode to the step sites on Ru(109) was confirmed by CO displacement experiments in Figure 68. Here, starting with the annealed and partially depleted N_2 layer, which exhibits the doublet feature, it was found that the high frequency N_2 species was preferentially displaced at 90 K by more strongly bound CO molecules. Thus, the low frequency N_2 species are more strongly bound and may be confidently assigned as step-bound N_2 species, based on five criteria developed in this study: (1) The low $\nu(N_2)$ compared to terrace-bound N_2; (2) The higher activation energy for desorption; (3) The greater propensity for removal by CO displacement; (4) The agreement of the observed vibrational frequency with that calculated for terminally-bound N_2 on the step sites; and (5) The absence of evidence for a spectroscopic doublet at any N_2 coverage on the Ru(001).

6.7.5 Studies of Isotopic N_2 Species Coadsorbed Together on Ru(109)

The high frequency accuracy of IRAS allows one to probe the subtle spectroscopic effects which occur when surface oscillators are slightly detuned from each other by means of isotopic labeling. The dynamic dipole-dynamic dipole interactions will be lower for isotopically-detuned oscillators compared to isotopically-tuned oscillators. In Figure 67 one may compare the spectrum of pure $^{14}N_2$ and pure $^{15}N_2$, with a 50% - 50% isotopic mixture of the two isotopomers at the same coverage, where the doublet $\nu(N_2)$ spectrum is observed. Three observations may be made: (1) The mixed isotopic layer does not show absorbance between the two doublets characteristic of the two isotopomer N_2 species, indicating that (a) N_2 dissociation and formation of $^{14}N^{15}N$ does not occur; and (b) that species such as $^{14}N_2$-Ru-$^{15}N_2$ are absent; (2) The 50%-50% layer exhibits 4 peak frequencies which are each shifted by 1-3 cm^{-1} to lower frequency compared to the isotopically pure layers of the same total coverage. This indicates that dynamic

dipole coupling effects (causing upward frequency shifts) are smaller for the mixed isotopomer layers as a result of oscillator detuning, an expected result. (3) The FWHM of the doublet features in the 50%-50% isotopomer mixed layer is larger than for the isotopomer pure layer, indicating that local isotopic inhomogeneity effects are being observed, where a statistical fraction of the isotopic molecules sense an environment containing more than 50% of the opposite isotopomer and hence suffer even smaller upward shifts due to dynamic dipole coupling.

6.7.6 N_2 Bonding to the Ru(109) Terrace Compared to Ru(001) – The Role of σ-donation

The presence of atomic steps on Ru(109) is expected to alter the electronic character of the terrace sites located between the nine atom wide steps, making the terrace sites less reactive toward CO than the Ru(001) plane. This is due to the lateral compressional effect of atomic step sites on the confined terraces bounded by atomic steps [255-260]. While there is no experimental structural evidence available for Ru(109) indicating that lateral compression exists, there is experimental and theoretical evidence for this effect (for CO bonding) on other metals [255-260]. The step edge atoms undergo an inward displacement to enhance their coordination with other metal atoms. This places the confined terrace metal atoms under compressive stress and causes their reactivity toward CO to be reduced as a result of the compression, causing increased filling of the antibonding metal d-band orbitals [45,261] compared to the Ru(001) surface.

Our experimental comparison of the reactivity toward N_2 on the terrace sites of Ru(109), compared to the Ru(001) surface are opposite to the above expectation for CO bonding. Thus, for both α_2-N_2 and α_3-N_2, the experimentally measured peak desorption temperatures and the

activation energies for desorption from the terrace sites are higher for Ru(109) compared to Ru(001) (Figure 62). Also, the singleton frequency for N_2 is ~10 cm^{-1} lower for adsorption on the terrace sites of Ru(109) compared to Ru(001) (Figure 63) indicting stronger binding of N_2 on Ru(109) terraces. This comparison therefore indicates that chemisorptive N_2 bonding occurs as a result of σ-N_2 donation to the metal (with minimal back-donation into the $2\pi^*$ orbital), and considerations of the involvement of metal d electrons do not apply. This conclusion is in agreement with the concept developed by de Paola et. al. [119] indicating that N_2 should be considered as a σ-donor molecule in its chemisorption on transition metals.

6.7.7 Highly Coordinated N_2 Bonding to Step Sites on Ru(109)

In addition to the terminally-bonded N_2 species detected spectroscopically in this work, the DFT calculations indicate that more highly coordinated N_2 species will also be present on the step sites of Ru(109). Thus, species S3 and S4 (Figure 70) involve 4-fold coordination of N_2 to step sites, causing the production of more strongly-bound low frequency species which would not be seen by our IRAS measurements. We are not able to determine whether the desorption of α_1-N_2 from Ru(109) involves these highly coordinated species. However, it is likely that these 4-fold coordinated N_2 species are involved in the activated dissociation of N_2 on Ru(109) [43].

6.8 CONCLUSIONS

The following observations have been made in a detailed comparison of N_2 chemisorption on the atomically-stepped Ru(109) surface with the Ru(001) surface.

(1). Thermal desorption from the atomic step sites on Ru(109) evolves N_2 in a well resolved high temperature α_1-N_2 desorption state near 200 K, which is not observed on Ru(001), except for a small coverage of this state due to random defect sites.

(2). Adsorbed N_2 on the step sites of Ru(109) exhibits a $\nu(N_2)$ mode which is ~ 9 cm^{-1} below the mode associated with N_2 on the terrace sites, indicating stronger terminal bonding of N_2 to step sites compared to terrace sites. This is verified by DFT calculations of the binding energy and vibrational frequency of terminally-bonded N_2.

(3). Desorption experiments clearly show the preferential retention of terminal step-bound N_2 to higher temperatures after desorption of terrace-bound N_2 has occurred from Ru(109).

(4). Dynamic dipole-dynamic dipole interaction effects are clearly observed as the N_2 coverage is increased on Ru(109), and studies of mixtures of $^{14}N_2$ and $^{15}N_2$ show that partial vibrational decoupling may be achieved by detuning using these isotopomers.

(5). The bonding of N_2 to terrace sites on Ru(109) is stronger than on Ru(001) as indicated by the singleton $\nu(N_2)$ frequency, the thermal desorption measurements, and DFT calculations. These observations indicate that N_2 is primarily σ-bonded to the Ru surfaces, since d-back donation into antibonding $2\pi^*$ CO orbitals would be expected to show the opposite trend in bonding.

(6). DFT calculations indicate that in addition to more strongly-bound terminal N_2 species, the atomic step sites also stabilize multiply coordinated N_2 species which would not be visible in IRAS. These species may represent the precursors to N_2 dissociation on Ru atomic step sites.

(7). The order of chemisorption bond strength of N_2 to Ru surface sites is: atomic steps > atomic terraces > Ru(001)

7.0 INTERACTION OF LI WITH ATOMIC STEPS ON RU: COMPARISON BETWEEN Ru(001) AND Ru(109)

The information contained in this chapter is based on the following research publication:

Yu Kwon Kim, **Gregg A. Morgan, Jr.,** and John T. Yates, Jr., *"Interaction of Li with Atomic Steps on Ru: Comparison between Ru(001) and Ru(109)"* Chem. Phys. Lett. **431** (2006) 313-316.

7.1 ABSTRACT

The interaction of Li with Ru was investigated on Ru(001) and Ru(109) using work function measurement, temperature-programmed desorption (TPD) and low-energy electron diffraction (LEED). Strong depolarization effects for Li atoms at atomic step sites are observed, causing the dipole moment of a chemisorbed Li atom at the limit of zero coverage to decrease from 10 D to 6 D. In contrast to the (n×n) incommensurate Li structures observed on Ru(001), the Ru(109) surface does not produce any ordered Li structures. In addition, the thermal desorption kinetics for Li from Ru(001) is virtually identical to that from Ru(109) at all coverages.

7.2 INTRODUCTION

The adsorption of alkali metals on metal surfaces has been widely studied [262]. This work has been motivated by the enhancement of thermionic emission upon the adsorption of alkali metals as well as by a variety of promotional effects in various catalytic reactions [263,264]. The understanding of alkali metal interactions with metal surfaces has been acquired over decades [122,123]. The general picture, based on the Langmuir-Gurney model, still governs our basic understanding [123]. In this model, partial charge transfer from alkali atoms to the metal substrate occurs. As the alkali metal coverage increases, depolarization effects set in causing a reduction in the dipole moment of the alkali atoms. While the above simple picture generally holds true, the detailed adsorption sites for alkali atoms vary significantly depending on the identity of the alkali atom as well as the structure of the substrate [265]. Interestingly, some recent studies indicate that catalytic promotional effects of alkali metals can be enhanced on atomically stepped metal surfaces [266-269]. Our recent study also shows that Li promotes the dissociation of the C-O bond on stepped Ru(109) at 85 K [270].

This report is focused on a comparative study of the interaction of Li with two different Ru single crystal surfaces, Ru(001) and Ru(109), to obtain an insight into the way Li interacts with Ru steps. Ru(109) presents about 12% double-atom height atomic steps separated by (001) terraces of 9 atom width [41,42], while Ru(001) has nominally less than 1% random defective steps. Our results indicate that Li interacts with Ru steps on the stepped Ru(109) surface from a very low Li coverage even when deposited at 85 K.

7.3 EXPERIMENTAL

All of the experiments reported here were performed in a stainless steel ultrahigh vacuum (UHV) chamber which was discussed in detail in Chapter 2. The various experimental conditions are also discussed in various sections Chapter 2.

A commercial Kelvin probe system (Besocke Delta Phi GmbH) was used to measure the work function change of the Ru crystal surfaces after each Li deposition and the work function change was plotted against Li coverage.

7.4 RESULTS

Figure 71 shows the resulting work function change, $\Delta\varphi$, for Li adsorption on clean Ru(001) and Ru(109) surfaces, respectively. The results indicate there is no meaningful dependence of the work function behavior on the substrate temperature (85 - 450 K) on Ru(109) within our measurement errors. The curves for both Ru crystals are typical for alkali metal adsorption on transition metal surfaces. The initial linear decrease to Li coverages of ~0.2 ML is followed by non-linear behavior to partial monolayer coverage, resulting in a minimum. Beyond this minimum, the work function change rises to the same level for both surfaces which is ~3.2 eV below that of the clean surface. Note that the initial slopes for the two Ru crystals are clearly different (see the inset for the initial slope difference in the low Li coverage regime). The measured initial slope for Ru(109) is 12 ± 1 eV/ML, while that of Ru(001) is 23 ± 1 eV/ML. Note also that the maximum negative shift for Ru(109) is -3.8 ± 0.2 eV, while that for Ru(001) is -4.5 ± 0.2 eV.

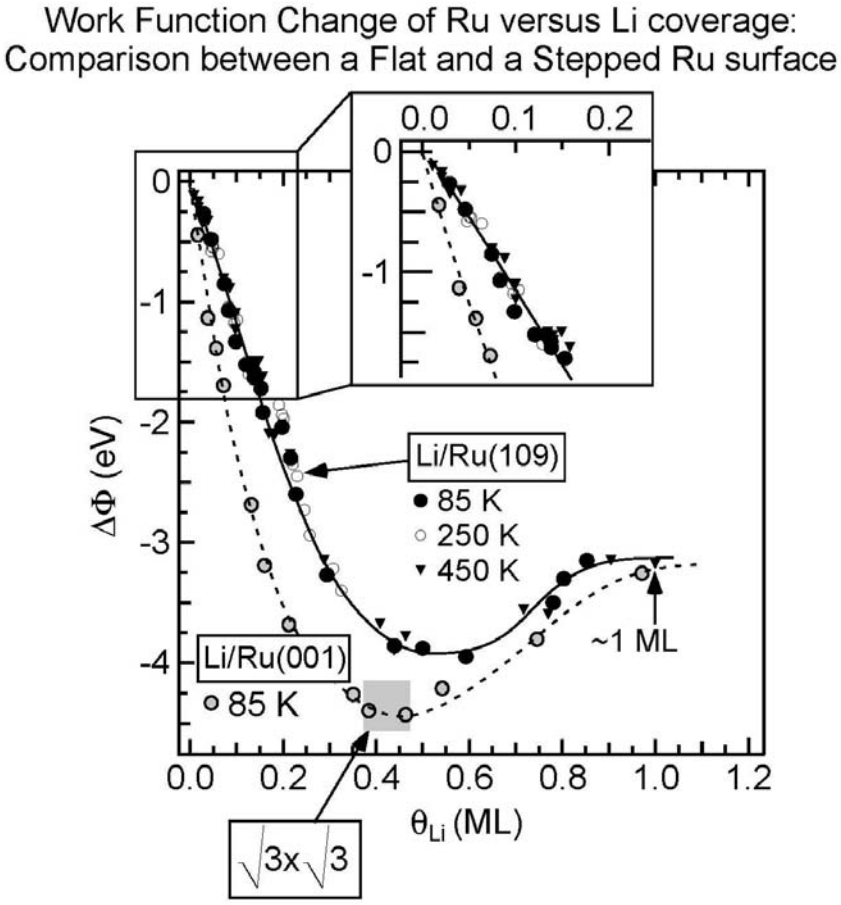

Figure 71: Work function change of Ru against Li coverage. The θ_{Li} is calculated from a area of Li TPD peaks, where the onset of the second-layer Li desorption peak is set to 1 ML. The lines are drawn to guide the eye.

The Li TPD spectra from the two Ru crystals are shown in Figure 72. The spectra for Li on both Ru crystals show typical desorption features of alkali metals adsorbed on metal surfaces. At the lowest Li coverage, the desorption peak appears at around 1000 K as a single broad feature. As the Li coverage increases, the desorption feature expands toward lower temperatures and the maximum peak temperature also shifts continuously toward lower temperatures until a sharp Li desorption peak starts to develop at 550 K. Note that the leading edge of the sharp Li desorption peak closely follows the Li TPD curve calculated from the Li vapor pressure curve, as shown as a dashed line in Figure 72. The Li coverage at which the sharp Li desorption peak is

first observed indicates the saturation of the first monolayer of Li on the Ru surfaces (1 ML). It is noted that the desorption kinetic behavior of Li on the two surfaces is remarkably similar. This suggests, in the low coverage limit, that random steps on the Ru(001) surface may govern the activation energy for desorption, since the Ru(001) and Ru(109) data do not show significant differences in behavior.

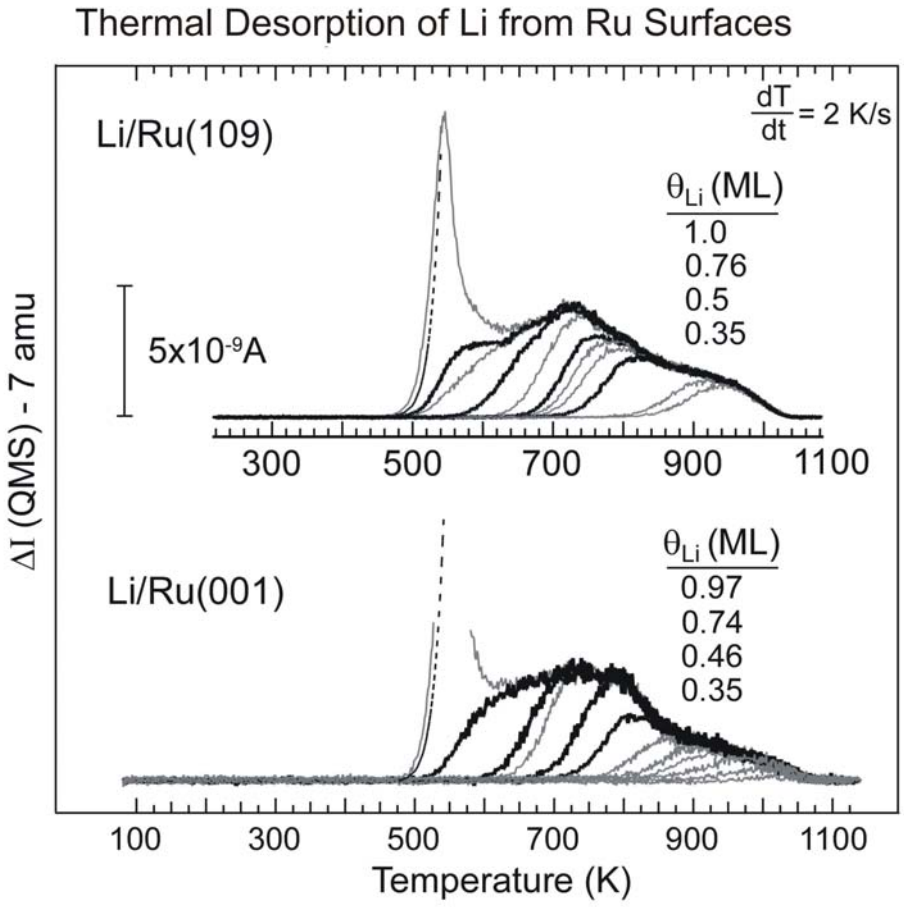

Figure 72: TPD spectra of Li (mass 7) obtained from Li adsorbed on Ru(001) and Ru(109), respectively. Li was deposited on Ru at 85 K. The dotted line is calculated from Li vapor pressure curve.

LEED patterns for Li overlayers grown on the two Ru crystals at 85 K are shown in Figure 73 at submonolayer Li coverages. The results on Ru(001) are quite consistent with early reports [155,271]. A very sharp and clear $\sqrt{3}\times\sqrt{3}$ pattern is obtained at ~0.4 ML [155] and a

series of incommensurate n×n phases at higher Li coverages up to 1 ML are also observed on Ru(001) [271].

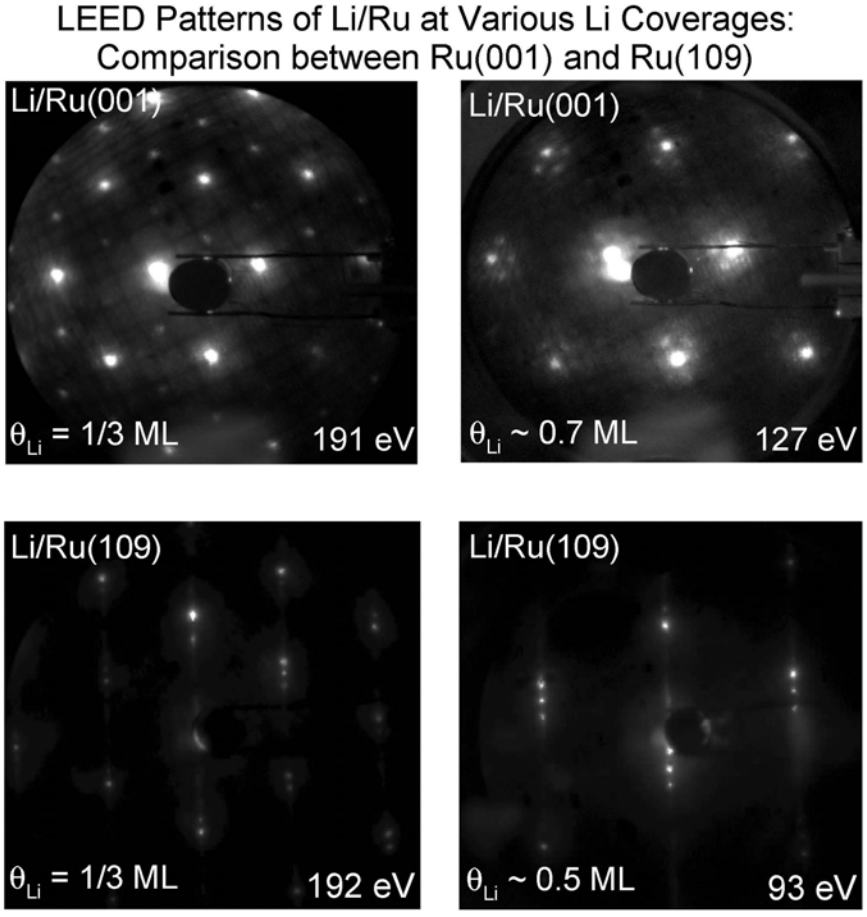

Figure 73: LEED patterns for Li/Ru(001) and Li/Ru(109) in the submonolayer Li coverage regime.

For the Ru(109) crystal, at zero coverage, triplet diffraction beams are seen, indicative of the stepped crystal structure [42]. Note there is no Li-induced superstructure formed on the stepped Ru(109) surface throughout the whole Li coverage range under investigation (up to 1 ML). No additional LEED beams are observed due to Li deposition. Instead, a gradual increase of background intensity with increasing Li coverage is observed.

While there is no meaningful variation in the LEED pattern for Li/Ru(109), Figure 74a and Figure 74b show a subtle change in the intensity profile of the triplet diffraction beams depending on the Li deposition temperature when the Li coverage is ~0.03 ML. The change is quite evident from Figure 74c, which indicates a sudden change in the intensity ratio of the two diffraction beams (P_2/P_1) at around ~120 K at the very low Li coverage regime. Note, however, that the temperature-dependency of the intensity ratio vanishes at Li coverages above 0.05 ML and shows no temperature-dependence (see Figure 74d).

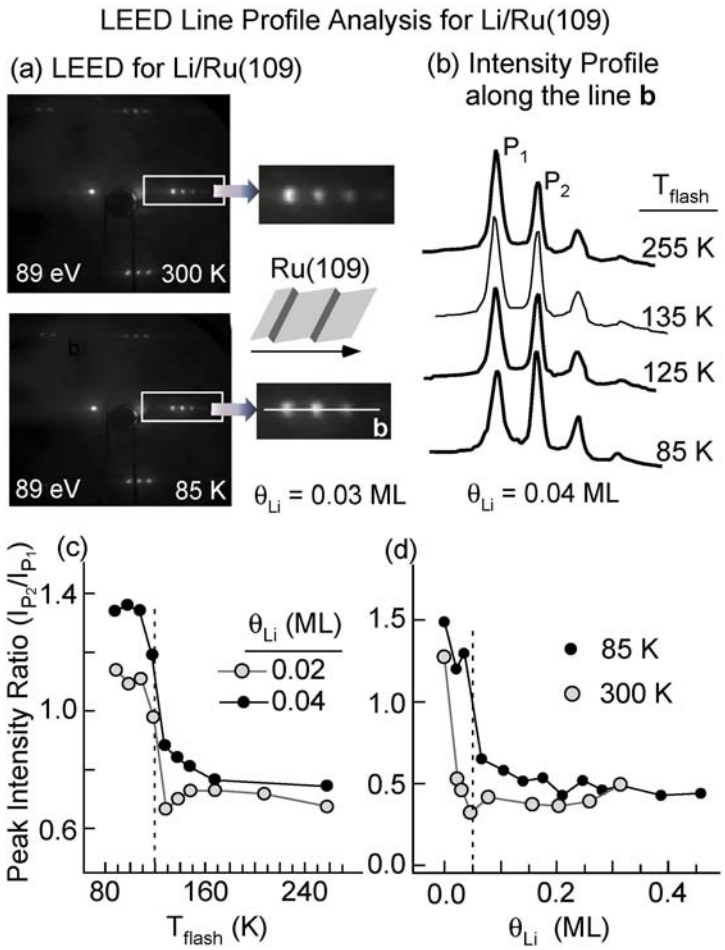

Figure 74: (a) LEED patterns from Li/Ru(109) (θ_{Li} = 0.03 ML) at the deposition temperature of 85 K as well as after subsequent flash to 300 K. (b) Intensity profile along the line b in (a) with increasing flash temperatures. (c) The peak intensity ratio (P_2/P_1) as in (b) against the flash temperature at two θ_{Li} = 0.02 and 0.04 ML. (d) The ratio (P_2/P_1) against Li coverage at two different Li deposition temperatures of 85 and 300 K.

7.5 DISCUSSION

From Figure 71, two notable differences between Ru(001) and Ru(109) can be found in the work function change curve: (1) the initial slope; and (2) the maximum negative shift are higher on Ru(001) than on Ru(109).

Based on the prevailing general picture [122,123], the observed differences between Ru(109) and Ru(001) are explained by the different Li-induced surface dipoles on both Ru crystals. From the measured initial slopes in the very low Li coverage range ($\theta_{Li} \leq 0.1$), we measured the initial dipole moment of Li (μ_0) on Ru(109) and Ru(001) to be ~6.0 D and ~10.0 D, respectively, using the analysis methods given in an early review [122]. A schematic picture comparing Li on the two surfaces is given in Figure 75.

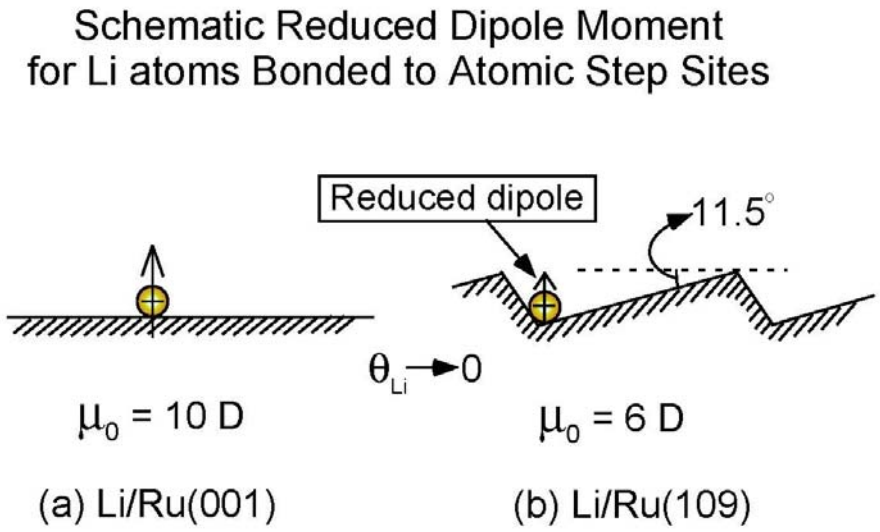

Figure 75: Schematic of the adsorption of Li on Ru(001) and Ru(109) at low Li coverages.

The smaller Li-induced dipole moment on Ru(109) is the result of Li interacting with Ru steps. The lack of change in the initial slope of the $\Delta\varphi$ vs. θ_{Li} curve over the temperature range

from 85 - 450 K indicates that Li migrates to the step sites at T ≥ 85 K. The facile Li migration on Ru(001) at low temperature is suggested from a diffusion barrier measurement on Ru(001) [272]. One may also rationalize the preference of Li to adsorb at metallic steps from a tendency of ionic alkali metals to occupy high-coordination sites. While there is no dependence of $d\Delta\varphi/d\theta_{Li}$ at temperatures above 85 K, indicating that Li migration to the step sites has occurred by 85 K, the subtle change in the LEED peak intensity ratio (Ip_2/Ip_1) at ~120 K, indicates that activated Li migration occurs along the step sites at a temperature which is above the temperature needed for Li atom migration across the terrace sites.

The reduction of the initial zero coverage dipole moment (μ_0) of Li from 10 D to 6 D when the Li atom migrates to an atomic step site may be related to two effects: (1) The Li atom, bound at the base of the step site interacts with negative charge density present at the step (Smoluchowski smoothing effect [165,273]), to result in depolarization of the Li atom, which effect may be further enhanced by the double atom height nature of the Ru step [42]; (2) The proximity of the metal surface of the step edge and the Li atoms provides a region for Li dipole depolarization due to the image charge effect.

For the two values of μ_0, differences in the one and two-dimensional geometries of step sites and terrace sites should not contribute at infinite dilution, but at higher coverages, Li dipole-dipole depolarization effects should differ.

The work function change due to Li adsorption, $\Delta\varphi$, approaches the same value of about -3.2 eV on both Ru crystals at θ_{Li} ~ 1 ML. Here the mutual interaction between Li atoms becomes dominant and induces depolarization, and the influence of substrate structure becomes less important at the high Li coverages.

On Ru(109), the maximum negative shift is achieved at a higher Li coverage (~0.6 ML), while on Ru(001), the work function minimum is located near 0.5 ML. This effect may also be due to structural differences in the Li layer at intermediate coverages on the two surfaces, as well as to the lower dipole moment of Li atoms at the atomic step sites.

The absence of Li-induced superstructures on the stepped Ru(109) may be explained from the anisotropic repulsion between Li atoms on Ru terrace planes. On Ru(001), the repulsion between Li atoms is isotropic since the (001) plane is assumed to be large enough to ignore the effect of random defective Ru steps. Ru(109), however, has narrow Ru terrace planes, which are 11.5°-off the surface normal. One boundary of the narrow Ru(001) terrace plane of Ru(109) is bounded by a Ru step and the other end is open space. Li atoms on Ru terraces are bounded on one side by the Ru atomic step while on the other side, the boundary is open. It is intuitively inferred that the anisotropic repulsive interaction would prevent Li atoms on Ru terraces from forming any isotropic ordered phase, in contrast to that observed on Ru(001).

7.6 CONCLUSION

The following effects have been observed for Li adsorption on an atomically stepped Ru(109) surface compared to the atomically smooth Ru(001) surface.

Li atoms migrate at ~85 K across Ru(001) terrace sites to the atomic steps on Ru(109). At about 120 K, Li atom rearrangements are observed for Li adsorbed on step sites.

The dipole moment at the limit of zero coverage for a Li atom bound to an atomic step is 6 D, compared to 10 D for a Li atom on a planar Ru(001) surface. This is attributed to

depolarization effects for the Li dipole in the vicinity of Ru metal atoms present at the atomic step site.

Long range repulsive isotropic forces between adsorbed Li atoms on Ru(001) result in the production of a range of incommensurate Li adlayers observed by LEED. At similar Li coverages on atomic terraces of Ru(109), no overlayer LEED structures are observed due to the anisotropy of repulsive forces expected due to the presence of step sites which interrupt the Ru(001) terraces.

The presence of ~12% of atomic step sites causes very little variation in the observed kinetics of desorption of Li at all coverages, comparing Ru(109) to Ru(001).

8.0 UNEXPECTED LOW-TEMPERATURE CO DISSOCIATION ON Ru BY Li PROMOTER ATOMS

The information contained in this chapter is based on the following research publication:

Yu Kwon Kim, **Gregg A. Morgan, Jr.,** and John T. Yates, Jr., *"Unexpected Low-Temperature CO Dissociation on Ru by Li Promoter Atoms"* Chem. Phys. Lett. **422** (2006) 350-353.

8.1 ABSTRACT

The dissociation of CO molecules on a stepped Ru surface in the presence of Li promoter atoms is probed by reflection-absorption infrared spectroscopy (RAIRS). We find that even at 85 K, Li adsorbate atoms cause the rupture of the C−O chemical bond.

8.2 INTRODUCTION

The coadsorption of carbon monoxide with alkali metals has been widely studied on a variety of transition metals [263], primarily to study promotion effects in a variety of catalytic reactions. The general picture of the promotion effect is that the molecular C−O bond is weakened, while

the metal-CO bond becomes stronger in the presence of alkali metals [274]. The detailed description of the above effect involves various models including the charge transfer mediated by the substrate [151,275], direct bonding interaction through complex formation [276], and electrostatic interaction [120,277,278].

The weakening of the C−O bond often leads to the enhancement of the CO dissociation probability on some metal substrates (Pd, Ru) [126,127], which can be detected by CO intermolecular isotope scrambling [109,124,279]. The formation of carbon dioxide from CO adsorbates has been also reported, suggesting CO dissociation on some transition metals (Cu, Ni) under elevated substrate temperatures and at critical alkali metal promoter coverages [280-282]. For most cases involving alkali metals as surface modifiers, the C−O bond is usually preserved at the adsorption temperature (~ 100 K), though the weakened C−O bond is evident from the large red shift of the CO absorption frequency in the infrared spectra [109].

Unlike other alkali metals (Na and K), the lightest alkali metal, Li has been rarely studied. The behavior of Li interacting with chemisorbed CO may differ from other alkali metals [124,283]. A strong interaction, leading to complex formation between CO and Li was inferred from the observation of stoichiometric CO adsorption on multilayers of Li on Ru(001) [124], which behavior was not observed for multilayer Na or K. In a lower Li coverage regime (~ 0.3 ML), stoichiometric alkali-CO surface complex formation was not observed since no codesorption of CO and Li was reported on Ru(001) [283]. Instead, the CO desorption temperature was observed to shift gradually to higher temperatures with increasing Li coverages [283].

Li is the lightest alkali metal with the smallest atomic diameter among alkali metals. Li is expected to induce a strong localized electric field in its vicinity when adsorbed on transition

metals. Therefore, Li may be more effective than any other alkali metals in promoting CO dissociation.

In this study, we employed a stepped Ru(109) surface to study the promotion effect of Li on CO dissociation. We have already demonstrated that CO dissociates on this surface by the observation of intermolecular isotope scrambling amongst CO molecules bound to the step sites and also by the absence of CO absorbance above 480 K where C + O recombination occurs [41]. Here we show by depositing a very small amount of Li at 85 K on Ru(109) containing a low coverage of CO, that a significant decrease of the absorbance of CO in the infrared occurs, which directly indicates the breakage of C-O bond even at temperatures as low as 85 K. Thus, Li is very reactive in dissociating the C−O chemical bond on Ru.

8.3 EXPERIMENTAL

All of the experiments reported here were performed in a stainless steel ultrahigh vacuum (UHV) chamber which was discussed in detail in Chapter 2. The experimental conditions are discussed in detail Chapter 2 as well. The infrared reflection-absorption spectra were collected using 2 cm^{-1} resolution averaged over 2000 scans.

8.4 RESULTS

Figure 76 shows two set of infrared spectra for θ_{CO} = 0.08, where for the right hand sequence, Li is deposited after CO adsorption at 85 K. Both sets of spectra show a decrease in integrated

absorbance in the CO band as the substrate is annealed to higher temperatures. The inset plots the integrated area of the CO absorption band as a function of annealing temperature.

For CO/Ru(109) with θ_{CO} = 0.08, Figure 76 indicates that a single IR absorption feature at 1996 cm^{-1} appears with a tail toward lower frequencies upon CO adsorption on Ru(109) at 85 K. As the substrate is annealed to 160 K, the absorption band gradually decreases to about 2/3 of its original intensity. At the same time, the featureless tail develops into a discrete absorption band at 1969 cm^{-1}. The loss of CO absorbance may indicate CO dissociation on the atomic step sites since CO desorption is not observed in the low temperature regime. When a small amount of Li (θ_{Li} = 0.03) is deposited on the CO/Ru(109) surface at 85 K, as shown in Figure 76, the CO absorption band suddenly decreases in intensity to less than 1/4 of its original intensity with a slight shift to 1983 cm^{-1}. After subsequent annealing, the CO absorption band further decreases in intensity without any noticeable shift and disappears completely after annealing above 160 K. The behavior of the integrated IR absorbance for the two experiments, without and with Li, is presented in the upper portion of Figure 76.

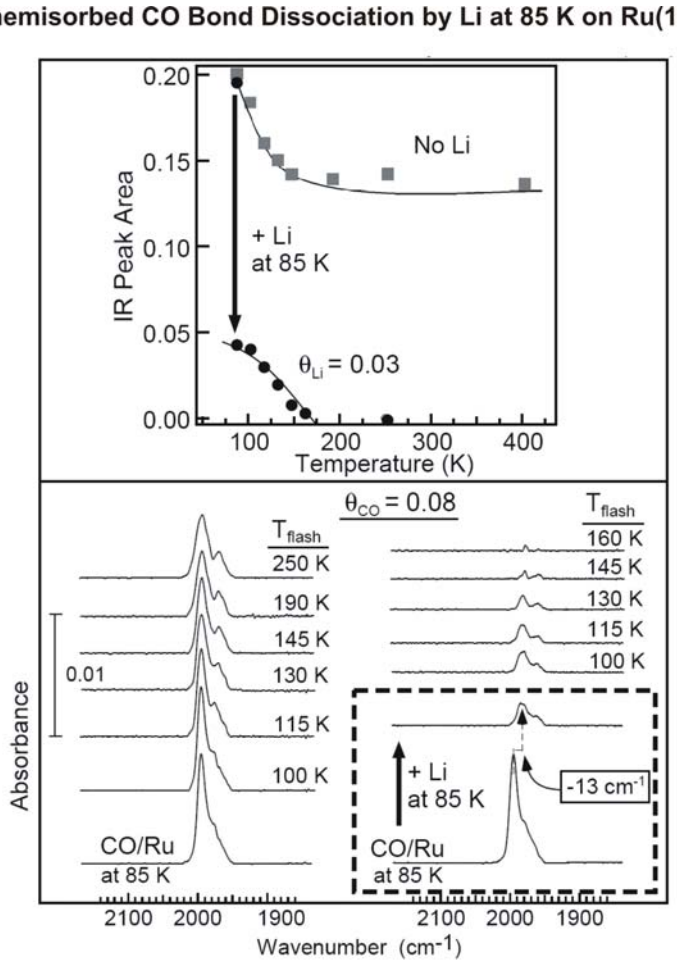

Figure 76: Infrared spectra of $^{12}C^{16}O$ taken at 85 K after adsorption on Ru(109) at 85 K and annealing to various temperatures. One spectral set was obtained without Li, and the other with Li coadsorption at 85 K. The inset plots the CO band integrated absorbance as a function of annealing temperature for the two set of data. The lines are drawn to guide the eye.

After the IR measurements, the TPD spectra of CO (m/e=28) were recorded as shown in Figure 77, where a comparison of the behavior without and with Li is shown. Two well-resolved desorption features are reproduced for CO/Ru(109), which are labeled as α_{CO} and β_{CO}, respectively. For the Li-treated CO/Ru(109) surface, it is noted that the α_{CO} and β_{CO} features decrease while a new CO desorption feature at higher temperatures develops. We observe that simultaneous desorption of Li does not occur at the CO desorption temperatures (not shown). The CO coverages measured for the two surfaces are compared in the upper portion of Figure 77

by the integrated area of the CO desorption features. The results indicate that no difference in the CO coverage is observed with and without Li modification. Since all evidence for a C–O absorption band disappeared by 160 K (see Figure 76), the CO desorption shown for the CO/Ru + Li in Figure 77 must be due to C + O recombination.

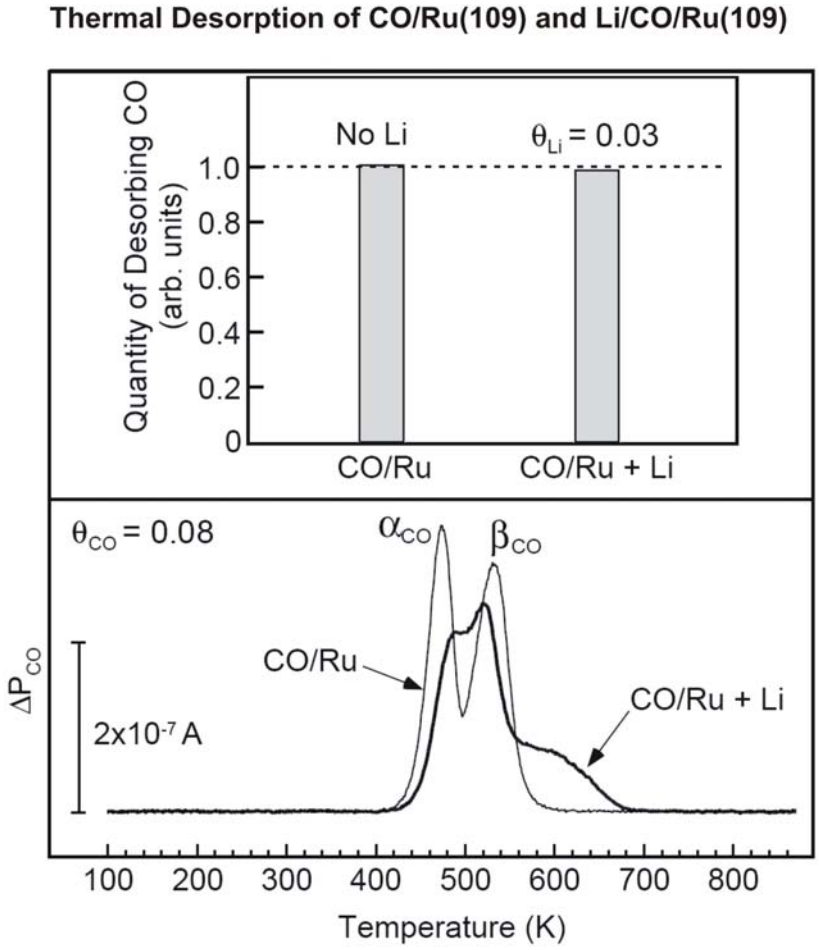

Figure 77: Thermal desorption spectra of CO taken after the IR measurements shown in Figure 76. The overall integrated areas of the CO desorption features for the two spectra are compared in the upper inset.

Figure 78 shows the Li-coverage-dependent variation in the integrated intensity of the IR absorption band when CO is adsorbed on Ru(109) with pre-deposited Li on it. The substrate temperature was kept to 450 K during the Li deposition to produce ordering of the Li adlayer. Then, the substrate was subsequently exposed to CO at 85 K up to the same coverage of θ_{CO} =

0.08 as used in Figure 76 and Figure 77. The resulting decrease in the integrated absorbance as shown in Figure 78 is non-linear with increasing Li coverage.

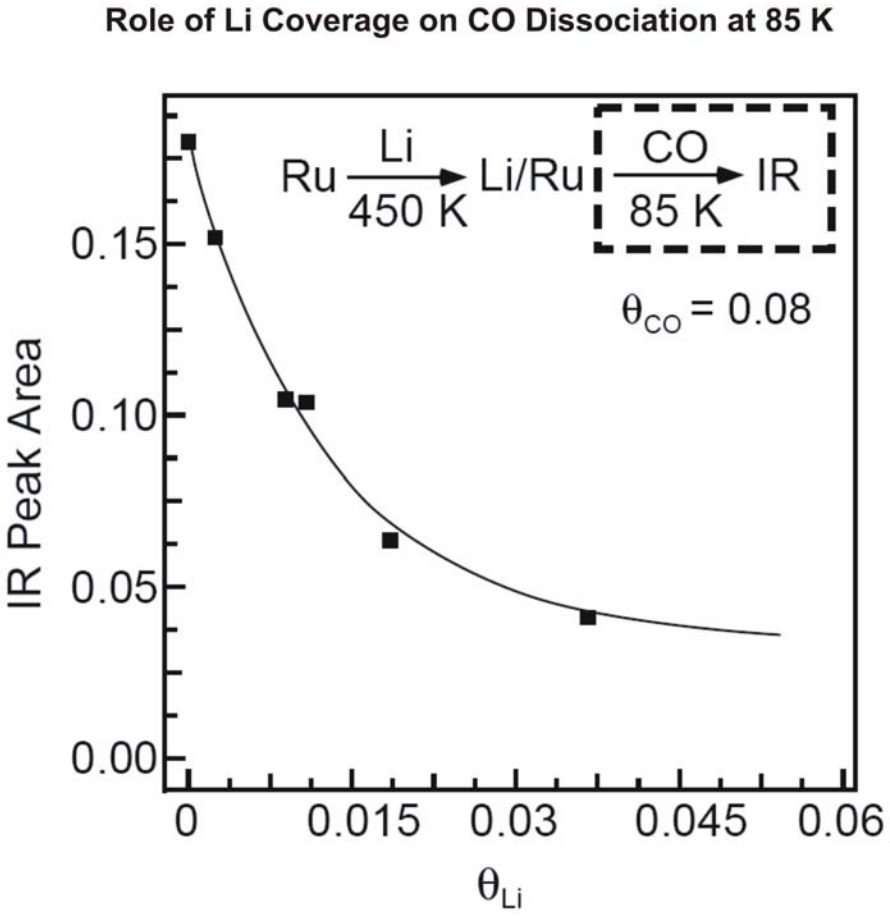

Figure 78: The CO peak intensities from the infrared spectra of CO adsorbed at 85 K on Li/Ru(109), plotted as a function of Li coverage.

8.5 DISCUSSION

The CO absorption band at 1996 cm^{-1} is due to the C−O stretching vibrational mode, which may shift in frequency depending on the CO coverage [42]. Since the CO coverage measured by TPD in Figure 77 indicates that there is no displacement of CO by Li deposition, the decrease of

the CO absorption band upon Li deposition at 85 K, as seen in Figure 76 is then caused by C−O bond breakage.

The annealing series in Figure 76 indicate two interesting changes in the CO absorption band on the pure CO layer: (1) the additional decrease up to 160 K in CO absorbance; (2) the slight shift in ν(CO) to lower frequency as coverage decreases.

For CO/Ru(001), it has been reported that annealing induces ordered CO islands, which produce two resolved IR absorption bands. CO molecules of lower frequency are due to CO species on the edge of ordered CO islands [91]. In the study reported here, the periodic steps on Ru(109) may produce CO islands which are even smaller than on Ru(001) producing a higher fraction of edge-CO molecules. The overall intensity drop during the annealing may be also related to the ordering process. However, early infrared spectroscopic studies on CO/Ru(001) indicate that the absorbance of the CO band is closely proportional to the CO coverage up to 0.3 ML, and the variation in intensity due to the ordering of CO is therefore rather small [91]. This information, taken together suggests that the decrease in CO absorbance of about 30 % upon annealing is mainly due to the dissociation of C−O bonds induced by the diffusion of CO to Ru steps on Ru(109).

For Li/CO/Ru(109), the additional intensity drop of the CO band absorbance up to 160 K in Figure 76 is, then, also explained by the same reasoning. The diffusion of CO (or Li) would allow CO to find nearby dissociation sites, which can be either Ru steps or some other sites promoted by Li atoms. The small red shift of the CO band by about 13 cm^{-1} upon Li deposition may be attributed to the reduced dipole coupling between CO molecules depopulated by CO dissociation. In addition, small electric field effects due to Li long range interaction with CO may also be involved.

In Figure 78, we note that the C−O bond dissociation increases non-linearly with the Li coverage. This suggests that the interaction between Li and CO is not stoichiometric in the low coverage regime ($\theta_{Li} \sim 0.05$; $\theta_{CO} \sim 0.08$). This argues against the possibility of a direct bonding interaction between Li and CO to produce a stoichiometric surface complex. This argument is also supported by our observation of TPD spectra of Li (not shown here) showing no high temperature shift of the Li desorption feature for Li + CO, indicating that there is no remaining oxygen to provide additional binding for Li. Thus, the interaction between undissociated CO and Li is expected to be indirect in nature.

Hoffmann reported the reaction of K + CO to produce K_2CO_3 on Ru(001) at 300 K under high CO pressure conditions at high coverages of K [127]. This produced a strong vibrational mode at 1471 cm^{-1}. A systematic inspection of all of our involving lower coverages of CO and Li interacting in the temperature range of 85 K – 250 K reveals no evidence of the band. We therefore attribute the disappearance of the ν(CO) mode induced by Li coadsorption to C−O chemical bond dissociation rather than to surface carbonate formation.

The Li-promoted dissociation of CO at 85 K is rather astonishing in that there has been no previous report indicating alkali-metal induced CO dissociation at such a low temperature. The effect of Li on CO dissociation is quite dramatic and evident from the depletion of the CO absorption band, which has not been observed for other alkali metals like K/Ru(001) [109]. The role of CO dissociation provided by Li atoms at step sites and by Li atoms at terrace sites is currently under investigation.

8.6 CONCLUSION

Li-promoted dissociation of CO molecules on Ru(109) has been directly probed by infrared reflection absorption spectroscopy. Interestingly, the CO dissociation effect due to Li is shown to occur even at 85 K.

9.0 ENHANCEMENT OF CATALYTIC PROMOTION ACTION OF Li ON Ru BY ATOMIC STEPS - COMPARISON OF CO DISSOCIATION ON Ru(109) AND Ru(001)

The information contained in this chapter is based on the following research publication:

Yu Kwon Kim, **Gregg A. Morgan, Jr.,** and John T. Yates, Jr., *"Enhancement of Catalytic Promotion Action of Li on Ru by Atomic Steps – Comparison of CO Dissociation on Ru(109) and Ru(001)"* Chem. Phys. Lett. **431** (2006) 317-320.

9.1 ABSTRACT

The Li-promoted CO dissociation on flat and atomically stepped Ru surfaces has been investigated by thermal desorption spectroscopy (TDS) and infrared reflection-absorption spectroscopy (IRAS). Li-induced dissociation of CO is observed to be greatly enhanced on stepped Ru(109) compared to Ru(001) from the scrambling of isotopic CO molecules as well as from the intensity reduction of the CO stretching mode. Interestingly, on Ru(001), Li produces a highly red-shifted CO stretching mode at ~1820 cm^{-1}, implying the formation of Li_xCO_y complexes. On the other hand, the preferential adsorption of Li by the atomic steps on Ru(109) impedes the formation of such complexes.

9.2 INTRODUCTION

Alkali metals are well recognized for their action as catalytic promoters on transition metal surfaces [263-265]. The dissociation of CO is a catalytic reaction step, which is strongly influenced by alkali metals added as promoters to transition metal catalysts [124,127,130,151,275,278,283-287], and this dissociation process is centrally important to catalytic reactions such as the Fischer-Tropsch reaction involving hydrogen and CO [49].

Among the alkali metals, strong promotional effects are often observed for Li. Some examples include the dissociation of H_2O on Li/Ni(775) [268], and the adsorption of CO on Li/Ag [288]. The co-desorption temperature of the Li-CO complex on Ru(001) is observed to be much higher (~ 840 K) than that for other alkali metals [124].

In this work, we compare the activity of Li for CO dissociation on two Ru model catalytic surfaces of Ru(001) and Ru(109). While Ru(001) exposes the basal hcp(0001) plane, Ru(109) contains Ru(001) terraces of 9 atom width separated by double height atomic steps, as shown in Figure 79. The reconstruction of the Ru(109) surface is reported to produce exclusively double-atom height Ru steps instead of single height steps (see Figure 79), as has been extensively discussed previously [42]. Direct comparisons between both Ru crystals have been carried out to determine the role of atomic steps on the action of Li atoms on chemisorbed CO. A careful review of the literature extending back to 1970 indicates that the cooperative action of Li promoter atoms and any transition metal containing controlled distributions of atomic steps has not been reported for the dissociation of chemisorbed CO.

We have previously shown that CO dissociates on the atomic step sites of Ru(109) [41], and also that Li atoms adsorbed on the Ru(109) drastically enhance the dissociation of the C-O

chemical bond of coadsorbed CO molecules even at 85 K [270] as observed by infrared spectroscopy. Further dissociation of CO molecules after annealing up to 160 K is attributed to the migration of the adsorbates (Li and CO) to the atomic step sites [270].

This work extends the previous infrared studies [270] by means of the investigation of the efficiency of the $^{12}C^{16}O + {}^{13}C^{18}O \rightarrow {}^{12}C^{18}O + {}^{13}C^{16}O$ reaction in the presence Li of on both Ru(001) and Ru(109). In addition, the spectroscopic detection of the Li_xCO_y /Ru surface species is investigated.

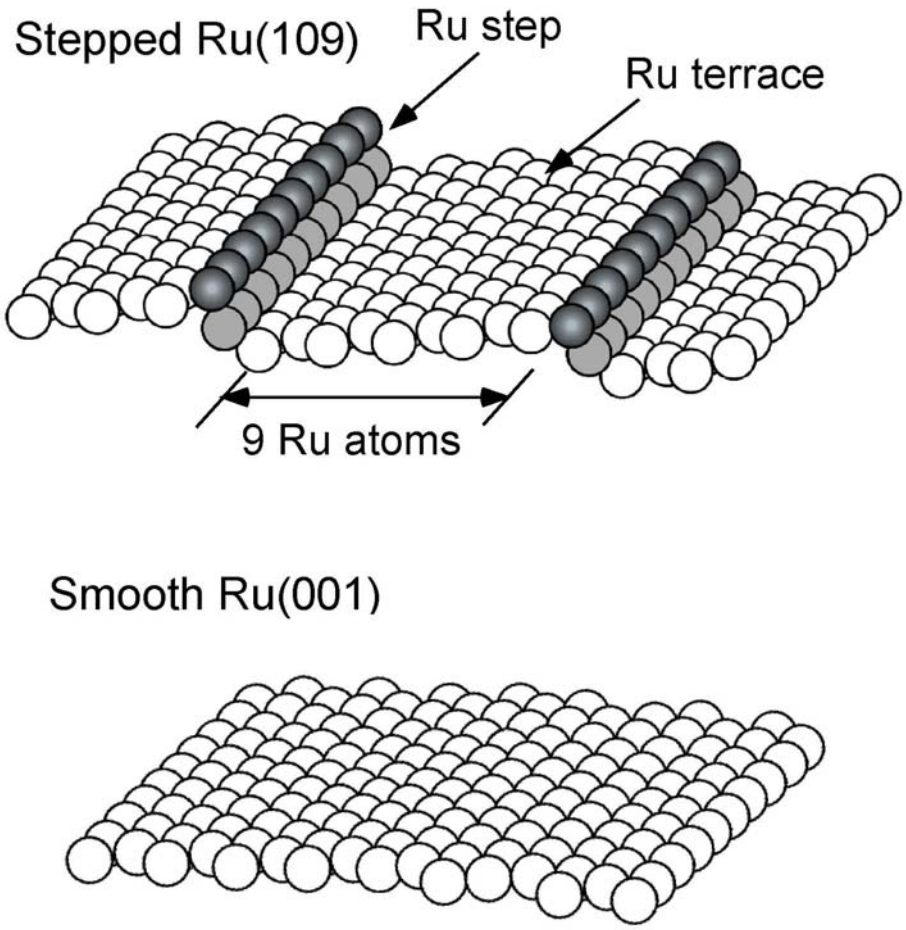

Figure 79: Schematic of Ru(001) and Ru(109) surfaces.

9.3 EXPERIMENTAL

All of the experiments reported here were performed in a stainless steel ultrahigh vacuum (UHV) chamber which was discussed in detail in Chapter 2. The experimental conditions are discussed in detail in various sections of Chapter 2. The infrared reflection-absorption spectra were collected using 2 cm^{-1} resolution averaged over 2000 scans.

9.4 RESULTS

Figure 80 shows a comparison of the CO TPD spectra from both Ru crystals. These results are very similar to those reported in previous work [41,42,94]. It is noted that for Ru(109), a high temperature CO state, labeled as β_{CO}, is evolved above ~480 K. This state originates from recombinative CO desorption from the step sites on Ru(109) and is not present on the smooth Ru(001) surface.

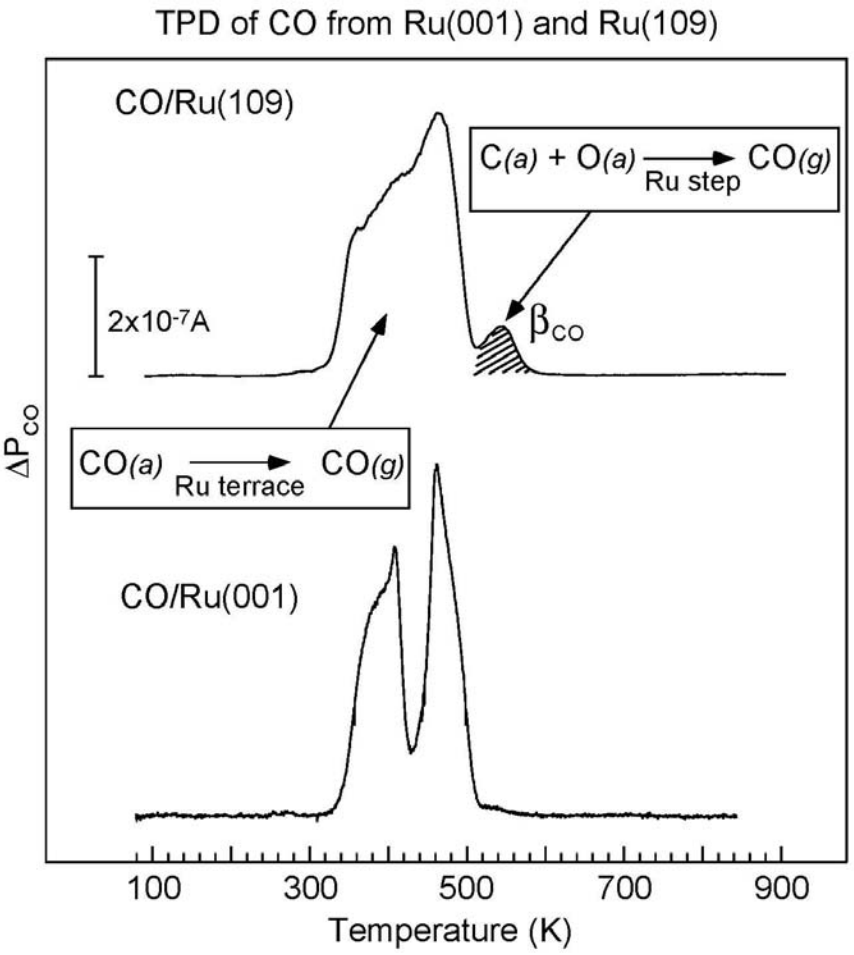

Figure 80: CO TPD spectra obtained from CO adsorbed on Ru(109) and Ru(001) up to saturation. Recombinative desorption of CO from Ru steps is emphasized by the hatched area (labeled as β_{CO}) [41].

Figure 81 shows a comparison of the desorption of isotopomers of CO in the isotopic scrambling experiment in which $^{12}C^{16}O$ and $^{13}C^{18}O$ are adsorbed together in a 50:50 ratio. In agreement with previous work [41,42], in Figure 81a, the isotopic scrambling reaction is observed for β-CO on Ru(109) above ~480 K, but the α-CO species does not exhibit isotopic scrambling. For Ru(001), in Figure 81b, little isotopic scrambling is observed, and that which is seen probably occurs on natural step defects.

When a small amount of Li is added, it is seen that all adsorbed CO (θ_{CO} = 0.08) molecules are isotopically scrambled on Ru(109) at θ_{Li} = 0.05 ML, but on Ru(001), only about

1/2 of the adsorbed CO is isotopically scrambled even at a higher Li coverage of 0.1 ML. For both Ru crystals, the isotopically scrambled CO desorption is observed to be shifted upwards slightly in temperature by Li adsorption.

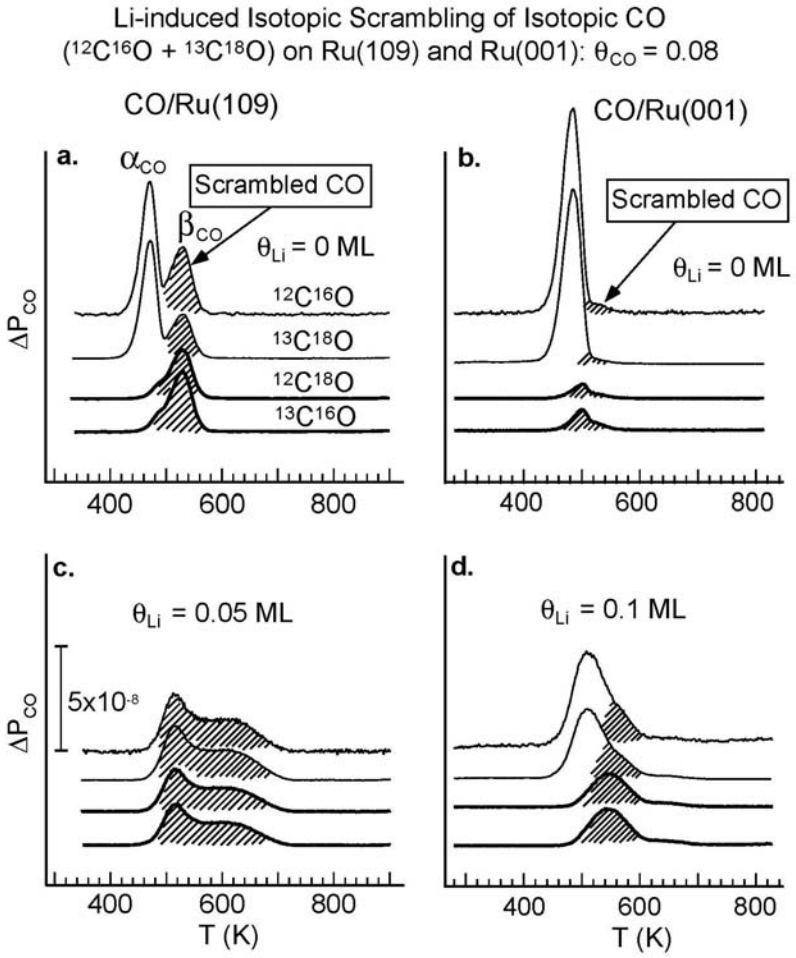

Figure 81: a **and** b **show CO TPD spectra obtained from isotopic CO mixtures (**$^{12}C^{16}O$**:**$^{13}C^{18}O$ **= 50: 50) adsorbed on the Ru(001) and Ru(109) surfaces.** c **and** d **are the TPD results from CO adsorbed on Li-covered Ru surfaces at low Li coverages. The hatched areas represent scrambled CO molecules. The CO coverage is fixed at** θ_{CO} **= 0.08, while the Li coverage is varied up to ~0.1 ML.**

Figure 82 shows infrared spectra of CO from CO molecules adsorbed on both Ru single crystal surfaces (θ_{CO} = 0.08) with coadsorbed Li at 85 K. On clean Ru crystals, the C-O stretching mode of CO adsorbed on both Ru surfaces appears near 2003 cm^{-1} on Ru(001) and near 1996 cm^{-1} on Ru(109). When a very small amount of Li is adsorbed (θ_{Li} ~ 0.02 ML), a clear

difference in the observed C-O stretching modes is observed. While only CO species with the carbonyl stretch mode at ~1986 cm^{-1} are observed on stepped Ru(109), *two distinct types of carbonyl stretching modes are observed on the Li-treated Ru(001) surface, near 1990 cm^{-1} and near 1834 cm^{-1}*. The CO band at ~1834 cm^{-1} for Ru(001) is redshifted from the original CO band (2003 cm^{-1}) by ~170 cm^{-1}.

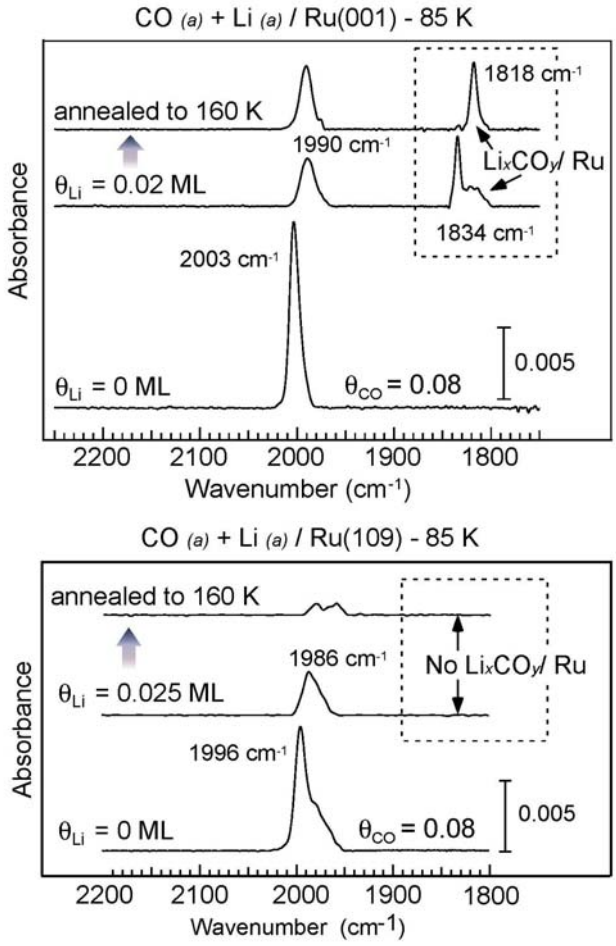

Figure 82: Infrared spectra of $^{12}C^{16}O$ taken at 85 K from co-adsorbed CO (θ_{CO} = 0.08) and Li (θ_{Li} = 0.02 ML) on Ru(001) and Ru(109) surfaces. The spectra taken after flashing the (CO+Li)-covered surfaces up to 160 K are also shown. No CO desorption occurs in these experiments.

When the Ru substrates are annealed up to 160 K, notable variations in the spectra for the two crystal surfaces are also observed. On Ru(109), the species at 1986 cm^{-1} loses significant intensity and shifts somewhat; on Ru(001), the analogous species does not shift appreciably and gains intensity. Also, the band at 1834 cm^{-1} shifts to 1818 cm^{-1} on Ru(001).

It is likely that the species possessing the large redshift (~1834 cm^{-1}) is a Li_xCO_y complex, and that the small redshift of the remaining CO species is due to long range effects of Li atoms on chemisorbed CO, as postulated previously for the K+CO/Ni(111) system [287].

9.5 DISCUSSION

In our previous report [270], extensive dissociation of CO is observed by infrared spectroscopy when Li and CO are coadsorbed on the stepped Ru(109) even at 85 K. As the substrate temperature is raised up to 160 K, further CO dissociation is observed.

The results of Figure 81 confirm the C-O bond dissociation of CO molecules in a different way. We define the desorption of isotopically scrambled CO as occurring when a statistically random mixture of CO isotopomers is evolved. In Figure 81, these regions are shown as hatched regions. The non-hatched regions do not involve recombination of C+O species. By probing scrambled isotopic CO molecules, the enhancement induced by Li atoms is compared between the two Ru crystals. It is seen that the fraction of isotopically scrambled CO is enhanced at very low Li coverages on both Ru crystals. For the same amount of CO molecules (θ_{CO} = 0.08), complete scrambling of CO is achieved at θ_{Li} = 0.05 ML on Ru(109), while partial scrambling of CO is observed on Ru(001) at an even higher Li coverage of 0.1 ML.

The enhancement of Li-induced CO dissociation on Ru(109) compared to Ru(001), observed in Figure 81, is the result of the combination of Li and atomic step sites in causing the CO dissociation-recombination process. The same effect may also be seen on Ru(001) where the small natural defect density is postulated to enhance the effect of added Li on CO dissociation (see Figure 81b and d).

The IRAS results shown in Figure 82 also indicate the enhanced CO dissociation by Li on the stepped Ru surface at 160 K. For the high frequency species, a reduction in absorbance at 160 K is caused by dissociation on the atomic steps, promoted by Li. This effect is not observed on Ru(001).

The presence of the large redshift (1834 cm^{-1}) on Ru(001) (see Figure 82) indicates a rather short-range(direct bonding) interaction between Li and CO with its C-O bond preserved. At very low Li coverages of only ~0.02 ML, it may be seen that a species possessing a low frequency carbonyl stretching mode near 1834 cm^{-1} is produced on Ru(001), while it is not observed on Ru(109) [270]. A species with this low carbonyl stretching frequency must be due to a chemical complex between Li and CO (Li_xCO_y) as reported by others for Li [124,286] and other alkali metals [127,284,287].

The conversion of the multiple CO band to a single band at ~1818 cm^{-1} upon annealing up to 160 K may be due to a change in structure, or bonding ratio in the Li_xCO_y complex, as indicated by early report [124].

We observe that the Li_xCO_y complex can form only on Ru(001) in the absence of steps; it cannot form on the stepped Ru surface. We postulate that the reason for this difference is the preferential adsorption of Li on Ru steps at 85 K, which prevents the formation of the Li_xCO_y complex on the terrace sites of Ru(109) under the low coverage conditions probed here.

9.6 CONCLUSIONS

The Li-promotional effect on the CO dissociation is explored on two Ru crystal surfaces. The results show that ;

(1) The enhanced promotional effect of Li on stepped Ru(109) for CO dissociation is due to the cooperative role of atomic steps and Li atoms.

(2) Atomic steps prevent the formation of Li_xCO_y surface complexes by preferentially adsorbing Li atoms.

10.0 INTERACTION BETWEEN CHEMISORBED N_2 AND Li PROMOTER ATOMS: A COMPARISON BETWEEN THE STEPPED Ru(109) AND THE ATOMICALLY-SMOOTH Ru(001) SURFACES

The information contained in this chapter is based on the following research publication:

Gregg A. Morgan, Jr., Yu Kwon Kim, and John T. Yates, Jr., *"Interaction between Chemisorbed N_2 and Li Promoter Atoms: A comparison between the Stepped Ru(109) and Atomically Smooth Ru(001) Surfaces."* Surf. Sci. (2007), accepted for publication.

10.1 ABSTRACT

We present a direct side-by-side comparison of the interaction of Li atoms and N_2 molecules on the atomically stepped Ru(109) single crystal surface and on the atomically smooth Ru(001) single crystal surface using infrared reflection absorption spectroscopy (IRAS) and temperature programmed desorption (TPD). At low adsorbate coverages there is spectroscopic evidence for the formation of a $Li_x(N_2)_y$ complex on the Ru(109) surface, whereas no such complex is observed on the Ru(001) surface. This complex is due to local interactions between an adsorbed Li atom and N_2 adsorbed on the atomic steps of Ru(109). The short-range interaction near the atomic steps is characterized by the development of several highly red-shifted $\nu(N_2)$ modes in

the region of ~2130 cm^{-1} in the IR spectra. Adsorbed N_2 molecules on both Ru(109) and Ru(001) also are influenced by the long range electrostatic field produced by Li adsorbate atoms, causing a red shift in the uncomplexed N_2 species, which monotonically increases as the Li coverage in increased. On the Ru(001) surface, small coverages of N_2 influenced by the long range effect of Li are initially chemisorbed parallel to the surface resulting in the absence of infrared activity. In addition we have also found that Li does not cause N-N bond scission on Ru(001) below 250 K.

10.2 INTRODUCTION

The role of alkali promoters in heterogeneous catalysis is widespread, and surface science studies have helped to understand the electronic origin of the alkali promoter action [120,121]. Promoters such as alkali metals are known to produce positive outward electric fields in their vicinity, and in the case of adsorbed CO, these electric fields weaken the C-O bond, causing a decrease in the vibrational frequency, dissociation, and even surface complex formation [109,124,126,127]. Thus the coadsorption of K with CO induces a reduction in C-O bond strength as well as a large reduction of ν(CO) [127,284,287]. These exceptionally large redshifts are characteristic of short-range interactions present in local $K_x(CO)_y$ complexes, or even potassium carbonate [127].

In addition to species with large redshifts in the coadsorption of CO with alkali metals, it is also observed that the ν(CO) mode is more slightly shifted to lower frequency upon interaction with alkali metals, where the shift is monotonic with increasing alkali coverage. This phenomenon is thought to be due to long range interactions which involve the electric field

resulting from the global coverage of the alkali [287], and which are observed for CO species that have not undergone a larger perturbation due to local complex formation.

The small size of the Li atom and its large surface dipole moment when adsorbed on Ru surfaces [156] suggests that it will be a good model alkali promoter atom for these studies. It has been reported, for example, that Li promotes H_2O dissociation on Ni(775) at low temperatures [268] as well as the dissociation of CO on Ru(109) at 85 K [270].

In this paper, we explore the interactions of Li atoms with chemisorbed N_2 on two surfaces- the atomically-smooth Ru(001) surface and the atomically-stepped Ru(109) surface containing double height atomic steps [42]. We ask what is the role of atomic steps on the alkali- N_2 interactions, observing both long and short range N_2-Li interactions. Fragmentary information exists concerning this question. It has been found that K promotes the dissociation of CO on Cu, but only in the presence of atomic step sites [280,289]. In another example, the dissociation of CO on Ru containing adsorbed Li atoms is enhanced when the atomically-stepped Ru(109) surface is compared with Ru(001) [290].

The Ru-N_2 chemisorption bond is weak compared to the Ru-CO bond. It is found that the Ru-N_2 bond is formed by donation of σ-electrons from the N_2 to Ru [33,119] which is exactly opposite to the bonding motif for CO, where back donation from the metal into the $2\pi^*$ orbital dominates.

Because of the high frequency sensitivity, infrared reflection absorption spectroscopy (IRAS) is employed in these studies, along with careful control of both the Li and N_2 coverage. In addition, temperature programmed desorption (TPD) is used to measure the coverage of both N_2 and Li. The same apparatus is employed for studies of both the Ru(001) surface and the Ru(109) surface facilitating accurate cross comparisons between the two crystals.

10.3 EXPERIMENTAL

All of the experiments reported here were performed in a stainless steel ultrahigh vacuum (UHV) chamber which was discussed in detail in Chapter 2. The experimental conditions are also discussed in detail in Chapter 2. The infrared reflection-absorption spectra were collected using 2 cm^{-1} resolution averaged over 2000 scans.

10.4 EXPERIMENTAL RESULTS

10.4.1 Li Addition to Preadsorbed N_2/Ru(001) and N_2/Ru(109)

10.4.1.1 Ru(001)

Figure 83a shows the spectral developments when Li atoms are deposited on Ru(001) containing θ_{N_2} = 0.14 at 85 K. The value of $\nu(N_2)$ monotonically decreases from 2208 cm^{-1} as the coverage of Li is increased, indicative of a long-range interaction between N_2 molecules and the global Li coverage. In addition, the FWHM of the N_2 vibrational band broadens to ~ 22 cm^{-1} as its integrated intensity decreases and as the frequency of the band center decreases to ~2132 cm^{-1}.

10.4.1.2 Ru(109)

Figure 83b shows the spectral developments for Li deposition on Ru(109) containing θ_{N_2} = 0.17 at 85 K. Initially there is a single vibrational band at 2199 cm^{-1}, corresponding to zero coverage of Li. For even the smallest Li coverage, θ_{Li} = 0.022, two separate effects are observed

when Li is deposited: (1) the slight shift of the original $\nu(N_2)$ mode to lower frequency; and (2) the production of three more strongly red-shifted $\nu(N_2)$ bands which are shown cross hatched in Figure 83b. This is evidence for two types of Li-N_2 interactions. One kind of interaction causes a relatively small frequency shift of uncomplexed N_2 molecules related to the global coverage (and the electric field) caused by the adsorbed Li. A second type of interaction causes the development of strongly perturbed N_2 molecules in $Li_x(N_2)_y$ complexes which exhibit larger negative frequency shifts. The $Li_x(N_2)_y$ complex is not necessarily a stoichiometric complex, but instead is likely due to a short-range interaction between adsorbed Li atoms and adsorbed N_2 molecules. As the coverage of deposited Li is increased, the integrated absorbance of the uncomplexed N_2 species gradually decreases as the complexed N_2 species develop. Furthermore, for increasing Li coverages, a monotonic decrease in $\nu(N_2)$ for the uncomplexed N_2 species is seen, and the suggestion of a similar gradual small frequency shift is also seen for the $\nu(N_2)$ modes associated with the $Li_x(N_2)_y$ species. In the limit, all uncomplexed N_2 species have been converted to complexed species, resulting in a broad $\nu(N_2)$ absorption band (FWHM = 29 cm^{-1}) centered at 2112 cm^{-1}.

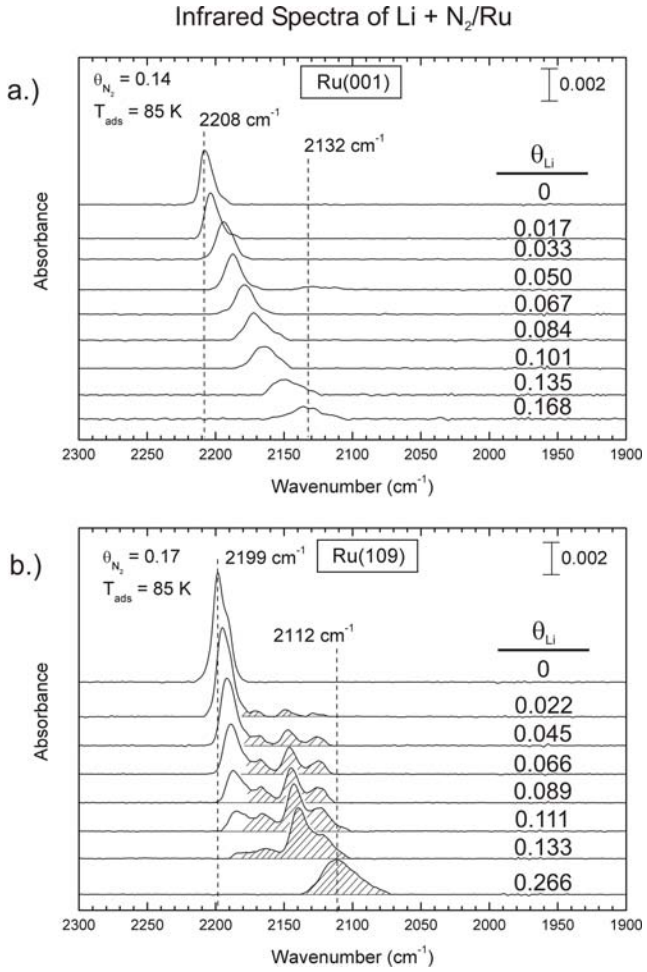

Figure 83: IR spectra following Li deposition on N_2 precovered Ru surfaces: (a) Ru(001) and (b) Ru(109). All spectra were recorded at 85 K and were averaged over 2000 scans with a resolution of 2 cm^{-1}.

It is of interest to compare on both surfaces the shift of $\nu(N_2)$ for the uncomplexed species, using this shift as a measure of the electric field caused by the global distribution of Li atoms. This is shown in Figure 84. The global effect of Li on reducing the frequency of uncomplexed N_2 species present on the stepped Ru(109) crystal is only ~ 1/3 of that observed for the atomically-smooth Ru(001) crystal. This indicates that significant electrostatic screening effects of the Li dipole are present on Ru(109) as measured by the frequency shift of uncomplexed chemisorbed N_2 molecules.

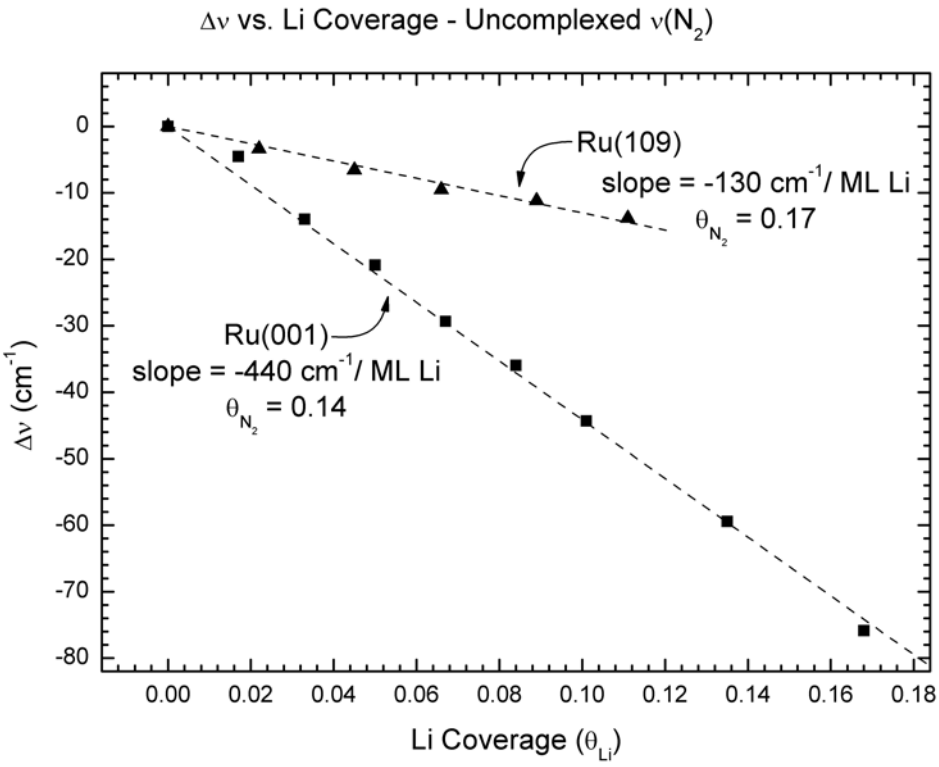

Figure 84: $\Delta\nu(N_2)$ vs θ_{Li} for Ru(109) and Ru(001). 1 ML on the Ru(109) surface corresponds to θ_{Li} = 0.86 and 1 ML on the Ru(001) surface corresponds to θ_{Li} = 0.76 based on Li TPD measurements.

10.4.2 Effect of Added Li to Step-bound N_2 on Ru(109)

By adjusting the temperature of N_2 adsorption on Ru(109) to 170 K, it is possible to populate only the step sites with chemisorbed N_2 [43,44]. This has permitted an experiment in which the effect of added Li can be measured for only the step-bound N_2. Figure 85 shows this experiment, where the starting coverage, θ_{N_2}, is 0.05. Initially, $\nu(N_2)$ = 2199 cm^{-1}, and at θ_{Li} = 0.018 the beginning of the formation of short-range $Li_x(N_2)_y$ complexes is first observed as shown by the cross-hatched spectral features. As the Li coverage is increased, uncomplexed step-bound N_2 species slowly disappear as complexed species form. This result, considered with

the data in Figure 83a and Figure 83b, suggest that the presence of atomic steps provides sites capable of forming $Li_x(N_2)_y$ species and that N_2 molecules adsorbed at atomic step sites are preferentially involved in the formation of the complex.

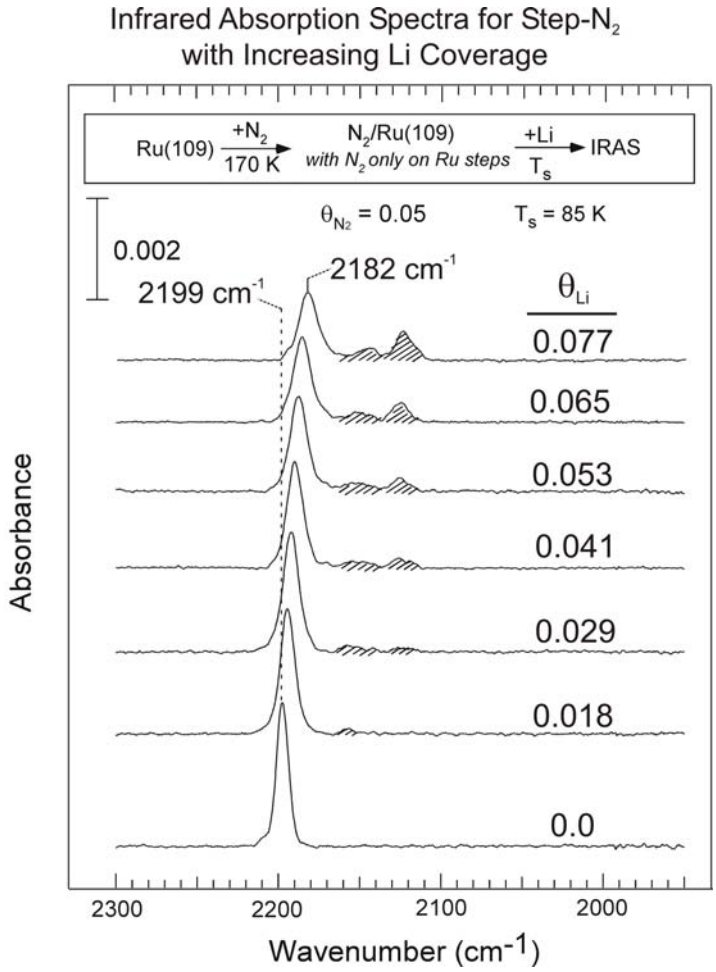

Figure 85: IR spectra (recorded at 85 K) of $^{14}N_2$ adsorbed on the step sites of Ru(109) at 170 K. Li was subsequently deposited on N_2/Ru(109) at 85 K.

10.4.3 Addition of N_2 to Li-precovered Ru(001) and Ru(109)

The interaction of chemisorbed N_2 with preadsorbed Li was investigated to determine whether new effects are present when the order of addition of the adsorbed species was reversed. Figure

86a shows experiments at 85 K, where Ru(001) was dosed with Li to a coverage of $\theta_{Li} = 0.08$. The initial N_2 coverage ($\theta_{N_2} = 0.021$) produces a mode at ~ 2194 cm^{-1}. This frequency is below the singleton mode observed for N_2 adsorption on clean Ru(001) [33], exhibiting a shift of -19 cm^{-1} from the singleton frequency on clean Ru(001), due to the long range interaction between N_2(a) and Li(a). As the coverage of N_2 is increased, an additional red shift of - 8 cm^{-1} occurs. This additional shift is likely due to the packing of N_2 species within the ordered Li layer [156], causing the average N_2-Li interaction distance to decrease.

When the same experiment is performed on Ru(109), an entirely different spectral pattern emerges, as shown in Figure 86b. Here, at the lowest coverages of N_2, only strongly red shifted $\nu(N_2)$ modes are observed on the Li-precovered surface, as shown by the cross-hatched features. As the N_2 coverage is increased, the modes assigned to $Li_x(N_2)_y$ increase in integrated absorbance, and a small red shift with increasing N_2 coverage is observed. In addition, a mode at higher frequency begins to form, and to shift slightly downward in frequency with increasing θ_{N_2}, reaching 2189 cm^{-1} at the highest N_2 coverage achieved. This feature on Ru(109) is assigned as uncomplexed chemisorbed N_2, red shifted slightly by long range interaction with Li(a).

Comparison of Figure 86 with experiments done with the opposite order of addition of adsorbates, Figure 83, shows that the same general behavior occurs irrespective of the order of addition of adsorbates to both Ru(001) and Ru(109).

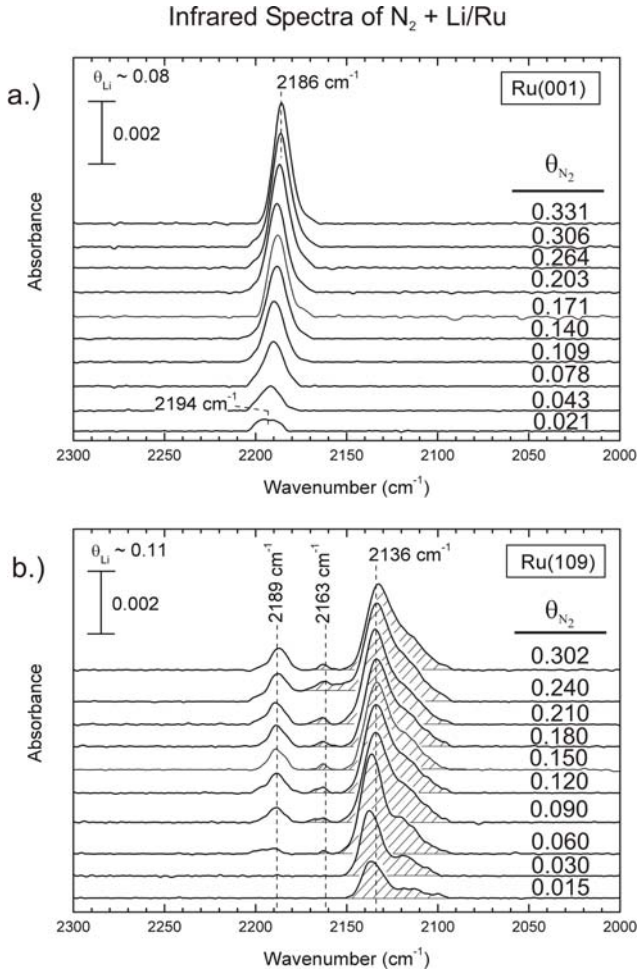

Figure 86: IR spectra of N_2 adsorption on Li-precovered Ru surfaces: (a) Ru(001) and (b) Ru(109).

10.4.4 Evidence of an Invisible N_2 Species on Li/Ru(001)

Using Ru(001) containing preadsorbed Li at θ_{Li} = 0.18 we discovered that the long range interaction between N_2(a) and Li(a) initially produces a surface species with very low or zero absorbance. Figure 87 shows a comparison of the spectral developments for N_2 adsorption on clean Ru(001) and N_2 adsorption on Li/Ru(001). Note the factor of 10 difference exists in the absorbance scales. In all cases on Li/Ru(001) the frequency of the adsorbed N_2 species is less

than the frequency on clean Ru(001), indicative of the long range electrostatic interaction between N_2(a) and Li(a).

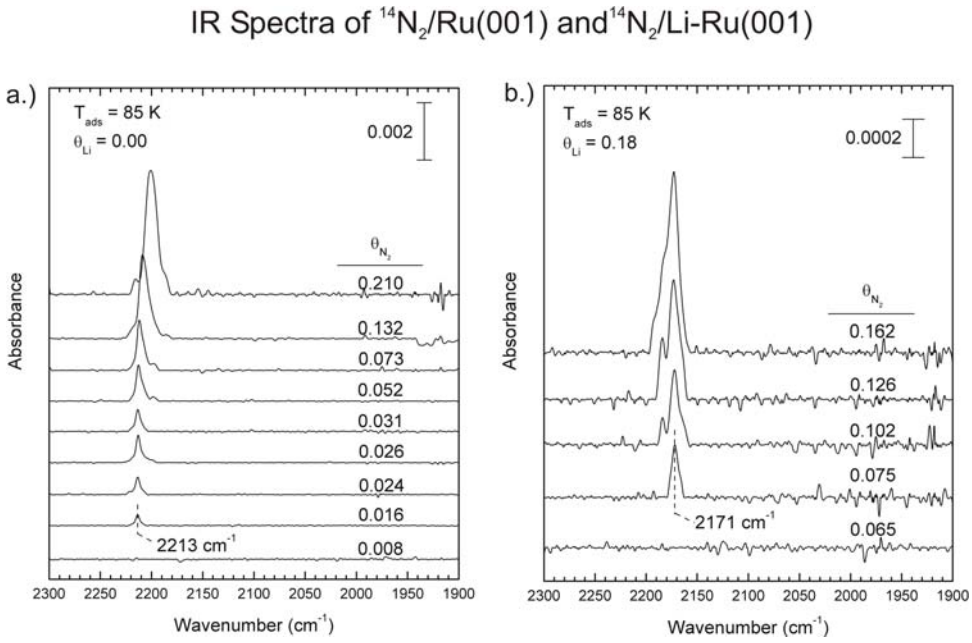

Figure 87: IR spectra of N_2 deposited at 85 K on (a) clean Ru(001) and (b) Li-precovered Ru(001) surfaces.

In addition however, the integrated $\nu(N_2)$ absorbance observed in Figure 87b for low coverages of N_2 is zero or near zero, and over the entire N_2 coverage range examined, the integrated absorbance of the $\nu(N_2)$ feature is smaller on Li/Ru(001) than on clean Ru(001). This comparison is shown in Figure 88, where initially the $\nu(N_2)$ feature exhibits zero integrated absorbance at the sensitivity level of these measurements up to $\theta_{N_2} = 0.065$. We interpret this as being due to the formation of highly inclined N_2 species on Ru(001), where the tilting effect is caused by the electrostatic field produced by long range effects of Li. Such inclined N_2(a) species would not be expected to exhibit a stretching mode in IRAS because of the cancellation of the dynamic dipole with its image in the metal. The negative frequency shift for the long range interactional effect on Ru(001) is significantly greater than that observed on Ru(109), where immediate $Li_x(N_2)_y$ formation is observed.

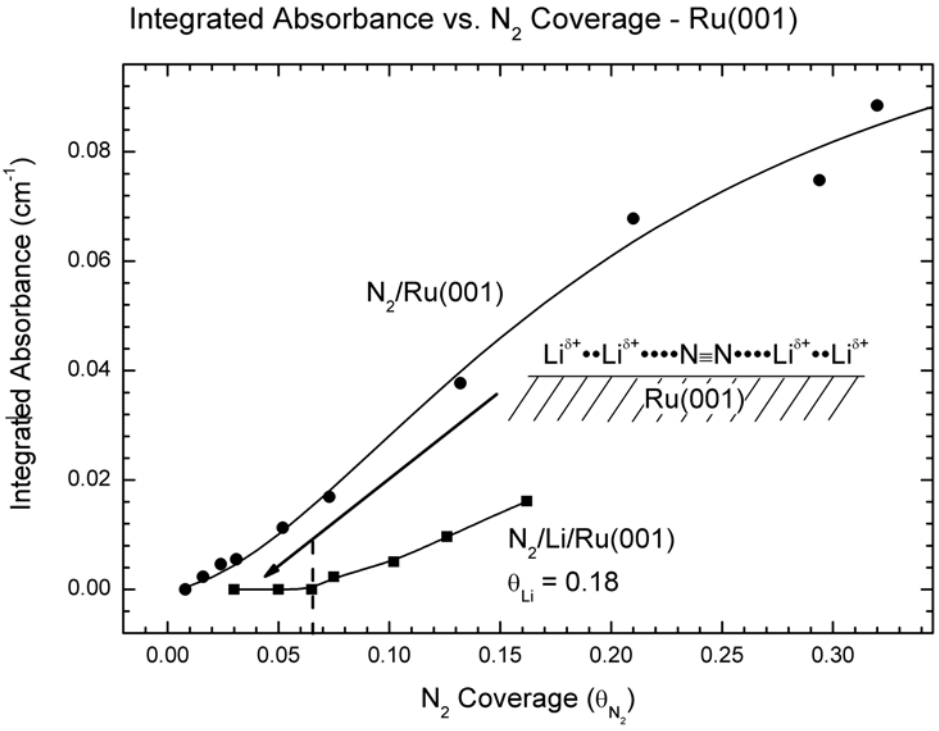

Figure 88: Integrated absorbance vs. θ_{N_2} for N_2 adsorption on clean and Li-precovered Ru(001) surfaces. The line is drawn in both cases to guide the eye.

10.4.5 Lack of N_2 Dissociation on Li/Ru(001)

It is well known that atomic step sites promote N_2 dissociation at elevated temperatures [34,35,43,44], whereas the Ru(001) surface is inactive for dissociation. Therefore, Ru(001) provides an ideal surface to test the role of Li promoter atoms on the catalyzed dissociation of chemisorbed N_2. Figure 89 shows a comparison of the temperature programmed desorption behavior of an equimolar mixture of $^{14}N_2$ and $^{15}N_2$, searching for the production of $^{14}N^{15}N$ as a result of N_2 dissociation. On clean Ru the low temperature states are observed to desorb without the formation of $^{14}N^{15}N$. The tiny amount of desorbing mass 29 species is due to the isotopic impurity level of the adsorbed N_2, which contained 2% $^{14}N^{15}N$. Note that no N_2 species are

evolved at high temperatures for clean Ru(001) in Figure 89a. In Figure 89b there is also no evidence of any isotopic mixing during the desorption of nitrogen as detected by the lack of formation of $^{14}N^{15}N$ in the low temperature desorption states. The high temperature state in the region of 700 K is due to the desorption of small amounts of contaminant CO species originating from the Li evaporator.

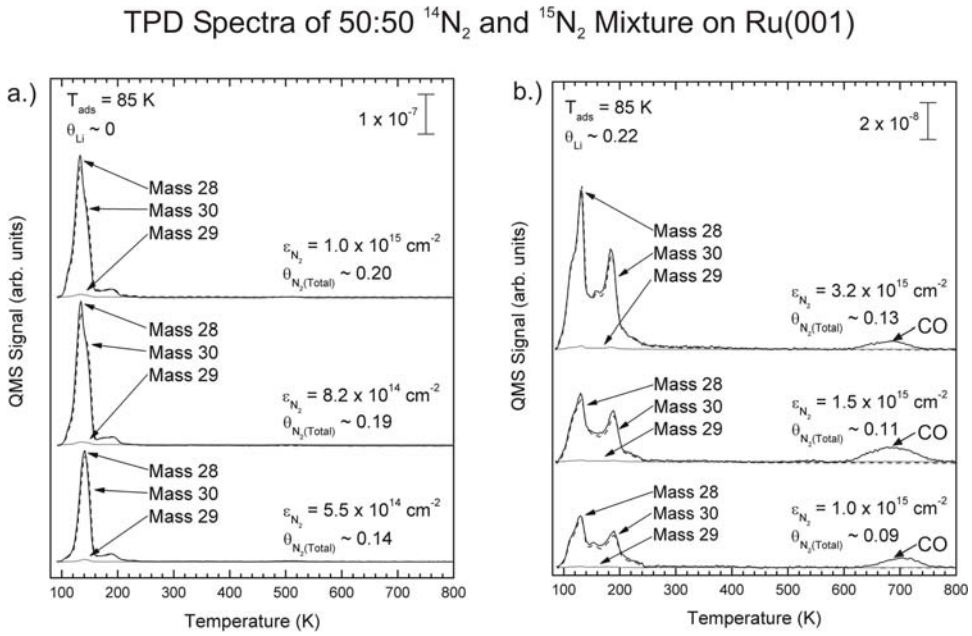

Figure 89: TPD of 50%-50% isotopic mixture adsorbed on (a) clean Ru(001) and (b) Li-precovered Ru(001) for various N_2 coverages. The heating rate was 2.0 K/s.

10.5 DISCUSSION

The results observed here for the Li-N_2 interaction on Ru single crystal surfaces bears a remarkable resemblance to the general observations made for K-CO interactions on Ni(111) [287,291]. In both systems, evidence for the formation of a mixture of local chemical complexes with the alkali, mixed with adsorbate species influenced only by long range electrostatic interactions with the alkali, have been found. These two modes of interaction are particularly

prominent spectroscopically at lower alkali metal coverages, where separate vibrational modes associated with each type of interaction are seen in the individual spectra.

10.5.1 Formation of $Li_x(N_2)_y$ Surface Complexes Exclusively on Ru(109) at Low Surface Coverages

Based on the IR spectral behavior, clear evidence for local complex formation is observed almost immediately upon adding small coverages of Li to N_2/Ru(109) (Figure 83b) or by adding N_2 to Li/Ru(109) (Figure 86b). In both cases a discrete set of low frequency $\nu(N_2)$ bands develops as the high frequency, non-complexed N_2 species is consumed (the non-complexed species is not formed initially in the latter case). The formation of the complex is unique for the stepped Ru(109) surface. It is well known that both N_2 and Li are mobile species at the adsorption temperature of 85 K [156], and also that both N_2 and Li preferentially bind to atomic step sites due to the higher binding energy of these sites for these adsorbates [44,156]. Thus, the step sites are able to bring the mobile N_2 and Li atoms together to form the localized $Li_x(N_2)_y$ species in an energetically stabilized complex on or near the atomic steps. The strong interaction of the two adsorbed species is probably due to short-range interactions rather than the formation of an actual stoichiometric complex. Species of this type do not form at low coverages of N_2 and Li on the atomically-smooth Ru(001) surface. It is very unlikely that comparable $Li_x(N_2)_y$ complexes exist in the absence of the appropriate Ru surface site, and indeed no examples of chemical compounds involving Li and N_2 are reported in the literature [292].

10.5.2 Contrary Behavior for $Li_x(CO)_y$ Formation on Ru Single Crystal Surfaces

In studies very similar to this, we have observed $Li_x(CO)_y$ formation only on the atomically smooth Ru(001) surface, using IRAS [290]. Careful comparisons to the behavior on Ru(109) were carried out finding no evidence for the complex on the stepped single crystal surface. It was postulated that in the case of low coverages of CO and Li on the stepped surface, the strong preference for CO adsorption on the step sites prevented $Li_x(CO)_y$ formation on the surface, an argument just opposite to that proposed here for the Li-N_2 system. It is likely that the weaker affinity of the Ru step sites for N_2 is responsible for this contrary behavior compared to CO. On Ru(001), the $Li_x(CO)_y$ complex formation is postulated to occur in the ordered arrays of Li atoms present on the surface [290].

10.5.3 Behavior of Li + N_2 at High Li Coverages

At high coverages of Li, the frequency of the broadened $\nu(N_2)$ mode observed on Ru(001) and on Ru(109) approaches a similar value in the range of ~2110 to ~2130 cm^{-1} (Figure 83a and Figure 83b). At these high Li coverages, the role of the atomic steps in controlling complex formation becomes less evident, and it is likely that a complicated mixture of N_2(a) and Li(a) species, influenced both locally and by long range electrostatic effects, is formed.

10.5.4 Long Range Li-N_2 Interactions on Ru Surfaces

The role of long range Li-N_2 interactions is particularly evident at low Li coverages for Ru(001) because of the absence of short-range $Li_x(N_2)_y$ complexes on this surface. Thus, in Figure 83b,

the two modes of interaction result in $\nu(N_2)$ vibrational bands that are observed at well separated $\nu(N_2)$ frequencies, and are evident at low θ_{Li}. The dipole moment of Li at zero coverage on Ru(001) is 10 D [156]. We may compare this to K(a) on Ni(111), which exhibits a zero coverage dipole moment of 7.4 D [287]. Both surfaces are atomically flat. On Ni(111), using CO as the detector of the influence of K, it was found, as with $Li/N_2/Ru(001)$, that smooth shifts of $\nu(CO)$ were seen as θ_K was increased [287], and a lattice sum model for the effect of the global electric field on the CO frequency was developed. We believe that the long-range Li-N_2 interactions observed here are also due to a buildup of the local electric field around uncomplexed N_2 species. Hence the uncomplexed N_2 species sample an electric field caused by the global coverage of surrounding Li atoms, and the negative frequency shift of $\nu(N_2)$ is due to the Stark effect [287]. The range of the interaction extends beyond 10 Å for the Li dipole based upon estimates made for K/CO/Ni(111) [287].

10.5.5 Production of Tilted N_2 Species due to Long Range Li-N_2 Interactions on Ru(001)

Figure 87 and Figure 88 show that on Ru(001) covered with low coverages of Li, there is a strong diminution of infrared intensity at all N_2 coverages, compared to comparable surface conditions on Ru(001) containing no Li. When N_2 is initially adsorbed on Li/Ru(001), no IR intensity is visible until $\theta_{N_2} = 0.065$. This observation suggests that initially the long range electrostatic interaction causes the N_2 molecules to tilt parallel to the surface, causing the N_2 dynamic dipole to be cancelled by image effects in the substrate. Since the dipole moment of Li at zero coverage is 10 D on Ru(001), compared to 6.0 D on Ru(109) (producing less electrostatic field) [156], the observation of the tilting effect on Ru(001) may be explained by this difference

in Li dipole moment. Also, the redshift in $\nu(N_2)$ on Ru(109) [-130 cm^{-1}/ML Li] is only about 1/3 of that found on Ru(001), indicating that long range electrostatic effects are smaller on the stepped Ru surface.

In addition to the higher global electrostatic field caused by Li on Ru(001) compared to Li on Ru(109), the presence of highly tilted N_2 species would be expected to contribute to additional red-shifting of $\nu(N_2)$ due to more favorable interactions of the N_2 dynamic dipole with its image in the metal substrate. Thus, the ~ 3-fold difference in the red shift seen in Figure 84 is due to a combination of physical effects on adsorbed N_2 molecules.

10.5.6 Absence of N-N Bond Scission on Li/Ru

Figure 89 shows that isotopic mixing does not occur in the low temperature desorption states on Ru(001) when N_2 is adsorbed in the presence of adsorbed Li. The lack of evidence for isotopic mixing between adsorbed isotopomer N_2 molecules suggests that Li is a poor promoter for the dissociation of N_2 on Ru at $T < 250$ K. The interaction of K and N_2 on Fe(111) indicates the development of a precursor to the dissociation of N_2 at low temperatures [293]. In addition, DFT calculations have indicated that the barrier for N_2 dissociation will be lower in the presence of larger alkali metals compared to Li [120].

10.6 CONCLUSIONS

The coadsorption of N_2 and Li on both Ru(001) and the atomically-stepped Ru(109) surface has been studied using infrared reflection absorption spectroscopy and temperature programmed desorption. The following was discovered:

(1) Evidence for the formation of a $Li_x(N_2)_y$ complex is found at low adsorbate coverages on the Ru(109) surface. This complex is not observed on Ru(001). It is likely that the complex is non-stoichiometric.

(2) The $Li_x(N_2)_y$ complex is characterized by several $\nu(N_2)$ modes in the 2130 cm^{-1} region. It is postulated that mobile Li and N_2 molecules preferentially adsorb, even at 85 K, in the vicinity of the atomic steps on Ru(109), where the additional stabilization of these species on step sites leads to the complex formation.

(3) In addition to short range Li-N_2 interactions in the complex on Ru(109), it is found on both Ru(001) and Ru(109) that long range electrostatic effects exist between Li(a) and N_2(a) molecules not involved in complex formation. These interactions produce smaller red shifts in $\nu(N_2)$, causing the frequency to monotonically decrease as θ_{Li} increases. Because of Li surface dipole screening effects for Li atoms at atomic steps on Ru(109) and for another reason mentioned in point (4) below, the long range red shift is about 1/3 of that observed for Ru(001).

(4) On Ru(001), where at low coverages only the long range electrostatic interaction effect exists, small coverages of N_2 can be chemisorbed without the production of a visible IR band. This suggests that at low coverages of Li and N_2, the N_2 molecules are tilted parallel to the surface, resulting in cancellation of the N_2 dynamic dipole as a result of image effects in the substrate. At higher N_2 coverages, IR intensity appears as N_2 species with smaller tilt angles develop, but the infrared intensity is always less than on Li/Ru(001) for equivalent coverages.

Tilting of N_2 species on Li/Ru(001) would be expected to also contribute to the larger red shift observed on Ru(001) compared to Ru(109) at comparable Li coverages as a result of image effects in the substrate.

(5) No evidence for N-N bond scission is observed on Li/Ru(001) below 250 K indicating that N_2 dissociation is not promoted by Li at these low temperatures.

APPENDIX A

ABSOLUTE CALIBRATION OF THE MICROCAPILLARY ARRAY BEAM DOSER

A microcapillary array molecular beam doser as shown in Figure 90 was employed in these studies for the accurate delivery of gas phase adsorbates to the surface of the crystal. The main advantage of using a molecular beam doser as compared to system dosing accomplished by backfilling the chamber through a leak valve is the minimization of the background pressure rise. The molecular beam doser must be absolutely calibrated for accurate and reproducible delivery of adsorbates.

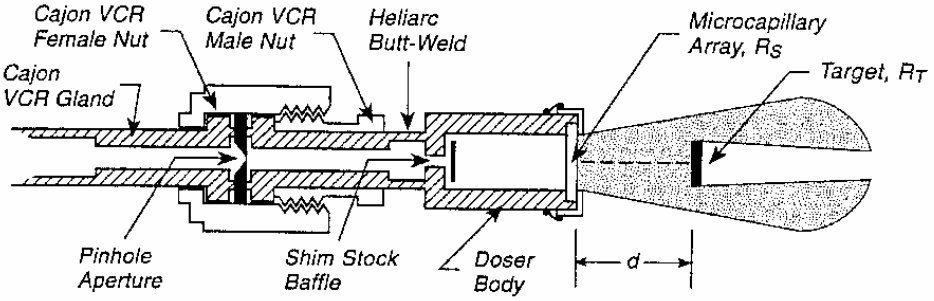

Figure 90: Design of a microcapillary array beam doser for accurate gas exposures to a single crystal surface. From Ref [134].

The main components of the doser are the pinhole aperture and the microcapillary array. The pinhole aperture used the experiments presented here was on the order of 5 μm diameter.

Upon passing through the aperture the gas molecules strike a shim stock baffle where the direction of the molecules becomes randomized. The gas then passes through the microcapillary array, resulting in a collimated flux of molecules. The microcapillary array consists of individual capillaries that are 10 μm in diameter and 1000 μm in length. The capillaries are then fused together to form a hexagonal array [134].

The absolute calibration of the molecular beam doser was accomplished using a somewhat modified version of the King and Wells method [294,295] for determining the sticking coefficient using a molecular beam of known flux that was similar to the method described by Kurtz et al. [296]. The intercepted fraction of the beam by the crystal was found to be ~28 % for Ru(109) and ~42 % for Ru(001) for our crystal-doser geometry, determined experimentally by the adsorption of low vapor pressure compounds such as HCHO, CH_3CHO, and $(CH_3)_2CO$, which have an initial sticking coefficient very close to unity on Ru at 85 K forming condensed multilayers as the coverage is increased. CO was used to calibrate the doser conductance and the QMS (UTI 100C) was used to monitor the partial pressure of CO (mass 28) throughout the calibration and a typical uptake curve of CO can be seen in Figure 91.

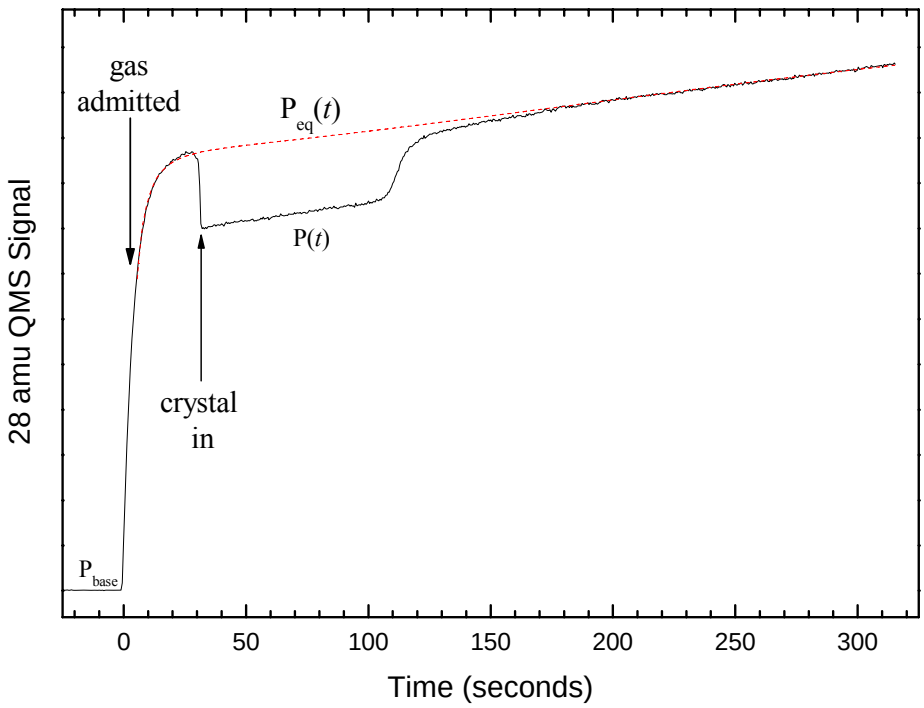

Figure 91: Uptake curve for CO adsorption on Ru(109) at 88 K.

After a steady baseline is achieved for mass 28, the CO is then admitted to the chamber causing the pressure to immediately rise from the baseline position, P_{base}, to a higher pressure, P. Within a minute or so the rate of incoming gas becomes almost balanced with the pumping speed of the chamber reaching a steady state equilibrium, P_{eq}. After reaching the equilibrium pressure, the crystal is rapidly translated into the molecular beam, causing the front side of the crystal to adsorb the gas, and hence the CO pressure to drop. The magnitude of the CO pressure drop is attributed to the fraction of gas adsorbed from the beam, which is determined from the sticking coefficient, S, as well as the fraction of the beam, f, intercepted by the crystal (f = 0.28 for Ru(109) and f = 0.42 for Ru(001) in our case). The sticking coefficient can be calculated as follows:

$$S = \frac{1}{f} * \frac{(P_{eq} - P(t))}{(P_{eq} - P_{base})} \tag{A.1}$$

where *P(t)* is the pressure at time t . As all of the available surface ruthenium sites become saturated, the sticking coefficient gradually drops to zero, the adsorption process stops, and the CO pressure curve merges with the steady level, P_{eq}. The P_{eq} is not exactly constant but instead gradually rises as the pumping speed of the chamber walls decreases during the exposure of CO to the chamber. It was necessary to simulate the behavior of $P_{eq}(t)$ as shown by the dashed line in Figure 91 in order to ensure an accurate analysis of the uptake curves. This simulation was achieved by fitting the region prior to adsorption and the region after the completion of the adsorption with a single curve.

The exposure, $\varepsilon_{beam}(t)$, from the CO molecular beam was calculated as

$$\varepsilon_{beam}(t) = C \cdot P_{ghl} \cdot (t - t_{in}) \tag{A.2}$$

where t_{in} is the time that the crystal was inserted into the beam, P_{ghl} is the pressure in the gas line behind the pinhole doser, and C is the conductance of the doser which is known from absolute calibration. In addition to the direct exposure from the doser, there is a minimal amount of background exposure (typically 2-3%) as compared to the direct exposure which was calculated as follows

$$\varepsilon_{bkg}(t) = \frac{P(t)}{(2\pi mkT)^{1/2}}(t - t_{admit}) \tag{A.3}$$

where t_{admit} is the actual time of gas admittance to the chamber.

The overall exposure is the combination of the direct exposure and the background exposure. The absolute coverage obtained from direct exposure, $\sigma(\varepsilon)$, is calculated according to the formula

$$\sigma(\varepsilon) = \int_o^{\varepsilon} S(\varepsilon) d\varepsilon \qquad \text{(A.4)}$$

where S(ε) is the sticking coefficient as a function of exposure, which changes as the adsorbate coverage increases. The background coverage was calculated using equation A.4 and incorporating equation A.3 for the background exposure, assuming a constant sticking coefficient. The direct exposure and background exposure were calculated independently of each other and then were added together to yield the total exposure vs. coverage plot below.

The resulting coverage vs. exposure data is presented in Figure 92 for Ru(109) and Figure 93 for Ru(001).

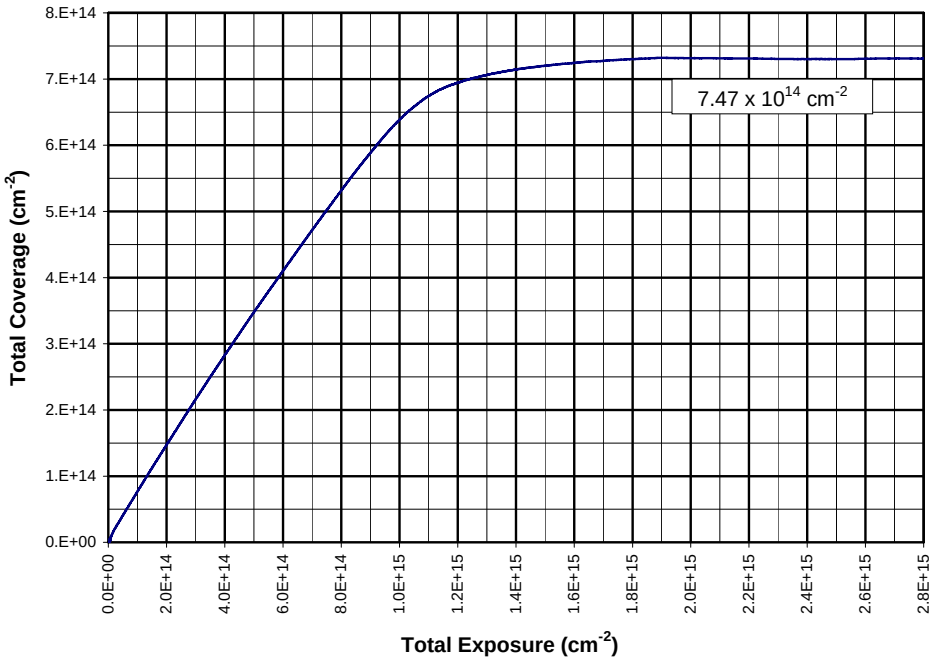

Figure 92: Coverage vs. exposure for CO adsorption on Ru(109) at 88 K. A saturation coverage corresponds to roughly 7.47×10^{14} cm^{-2} ($\theta_{CO} = 0.54$ relative to the available Ru surface atoms). The saturation coverage is achieved by an exposure of at least 1.7×10^{15} cm^{-2}.

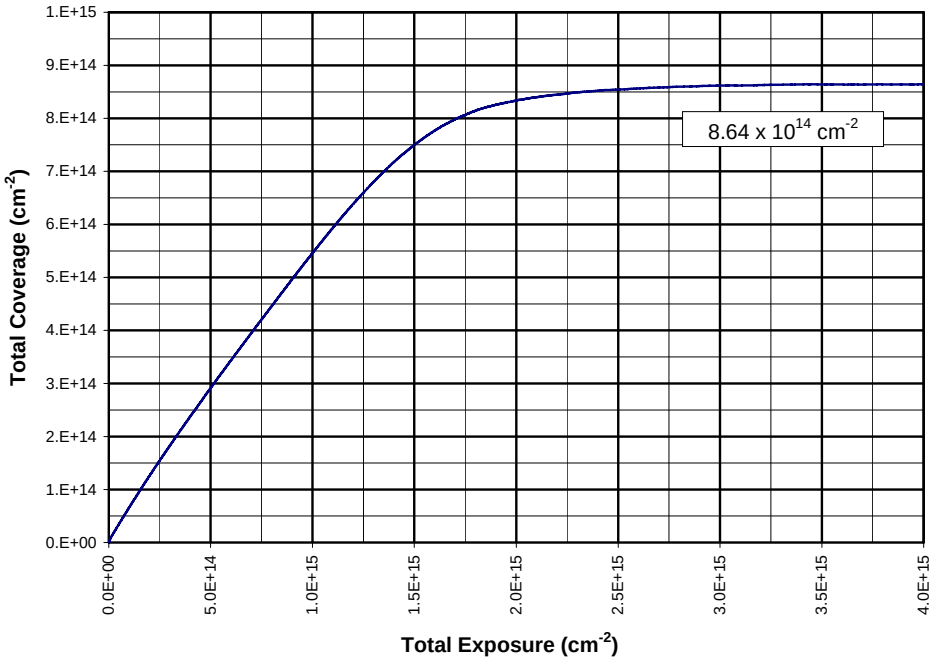

Figure 93: Coverage vs. exposure for CO adsorption on Ru(001) at 88 K. A saturation coverage corresponds to roughly 8.64×10^{14} cm^{-2} ($\theta_{CO} = 0.55$ relative to the available Ru surface atoms). The saturation coverage is achieved by an exposure of at least 2.5×10^{15} cm^{-2}.

A series of thermal desorption spectra were recorded at increasing coverage using the previously determined exposures as the starting point with a LEED image being taken following each exposure prior to each desorption spectrum. At a coverage of $\theta_{CO} = 0.33$ the $\sqrt{3} \times \sqrt{3}$ R30° structure of CO on Ru is at its maximum intensity. The area of the corresponding TPD trace with the maximum intensity of the $\sqrt{3} \times \sqrt{3}$ R30° structure of CO was used as a reference point by equating this coverage to 1/3 of the available surface atoms. In conjunction with the area of the TPD traces the saturation coverage was determined to be $\theta_{CO} = 0.54$ and $\theta_{CO} = 0.55$ (relative to the available ruthenium surface atoms) for Ru(109) and Ru(001), respectively. This information was then used to back calculate the actual conductance of the doser which was found to be 1.18×10^{13} $Torr^{-1}$ s^{-1}.

The conductance of the pinhole doser is usually determined directly by measuring the pressure drop of N_2 (or some other inert gas) behind the doser during effusion through the pinhole using a 0-10 Torr Baratron capacitance manometer. The data can then be plotted logarithmically against time, t, (as seen in Figure 94) to provide a linear curve in which the slope is related to the conductance of the pinhole by:

$$\frac{dn}{Pdt} = -\frac{V}{kT}\left[\frac{d(\ln P / P_0)}{dt}\right] \qquad \text{(A.5)}$$

where V is the volume behind the pinhole, T is the temperature in Kelvin, n is the number of molecules, and P is the backing pressure. The measured conductance of the pinhole aperture was found to be 1.14×10^{14} $Torr^{-1}$ s^{-1}.

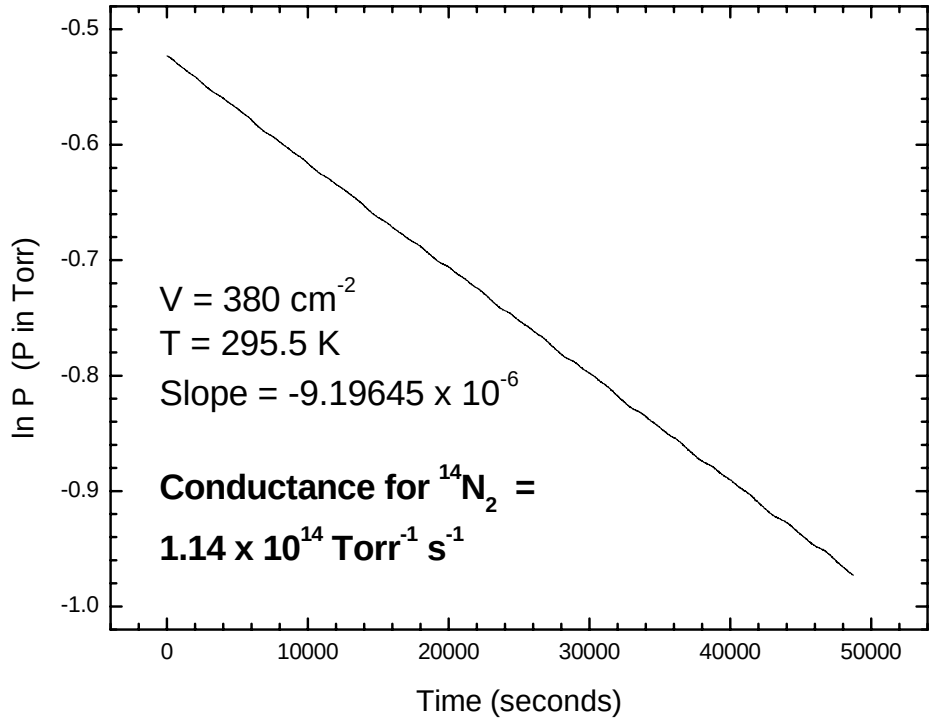

Figure 94: Calibration of the pinhole aperture using $^{14}N_2$.

From the TPD experiments of CO/Ru(109) and the various LEED images the maximum coverage of CO was determined to be 7.47×10^{14}cm^{-2} for Ru(109) ($\theta_{CO} = 0.54$ relative to the available Ru surface atoms). We have also determined the maximum CO coverage to be 8.64×10^{14} cm^{-2} for Ru(001) ($\theta_{CO} = 0.55$ relative to the available Ru surface atoms). When the measured conductance of the doser was used in the coverage calculation from Equation A.4 the coverage was found to be approximately 5.1 monolayers. It was therefore necessary to adjust the conductance of the doser to yield the correct saturation coverage. This analysis permits an indirect calculation of the doser conductance for CO. The calculated doser conductance for CO was then used in the determination of the correlation between exposure, sticking coefficient, and coverage for N_2 adsorption as determined from the N_2 uptake curve. The uptake cureve for N_2 adsorption on Ru(001) is shown in Figure 95. The uptake for N_2 adsorption on Ru(109) is

similar to that observed for Ru(001). These measurements indicate that an exposure of ~2.5 × 10^{15} cm^{-2} produces a saturation coverage of N_2 on both Ru surfaces when adsorbed at 75 K, and gives an absolute calibration of the N_2 coverage as measured in the TPD spectra. The correlation between the coverage and the exposure is plotted in Figure 96.

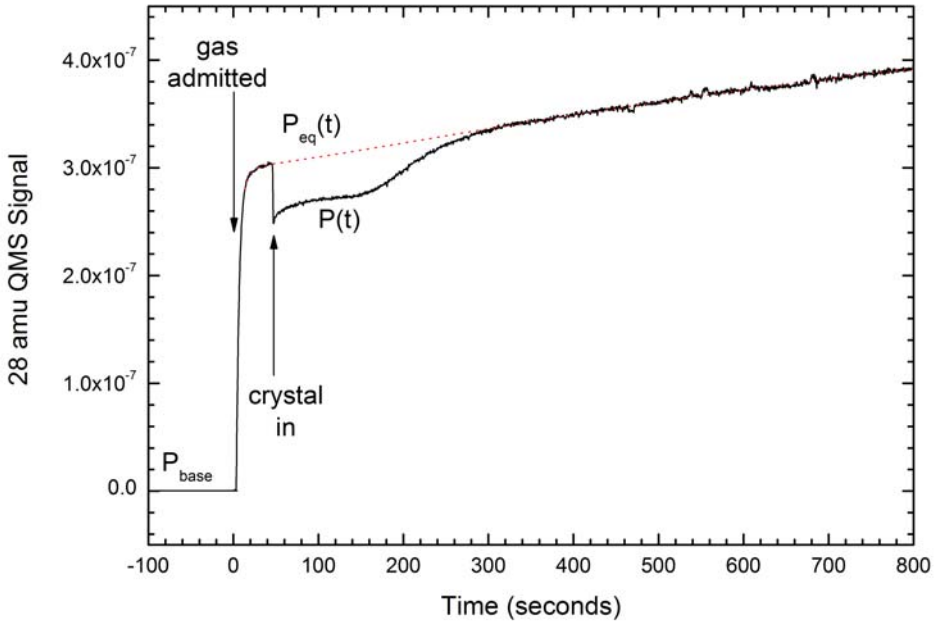

Figure 95: Uptake curve for N_2 adsorption on Ru(001) at 85 K.

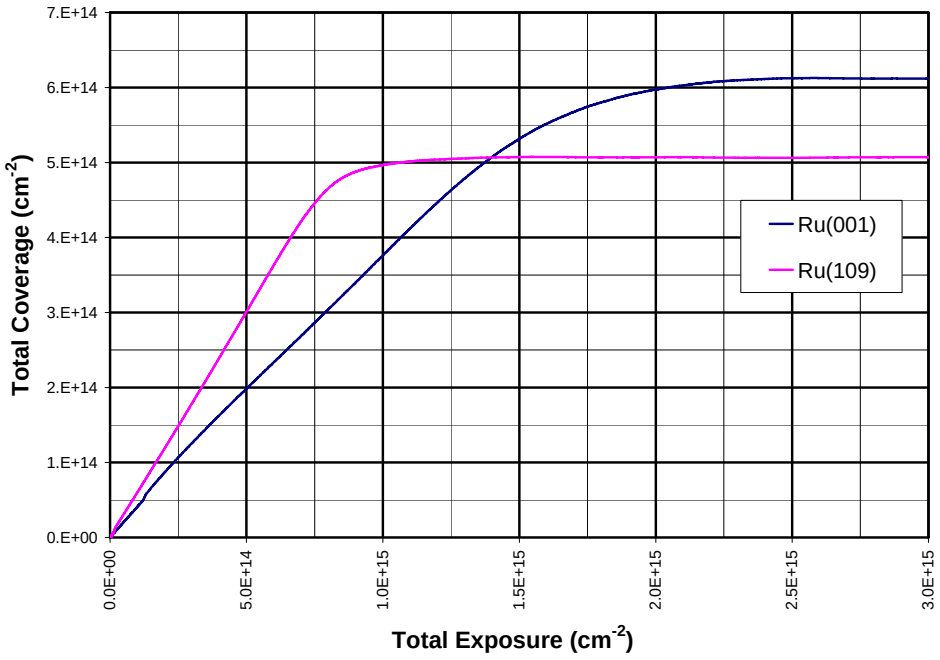

Figure 96: Coverage vs. exposure for N_2 adsorption on Ru(001) and Ru(109) at 85 K. A saturation coverage corresponds to roughly 6.12×10^{14} cm^{-2} for Ru(001) and 5.07×10^{14} cm^{-2} for Ru(109) ($\theta_{N_2} = 0.39$ and $\theta_{N_2} = 0.37$, respectively, relative to the available Ru surface atoms). The saturation coverage is achieved by an exposure of at least 2.5×10^{15} cm^{-2} for Ru(001) and 1.5×10^{15} cm^{-2} for Ru(109).

The difference between the actual measured conductance and the experimentally back calculated conductance of the pinhole does not constitute a major experimental problem. This major difference is most likely attributed to an internal leak in the volume of the gas line where the gas was stored during effusion through the pinhole doser. The gas, when stored in the backing volume of the pinhole doser, effuses into an adjacent section of the gas line. During a typical conductance measurement, the gas therefore not only effuses through the pinhole as expected, but also through one of the valves to an adjacent section of the gas line. This would lead to the observed imaginary increase in the measured conductance of the pinhole doser. During a typical dosing experiment, the exposure time is approximately 75-240 seconds, whereas the conductance measurements are performed over a period of 10^5 seconds. During a typical exposure of gas to the crystal, there is essentially no change in the overall pressure of the gas

stored in the line. This means that the internal leak is not a factor when determining the exposure of gas to the surface of the crystal.

APPENDIX B

LIST OF PUBLICATIONS (in ascending Chronological Order)

1. T. S. Zubkov, **G. A. Morgan, Jr.**, and J. T. Yates, Jr. "*Spectroscopic Detection of CO Dissociation on Defect Sites on Ru(109): Implications for Fischer-Tropsch Catalytic Chemistry*" Chem. Phys. Lett. **362** (2002) 181-184.

2. T. S. Zubkov, **G. A. Morgan, Jr.**, J. T. Yates, Jr., O. Kühlert, M. Lisowski, R. Schillinger, D. Fick, and H. J. Jänsch. *"The Effect of Atomic Steps on Adsorption and Desorption of CO on Ru(109)"* Surf. Sci. **526** (2003) 57-71.

3. **G. A. Morgan, Jr.**, D. C. Sorescu, T. S. Zubkov, and J. T. Yates, Jr., *"The Formation and Stability of Adsorbed Formyl as a Possible Intermediate in Fischer-Tropsch Chemistry on Ruthenium"* J. Phys. Chem. B. **108** (2004) 3614-3624.

4. **G. A. Morgan, Jr.**,Y. K. Kim, and J. T. Yates, Jr. *"Electron-Stimulated Dissociation of Molecular N_2 Adsorbed on Ru(109): A TPD and IRAS investigation"* Surf. Sci. **598** (2005) 1-13.

5. Y. K. Kim, **G. A. Morgan, Jr.,** and J. T. Yates, Jr., *"Site-Specific Dissociation of N_2 on the Stepped Ru(109) Surface"* Surf. Sci. **598** (2005) 14-21.

6. Y. K. Kim, **G. A. Morgan, Jr.,** and J. T. Yates, Jr., *"Unexpected Low-Temperature CO Dissociation on Ru by Li Promoter Atoms"* Chem. Phys. Lett. **422** (2006) 350-353.

7. Y. K. Kim, **G. A. Morgan, Jr.,** and J. T. Yates, Jr., *"Interaction of Li with Atomic Steps on Ru: Comparison Between Ru(001) and Ru(109)"* Chem. Phys. Lett. **431** (2006) 313-316.

8. Y. K. Kim, **G. A. Morgan, Jr.,** and J. T. Yates, Jr., *"Enhancement of Catalytic Promotion action of Li on Ru by Atomic steps – Comparison of CO dissociation on Ru(109) and Ru(001)"* Chem. Phys. Lett. **431** (2006) 317-320.

9. Y. K. Kim, **G. A. Morgan, Jr.,** and J. T. Yates, Jr., *"Role of Atomic Defect Sites on the Catalytic Oxidation of Carbon Monoxide – Comparison Between Ru(001) and Ru(109) Single Crystal Surfaces"* J. Phys. Chem. C. **111** (2007) 3366-3368.

10. **G. A. Morgan, Jr.,** D. C. Sorescu, Y. K. Kim, and J. T. Yates, Jr., *"Comparison of the Adsorption of N_2 on Ru(109) and Ru(001) – A Detailed Look at the Role of Atomic Step and Terrace Sites"* Surf. Sci. (2007), In Press.

11. **G. A. Morgan, Jr.,** Y. K. Kim, and J. T. Yates, Jr., *"Interaction between Chemisorbed N_2 and Li Promoter Atoms: A Comparison Between the Stepped Ru(109) and Atomically Smooth Ru(001) Surfaces"* Surf. Sci (2007), In press.

BIBLIOGRAPHY

[1] H.S. Taylor. *"A Theory of the Catalytic Surface"* Proc. Roy. Soc. (London) **108A** (1925) 105-111.

[2] B. Bachiller-Baeza, I. Rodriguez-Ramos, and A. Guerrero-Ruiz. *"Influence of Mg and Ce Addition to Ruthenium Based Catalysts Used in the Selective Hydrogenation of α,β-unsaturated Aldehydes"* App. Cat. A: General **205** (2001) 227-237.

[3] Y.K. Kim, G.A. Morgan, Jr., and J.T. Yates, Jr. *"Role of Atomic Step Defect Sites on the Catalytic Oxidation of Carbon Monoxide: Comparison between Ru(001) and Ru(109) Single-Crystal Surfaces"* J. Phys. Chem. C. **111** (2007) 3366-3368.

[4] I.V. Yudanov, R. Sahnoun, K.M. Neyman, N. Roesch, J. Hoffmann, S. Schauermann, V. Johanek, H. Unterhalt, G. Rupprechter, J. Libuda, and H.-J. Freund. *"CO Adsorption on Pd Nanoparticles. Density Functional and Vibrational Spectroscopy Studies"* J. Phys. Chem. B. **107** (2003) 255-264.

[5] M. Boudart. *"Catalysis by Supported Metals"* Adv. Catal. **20** (1969) 153-166.

[6] C.R. Henry. *"Surface Studies of Supported Model Catalysts"* Surf. Sci. Rep. **31** (1998) 231-325.

[7] B.C. Gates. *"Models of Metal Catalysts: Beyond Single Crystals"* Topics in Catalysis **14** (2001) 173-180.

[8] J.A. Dillon, Jr., R.E. Schlier, and H.E. Farnsworth. *"Some Surface Properties of Silicon-Carbide Crystals"* J. Appl. Phys. **30** (1959) 675-679.

[9] H.E. Farnsworth, R.E. Schlier, T.H. George, and R.M. Burger. *"Application of the Ion Bombardment Cleaning Method to Titanium, Germanium, Silicon, and Nickel as Determined by Low Energy Electron Diffraction"* J. Appl. Phys. **29** (1958) 1150-1161.

[10] H.E. Farnsworth, R.E. Schlier, T.H. George, and R.M. Burger. *"Ion Bombardment Cleaning of Germanium and Titanium as Determined by Low Energy Electron Diffraction"* J. Appl. Phys. **26** (1955) 252-253.

[11] E.J. Scheibner, L.H. Germer, and C.D. Hartman. *"Apparatus for Direct Observation of Low-Energy Electron Diffraction Patterns"* Rev. Sci. Instrum. **31** (1960) 112-114.

[12] R.E. Schlier, and H.E. Farnsworth. *"Structure and Adsorption Characteristics of Clean Surfaces of Germanium and Silicon"* J. Chem. Phys. **30** (1959) 917-926.

[13] R.E. Schlier, and H.E. Farnsworth. *"Low Energy Electron Diffraction Investigation of Chemisorbed Gases on the (100) Faces of Copper and Nickel SIngle Crystals"* J. Appl. Phys. **25** (1954) 1333-1336.

[14] H.E. Farnsworth. *"Fine Structure of Electron Diffraction Beams from a Gold Crystal and from a Silver Film on a Gold Crystal"* Phys. Rev. **43** (1933) 900-906.

[15] H.E. Farnsworth. *"Investigation of Certain Effects Accompanying the Diffraction of Low Speed Electrons"* Phys. Rev. **49** (1936) 598-605.

[16] H.E. Farnsworth. *"Penetration of Low Speed Diffracted Electrons"* Phys. Rev. **49** (1936)

[17] H.E. Farnsworth. *"Electron Emission and Diffraction by a Copper Crystal"* Phys. Rev. **34** (1929) 679-691.

[18] H.E. Farnsworth. *"Diffraction of Low Speed Electrons by Single Crystals of Copper and Silver"* Phys. Rev. **40** (1932) 684-712.

[19] C.R. Arumainayagam, C.E. Tripa, J. Xu, and J.T. Yates, Jr. *"IR Spectroscopy of Adsorbed Dinitrogen: A Sensitive Probe of Defect Sites on Pt(111)"* Surf. Sci. **360** (1996) 121-127.

[20] M. Rocca, L. Savio, and L. Vattuone. *"Dynamics of the Gas-Surface Interaction in Presence of Well Defined Defects"* Surf. Sci. **502-503** (2002) 331-340.

[21] R.G. Greenler, K.D. Burch, K. Kretzschmar, R. Klauser, A.M. Bradshaw, and B.E. Hayden. *"Stepped Single-Crystal Surfaces as Models for Small Catalyst Particles"* Surf. Sci. **152-153** (1985) 338-345.

[22] G.A. Somorjai. Introduction to Surface Chemistry and Catalysis. New York: Wiley, (1994).

[23] G. Ertl. *"Dynamics of Reactions at Surfaces"* Adv. Catal. **45** (2000) 1-69.

[24] R. Kose, W.A. Brown, and D.A. King. *"Energetics and Kinetics of Step-Terrace Adsorbate Distribution: C_2H_2 on Pt(211)"* J. Am. Chem. Soc. **121** (1999) 4845-4851.

[25] H.R. Siddiqui, P.J. Chen, X. Guo, and J.T. Yates, Jr. *"A Comparative Kinetic Study of Xenon Adsorption on a Flat Pt(111) and Stepped Platinum(557) and Platinum(112) Surfaces"* J. Chem. Phys. **92** (1990) 7690-7699.

[26] J.T. Yates, Jr. *"Surface Chemistry at Metallic Step Defect Sites"* J. Vac. Sci. Technol., A **13** (1995) 1359-1367.

[27] R.Q. Hwang, and R.J. Behm. *"Scanning Tunneling Microscopy Studies on the Growth and Structure of Thin Metallic Films on Metal Substrates"* J. Vac. Sci. Technol., B **10** (1992) 256-261.

[28] J.I. Pascual, J.J. Jackiw, K.F. Kelly, H. Conrad, H.P. Rust, and P.S. Weiss. *"Local Electronic Structural Effects and Measurements on the Adsorption of Benzene on Ag(110)"* Phys. Rev. B: Condens. Matter **62** (2000) 12632-12635.

[29] C.E. Tripa, T.S. Zubkov, J.T. Yates, Jr., M. Mavrikakis, and J.K. Nørskov. *"Molecular N_2 Chemisorption-Specific Adsorption on Step Defect Sites on Pt Surfaces"* J. Chem. Phys. **111** (1999) 8651-8658.

[30] J. Xu, and J.T. Yates, Jr. *"Catalytic Oxidation of Carbon Monoxide on Platinum (335): a Study of the Active Site"* J. Chem. Phys. **99** (1993) 725-732.

[31] T. Zambelli, J. Wintterlin, J. Trost, and G. Ertl. *"Identification of the 'Active Sites' of a Surface-Catalyzed Reaction"* Science **273** (1996) 1688-1690.

[32] P. Hollins. *"The Influence of Surface Defects on the Infrared Spectra of Adsorbed Species"* Surf. Sci. Rep. **16** (1992) 51-94.

[33] G.A. Morgan, Jr., D.C. Sorescu, Y.K. Kim, and J.T. Yates, Jr. *"Comparison of the Adsorption of N_2 on Ru(109) and Ru(001) – A Detailed Look at the Role of Atomic Step and Terrace Sites"* Accepted for publication, Surface Science (2007)

[34] S. Dahl, Á. Logadóttir, R.C. Egeberg, J.H. Larsen, I. Chorkendorff, E. Tornqvist, and J.K. Nørskov. *"Role of Steps in N_2 Activation on Ru(0001)"* Phys. Rev. Lett. **83** (1999) 1814-1817.

[35] S. Dahl, E. Tornqvist, and I. Chorkendorff. *"Dissociative Adsorption of N_2 on Ru(0001): A Surface Reaction Totally Dominated by Steps"* J. Catal. **192** (2000) 381-390.

[36] P. Gambardella, Z. Sljivancanin, B. Hammer, M. Blanc, K. Kuhnke, and K. Kern. *"Oxygen Dissociation at Pt Steps"* Phys. Rev. Lett. **87** (2001) 056103/056101-056103/056104.

[37] A.T. Gee, and B.E. Hayden. *"The Dynamics of O_2 Adsorption on Pt(533): Step Mediated Molecular Chemisorption and Dissociation"* J. Chem. Phys. **113** (2000) 10333-10343.

[38] H. Orita, H. Kondoh, and H. Nozoye. *"Decomposition of PF_3 on Ni(755) and Coadsorption with Ethylcyclohexane: Comparing the Results of PF_3 with CO"* J. Catal. **197** (2001) 244-250.

[39] H. Orita, H. Kondoh, and H. Nozoye. *"Decomposition of N_2O on Ni(755) and the Character of the Atomic Oxygen Deposited at Step Sites"* J. Catal. **177** (1998) 217-223.

[40] M.B. Raschke, and U. Hoefer. *"Influence of Steps and Defects on the Dissociative Adsorption of Molecular Hydrogen on Silicon Surfaces"* Applied Physics B: Lasers and Optics **B68** (1999) 649-655.

[41] T. Zubkov, G.A. Morgan, Jr., and J.T. Yates, Jr. *"Spectroscopic Detection of CO Dissociation on Defect Sites on Ru(109). Implications for Fischer-Tropsch Catalytic Chemistry"* Chem. Phys. Lett. **362** (2002) 181-184.

[42] T. Zubkov, G.A. Morgan, Jr., J.T. Yates, Jr., O. Kuhlert, M. Lisowski, R. Schillinger, D. Fick, and H.J. Jänsch. *"The Effect of Atomic Steps on Adsorption and Desorption of CO on Ru(109)"* Surf. Sci. **526** (2003) 57-71.

[43] Y.K. Kim, G.A. Morgan, Jr., and J.T. Yates, Jr. *"Site-Specific Dissociation of N_2 on the Stepped Ru(109) Surface"* Surf. Sci. **598** (2005) 14-21.

[44] G.A. Morgan, Jr., Y.K. Kim, and J.T. Yates, Jr. *"Electron-Stimulated Dissociation of Molecular N_2 Adsorbed on Ru(109). A TPD and IRAS Investigation"* Surf. Sci. **598** (2005) 1-13.

[45] B. Hammer, and J.K. Nørskov. *"Theoretical Surface Science and Catalysis - Calculations and Concepts"* Adv. Catal. **45** (2000) 71-129.

[46] B. Hammer, and J.K. Nørskov. *"Electronic Factors Determining the Reactivity of Metal Surfaces"* Surf. Sci. **343** (1995) 211-220.

[47] Z. Song, J.I. Pascual, H. Conrad, K. Horn, and H.P. Rust. *"Surface states of d character imaged by scanning tunneling microscopy"* Surf. Sci. **491** (2001) 39-47.

[48] B. Hammer, O.H. Nielsen, and J.K. Nørskov. *"Structure Sensitivity in Adsorption: CO Interaction with Stepped and Reconstructed Pt Surfaces"* Catal. Lett. **46** (1997) 31-35.

[49] R.B. Anderson. The Fischer-Tropsch Synthesis. New York: Academic Press, (1984) Page 2.

[50] H.H. Storch, N. Golumbic, and R.B. Anderson. The Fischer-Tropsch and Related Syntheses. New York, London: John Wiley & Sons; Chapman & Hall, (1951) Page 1.

[51] A.A. Adesina. *"Hydrocarbon Synthesis via Fischer-Tropsch Reaction: Travails and Triumphs"* App. Cat. A: General **138** (1996) 345-367.

[52] M.E. Dry. *"The Fischer-Tropsch Process - Commercial Aspects"* Catal. Today **6** (1990) 183-206.

[53] P. Sabatier, and J.B. Senderens. Comptes Rendus Hebdomadaires **134** (1902) 514.

[54] P. Biloen, J.N. Helle, and W.M.H. Sachtler. *"Incorporation of Surface Carbon into Hydrocarbons during Fischer-Tropsch Synthesis: Mechanistic Implications"* J. Catal. **58** (1979) 95-107.

[55] R.C. Brady, III, and R. Pettit. *"Mechanism of the Fischer-Tropsch reaction. The Chain Propagation Step"* J. Am. Chem. Soc. **103** (1981) 1287-1289.

[56] B.H. Davis. *"Fischer-Tropsch Synthesis: Current Mechanism and Futuristic Needs"* Fuel Processing Technology **71** (2001) 157-166.

[57] M.E. Dry. *"Practical and Theoretical Qspects of the Catalytic Fischer-Tropsch Process"* App. Cat. A: General **138** (1996) 319-344.

[58] M.E. Dry, T. Shingles, and C.S.v.H. Botha. *"Factors Influencing the Formation of Carbon on Iron Fischer-Tropsch Catalysts. I. Influence of Promoters"* J. Catal. **17** (1970) 341-346.

[59] S.A. Eliason, and C.H. Bartholomew. *"Reaction and Deactivation Kinetics for Fischer-Tropsch Synthesis on Unpromoted and Potassium-Promoted Iron Catalysts"* App. Cat. A: General **186** (1999) 229-243.

[60] J.J.C. Geerlings, M.C. Zonnevylle, and C.P.M. De Groot. *"Structure Sensitivity of the Fischer-Tropsch Reaction on Cobalt Single Crystals"* Surf. Sci. **241** (1991) 315-324.

[61] R.W. Joyner. *"The Role of Surface Science Studies in Elucidating the Mechanism of the Fischer-Tropsch Hydrocarbon Synthesis"* Vacuum **38** (1988) 309-315.

[62] M. Leconte. *"An Approach to the Mechanisms of C-C Bond Formation and Cleavage on Metal Surfaces using Model Elementary Reaction Steps of Organometallic Chemistry"* J. Mol. Catal. **86** (1994) 205-220.

[63] P.M. Maitlis, R. Quyoum, H.C. Long, and M.L. Turner. *"Towards a Chemical Understanding of the Fischer-Tropsch Reaction: Alkene Formation"* App. Cat. A: General **186** (1999) 363-374.

[64] M.J. Overett, R.O. Hill, and J.R. Moss. *"Organometallic Chemistry and Surface Science: Mechanistic Models for the Fischer-Tropsch Synthesis"* Coord. Chem. Rev. **206-207** (2000) 581-605.

[65] C.K. Rofer-DePoorter. *"A Comprehensive Mechanism for the Fischer-Tropsch Synthesis"* Chem. Rev. **81** (1981) 447-474.

[66] M.A. Vannice. *"Catalytic Synthesis of Hydrocarbons from Hydrogen-Carbon Monoxide Mixtures over the Group VIII Metals. I. Specific Activities and Product Distributions of Supported Metals"* J. Catal. **37** (1975) 449-461.

[67] A.M. Bradshaw. *"The Sructure and Chemistry of Adsorbed Carbon Monoxide"* Surf. Sci. **80** (1979) 215-225.

[68] R.R. Ford. *"Carbon Monoxide Adsorption on the Transition Metals"* Adv. Catal. **21** (1970) 51-150.

[69] R.W. Joyner. *"Electron Spectroscopy Applied to the Study of Reactivity at Metal Surfaces - a Review"* Surf. Sci. **63** (1977) 291-314.

[70] D. Menzel. *"Photoelectron Spectroscopy of Adsorption Layers"* Critical Reviews in Solid State and Materials Sciences **7** (1978) 357-384.

[71] N. Sheppard, and T.T. Nguyen. *"The Vibrational Spectra of Carbon Monoxide Chemisorbed on the Surfaces of Metal Catalysts - a Suggested Scheme of Interpretation"* Advances in Infrared and Raman Spectroscopy **5** (1978) 67-148.

[72] E.L. Muetterties. *"Metal Clusters in Catalysis. VIII. Reduction of Triple Bonds"* Bull. Soc. Chim. Belg. **85** (1976) 451-470.

[73] E.L. Muetterties, and J. Stein. *"Mechanistic Features of Catalytic Carbon Monoxide Hydrogenation Reactions"* Chem. Rev. **79** (1979) 479-490.

[74] C. Masters. *"The Fischer-Tropsch Reaction"* Adv. Organomet. Chem. **17** (1979) 61-103.

[75] M. Barber, J.C. Vickerman, and J. Wolstenholme. *"Adsorption and Surface Reactivity of Metals by Secondary Ion Mass Spectrometry. 1. Adsorption of Carbon Monoxide on*

Nickel and Copper" Journal of the Chemical Society, Faraday Transactions 1: Physical Chemistry in Condensed Phases **72** (1976) 40-50.

[76] R. Bouwman, and I.L.C. Freriks. *"In Situ Fourier Transform Infrared Spectroscopic Study of the Interaction of Carbon Monoxide with Nickel/Silicon Dioxide in the Absence and Presence of Hydrogen at 70-180°C"* Applic. Surf. Sci. **4** (1980) 21-36.

[77] M.E. Bridge, K.A. Prior, and R.M. Lambert. *"The Effects of Surface Carbide Formation on the Adsorption-Desorption Kinetics of Carbon Monoxide on Smooth and Stepped Cobalt Surfaces"* Surf. Sci. **97** (1980) L325-L329.

[78] G. Broden, G. Gafner, and H.P. Bonzel. *"A UPS and LEED/Auger Study of Adsorbates on Iron (110)"* App. Phys. **13** (1977) 333-342.

[79] G. Broden, T.N. Rhodin, C. Brucker, R. Benbow, and Z. Hurych. *"Synchrotron Radiation Study of Chemisorptive Bonding of Carbon Monoxide on Transition Metals - Polarization Effect on Iridium(100)"* Surf. Sci. **59** (1976) 593-611.

[80] R.W. Joyner, and M.W. Roberts. *"Evidence for the Nature of Carbon Monoxide Adsorbed on Nickel from Electron Spectroscopy"* Journal of the Chemical Society, Faraday Transactions 1: Physical Chemistry in Condensed Phases **70** (1974) 1819-1824.

[81] R.W. Joyner, and M.W. Roberts. *"Oxygen (1s) Binding Energies in Carbon Monoxide Adsorption on Metals"* Chem. Phys. Lett. **29** (1974) 447-448.

[82] K. Kishi, and M.W. Roberts. *"Carbon Monoxide Adsorption on Iron 85-350 K as Revealed by X-ray and Vacuum Ultraviolet [Helium(He II)] Photoelectron Spectroscopy"* Journal of the Chemical Society, Faraday Transactions 1: Physical Chemistry in Condensed Phases **71** (1975) 1715-1720.

[83] J.G. McCarty, and H. Wise. *"Dissociative Chemisorption of Carbon Monoxide on Ruthenium"* Chem. Phys. Lett. **61** (1979) 323-326.

[84] V. Perrichon, M. Primet, N. Nahon, and P. Turlier. *"Modes of Carbon Monoxide Adsorption on an Iron/Aluminum Oxide Catalyst"* Comptes Rendus des Seances de l'Academie des Sciences, Serie C: Sciences Chimiques **289** (1979) 149-152.

[85] K.A. Prior, K. Schwaha, and R.M. Lambert. *"Surface Chemistry of the non-Basal Planes of Cobalt: the Structure, Stability, and Reactivity of Cobalt (102)-Carbon Monoxide"* Surf. Sci. **77** (1978) 193-208.

[86] T.N. Rhodin, and C.F. Brucker. *"Effect of Surface Deactivation on Molecular Chemisorption: Carbon Monoxide on a Iron(100) Surface"* Solid State Commun. **23** (1977) 275-279.

[87] G. Wedler, K.G. Colb, G. McElhiney, and W. Heinrich. *"An Investigation of the Interaction of Carbon Monoxide with Polycrystalline Iron Films"* Applications of Surface Science (1977-1985) **2** (1978) 30-42.

[88] K.Y. Yu, W.E. Spicer, I. Lindau, P. Pianetta, and S.F. Lin. *"UPS Studies of the Bonding of Molecular Hydrogen, Molecular Oxygen, Carbon Monoxide, Ethylene, and Acetylene on Iron and Copper"* Surf. Sci. **57** (1976) 157-183.

[89] I.M. Ciobîcă, G.J. Kramer, Q. Ge, M. Neurock, and R.A. van Santen. *"Mechanisms for Chain Crowth in Fischer-Tropsch Synthesis over Ru(001)"* J. Catal. **212** (2002) 136-144.

[90] R.M. Hammaker, S.A. Francis, and R.P. Eischens. *"Infrared Study of Intermolecular Interactions for Carbon Monoxide Chemisorbed on Platinum"* Spectrochimica Acta **21** (1965) 1295-1309.

[91] H. Pfnür, D. Menzel, F.M. Hoffmann, A. Ortega, and A.M. Bradshaw. *"High-Resolution Vibrational Spectroscopy of Carbon Monoxide on Ruthenium(001): the Importance of Lateral Interactions"* Surf. Sci. **93** (1980) 431-452.

[92] G.E. Thomas, and W.H. Weinberg. *"The Vibrational Spectrum and Adsorption Site of Carbon Monoxide on the Ruthenium(001) Surface"* J. Chem. Phys. **70** (1979) 1437-1439.

[93] R.L.C. Wang, H.J. Kreuzer, P. Jakob, and D. Menzel. *"Lateral Interactions in Coadsorbate Layers: Vibrational Frequency Shifts"* J. Chem. Phys. **111** (1999) 2115-2122.

[94] H. Pfnür, P. Feulner, and D. Menzel. *"The Influence of Absorbate Interactions on Kinetics and Equilibrium for Carbon Monoxide on Ruthenium(001). II. Desorption Kinetics and Equilibrium"* J. Chem. Phys. **79** (1983) 4613-4623.

[95] E. Shincho, C. Egawa, S. Naito, and K. Tamura. *"The Behavior of Carbon Monoxide Adsorbed on Ruthenium(1,1,10) and Ruthenium(001); the Dissociation of Carbon Monoxide at the Step Sites of the Ruthenium(1,1,10) Surface"* Surf. Sci. **149** (1985) 1-16.

[96] M.A. Henderson, G.E. Mitchell, and J.M. White. *"The Coadsorption of Ethylene and Carbon Monoxide on Ruthenium(001)"* Surf. Sci. **203** (1988) 378-394.

[97] J.C. Fuggle, E. Umbach, P. Feulner, and D. Menzel. *"Electron Induced Dissociation of Carbon Monoxide on Ruthenium(001). A Study by Thermal Desorption and Electron Spectroscopies"* Surf. Sci. **64** (1977) 69-84.

[98] J. Wang, Y. Wang, and K. Jacobi. *"Dissociation of CO on the Ru(1120) Surface"* Surf. Sci. **488** (2001) 83-89.

[99] E.D. Westre, D.E. Brown, J. Kutzner, and S.M. George. *"Anisotropy and Coverage Dependence of CO Surface Diffusion on Ru(S)-[15(001)*2(100)]"* Surf. Sci. **302** (1994) 280-294.

[100] N.D. Shinn, and T.E. Madey. *"Oxygen-Induced Carbon Monoxide Reorientation on Chromium(110)"* J. Vac. Sci. Technol., A **3** (1985) 1673-1677.

[101] N.D. Shinn, and T.E. Madey. *"Carbon Monoxide Chemisorption on Chromium(110): Evidence for a Precursor to Dissociation"* J. Chem. Phys. **83** (1985) 5928-5944.

[102] N.D. Shinn, and T.E. Madey. *"Unusual Carbon-Oxygen Bond Weakening on a Clean Metal Surface: Carbon Monoxide on Chromium(110)"* Phys. Rev. Lett. **53** (1984) 2481-2484.

[103] C. Benndorf, B. Krueger, and F. Thieme. *"Unusually Low Stretching Frequency for Carbon Monoxide Adsorbed on Iron(100)"* Surf. Sci. **163** (1985) L675-L680.

[104] J.P. Lu, M.R. Albert, and S.L. Bernasek. *"Adsorption and Dissociation of Carbon Monoxide on Iron(100) at Low Coverage"* Surf. Sci. **217** (1989) 55-64.

[105] D.W. Moon, S.L. Bernasek, J.P. Lu, J.L. Gland, and D.J. Dwyer. *"Activation of Carbon Monoxide on Clean and Sulfur Modified Iron(100)"* Surf. Sci. **184** (1987) 90-108.

[106] F. Zaera, E. Kollin, and J.L. Gland. *"Observation of an Unusually Low C-O Stretching Frequency: Carbon Monoxide Chemisorption on a Molybdenum(100) Surface"* Chem. Phys. Lett. **121** (1985) 464-468.

[107] J.G. Chen, M.L. Colaianni, W.H. Weinberg, and J.T. Yates, Jr. *"Direct Vibrational Detection of Surface Reaction Channels Leading to Carbon Monoxide Dissociation and to its Inhibition on Molybdenum(110)"* Chem. Phys. Lett. **177** (1991) 113-117.

[108] M.L. Colaianni, J.G. Chen, W.H. Weinberg, and J.T. Yates, Jr. *"The Adsorption and Dissociation of Carbon Monoxide on Clean and Oxygen-Modified Molybdenum(110) Surfaces"* J. Am. Chem. Soc. **114** (1992) 3735-3743.

[109] F.M. Hoffmann, and R.A. De Paola. *"Anomalous Carbon-Oxygen Bond Weakening of Side-on-Bonded Carbon Monoxide on a Potassium-Promoted Ruthenium(001) Surface"* Phys. Rev. Lett. **52** (1984) 1697-1700.

[110] K. Tamaru, in: J.R. Jennings (Ed.), Catalytic Ammonia Synthesis: Fundamentals and Practice,*"The History of the Developmen of Ammonia Synthesis"* New York: Plenum Press, (1991) Page 8.

[111] B.E. Smith. *"Nitrogenase Reveals Its Inner Secrets "* Science **297** (2002) 1654-1655.

[112] M.D. Fryzuk. *"Ammonia Transformed"* Nature **427** (2004) 498-499.

[113] S. Schwegmann, A.P. Seitsonen, H. Dietrich, H. Bludau, H. Over, K. Jacobi, and G. Ertl. *"The Adsorption of Atomic Nitrogen on Ru(0001): Geometry and Energetics"* Chem. Phys. Lett. **264** (1997) 680-686.

[114] K. Jacobi. *"Nitrogen on Ruthenium Single-Crystal Surfaces"* Phys. Status Solidi A **177** (2000) 37-51.

[115] A.B. Anton, N.R. Avery, B.H. Toby, and W.H. Weinberg. *"The Chemisorption of Nitrogen on the (001) Surface of Ruthenium"* J. Electron Spectrosc. Relat. Phenom. **29** (1983) 181-186.

[116] Á. Logadóttir, and J.K. Nørskov. *"Ammonia Synthesis over a Ru(0001) Surface Studied by Density Functional Calculations"* J. Catal. **220** (2003) 273-279.

[117] K.W. Kolasinski. Surface Science: Foundations of Catalysis and Nanoscience. West Sussex: John Wiley and Sons Ltd., (2002) Page 227.

[118] R.A. De Paola, and F.M. Hoffmann. *"The Role of σ-Donation in the Bonding of Molecular Nitrogen on Clean and Modified Ru(001) Surfaces"* Chem. Phys. Lett. **128** (1986) 343-346.

[119] R.A. De Paola, F.M. Hoffmann, D. Heskett, and E.W. Plummer. *"Adsorption of Molecular Nitrogen on Clean and Modified Ruthenium(001) Surfaces: the Role of σ-Bonding"* Phys. Rev. B: Condens. Matter **35** (1987) 4236-4249.

[120] J.J. Mortensen, B. Hammer, and J.K. Nørskov. *"Alkali Promotion of N_2 Dissociation over Ru(0001)"* Phys. Rev. Lett. **80** (1998) 4333-4336.

[121] J.J. Mortensen, B. Hammer, and J.K. Nørskov. *"A Theoretical Study of Adsorbate-Adsorbate Interactions on Ru(0001)"* Surf. Sci. **414** (1998) 315-329.

[122] T. Aruga, and Y. Murata. *"Alkali-Metal Adsorption on Metals"* Prog. Surf. Sci. **31** (1989) 61-130.

[123] R.D. Diehl, and R. McGrath. *"Current Progress in Understanding Alkali Metal Adsorption on Metal Surfaces"* J. Phys.: Condens. Matter **9** (1997) 951-968.

[124] H.J. Jänsch, C. Huang, A. Ludviksson, and R.M. Martin. *"Reaction of Li with CO on Ru(001) and Ag/Ru(001) Substrates"* Surf. Sci. **315** (1994) 9-26.

[125] G.A. Morgan, Jr., Y.K. Kim, and J.T. Yates, Jr. *"Interaction between Chemisorbed N_2 and Li Promoter Atoms: A Comparison between the Stepped Ru(109) and the Atomically-Smooth Ru(001) Surfaces"* Accepted for Publication, Surface Science (2007).

[126] S.J. Pratt, and D.A. King. *"Coverage Dependent Promoter Action: K Coadsorption and Reactions with CO and CO_2 on Pd{1 1 0}"* Surf. Sci. **540** (2003) 185-206.

[127] M.D. Weisel, J.L. Robbins, and F.M. Hoffmann. *"In-situ FT-IRAS Study of the Hydrogenation of Carbon Monoxide on Ruthenium(001): Potassium-Promoted Synthesis of Formate"* J. Phys. Chem. **97** (1993) 9441-9450.

[128] O. Hinrichsen, F. Rosowski, A. Hornung, M. Muhler, and G. Ertl. *"The Kinetics of Ammonia Synthesis over Ru-Based Catalysts. 1. The Dissociative Chemisorption and Associative Desorption of N_2"* J. Catal. **165** (1997) 33-44.

[129] S.R. Tennison, in: J.R. Jennings (Ed.), Catalytic Ammonia Synthesis: Fundamentals and Practice,*"Alternative Noniron Catalysts"* New York: Plenum Press, (1991) Page 303.

[130] P.J. Feibelman, and D.R. Hamann. *"Modification of Transition Metal Electronic Structure by Phosphorus, Sulfur, Chlorine and Lithium Adatoms"* Surf. Sci. **149** (1985) 48-66.

[131] J.K. Nørskov, S. Holloway, and N.D. Lang. *"Microscopic Model for the Poisoning and Promotion of Adsorption Rates by Electronegative and Electropositive Atoms"* Surf. Sci. **137** (1984) 65-78.

[132] J.K. Nørskov, and P. Stoltze. *"Theoretical Aspects of Surface Reactions"* Surf. Sci. **189/190** (1987) 91-105.

[133] M. Trenary, K.J. Uram, and J.T. Yates, Jr. *"An Infrared Reflection-Absorption Study of Carbon Monoxide Chemisorbed on Clean and Sulfided Nickel(111) - Evidence for Local Surface Interactions"* Surf. Sci. **157** (1985) 512-538.

[134] J.T. Yates, Jr. Experimental Innovations in Surface Science. New York: AIP Press, Springer-Verlag, (1998) Pages 138-141; 604-615.

[135] J. Xu, H.J. Jänsch, and J.T. Yates, Jr. *"Cryogenic Trick for Enhanced Cooling Using Liquid Nitrogen"* J. Vac. Sci. Technol., A **11** (1993) 726-727.

[136] J.T. Yates, Jr. Experimental Innovations in Surface Science. New York: AIP Press, Springer-Verlag, (1998) Pages 572-573.

[137] M.J. Bozack, L. Muehlhoff, J.N. Russell, Jr., W.J. Choyke, and J.T. Yates, Jr. *"Methods in Semiconductor Surface Chemistry"* J. Vac. Sci. Technol., A **5** (1987) 1-8.

[138] R. Dennert, M. Sokolowski, and H. Pfnür. *"Ordered Phases and Phase Diagram of Sulfur Adsorbed on Ru(001)"* Surf. Sci. **271** (1992) 1-20.

[139] P. Feulner, and D. Menzel. *"The Adsorption of Hydrogen on Ruthenium(001): Adsorption States, Dipole Moments and Kinetics of Adsorption and Desorption"* Surf. Sci. **154** (1985) 465-488.

[140] G. Held, H. Pfnür, and D. Menzel. *"A LEED-IV Investigation of the Ru(001)-p(2 x 1)-H Structure"* Surf. Sci. **271** (1992) 21-31.

[141] H.D. Ebinger, H. Arnolds, C. Polenz, B. Polivka, W. Preyss, R. Veith, D. Fick, and H.J. Jänsch. *"Adsorption and Diffusion of Li on a Ru(001) Surface. A NMR Study"* Surf. Sci. **412/413** (1998) 586-615.

[142] W. Preyss, M. Detje, H.D. Ebinger, H.J. Jänsch, C. Polenz, B. Polivka, R. Veith, and D. Fick. *"Nuclear Spin Relaxation of ^{8}Li Adsorbed on Surfaces"* Hyperfine Interact. **110** (1997) 295-312.

[143] K. Wandelt, J. Hulse, and J. Küppers. *"Site-Selective Adsorption of Xenon on a Stepped Ruthenium(0001) Surface"* Surf. Sci. **104** (1981) 212-239.

[144] D.W. Goodman, and J.M. White. *"Measurement of Active Carbon on Ruthenium (110): Relevance to Catalytic Methanation"* Surf. Sci. **90** (1979) 201-203.

[145] D.W. Goodman, T.E. Madey, M. Ono, and J.T. Yates, Jr. *"Interaction of Hydrogen, Carbon Monoxide, and Formaldehyde with Ruthenium"* J. Catal. **50** (1977) 279-290.

[146] M. Lisowski. Alkaliadsorption and Gestuften Ru(0001)-Oberflächen (Alkali Adsorption on Vicinal Ru(0001) Surface). Diplomarbeit, Ruprecht-Karls-Universität, Heidelberg, Germany (2000).

[147] P.D. Reed, C.M. Comrie, and R.M. Lambert. *"Chemisorption, Surface Structural Chemistry, and Electron Impact Properties of Carbon Monoxide on Ruthenium(101)"* Surf. Sci. **59** (1976) 33-45.

[148] L.A. Davis, N.C. MacDonald, P.W. Palmberg, G.E. Riach, R.E. Weber, and Editors. Handbook for Auger Electron Spectroscopy. A Reference Book of Standard Data for Identification and Interpretation of Auger Electron Spectroscopy Data, 2nd Ed, (1976).

[149] H.L. Pickering, and H.C. Eckstrom. *"Heterogeneous Reaction Studies by Infrared Absorption"* J. Phys. Chem. **63** (1959) 512-517.

[150] P. Hollins. *"Surface Infrared Spectroscopy"* Vacuum **45** (1994) 705-714.

[151] F.M. Hoffmann. *"Infrared Reflection-Absorption Spectroscopy of Adsorbed Molecules"* Surf. Sci. Rep. **3** (1983) 107-192.

[152] Z. Xu, and J.T. Yates, Jr. *"A New Fourier Transform Infrared Reflection-Absorption Spectrometer and Effective Background Subtraction Method"* J. Vac. Sci. Technol., A **8** (1990) 3666-3668.

[153] J.T. Yates, Jr. Experimental Innovations in Surface Science. New York: AIP Press, Springer-Verlag, (1998) Pages 694-695.

[154] J.T. Yates, Jr. Experimental Innovations in Surface Science. New York: AIP Press, Springer-Verlag, (1998) Pages 584-587; 628-631.

[155] C. Bromberger, H.J. Jänsch, and D. Fick. *"Determination of the Coverage Dependent Work Function for Li Adsorbed on Ru(001)"* Surf. Sci. **506** (2002) 129-136.

[156] Y.K. Kim, G.A. Morgan, Jr., and J.T. Yates, Jr. *"Interaction of Li with Atomic Steps on Ru: Comparison between Ru(001) and Ru(109)"* Chem. Phys. Lett. **431** (2006) 313-316.

[157] K. Besocke, and S. Berger. *"Piezoelectric Driven Kelvin Probe for Contact Potential Difference Studies"* Rev. Sci. Instrum. **47** (1976) 840-842.

[158] H.A. Engelhardt, P. Feulner, and H. Pfnür. *"An Accurate and Versatile Vibrating Capacitor for Surface and Adsorption Studies"* J. Phys. E; Sci. Instr. **10** (1977) 1133-1136.

[159] http://www.kelvinprobe.info

[160] G.A. Somorjai. Principles of Surface Chemistry. Englewood Cliffs, New Jersey: Prentice Hall, INC., (1972) Pages 158-164.

[161] J.C. Rivière, in: M. Green (Ed.), Solid State Surface Science,*"Work Function: Measurements and Results"* New York: Marcel Dekker, (1969) Pages 179-284.

[162] R. Gomer. Field Emission and Field Ionization. New York: American Institute of Physics, (1961) Pages 3-6.

[163] A. Zangwill. Physics at Surfaces. New York: Cambridge University Press, (1988) Pages 57-63.

[164] H. Lüth. Surfaces and Interfaces of Solid Materials. New York: Spinger-Verlag, (1997) Pages 499-505.

[165] R. Gomer. *"Work Function in Field Emission. Chemisorption"* J. Chem. Phys. **21** (1953) 1869-1876.

[166] http://g.droval.online.fr/studies/p_bsc4/1theory/kelvinprobe.html

[167] S.R. Morrison. The Chemical Physics of Surfaces. New York: Plenum Press, (1977) Pages 59-60.

[168] P.A. Redhead. *"Thermal Desorption of Gases"* Vacuum **12** (1962) 203-211.

[169] H. Dietrich, P. Geng, K. Jacobi, and G. Ertl. *"Sticking Coefficient for Dissociative Adsorption of N_2 on Ru Single-Crystal Surfaces"* J. Chem. Phys. **104** (1996) 375-381.

[170] B. Sakakini, B. Steeples, N. Dunhill, and J.C. Vickerman. *"Hydrogenation of Carbon Monoxide over a Ruthenium(0001) Single Crystal Surface"* Stud. Surf. Sci. Catal. **48** (1989) 817-824.

[171] M.C. Wu, D.W. Goodman, and G.W. Zajac. *"The Characterization of Carbonaceous Species from CO Hydrogenation on Single Crystal Ru(0001) and Ru(1120) Catalysts with High Resolution Electron Energy Loss Spectroscopy"* Catal. Lett. **24** (1994) 23-30.

[172] F.M. Hoffmann, and M.D. Weisel. *"In-situ Observation of a Formate Intermediate During Carbon Monoxide Hydrogenation Over Alkali-Promoted Ruthenium(001) at High Pressures"* Surf. Sci. **253** (1991) L402-L406.

[173] M.D. Weisel, J.G. Chen, and F.M. Hoffmann. *"Characterization of a Carbon Monoxide/Hydrogen Reaction Intermediate by FT-IRAS: Potassium Formate on Ruthenium(001)"* J. Electron Spectrosc. Relat. Phenom. **54-55** (1990) 787-794.

[174] M.A. Henderson, and J.T. Yates, Jr. *"One-Dimensional Carbon Monoxide Island Formation in the Coadsorption of Hydrogen and Carbon Monoxide on the Steps of Platinum(112)"* Surf. Sci. **268** (1992) 189-204.

[175] D.E. Peebles, J.R. Creighton, D.N. Belton, and J.M. White. *"Coadsorption of Hydrogen and Carbon Monoxide on Nickel and Platinum"* J. Catal. **80** (1983) 482-485.

[176] H. Wang, R.G. Tobin, D.K. Lambert, G.B. Fisher, and C.L. DiMaggio. *"H-CO Interactions on the Terraces and Step Edges of a Stepped Pt Surface"* Surf. Sci. **330** (1995) 173-181.

[177] M. Kiskinova, and G. Bliznakov. *"Adsorption and Coadsorption of Carbon Monoxide and Hydrogen on Palladium(111)"* Surf. Sci. **123** (1982) 61-76.

[178] J. Bauhofer, M. Hock, and J. Küppers. *"Coadsorption of Hydrogen and Carbon Monoxide at Nickel(110) Surfaces"* J. Electron Spectrosc. Relat. Phenom. **44** (1987) 55-64.

[179] J.M. White. *"Surface Interactions in Nonreactive Coadsorption: Hydrogen and Carbon Monoxide on Transition Metal Surfaces"* J. Phys. Chem. **87** (1983) 915-924.

[180] J. Braun, K.L. Kostov, G. Witte, and C. Woell. *"CO Overlayers on Ru(0001) Studied by Helium Atom Scattering: Structure, Dynamics, and the Influence of Coadsorbed H and O"* J. Chem. Phys. **106** (1997) 8262-8273.

[181] P. Jakob, M. Gsell, and D. Menzel. *"Interactions of Adsorbates with Locally Strained Substrate Lattices"* J. Chem. Phys. **114** (2001) 10075-10085.

[182] C.H. Mak, A.A. Deckert, and S.M. George. *"Effects of Coadsorbed Carbon Monoxide on the Surface Diffusion of Hydrogen on Ruthenium(001)"* J. Chem. Phys. **89** (1988) 5242-5250.

[183] D.E. Peebles, J.A. Schreifels, and J.M. White. *"The Interaction of Coadsorbed Hydrogen and Carbon Monoxide on Ruthenium (001)"* Surf. Sci. **116** (1982) 117-134.

[184] B. Riedmüller, D.C. Papageorgopoulos, B. Berenbak, R.A. van Santen, and A.W. Kleyn. *"'Magic' Island Formation of CO Coadsorbed with H on Ru(0001)"* Surf. Sci. **515** (2002) 323-336.

[185] E.D. Williams, P.A. Thiel, W.H. Weinberg, and J.T. Yates, Jr. *"Segregation of Coadsorbed Species: Hydrogen and Carbon Monoxide on the (111) Surface of Rhodium"* J. Chem. Phys. **72** (1980) 3496-3505.

[186] W.H. Weinberg. *"Eley-Rideal Surface Chemistry: Direct Reactivity of Gas Phase Atomic Hydrogen with Adsorbed Species"* Acc. Chem. Res. **29** (1996) 479-487.

[187] W.J. Mitchell, Y. Wang, J. Xie, and W.H. Weinberg. *"Hydrogenation of Carbon Monoxide at 100 K on the Ruthenium(001) Surface: Spectroscopic Identification of Formyl Intermediates"* J. Am. Chem. Soc. **115** (1993) 4381-4382.

[188] W.J. Mitchell, J. Xie, T.A. Jachimowski, and W.H. Weinberg. *"Carbon Monoxide Hydrogenation on the Ru(001) Surface at Low Temperature Using Gas-Phase Atomic Hydrogen: Spectroscopic Evidence for the Carbonyl Insertion Mechanism on a Transition Metal Surface"* J. Am. Chem. Soc. **117** (1995) 2606-2617.

[189] W.J. Mitchell, J. Xie, Y. Wang, and W.H. Weinberg. *"Carbon Monoxide Hydrogenation on the Ru(001) Surface at Low Temperature using GasPhase Atomic Hydrogen"* J. Electron Spectrosc. Relat. Phenom. **64-65** (1993) 427-433.

[190] G. Kresse, and J. Furthmueller. *"Efficient Iterative Schemes for Ab Initio Total-Energy Calculations using a Plane-Wave Basis Set"* Phys. Rev. B: Condens. Matter **54** (1996) 11169-11186.

[191] G. Kresse, and J. Furthmuller. *"Efficiency of Ab-Initio Total Energy Calculations for Metals and Semiconductors using a Plane-Wave Basis Set"* Computational Materials Science **6** (1996) 15-50.

[192] G. Kresse, and J. Hafner. *"Ab Initio Molecular Dynamics for Open-Shell Transition Metals"* Phys. Rev. B: Condens. Matter **48** (1993) 13115-13118.

[193] D. Vanderbilt. *"Soft Self-Consistent Pseudopotentials in a Generalized Eigenvalue Formalism"* Phys. Rev. B: Condens. Matter **41** (1990) 7892-7895.

[194] G. Kresse, and J. Hafner. *"Norm-Conserving and Ultrasoft Pseudopotentials for First-Row and Transition Elements"* J. Phys.: Condens. Matter **6** (1994) 8245-8257.

[195] M. Methfessel, and A.T. Paxton. *"High-Precision Sampling for Brillouin-Zone Integration in Metals"* Phys. Rev. B: Condens. Matter **40** (1989) 3616-3621.

[196] J.P. Perdew, J.A. Chevary, S.H. Vosko, K.A. Jackson, M.R. Pederson, D.J. Singh, and C. Fiolhais. *"Atoms, Molecules, Solids, and Surfaces: Applications of the Generalized Gradient Approximation for Exchange and Correlation"* Phys. Rev. B: Condens. Matter **46** (1992) 6671-6687.

[197] G. Kresse, and J. Hafner. *"Ab Initio Molecular Dynamics of Liquid Metals"* Phys. Rev. B: Condens. Matter **47** (1993) 558-561.

[198] H.J. Monkhorst, and J.D. Pack. *"Special Points for Brillouin-Zone Integrations"* Phys. Rev. B: Condens. Matter **13** (1976) 5188-5192.

[199] B.J. Berne, G. Ciccotti, and D.F. Coker, Eds. Classical Quantum Dynamics in Condensed Phase Simulations. Singapore: World Scientific,(1998).

[200] G. Mills, H. Jonsson, and G.K. Schenter. *"Reversible Work Transition State Theory: Application to Dissociative Adsorption of Hydrogen"* Surf. Sci. **324** (1995) 305-337.

[201] D.R. Linde, Ed. CRC Handbook of Chemistry and Physics. Boca Raton, Fl,(2001).

[202] E. Hirota. *"Third-Order Anharmonic Potential Constants and Equilibrium Structures of the Formyl and Hydroperoxyl Radicals"* J. Mol. Struct. **146** (1986) 237-252.

[203] D.E. Milligan, and M.E. Jacox. *"Infrared Spectrum of HCO"* J. Chem. Phys. **41** (1964) 3032-3036.

[204] C.B. Dane, D.R. Lander, R.F. Curl, F.K. Tittel, Y. Guo, M.I.F. Ochsner, and C.B. Moore. *"Infrared Flash Kinetic Spectroscopy of Formyl Radical (HCO)"* J. Chem. Phys. **88** (1988) 2121-2128.

[205] D.E. Milligan, and M.E. Jacox. *"Matrix-Isolation Study of the Infrared and Ultraviolet Spectra of the Free Radical HCO. The Hydrocarbon Flame Bands"* J. Chem. Phys. **51** (1969) 277-288.

[206] J.M. Bowman, J.S. Bittman, and L.B. Harding. *"Ab Initio Calculations of Electronic and Vibrational Energies of Oxomethyl (HCO) and Hydroxymethylidyne (HOC)"* J. Chem. Phys. **85** (1986) 911-921.

[207] A.B. Anton, J.E. Parmeter, and W.H. Weinberg. *"Adsorption of Formaldehyde on the Ru(001) and Ru(001)-p(2 × 2)O Surfaces"* J. Am. Chem. Soc. **108** (1986) 1823-1833.

[208] H. Ibach, and D.L. Mills. Electron Energy Loss Spectroscopy and Surface Vibrations. New York: Academic Press, (1982).

[209] J.T. Yates, Jr., and R.R. Cavanagh. *"Search for Chemisorbed Formyl Radical: the Interaction of Formaldehyde, Glyoxal, and Atomic Hydrogen + Carbon Monoxide with Rhodium"* J. Catal. **74** (1982) 97-109.

[210] A.T. Capitano, A.M. Gabelnick, and J.L. Gland. *"Gas Phase Atomic Hydrogen Reacting with Molecular and Atomic Oxygen to form Water on the Pt(111) Surface"* Surf. Sci. **419** (1999) 104-113.

[211] J.A. Schwarz. *"Adsorption-Desorption Kinetics of Hydrogen from Clean and Sulfur-Covered Ruthenium(001)"* Surf. Sci. **87** (1979) 525-538.

[212] K.-J. Aika, and K. Tamaru. Ammonia: Catalysis and Manufacture. Berlin: Springer-Verlag, (1995) Page 103.

[213] L.R. Danielson, M.J. Dresser, E.E. Donaldson, and J.T. Dickinson. *"Adsorption and Desorption of Ammonia, Hydrogen, and Nitrogen on Ruthenium (0001)"* Surf. Sci. **71** (1978) 599-614.

[214] L. Diekhöner, A. Baurichter, H. Mortensen, and A.C. Luntz. *"Observation of Metastable Atomic Nitrogen Adsorbed on Ru(0001)"* J. Chem. Phys. **112** (2000) 2507-2515.

[215] L. Diekhöner, H. Mortensen, A. Baurichter, and A.C. Luntz. *"Coverage Dependence of Activation Barriers: Nitrogen on Ru(0001)"* J. Vac. Sci. Technol., A **18** (2000) 1509-1513.

[216] K. Jacobi, H. Dietrich, and G. Ertl. *"Nitrogen Chemistry on Ruthenium Single-Crystal Surfaces"* Appl. Surf. Sci. **121/122** (1997) 558-561.

[217] H. Dietrich, K. Jacobi, and G. Ertl. *"Coverage, Lateral Order, and Vibrations of Atomic Nitrogen on Ru(0001)"* J. Chem. Phys. **105** (1996) 8944-8950.

[218] R.C. Egeberg, S. Dahl, Á. Logadóttir, J.H. Larsen, J.K. Nørskov, and I. Chorkendorff. *"N_2 Dissociation on Fe(110) and Fe/Ru(0001). What is the Role of Steps?"* Surf. Sci. **491** (2001) 183-194.

[219] L. Romm, G. Katz, R. Kosloff, and M. Asscher. *"Dissociative Chemisorption of N_2 on Ru(001) Enhanced by Vibrational and Kinetic Energy: Molecular Beam Experiments and Quantum Mechanical Calculations"* J. Phys. Chem. B. **101** (1997) 2213-2217.

[220] H. Shi, and K. Jacobi. *"Evidence for Physisorbed N_2 in the Monolayer on Ru(001) at 40 K"* Surf. Sci. **278** (1992) 281-285.

[221] H. Shi, K. Jacobi, and G. Ertl. *"Dissociative Chemisorption of Nitrogen on Ru(0001)"* J. Chem. Phys. **99** (1993) 9248-9254.

[222] H. Bludau, M. Gierer, H. Over, and G. Ertl. *"A Low-Energy Electron Diffraction Analysis of the (√3×√3)R30° Structure of Molecular Nitrogen Adsorbed on Ru(0001)"* Chem. Phys. Lett. **219** (1994) 452-456.

[223] J. Trost, T. Zambelli, J. Wintterlin, and G. Ertl. *"Adsorbate-Adsorbate Interactions from Statistical Analysis of STM images: N/Ru(0001)"* Phys. Rev. B: Condens. Matter **54** (1996) 17850-17857.

[224] T. Zambelli, J. Trost, J. Wintterlin, and G. Ertl. *"Diffusion and Atomic Hopping of N AAtoms on Ru(0001) Studied by Scanning Tunneling Microscopy"* Phys. Rev. Lett. **76** (1996) 795-798.

[225] T. Birchem, and M. Muhler. *"Ion Beam-Induced Dissociative Chemisorption of Nitrogen on Ru(0001)"* Surf. Sci. **334** (1995) L701-L704.

[226] H. Mortensen, E. Jensen, L. Diekhoner, A. Baurichter, A.C. Luntz, and V.V. Petrunin. *"State Resolved Inelastic Scattering of N_2 from Ru(0001)"* J. Chem. Phys. **118** (2003) 11200-11209.

[227] B. Hammer. *"Coverage Dependence of N_2 Dissociation at an N, O, or H Precovered Ru(0001) Surface Investigated with Density Functional Theory"* Phys. Rev. B: Condens. Matter **63** (2001) 205423/205421-205423/205428.

[228] A.B. Anton, N.R. Avery, T.E. Madey, and W.H. Weinberg. *"The Coadsorption of Nitrogen with Carbon Monoxide and Oxygen on the Ruthenium(001) Surface: Local Chemical Interactions in Mixed Overlayers"* J. Chem. Phys. **85** (1986) 507-518.

[229] M. Gruyters, and K. Jacobi. *"High-Resolution Electron Energy Loss Spectroscopy Study of Chemisorbed and Physisorbed N_2 on Ru(1,0, -1 ,0)"* Surf. Sci. **336** (1995) 314-320.

[230] P. Feulner, and D. Menzel. *"Unusual Coverage Dependence of a Sticking Coefficient: Nitrogen/Ruthenium(001)"* Phys. Rev. B: Condens. Matter **25** (1982) 4295-4297.

[231] C.M. Chan, R. Aris, and W.H. Weinberg. *"An Analysis of Thermal Desorption Mass Spectra. I"* Applications of Surface Science (1977-1985) **1** (1978) 360-376.

[232] H. Dietrich, K. Jacobi, and G. Ertl. *"Vibrational Analysis of the NH + N Coadsorbate on Ru(0001)"* Surf. Sci. **377-379** (1997) 308-312.

[233] H. Rauscher, K.L. Kostov, and D. Menzel. *"Adsorption and Decomposition of Hydrazine on Ruthenium(001)"* Chem. Phys. **177** (1993) 473-496.

[234] B. Hammer. *"Bond Activation at Monatomic Steps: NO Dissociation at Corrugated Ru(0001)"* Phys. Rev. Lett. **83** (1999) 3681-3684.

[235] K. Honkala, A. Hellman, I.N. Remediakis, A. Logadottir, A. Carlsson, S. Dahl, C.H. Christensen, and J.K. Nørskov. *"Ammonia Synthesis from First-Principles Calculations"* Science **307** (2005) 555-558.

[236] L. Romm, O. Citri, R. Kosloff, and M. Asscher. *"A Remarkable Heavy Atom Isotope Effect in the Dissociative Chemisorption of Nitrogen on Ru(001)"* J. Chem. Phys. **112** (2000) 8221-8224.

[237] Z. Cao, H. Wan, and Q. Zhang. *"Density Functional Characterization of N_2 Dissociation on the Step of Ruthenium Clusters"* J. Chem. Phys. **119** (2003) 9178-9182.

[238] M.J. Murphy, J.F. Skelly, A. Hodgson, and B. Hammer. *"Inverted Vibrational Distributions from N_2 Recombination at Ru(001): Evidence for a Metastable Molecular Chemisorption Well"* J. Chem. Phys. **110** (1999) 6954-6962.

[239] M.E. Brubaker, and M. Trenary. *"Analysis of Dipole-Dipole Coupling in Isotopic Mixtures of molecular Nitrogen on Nickel(110)"* J. Chem. Phys. **90** (1989) 4651-4659.

[240] M.E. Brubaker, and M. Trenary. *"Dipole-Dipole Coupling in the Nitrogen Overlayer on Nickel(110)"* J. Electron Spectrosc. Relat. Phenom. **44** (1987) 47-54.

[241] M.E. Brubaker, and M. Trenary. *"Adsorbate Ordering Processes and Infrared Spectroscopy: an FT-IRAS Study of Molecular Nitrogen Chemisorbed on the Nickel (110) Surface"* J. Chem. Phys. **85** (1986) 6100-6109.

[242] A. Quick, V.M. Browne, S.G. Fox, and P. Hollins. *"Interactions of Nitrogen Molecules Adsorbed on Smooth and Roughened Nickel(111) Surfaces"* Surf. Sci. **221** (1989) 48-60.

[243] M. Bertolo, and K. Jacobi. *"Adsorption of Nitrogen on the Palladium(111) Surface at 20 K. I. Chemisorption and Physisorption in the Monolayer"* Surf. Sci. **265** (1992) 1-11.

[244] J.J. Mortensen, Y. Morikawa, B. Hammer, and J.K. Nørskov. *"Density Functional Calculations of N_2 Adsorption and Dissociation on a Ru(0001) Surface"* J. Catal. **169** (1997) 85-92.

[245] J.J. Mortensen, Y. Morikawa, B. Hammer, and J.K. Nørskov. *"A Comparison of N_2 and CO Adsorption on Ru(001)"* Z. Phys. Chem. (Munich) **198** (1997) 113-122.

[246] P.E. Blöchl. *"Projector Augmented-Wave Method"* Phys. Rev. B: Condens. Matter **50** (1994) 17953-17979.

[247] G. Kresse, and D. Joubert. *"From Ultrasoft Pseudopotentials to the Projector Augmented-Wwave Method"* Phys. Rev. B: Condens. Matter **59** (1999) 1758-1775.

[248] J.P. Perdew, K. Burke, and M. Ernzerhof. *"Generalized Gradient Approximation Made Simple"* Phys. Rev. Lett. **77** (1996) 3865-3868.

[249] S. Efrima. *"Vibrational Behavior of Molecules Adsorbed on Metallic Surfaces: the Role of Metal-Molecule Charge Transfer"* Surf. Sci. **114** (1982) L29-L34.

[250] S. Efrima, and H. Metiu. *"The Role of the Electrostatic Interaction in Shifting the Vibrational Frequencies for Two Adsorbed Molecules"* Surf. Sci. **109** (1981) 109-126.

[251] G. Blyholder. *"Molecular Orbital View of Chemisorbed Carbon Monoxide"* J. Phys. Chem. **68** (1964) 2772-2778.

[252] G.D. Mahan, and A.A. Lucas. *"Collective Vibrational Modes of Adsorbed Carbon Monoxide"* J. Chem. Phys. **68** (1978) 1344-1348.

[253] M. Scheffler. *"The Influence of Lateral Interactions on the Vibrational Spectrum of Adsorbed Carbon Monoxide"* Surf. Sci. **81** (1978) 562-570.

[254] G. Blyholder. *"CNDO Model of Carbon Monoxide Chemisorbed on Nickel"* J. Phys. Chem. **79** (1975) 756-761.

[255] S. Durukanoglu, A. Kara, and T.S. Rahman. *"Local Structural and Vibrational Properties of Stepped Surfaces: Cu(211), Cu(511), and Cu(331)"* Phys. Rev. B: Condens. Matter **55** (1997) 13894-13903.

[256] S. Durukanoglu, and T.S. Rahman. *"Atomic Relaxations and Thermodynamics on Cu(410)"* Surf. Sci. **409** (1998) 395-402.

[257] D. Farkas, R. Politano, and I.C. Oppenheim. *"Atomistic Structure of Stepped Surfaces"* Surf. Sci. **360** (1996) 282-288.

[258] P. Jiang, F. Jona, and P.M. Marcus. *"Step Profiles Predicted with the Modified Point-Ion Model for Eight Face-Centered- and Body-Centered-Cubic Surfaces"* Phys. Rev. B **35** (1987)

[259] A. Kara, P. Staikov, T.S. Rahman, J. Radnik, R. Biagi, and H.-J. Ernst. *"High-Frequency Phonon Modes on Stepped and Kinked Cu Surfaces: Experiments and Theory"* Phys. Rev. B: Condens. Matter **61** (2000) 5714-5718.

[260] C.Y. Wei, S.P. Lewis, E.J. Mele, and A.M. Rappe. *"Structure and Vibrations of the Vicinal Copper(211) Surface"* Phys. Rev. B: Condens. Matter **57** (1998) 10062-10068.

[261] M. Mavrikakis, B. Hammer, and J.K. Nørskov. *"Effect of Strain on the Reactivity of Metal Surfaces"* Phys. Rev. Lett. **81** (1998) 2819-2822.

[262] H.P. Bonzel, A.M. Bradshaw, G. Ertl, and Editors. Materials Science Monographs, 57: Physics and Chemistry of Alkali Metal Adsorption, (1989).

[263] H.P. Bonzel. *"Alkali-Metal-Affected Adsorption of Molecules on Metal Surfaces"* Surf. Sci. Rep. **8** (1987) 43-125.

[264] H.P. Bonzel. *"Alkali-Promoted Gas Adsorption and Surface Reactions on Metals"* J. Vac. Sci. Technol., A **2** (1984) 866-872.

[265] R.D. Diehl, and R. McGrath. *"Structural Studies of Alkali Metal Adsorption and Coadsorption on Metal Surfaces"* Surf. Sci. Rep. **23** (1996) 43-172.

[266] I.A. Bönicke, F. Thieme, and W. Kirstein. *"The Interaction of Carbon Monoxide with the Pure and Potassium-Promoted Cu(332) Surface"* Surf. Sci. **395** (1998) 138-147.

[267] C. Mundt, and C. Benndorf. *"The Coadsorption of Sodium and Water on Ni(s)(111)"* Surf. Sci. **307-309** (1994) 28-33.

[268] C. Mundt, and C. Benndorf. *"H_2O Adsorption on Alkali (Li, Na and K) Precovered Ni(775)"* Surf. Sci. **405** (1998) 121-137.

[269] A.G. Norris, M.J. Scantlebury, A.W. Munz, T. Bertrams, E. Dudzik, P. Finetti, P.W. Murray, and R. McGrath. *"An STM study of the Potassium-Induced Removal of the Ni(100)(2*2)p4g-N Reconstruction"* Surf. Sci. **424** (1999) 74-81.

[270] Y.K. Kim, G.A. Morgan, Jr., and J.T. Yates, Jr. *"Unexpected Low-Temperature CO Dissociation on Ru by Li Promoter Atoms"* Chem. Phys. Lett. **422** (2006) 350-353.

[271] M. Gierer, H. Over, H. Bludau, and G. Ertl. *"Incommensurate Structures and Epitaxial Growth of Li on Ru(0001): a Quantitative Low Energy Electron Diffraction Study"* Phys. Rev. B: Condens. Matter **52** (1995) 2927-2934.

[272] H.D. Ebinger, H.J. Jänsch, C. Polenz, B. Polivka, W. Preyss, V. Saier, R. Veith, and D. Fick. *"NMR Observation of Diffusion Barriers for Lithium Adsorbed on Ru(001)"* Phys. Rev. Lett. **76** (1996) 656-659.

[273] R. Smoluchowski. *"Anisotropy of the Electron Work Function of Metals"* Phys. Rev. **60** (1941) 661-674.

[274] N. Al-Sarraf, J.T. Stuckless, and D.A. King. *"Direct Measurement of Potassium-Promoted Change in Heat of Adsorption of Carbon Monoxide on Nickel(100)"* Nature **360** (1992) 243-245.

[275] E. Wimmer, C.L. Fu, and A.J. Freeman. *"Catalytic Promotion and Poisoning: All-Electron Local-Density-Functional Theory of Carbon Monoxide on Nickel(001) Surfaces Coadsorbed with Potassium or Sulfur"* Phys. Rev. Lett. **55** (1985) 2618-2621.

[276] D. Heskett, I. Strathy, E.W. Plummer, and R.A. De Paola. *"Photoemission and Electron Energy Loss Spectroscopy Investigation of Carbon Monoxide + Potassium/Copper(100)"* Phys. Rev. B: Condens. Matter **32** (1985) 6222-6237.

[277] M. Filali Baba, C. Mijoule, N. Godbout, and D.R. Salahub. *"Coadsorption of K and CO on Pd Clusters: a Density Functional Study"* Surf. Sci. **316** (1994) 349-358.

[278] J.K. Nørskov, S. Holloway, and N.D. Lang. *"Microscopic model for the poisoning and promotion of adsorption rates by electronegative and electropositive atoms"* Surf. Sci. **137** (1984) 65-78.

[279] R.A. DePaola, J. Hrbek, and F.M. Hoffmann. *"Potassium Promoted Carbon-Oxygen Bond Weakening on Ruthenium(001). I. Through-Metal Interaction at Low Potassium Precoverage"* J. Chem. Phys. **82** (1985) 2484-2498.

[280] L. Bech, J. Onsgaard, S.V. Hoffmann, and P.J. Godowski. *"CO Dissociation on K-Modified Cu(112) and Cu(117)"* Surf. Sci. **482-485** (2001) 243-249.

[281] A. Cupolillo, G. Chiarello, F. Veltri, D. Pacile, M. Papagno, V. Formoso, E. Colavita, and L. Papagno. *"CO Dissociation and CO_2 Formation Catalysed by Na Atoms Adsorbed on Ni(111)"* Chem. Phys. Lett. **398** (2004) 118-122.

[282] J. Onsgaard, S.V. Hoffmann, P.J. Godowski, P. Moller, J.B. Wagner, A. Groso, A. Baraldi, G. Comelli, and G. Paolucci. *"Dissociation of CO and Formation of Carbonate on a Stepped, K-Modified Cu(115) Surface"* Chem. Phys. Lett. **322** (2000) 247-254.

[283] H.J. Jänsch, C. Polenz, C. Bromberger, M. Detje, H.D. Ebinger, B. Polivka, W. Preyss, R. Veith, and D. Fick. *"The Interaction of CO and Li at a Ru(001) Surface. A Thermal Desorption Study"* Surf. Sci. **495** (2001) 120-128.

[284] L.H. Dubois, B.R. Zegarski, and H.S. Luftman. *"Complex Carbon Monoxide-Potassium Interactions on Copper(100): An Electron Energy Loss, Thermal Desorption, and Work Function Study"* J. Chem. Phys. **87** (1987) 1367-1375.

[285] A.J. Freeman, C.L. Fu, and E. Wimmer. *"Total Energy All-Electron Theory of Surface Structural, Electronic, and Magnetic Properties"* J. Vac. Sci. Technol., A **4** (1986) 1265-1270.

[286] R. Tero, T. Sasaki, and Y. Iwasawa. *"CO Adsorption on c(2*2)-Li/Cu(100). Interaction between CO and Li on Unreconstructed Cu(100) Surfaces"* Surf. Sci. **448** (2000) 250-260.

[287] K.J. Uram, L. Ng, and J.T. Yates, Jr. *"Electrostatic Effects between Adsorbed Species - the Potassium-Carbon Monoxide Interaction on Nickel(111) as Studied by Infrared Reflection-Absorption Spectroscopy"* Surf. Sci. **177** (1986) 253-277.

[288] H.J. Jänsch, C. Huang, A. Ludviksson, J.D. Redding, H. Metiu, and R.M. Martin. *"Lithium Promoted Adsorption of Carbon Monoxide on Silver/Ruthenium(001)"* Surf. Sci. **222** (1989) 199-212.

[289] J. Onsgaard, L. Bech, C. Svensgaard, P.J. Godowski, and S.V. Hoffmann. *"Reactions on Alkali-Modified Low-Index Stepped Cu Surfaces"* Prog. Surf. Sci. **67** (2001) 205-216.

[290] Y.K. Kim, G.A. Morgan, Jr., and J.T. Yates, Jr. *"Enhancement of Catalytic Promotion Action of Li on Ru by Atomic Steps - Comparison of CO Dissociation on Ru(109) and Ru(001)"* Chem. Phys. Lett. **431** (2006) 317-320.

[291] K.J. Uram, L. Ng, M. Folman, and J.T. Yates, Jr. *"Direct Vibrational Spectroscopic Observations of Mixed Long Range and Short Range Adsorbate Interactions: the Potassium + Carbon Monoxide Interaction on Nickel(111)"* J. Chem. Phys. **84** (1986) 2891-2895.

[292] A careful search of the literature from 1965-2006 has been carried out using the keywords nitrogen, adsorption, alkali metal, and compound. No evidence of Li-N_2 compound formation has been reported.

[293] L.J. Whitman, C.E. Bartosch, W. Ho, G. Strasser, and M. Grunze. *"Alkali-Metal Promotion of a Dissociation Precursor: Molecular Nitrogen on Iron(111)"* Phys. Rev. Lett. **56** (1986) 1984-1987.

[294] C.C. Cheng, R.M. Wallace, P.A. Taylor, W.J. Choyke, and J.T. Yates, Jr. *"Direct Determination of Absolute Monolayer Coverages of Chemisorbed Acetylene and Ethylene on Silicon(100)"* J. Appl. Phys. **67** (1990) 3693-3699.

[295] D.A. King, and M.G. Wells. *"Molecular Beam Investigation of Adsorption Kinetics on Bulk Metal Targets. Nitrogen on Tungsten"* Surf. Sci. **29** (1972) 454-482.

[296] R.L. Kurtz, N. Usuki, R. Stockbauer, and T.E. Madey. *"Measurements of Electron Attenuation Lengths in Condensed Molecular Solids"* J. Electron Spectrosc. Relat. Phenom. **40** (1986) 35-58.